LEES, L.
KUBOTA, T.
SIGAL, A.

STABILITY THEORY FOR CROSS-HATCHING

Part II. An Experiment on Turbulent Boundary Layer over a Wavy Wall

by

L. Lees, T. Kubota, and A. Sigal

California Institute of Technology

Pasadena, California 91109

Contract No. F 04701-68-C-0151

TECHNICAL REPORT SAMSO TR 72-34 Vol. II

Distribution limited to U. S. Government agencies only; test and evaluation 14 Feb. 72. Other requests for this document must be referred to SAMSO (RSSE).

SPACE AND MISSILE SYSTEMS ORGANIZATION

AIR FORCE SYSTEMS COMMAND

Norton Air Force Base, California 92409

CIT, Misc.

STABILITY THEORY FOR CROSS-HATCHING

Part II. An Experiment on Turbulent Boundary Layer over a Wavy Wall

by

L. Lees, T. Kubota, and A. Sigal

California Institute of Technology

Pasadena, California 91109

Contract No. F 04701-68-C-0151

TECHNICAL REPORT SAMSO TR 72-34 Vol. II

Distribution limited to U. S. Government agencies only; test and evaluation 14 Feb. 72. Other requests for this document must be referred to SAMSO (RSSE).

SPACE AND MISSILE SYSTEMS ORGANIZATION

AIR FORCE SYSTEMS COMMAND

Norton Air Force Base, California 92409

FOREWORD

This report was prepared by the California Institute of Technology, Pasadena, California under USAF Contract F04701-68-C-0151, Project "Research on Fluid Mechanics of Striation Ablation." The work was administered under the direction of the Space and Missile Systems Organization, Air Force Systems Command.

This report covers work performed between 1 September 1968 to 15 August 1971.

Professors Lester Lees and Toshi Kubota were the Co-Principal Investigators, and Mr. Asher Sigal was a Graduate Research Assistant.

The manuscript of this report was released by the authors in January 1972.

This technical report has been reviewed and is approved.

ABSTRACT

An experimental investigation of turbulent boundary layer flow over wavy surfaces was conducted at low speed. Two models with the ratio of the amplitude to the wave length $a/\lambda = 0.03$ and wave lengths $\lambda = 6''$ and $12''$ were tested in an open-circuit wind tunnel. The free stream velocity was 15.4 m/sec, giving Reynolds number $Re = 2.54 \times 10^4$ per inch. Boundary-layer thickness varied from $\delta = 1.5''$ to $\delta = 4.1''$ by means of boundary-layer trips of various height, in order to change the ratio λ/δ. The following measurements were taken: wall pressure distribution, average velocity and turbulence level, wall stress distribution, static and total pressures, and shear stress distribution across the layer.

Wall pressure perturbation is much lower than predicted by uniform, inviscid theory and is slightly non-symmetric. Wall stress distribution has a peak with $C_f/C_{f_o} = 1.2$ upstream of the crest and a dip of $C_f/C_{f_o} = 0.6$ upstream of the trough.

The turbulence intensities and shear stress distributions near the wall show oscillatory modulation superimposed on the reference flat plate profiles. The amplitude of the oscillations decays exponentially toward the edge of the layer, so that in the outer part of the layer the turbulence quantities are practically independent of the longitudinal position.

TABLE OF CONTENTS

Table of Contents (Cont'd)

Table of Contents (Cont'd)

LIST OF FIGURES

List of Figures (Cont'd)

List of Figures (Cont'd)

LIST OF SYMBOLS

A, B, C, D	calibration constants of X-array hot-wire probe
A^1	constant in Van Driest damping factor
a	amplitude of wavy wall
C	constant in Coles' Law of the Wall (= 5.0)
C_D	drag coefficient
C_f	$\tau_w / \frac{1}{2} \rho U_0^2$, skin friction coefficient
C_τ	$\tau / \frac{1}{2} \rho U_0^2$, turbulent shear stress coefficient
C_p	$(p-p_0) / \frac{1}{2} \rho U_0^2$, pressure coefficient
C_o	Integration constant (Appendix B)
d	Stanton tube dimension
E	hot-wire probe output voltage
H	height of test section
H	δ^* / ϑ, form factor
h	boundary layer compensation height (Sec. II.6)
K	calibration constant
ℓ	mixing length
ℓ_s	mixing length based on Sawyer's theory
ℓ^t	mixing length based on total velocity
p	pressure
p_d	$\frac{1}{2} \rho U_0^2$, dynamic pressure
p_m	probe's measured pressure (Sec. II.4)
p_p	Preston probe pressure
p_s	static pressure
p_t	Pitot pressure
p_w	wall pressure

List of Symbols (Cont'd)

p_o	reference pressure (measured at STN 5, sidewall port)
Q	resultant velocity (Sec. II. 7)
q	$(\overline{u}'^2 + \overline{v}'^2 + \overline{w}'^2)^{\frac{1}{2}}$
R	radius of curvature
u, v, w	velocity components
u_r	reference velocity (Sec. V. 1)
u′, v′, w′	turbulent velocity components
U_0	reference velocity freestream velocity measured at STN $4\frac{1}{2}$)
U^t	$(\overline{U}^2+2(p-p_o)/\rho)^{\frac{1}{2}}$, total velocity (Sec. V. 4)
u_τ	$(\tau_w/\rho)^{\frac{1}{2}}$, friction velocity
u+	u/u_τ, normalized velocity
X	Mellor-Herring parameter (Sec. V. 7)
x	coordinate along centers of surface wave
y	distance from wavy wall
y_s	surface of wavy wall
y_w	wall layer thickness (Appendix B)
y+	$y\, u_\tau/\nu$, normalized distance from the wall
α	$2\pi/\lambda$
β	$\delta^* dp/dx/\tau_w$, Clauser's parameter
δ	boundary layer thickness
δ^*	displacement thickness
ϵ	eddy viscosity
ϵ	$2\pi a/\lambda$
η	integration variable

List of Symbols (Cont'd)

θ	momentum thickness
ϑ	inclination angle
κ	von Kármán constant (= 0.41)
λ	wave length
μ	u_τ / U_0
μ	dE/du, X-array probe calibration curve slope
ν	kinematic viscosity
$\overline{\pi}$	wake constant in Law of the Wake
ρ	air density
σ	slope (Sec. V.4)
τ	turbulent shear stress
τ_w	wall shear stress
φ	velocity potential
χ	Mellor-Herring parameter (Sec. V.7)
ψ	streamline coordinate

Abbreviations

STN	station of survey (measured in ft. along test section)
STN ( )	station of survey (along wavy wall, Sec. IV.1)
WW	wavy wall model
meas.	measured value

Superscripts

$-$	average value
$'$	R.M.S. value
t	based on total velocity

I. INTRODUCTION

In the last few years a study was conducted at GALCIT in connection with the phenomena of cross-hatching ablation. This phenomena is the formation of diamond shaped waves on surfaces undergoing ablation in flight test and in a variety of ground test facilities, for many types of ablative materials. The surface waves have characteristic length and sweep angle with respect to the flow direction. At the present time, the phenomena is not yet completely understood. In particular, it has not yet been established whether the phenomena is a reflection of a periodic phenomena in the structure of supersonic turbulent boundary layer or a result of unstable interaction between the flow and the ablation process. But, regardless of the initiation of the surface pattern, it is commonly agreed that the process of the growth of waves has to be considered as a closed loop cycle, i.e., once striation starts the resulting change in surface geometry is fed back into the boundary layer, causing significant changes in the distribution of such aerodynamic quantities as pressure, wall stress and heat transfer that are responsible for the formation of the surface waves.

In order that one can close the loop of the process, it is necessary to be able to evaluate the interaction between turbulent boundary layer and a wavy wall. The present study is aimed at this interaction. Before proceeding to describe the specific goals of the experiment, the state of art of such computation is briefly reviewed. This survey is based on the proceedings of the AFOSR-IFP-Stanford Conference on Computation of Turbulent Boundary Layers.[1]

Computational methods of turbulent boundary layers are usually divided into two groups: integral methods and differential methods. Because of the curvature of the streamlines, it is apparent that the velocity profiles commonly used in integral methods (e.g., Coles' Law of the Wake, Power Law) will not properly describe the situation. Also, the validity of the friction laws applicable to flat surfaces (e.g. Ludwig and Tillmann)[10] is in doubt. Therefore, studies performed at GALCIT were devoted to the development of differential computational methods.*

The differential methods depend on some models that relate Reynolds stresses to the flow conditions. These commonly used models relate the turbulent stresses either to the mean flow quantities or to the turbulent energy. Common to all the methods is the use of empirical functions and constants. Most of these functions and constants were derived from the results of experiments with boundary layers over flat surfaces.

A serious question constantly asked is the validity of these laws: How much can their range of applicability be stretched? More specifically for the present problem: May these laws be used where curvature effects are of importance?

Curvature effect on turbulent boundary layer was the topic of several investigations. Wattendorf[3] studied a fully developed turbulent flow in a channel. He found that the eddy viscosity and the mixing length increase near the outer wall and decrease near the inner wall of the curved channel. He also found a strong change in shape parameter

---

* Kubota, T., "Analysis of Turbulent Boundary Layer Over Wavy Surface," in preparation.

of the inner and outer boundary layers through changes of the exponent in the power law. Later Eskinazi[4] conducted a similar study using hot wire anemometry. He found strong changes in the turbulence intensities and in the Reynolds stresses between the inner and outer walls of the channel. Sawyer[5] devised a first order theory for the effect of curvature on the mixing process. His theory is based on the modification of mixing length by the presence of centrifugal acceleration.

Two publications, based on experimental studies, apply directly to the present interaction problem. Motzfeld[6] studied turbulent boundary layer flow over five different wave shapes. He found strong changes in velocity profiles, mainly near the crest and the trough. More recently Kendall[7] studied the interaction between turbulent boundary layer and a moving wavy wall. Through an extensive use of hot wire anemometry, he showed strong modulation of turbulent intensities, and appreciable phase shift of the Reynolds stress and wall shear with respect to the surface wave. These findings indicate that, indeed, the problem at hand cannot be treated as equilibrium flow. This conclusion encouraged the decision to proceed with wind tunnel experiments aimed at better understanding of the wave-boundary layer interaction.

One of the keys to the understanding of the origin of cross-hatching ablation is the mechanism of selection of wave length. One suggestion is that there exists a preferred wave length, which gives the largest amplification rate and therefore shows up first and dominates the surface pattern. One of the objectives of the test is to find out whether indeed the spacing ratio λ/δ is of importance in modulating

the turbulent intensities, especially the Reynolds stresses and wall stress.

A compilation of the transverse spacing and surface pattern angle is found in Figures (11) and (12) of reference.[2] Typically, the transverse spacing ratio is 2 to 4 times the boundary layer thickness. It was decided to cover this ratio in the present text.

Preliminary velocity survey on the floor of the test section showed that by tripping boundary layer thickness can be changed between 2" to 4". It was decided to build two models, with wave lengths of 6" and 12", so that the ratio λ/δ of 1.5 to 6 can be covered. Based on the results of Motzfeld[6] and Kendall,[7] amplitude to wave length ratio of 0.03 was chosen, since for this value, appreciable changes in all flow quantities occur, but without any separation.

II. TEST FACILITY AND INSTRUMENTATION

II. 1. Wind Tunnel

The experiment was conducted at JPL* in an open circuit, low speed wind tunnel. The test section is 2' x 2' by 10' long. The majority of tests were carried out at a free stream speed of 15.4 m/sec.

The wind tunnel is driven by a constant-speed motor, which is linked by a magnetic clutch to a fan. The rate of rotation of the fan is determined by the amount of slip in the clutch, which is set by a speed controller. The driving section of the tunnel leads to a 6.5' x 6.5' settling chamber equipped with eight layers of fine mesh screen, followed by a contraction section and the test section. The general view and dimensions of the wind tunnel are shown in Figure (1). A photograph of the experimental setup is shown in Figure (2).

The test section was designed and built especially for the present experiment. It is constructed of plywood sheets, framed in a welded aluminum structure. The wood was sealed and polished to a smooth surface. The front panel of the test section is a lucite plate, to allow optical measurements. The floor of the test section is supported on an adjustable frame, which is hinged at the upstream edge. This provision was made in order to allow constant pressure test section, as will be explained in detail in Section II. 6.

A traverse mechanism is mounted on a wide channel section, which rests on the top of the test section. It can slide by hand from STN 4 to STN 9.5. The arm of the mechanism, which carries the

---

* Jet Propulsion Laboratory, California Institute of Technology, Pasadena, California.

probes, protrudes through a slit along the center of the ceiling. The slit can be sealed by thin plastic strips to prevent spillage. The arm is driven by a lead screw, powered by a D. C. motor. The motor is driven by a variable speed controller. The stroke of the arm is 8". A mechanical counter is geared to the lead screw and is used to indicate the vertical position of the probes, with accuracy of 0.001".

A cathetometer with accuracy of 0.05 mm is used to obtain the initial position of the probes, above the surface, at the beginning of each run.

The wind-tunnel is located in an air conditioned laboratory. Room temperature was kept 73 ± 2° F. The barometric pressure was measured several times during the test period, and was found 729 ± 1 mm Hg. For these conditions:

$$\rho = 0.1188 \text{ Kg/m}^2/\text{sec.}^2 \quad ,$$

$$\nu = 0.000605 \text{ m in/sec.} \quad .$$

II. 2. Wavy Wall Models

Two models were designed and built for the present test, both with nominal amplitude to wave length ratio of 0.03. Each has five waves, with the following lengths:

$$WW1 : \lambda = 12" \quad ,$$

$$WW2 : \lambda = 6" \quad .$$

The models were constructed by using the following technique (see Figure (3) for details): An aluminum frame, 24" wide and 5 x λ" long was built out of flat material. On the two side frames, holes were

drilled, with their centers along a sine curve of the desired amplitude and wave length. Two layers of aluminum sheeting were deformed to the sine-curve shape and held in place by pairs of rods spanning the frame through the holes on the sides. Epoxy cement was applied, in generous quantities, on the underside of the lower sheet, thus glueing the sheet, the lower rods and the frame into a solid unit. After the epoxy was cured, the upper rods and sheet were removed.

For the measurement of wall pressure, a row of ports, 0.020" in diameter were drilled 0.5" off the centerline of the models. The spacing is 1" for WW1 and 0.75" for WW2. This operation was done on a milling machine to assure accuracy in spacing the ports. At the time that the models were mounted on the milling machine, the wave form was measured with a 0.001" accuracy indicator. It was found that because of the deformation of the rods, the actual amplitude of the wave is lower than planned. But, measurement in several transverse planes showed that the center 20" of the models were flat in this direction. The measured wave form is shown in Figure (4) from which it was found:

WW 1: $a = 0.335"$, $a/\lambda = 0.0279$

WW 2: $a = 0.157"$, $a/\lambda = 0.0261$.

Finally, the models were polished to a shiny, wax coated surface.

For a surface shape

$$y_s = -a \sin\left(\frac{2\pi x}{\lambda}\right)$$

the radius of curvature is

$$R = \frac{(1 + y'^2)^{\frac{3}{2}}}{y''}$$

$$= \frac{1 + \left(2\pi \frac{a}{\lambda}\right)^2 \cos^2\left(\frac{2\pi x}{\lambda}\right)^{\frac{3}{2}}}{-a\left(\frac{2\pi}{\lambda}\right)^2 \sin\left(\frac{2\pi x}{\lambda}\right)} \quad .$$

The minimum (absolute value) of the radius of curvature is

$$R_{min} = \frac{a}{\left(2\pi \frac{a}{\lambda}\right)^2} \quad ,$$

which for the two models give:

WW 1: $R_{min} = 10.3''$,

WW 2: $R_{min} = 5.8''$.

II. 3. Wind-Tunnel Boundary Corrections

The linearized velocity potential of inviscid flow over a wavy wall is (i. e. [8]):

$$\varphi_0 = U_0 a \sin\left(\frac{2\pi x}{\lambda}\right) e^{-\frac{2\pi y}{\lambda}} \quad .$$

On the other hand, for a channel formed by a wavy wall of the same amplitude and a straight wall at a distance H apart is:

$$\varphi_1 = U_0 a \sin\left(\frac{2\pi x}{\lambda}\right) e^{-\frac{2\pi y}{\lambda}} \frac{1+e^{4\pi \frac{y-H}{\lambda}}}{1+e^{-\frac{4\pi H}{\lambda}}} \quad .$$

Though the wavy wall models are finite in length, the ratio of the two expressions given above will be used as a measure to the possible effect of the top wall of the test section

$$\frac{\varphi_1}{\varphi_0} = \frac{1+e^{4\pi\frac{y-H}{\lambda}}}{1+e^{-\frac{4\pi H}{\lambda}}}$$

For H = 24", and λ = 6" or 12", this ratio is practically a unity near the wavy wall ($y \sim 0$) and up to the center of the test section ($y \sim \frac{1}{2}H$). Hence it is concluded that the top wall effect is null.

II. 4. Pressure Measurement

The heart of the pressure measurement system is a Statham* transducer with a range of ± 0.2 PSID. The sensitive element of this transducer is a four arm strain gage bridge. The excitation voltage to the bridge is provided by a regulated D. C. power supply, operated with a battery connected as an external reference. See Figure (6). This arrangement assures excellent stability of the supply voltage. The output of the bridge is amplified and filtered, and then read by a digital voltmeter. The same voltmeter is used to adjust the bridge input voltage before each test.

A Betz, silicon-oil micromanometer, is used to calibrate the transducer. The readout is accurate to 0.02 mm. The electronic circuit that was described above was used during the calibration.

The transducer (P5TC-0.2D-350) was calibrated at the beginning of the test giving the constant K = 5.5017 gr/cm^2/mV at 12V input. The deviation from linearity and zero shift were less than 0.1% of full scale. Two calibration checks were done during the test, which showed deviations of less than 0.2% in K.

---

* Statham Instrument Co., Los Angeles, California

II. 5. Calibration of the Test Section

The goal of this calibration is to establish relation between the airspeed in the test section and the setting of the driving fan's speed control. Such relation is essential for the calibration of the hot-wire and pressure probes, as will be discussed below.

Calibration tests were run with plain floor mounted parallel to the ceiling, with a boundary layer trip T = 0.5" mounted 6" upstream of the entrance to the test section.

A Pitot tube was mounted at STN 5, at the center of the test section, aligned along its axis. The transducer and measuring system described in Section II. 4. were used to measure directly the dynamic pressure as the difference between the Pitot pressure and the static pressure from the sidewall port at the same station. The airspeed is computed from $p_d = \frac{1}{2} \rho U^2$. Figure (7) shows the result of the calibration.

Repeatability of the airspeed was tested by turning the tunnel on and off several times. Stability was tested by running it for a long time ($\sim$ 1 hr.). Both tests showed that at speed control 7, variations in airspeed are within $\pm$ 1%.

II. 6. Compensation for Boundary Layer Growth

The thickening of the boundary layer along the walls of a parallel test section causes a reduction in the effective cross section area, by displacement effect. This forces the flow to accelerate and the static pressure to decrease in downstream direction. The effect is unwanted in the present experiment and an attempt was made to compensate for it.

In order to maintain a constant pressure test section, the floor is tilted such that it forms a slightly divergent tunnel. For complete cancellation of the unwanted pressure gradient, the increase in cross section area must be equal to the increase in boundary layer displacement.

The amount of divergence was determined experimentally for the four boundary layer trips that were used in the test. It was done according to the following procedure: The static pressure was measured along the center of the back side wall of the tunnel at STN's 6, 7, 8 and 9, with STN 5 as reference, while the exit end of the floor was lowered by h_c = 0, 1" and 2". Then, by interpolation followed by trial and error the best h_c was found, for minimum variation of static pressure along the test section. Sample results (for T = 0.5") of the process, together with the geometrical data are given in Figure (8). The values of h_c, for the other cases are:

T (in)	h_c (in)
0.05	0.7
0.25	0.5
0.50	0.9
0.75	0.7

Note that Figure (8) shows a slight scatter in the static pressure distribution along the test section. This was found repeatable and caused by small waviness in the back wall plate. The pressure gradients associated with this are less than 1% of that generated by the wavy wall models, and hence are considered insignificant.

All the results presented below were taken with floor tilted for best boundary layer compensation.

II. 7. Velocity Measurements

Airspeed measurements were made by means of hot wire anemometry. The equipment is a constant temperature, linearized output set made by DISA.*

For the measurement of average velocity and turbulence level, type 55A25 miniature, straight prong, single sensor probe was used. The sensing wire is Pt-coated tungsten, 0.005 mm diameter by 1.2 mm long.

Two channels of measurement were used. Each channel consisted of a constant temperature anemometer, a linearizer and an RMS unit, as shown in Figure (9).

The probes were calibrated at the center of the test section, under the same conditions as described in Section II. 5. The results for three probes that were used in the test are shown in Figure (10).

A single element probe with its sensor parallel to the surface, does not distinguish between longitudinal (u) and normal (v) velocity components. Its output is proportional to the resultant velocity which is:

$$q = [(U + u')^2 + (V + v')^2]^{\frac{1}{2}}$$

Assume that $\overline{u'^2} \ll U^2$, $\overline{v'^2} \ll V^2$, the D. C. and R. M. S. values of this signal are proportional to:

---

* DISA - S and B, Inc., Franklin Lakes, New Jersey

$$\bar{Q} = (U^2 + V^2)^{\frac{1}{2}} \quad ,$$

$$Q' = \left(\frac{U^2}{U^2+V^2} \overline{u'^2} + \frac{V^2}{U^2+V^2} \overline{v'^2} + \frac{2UV}{U^2+V^2} \overline{u'v'} \right)^{\frac{1}{2}} \quad .$$

In order that distinction is made between results obtained by a single element and an X-array hot wire probe, notation ($\bar{Q}$, Q') will be used for the first one.

The readout of the anemometer's D.C. meter, the R.M.S. unit and the vertical position indicator were recorded on coding charts. The data was manually key-punched for computer processing and plotting.

II.8. Freestream Flow Conditions

In order to find the uniformity of the flow outside of the boundary layer, and its turbulence level, velocity survey was performed using a single sensor hot wire probe. The survey was done above plain floor, at STN 5, with boundary layer trip T = 0.5" and covered the range from 6" to 14" of distance from the floor.

The results are shown in Figure (11), from which the following is concluded: The deviation of the average velocity, from its value at the centerline, does not exceed 0.5%. The free stream turbulence level is 0.83%, but it exists only above the centerline of the test section. The turbulence level increases sharply toward the edge of the boundary layer.

III. TEST REFERENCE CONDITIONS

III. 1. Reference Boundary-Layer Profiles

As mentioned in the introduction, a trip was inserted about 6" upstream of the entrance to the test section in order to thicken the boundary layer. Square bars of different thicknesses were used, except one case: T = 0.75". It was found that such a thick trip generated velocity profile with practically no wake component and unusual turbulence distribution near the edge of the boundary layer. After trial and error, a 0.25" bar, mounted on 0.5" high legs gave good results. This combination trip is still referred to as 0.75" high.

The boundary layer on the plain floor was surveyed, by means of a single sensor probe, in order to provide knowledge about the oncoming flow and as reference to compare with. STN 6 and STN 7 were surveyed in order to serve as reference to WW2 and WW1 respectively. This is illustrated graphically in Figure (12). At each station, survey was carried out for three trip heights according to the following table:

T in.	U_e m/sec.	STN 6	STN 7
0.05	15.54		+
0.25	15.43	+	+
0.50	15.43	+	+
0.75	15.41	+	

The results are shown in Figure (13), where normalized average velocity ($\overline{U}/U_e$) and turbulence level (Q'/U_e) are plotted against distance from the wall on logarithmic scale. Note that all cases show maximum

turbulence level of about $Q'/U_e = 0.107$ at a distance 0.01-0.013" from the wall, depending on boundary layer thickness.

III. 2. Law of the Wake Fitting to the Data

To gain qualitative knowledge about the reference boundary layer profiles they were analyzed by fitting Coles'[9] Law of the Wake similarity profiles to the experimental data.

Recall, from[9] the Law of the Wake:

$$\frac{u}{u_\tau} = C + \frac{1}{\kappa} \ell n \left(\frac{y\, u_\tau}{\nu} \right) + 2 \frac{\bar{\pi}}{\kappa} \sin^2 \left(\frac{\pi}{2} \frac{y}{\delta} \right) \qquad (1)$$

with: $C = 5.0$

$\kappa = 0.41$

Parameter $\bar{\pi}$ can be eliminated from (1) by using edge conditions:

$$u = u_e \ @ \ y = \delta$$

$$2 \frac{\bar{\pi}}{\kappa} = \frac{u_e}{u_\tau} - C - \frac{1}{\kappa} \ell n \left(\frac{\delta u_\tau}{\nu} \right) \qquad (2)$$

Substitute (2) into (1), and one finds:

$$u = u_\tau \left[C + \frac{1}{\kappa} \left(\frac{y\, u_e}{\nu} \right) \right] + \left[u_e - u_\tau \left(C + \frac{1}{\kappa} \ell n \left(\frac{\delta\, u_\tau}{\nu} \right) \right) \right] \sin^2 \left(\frac{\pi}{2} \frac{y}{\delta} \right) \qquad (3)$$

Eq. (3) contains two parameters, namely u_τ and δ. A computer program was written to evaluate these parameters for least square deviation from the experimental data. Points with $y+ = y\, u_\tau / \nu < 60$ or $u/u_e > 1$ were omitted from the fitting process. The program uses a standard subroutine (LSQENP in CIT routine library) to find the desired parameters.

The best fit curves, together with the data, are shown in Figure (14) for all reference profiles. The presentation is in universal coordinates, i.e. $u+ = u/u_\tau$ vs. $y+ = y\, u_\tau/\nu$. The important parameters are tabulated below:

T in.	STN	U_τ m/sec	δ in.	$\bar{\pi}$	C_f
0.05	7	0.61	1.50	0.59	0.00301
0.25	6	0.59	1.96	0.51	0.00297
0.25	7	0.58	2.43	0.51	0.00286
0.50	6	0.60	3.08	0.21	0.00306
0.50	7	0.59	3.41	0.23	0.00298
0.75	6	0.61	3.70	0.23	0.00293

After knowing reference boundary layer thicknesses, it is possible to summarize the range of λ/δ parameter for the present test.

T in.	STN	δ in.	λ/δ for WW1	λ/δ for WW2
0.05	7	1.50	8.00	
0.25	6	1.96		3.06
0.25	7	2.43	4.93	
0.50	6	3.08		1.95
0.50	7	3.41	3.52	
0.75	6	3.70		1.62

III. 3. Boundary Layer Thickness and Shape Factor

The displacement thickness (δ^*) and the momentum thickness (θ), are uniquely determined by the thickness (δ) and the wake component coefficient ($\bar{\pi}$). But, since numerical integration was incorporated in the data processing program, the two quantities were evaluated this way. By definition:

$$\delta^* = \int_o^\delta \left(1 - \frac{u}{u_e}\right) dy \quad ,$$

$$\theta = \int_o^\delta \frac{u}{u_e}\left(1 - \frac{u}{u_e}\right) dy \quad .$$

The results, together with the shape factor $H = \delta^*/\theta$ are summarized in the table below.

Note that the reference profiles are not similar. The shape factor varies from 1.25 to 1.34.

T in.	STN	δ in.	δ^* in.	θ in.	H
0.05	7	1.50	0.226	0.189	1.34
0.25	6	1.96	0.282	0.213	1.33
0.25	7	2.43	0.344	0.262	1.31
0.50	6	3.08	0.356	0.284	1.25
0.50	7	3.41	0.388	0.307	1.27
0.75	6	3.70	0.425	0.334	1.27

A check on the quality of the reference profiles is a comparison between the actual skin friction coefficient and that evaluated by

Ludwig and Tillmann friction law.[10] This commonly used law predicts:

$$C_f = 0.246\ 10^{-0.678H}\ Re_\theta^{-0.268}$$

Coles' presentation of this law (Figure No. 11 of [9]), in terms of $\overline{\pi}$ rather than H is used. His correlation is plotted in Figure (15), on C_f-Re_θ coordinates.

For presentation of the test data, the following is used:
$C_f = 2(u_\tau/U_0)^2$ from results of fitting law of the wake to the data;
$Re_\theta = U_0\ \theta/\nu$ from results of integration reported before.

The comparison is shown in Figure (15). It is observed that present test data falls very close to the correlation, which shows that the oncoming boundary layer is fully turbulent and equilibrated.

IV. MEASUREMENTS AND RESULTS

The models were mounted in the test section with their front end at STN 5, as shown in Figure (12). The leading edge of the models is at the same height as the flat plate that composes the upstream part of the floor. In the case of the short WW2, another plate was installed behind the trailing edge to complete the floor to the full length of the test section.

The test was conducted with floor divergence as for the plain floor (Section II. 6).

IV. 1. Wall Pressure

The distribution of static pressure on the two models was measured by a series of ports, 0. 020" in diameter, located 0. 5" off of the center line. The ports are spaced 1" apart for WW1 and 0. 75" for WW2. The measurements were done for the different boundary layer trip heights, as mentioned in Section III. 2.

The transducer and measuring scheme that were described in Section II. 5 were used. The reference pressure is the port located at STN 5 on the side wall of the test section. The wall ports were connected in turns to the transducer.

The results were reduced to the non-dimensional form:

$$Cp_w = \frac{p_w - p_0}{\frac{1}{2} \rho U_0^2}$$

where p_0 is the reference pressure and U_0 is reference speed measured 6" ahead of the leading edge of the model outside the boundary layer.

Since the effect of boundary layer thickness upon wall pressure was found to be very small, the complete distribution is shown for one case only (T = 0.5") in Figure (16). For the two models, we observe that the first and last waves show lower pressure peaks than the three center waves that are about equal in shape and amplitudes. This reflects the surface shape as mentioned in Section II.2. Note that the first wave of WW2 had a local kink at $x \sim 5"$. This gave abnormal result that was not included.

A summary of all the cases for wave No. 3 only is given in Figure (17), together with results from other sources. The following observations are made:

(i) The maximum positive pressure peak is lower by 31% for WW1 and 20% for WW2 from the maximum negative value.

(ii) The positive part of the pressure curve occupies more than half wave: it covers 188° for WW1 and 191° for WW2.

(iii) The inviscid, uniform flow, linearized theory for flow over a wavy wall predicts

$$|Cp_w|_{\nu=0} = 4\pi \frac{a}{\lambda} \quad .$$

For the present models this gives

$$\text{WW1: } |Cp_w|_{\nu=0} = 0.352$$

$$\text{WW2: } |Cp_w|_{\nu=0} = 0.340 \quad .$$

The actual measured values are considerably lower than the above values. For example, for T = 0.5" we have:

Model	STN	$Cp_{w(meas.)}$	$\frac{Cp_{w(meas.)}}{Cp_{w(\nu=0)}}$
WW 1	max.	0.175	0.497
WW 1	min.	-0.255	0.725
WW 2	max.	0.155	0.440
WW 2	min.	-0.195	0.554

The asymmetry in pressure distribution gives rise to form drag, defined by:

$$C_{D_p} = \frac{1}{\lambda} \int_0^{\lambda} Cp_w \, y_s' \, dx \quad .$$

This integral was evaluated graphically for T = 0.5". The results for the two models are:

WW 1: $C_{D_p} = 0.0012$

WW 2: $C_{D_p} = 0.0017$.

Comparison between the present results and those of Kendall[7] and Motzfeld[6] shows consistency in the trough area. On the other hand, present measurements show lower crest pressure than expected from Kendall's presentation of reduced pressure coefficient (Figure 4 of [7]).

From the pressure curve, the following four stations were chosen for further survey inside the boundary layer:

STN	Defined by	Phase Angle (deg.)	
		WW1	WW2
(1)	$Cp_w = 0, dp/dx > 0$	-3	-5
(2)	Cp_w = max.	+6	+9
(3)	$Cp_w = 0, dp/dx < 0$	+5	+6
(4)	Cp_w = min.	+2	+5

IV. 2. Velocity Profiles

The first field survey was the measurement of average velocity profiles and turbulence level, using a single sensor hot-wire probe. Each of the two models was surveyed at the four stations, listed in the table given above.

The results of the survey are presented in two forms. The first (Figure (18)), on a linear y-scale with velocity and turbulence profiles, are shown at the station where they were taken. For comparison, the plain floor profiles and for reference the wall pressure are also shown. In the second form (Figure (19)), log (y)-scale is used, as is common for presentation of turbulent boundary layer data.

The following observations are typical to all the cases tested.

(i) At the crest, the velocity profiles are full at a very close distance from the wall. A typical value is $Q/U_0 = 0.7$ at $y = 0.025''$.

(ii) On the other hand, the trough profiles grow slowly near the wall. This shows also in a relatively low ($Q'/U_0 \sim 0.08$) turbulence level near the wall. At a distance of $0.15''$ from the wall turbulence and slope of velocity increase.

(iii) The two profiles corresponding to $Cp_w = 0$ have the same shape for distances from the wall larger than 0.15". Only in the wall layer they come apart, which shows also in differences in turbulence level near the wall.

(iv) Among the four stations surveyed, the largest turbulence level for WW1 was found at the crest, with $Q'/U_0 = 0.12$. For WW2, it takes place at the uphill slope with $Q'/U_0 = 0.13$.

(v) At distances from the wall where the reference profiles possess a semilogarithmic section, the present profiles show a small degree of waviness. This phenomena will be observed throughout the data that will be discussed below.

(vi) There exists a correspondence between the slope $\partial\bar{U}/\partial y$ of the mean velocity profiles and the turbulence intensity. High slopes are always accompanied by increased turbulence intensity (i.e. the crest profile near the wall) while low slopes are correlated to reduced intensity (i.e. the trough profile near the wall).

Effect of Boundary Layer Trip

One of the goals of this experiment is to find an effect of λ/δ on the behavior of the boundary layer, especially on the modulation of turbulent quantities. Therefore, a cross plot of the result was done (Figure (20)) with boundary layer trip height as parameter.

It is observed that for the two models and the four stations of survey, the behavior of the wall layer is almost independent of the boundary layer thickness. This shows up for the mean velocity and the turbulence intensity distributions at distances from the wall up to 0.2"

Development of the Flow

The two models in the present test are composed of five waves each. Only the center wave was surveyed for velocity and turbulence level distribution. A question rose on how the reported results represent a situation over a long train of waves. In other words, how many waves does it take for the boundary layer to become periodic.

To answer this question, waves No. 2 and 4 of WW1, with T = 0.50", were surveyed at four stations, as defined for wave No. 3. The results for velocity distribution are shown in Figure (21). Though there are small differences between the cases, which might be the result of experimental errors and minor differences in the wave form, there is no consistent trend in the shape of the profiles. The same was found true for the turbulence level. Hence it is concluded that the data discussed above is in fact representative of a long wavy wall.

Test for Two-Dimensionality

Final test for the quality of the results is for two-dimensionality of the flow. This test was conducted for WW1 with T = 0.50" at the four stations of survey. A dog-leg extension was attached to the arm of the traverse mechanism. The probe was attached to the extension, thus enabling the survey at 4" from the centerline of the test section.

Results are presented in Figure (22), together with the center-line profiles, for comparison. Again, small differences are found, but there is no change in shape that implies deviation from two-dimensionality at the center core of the test section.

IV. 3. Wall Stress

Preston Tube Probe

A flat-mouth preston tube was used to evaluate the wall shear. When the tip of such probe touches a wall, it measures an overpressure given by:[11], [12]

$$p_p - p_w = \frac{K}{d^2} \int_S \tfrac{1}{2} \rho u^2 \, d\sigma$$

where S is the area of the opening of the probe and d is its characteristic height and the calibration factor K is a function of the shape of the probe and the velocity profile. In the case of similarity profiles, for which $u/u_\tau = f(u_\tau y/\nu)$, K becomes a function only of the shape and $u d/\nu$. In the present situation, similarity profiles do not exist because of the curvature effect and the associated pressure gradients. Hence,

no simple calibration can be provided for the desired K. To overcome this problem, it was decided to use a probe which will be fully submerged in the linear portion of the viscous sublayer. Therein, the velocity is given by:

$$\frac{u}{u_\tau} = \frac{u_\tau}{\nu} y \quad ,$$

and the calibration factor K can be considered as a constant.

The thickness of the viscous sublayer can be estimated from the results of a similarity-law fit to the plain floor boundary layer profiles (Section III. 2). For example, for T = 0. 25", u_τ = 0. 6 m/sec. Hence:

$$y = 0.001\ y+ \quad .$$

If the viscous sublayer extends up to y+ = 5, say, its edge is 0. 005" above the surface.

But, from the results of the previous section, wall shear is expected to reach a maximum at or near the crest. This maximum is accompanied by the thinning of the sublayer. To estimate the minimum thickness of the sublayer, wall shear distribution measured by Kendall (Figure 15 of Ref. (7)) is used. There it was found that the maximum value of C_f/C_{f_o} is 1. 3. But, for y+ = 5:

$$\frac{y_1}{y} = \frac{u_\tau}{u_{\tau 1}}$$

$$= (C_f/C_{f_1})^{\frac{1}{2}}$$

$$\simeq 0.877 \quad .$$

Hence the smallest sublayer thickness is expected to be:

$$y_{min} = 0.0044''$$

Finally, an evaluation is made of the effect of streamwise pressure gradient on the deviation from a linear laminar sublayer profile. In the sublayer (cf. [11], [12]):

$$u = \frac{\tau_w}{\rho \nu} y + \frac{1}{2\rho\nu} \frac{dp}{dx} y^2 + \ldots ,$$

which can be rewritten in a non-dimensional form as:

$$\frac{u}{u_\tau} = y^+ \left[1 + \frac{1}{4 \frac{\lambda u_\tau}{\nu}} \frac{d\, Cp_w}{d(\frac{x}{\lambda})} y^+ + \ldots \right]$$

The most severe case is WW2, with $\lambda = 6''$. There, based on a flat floor friction velocity:

$$\frac{\lambda u_\tau}{\nu} = 6000 ,$$

the normalized wall pressure gradient parameter, from Figure (17) is:

$$\frac{dCp_w}{d(\frac{x}{\lambda})} = 1.2 .$$

At the edge of the viscous sublayer ($y^+ = 5$) we find

$$\frac{1}{4 \frac{\lambda u_\tau}{\nu}} \frac{dCp_w}{d(\frac{x}{\lambda})} y^+ = \frac{1}{4000} .$$

Hence, the nonlinear term can be neglected compared to the leading, linear one, for $y^+ < 5$.

The probe was designed to have the upper edge of its opening less than 0.0044" from the wall. Its general dimensions and a comparator picture of its front end are given in Figure (23).

Method of Measurement

Because of the large variation in wall static pressure, the measurements were obtained by recording the pressure difference $(p_p - p_w)$ at each station that has a static pressure port. At each station, the tip of the probe was aligned on a normal to the flow direction at a distance 0.7" to the side of the static port. The measuring schematic of Figure (6) was used, with the Preston tube connected to one side of the transducer and the wall port to the other. This arrangement is shown in Figure (23c).

The calibration of the probe was made on the plain floor, under the same conditions used for the measurement of the reference velocity profiles. The value measured is given by:

$$(p_p - p_w)_o = \frac{K}{d^2} \int_S \tfrac{1}{2} \rho u^2 \, d\sigma$$

$$= \frac{K\rho}{2\,d^2} \left(\frac{\partial u}{\partial y}\right)^2_{w,\,o} \int_S y^2 \, d\sigma$$

$$= \frac{K^1 \rho}{2} \left(\frac{\partial u}{\partial y}\right)^2_{w,\,o} d^2 \quad .$$

This can be rewritten in a non-dimensional form

$$\frac{(p_p - p_w)_o \, d^2}{\rho \nu^2} = \frac{K^1}{2} \left[\frac{\tau_w \, d^2}{\rho \nu^2}\right] \quad ,$$

which is a linear form of Preston's[14] original expression:

$$\frac{(p_p - p_w)_o \, d^2}{\rho \nu^2} = F\left(\frac{\tau_w \, d^2}{\rho \nu^2}\right)^2 .$$

Therefore, the ratio of skin friction coefficients becomes

$$\frac{C_f}{C_{f_o}} = \frac{\tau_w}{\tau_{w_o}} = \left(\frac{p_p - p_w}{(p_p - p_w)_o}\right)^{\frac{1}{2}} .$$

The sensitivity of the pressure difference $(p_p - p_w)$ to the inclination angle of the probe was examined in the range $0 \leq \vartheta \leq 8°$. The results given in Figure (23), show almost no change in this range.

The magnitude of change in p_w caused by the proximity of the probe was also measured on the plain floor. The probe was moved across the boundary layer until it touched the floor and changes in p_w were recorded. The corresponding changes in Cp_w are also shown in Figure (23). Since $\Delta Cp_w/Cp_p$ is less than 2%, no correction for this effect was incorporated in the data reduction.

A few factors make this measurement difficult and susceptible to errors. 1) At the slopes, where dp_w/dx is large, small deviations of the tip of the probe, from the transverse line, can cause appreciable error. 2) At the valley, optical inspection of the orientation of the probe at the surface was impossible. 3) Turning the flow on and off many times during the test can cause changes in U_o.

Measurements

Wave No. 3 of the two models, and its vicinity, was surveyed with all of the boundary layer trips. As will be shown below, WW2 gave an unusual wall shear distribution. In order to gain confidence in this peculiar behavior, four additional static pressure ports were

fixed between the existing ones. The results, in a non-dimensional form C_f/C_{f_o} are presented in Figure (24).

The scatter in the data is large, reflecting the difficulties mentioned above. Therefore, no consistent trend of the effect of boundary layer height can be discerned from the present results. Nevertheless, the shape and phase angles of the wall stress distribution are apparent.

WW1: The wall stress reaches a peak with $C_f/C_{f_o} = 1.18$ and a phase shift of 45° upwind of the crest. The minimum value is $C_f/C_{f_o} = 0.63$, with a phase shift of 30° upwind of the trough.

WW2: The maximum wall stress is $C_f/C_{f_o} = 1.25$, a phase shift of 20° upwind of the crest. Proceeding downwind, the curve declines sharply to a value of 0.7, at about 50° downwind of the crest. At the center of the downhill slope, a second, low peak is observed, followed by a gradual increase, from a value of 0.65, along the uphill slope to the next peak.

Kendall* found a behavior similar to that of WW2 in an unpublished extension of his moving wave experiment.[7] This occurred with waves moving into the wind, hence increasing wall pressure gradients.

The wall shear curves have been integrated to find the skin friction drag coefficient defined by:

$$C_{D_f} = \frac{1}{\lambda} \int_o^\lambda C_p \, dx \qquad (\cos y' \simeq 1) \quad .$$

The results are:

WW1: $C_{D_f} = 0.0027$, WW2: $C_{D_f} = 0.0028$.

* Kendall, J. M. Jr.: Private Communication

The results so far, including wall pressure, shear stress and velocity profiles, do not show a significant effect of the ratio δ/λ. It was therefore decided to proceed and do the flow field surveys with one boundary layer trip only. T = 0.5" was chosen arbitrarily for the rest of the test.

IV. 4. Static Pressure Survey

The distribution of static pressure along the surface of the wavy walls was described in Section IV. 1. Here the technique and results of the static pressure survey within the boundary layer are reported. The knowledge of the distribution across the boundary layer is of importance, since its gradients considerably alter the velocity profiles.

The measurement of static pressure in non-uniform flow fields is known to be difficult. In the present investigation this difficulty is amplified because of the curvature of the streamlines and the consequent changes in the turbulent quantities. It was decided, therefore, to try three possible probes and find which of them demonstrates minimum sensitivity to flow direction and turbulence.

The calibrations of the three probes, whose forms are described below, was carried out in two steps:

(i) Calibration in the free stream to find sensitivity to airspeed or to Reynolds number. This was accomplished with plain floor, using boundary layer trip T = 0.50", and with the probe oriented along the centerline at STN 6.

(ii) Calibration in the boundary layer in order to determine the effect of turbulence and of the proximity of a solid wall on the probe reading. Again, this was accomplished

using the plain floor, tilted to provide constant pressure for boundary layer trip T = 0.50". Recall that Figure (13c) describes the average velocity and turbulence level for these test conditions.

Disc Probe

This probe is recommended by Bryer et. al.[15] for survey of two-dimensional flow fields where the direction of flow is not well known. Results of calibration of such probe (Figure 12 of [15]) show that it measures $Cp_m = -0.12$ and that this value remains almost constant for angles of attack in the range $\pm 20^\circ$.

The probe that was tried in the present test is described in the upper part of Figure (25). It was aligned carefully along the centerline of the test section, with its plane perpendicular to the floor.

Results of the calibration in free stream are shown in the lower part of Figure (25). The average measured pressure coefficient is $Cp_m = -0.14$, and the deviations do not exceed ± 0.003 in Cp_m.

The results of pressure coefficient, measured within the boundary layer are presented in two forms: The first is normalized by edge velocity U_o and the second by local velocity $\overline{U}$

$$(1)\quad Cp_{m,o} = \frac{p - p_o}{\frac{1}{2}\rho U_o^2}$$

$$(2)\quad Cp_{m,\ell} = \frac{p - p_o}{\frac{1}{2}\rho \overline{U}^2}$$

The dependence of these two coefficients on the height above the surface is plotted in Figure (26). The velocity profile of the boundary layer is also shown for reference. We observe that the two curves

have a strong gradient near the wall, which reflect interference. The $Cp_{m,o}$ curve grows monotonically toward the free stream value outside the boundary layer, while $Cp_{m,\ell}$ has a peak at h = 0.5" which is apparently caused by the turbulence.

Sphere Probe

This probe consists of 1/8" diameter sphere with four equally distributed pressure taps inclined at 42° with respect to the free stream direction. The inclination angle of 42° was chosen because the surface pressure vanishes at that location for subcritical Reynolds numbers.[16]

Indeed, calibration in free stream (Figure (27)) shows almost zero pressure coefficient. Actual values range from $Cp_m = -0.001$ at $U_o = 7.5$ m/sec to $Cp_m = 0.003$ at $U_o = 15.7$ m/sec.

Calibration inside a boundary layer (Figure (28)) shows a strong gradient near the wall, a plateau of $Cp_m = 0.032$ that ranges from h = 0.9" to h = 2.0", and a gradual decrease toward the free stream value for h > 5.0".

Needle Probe

This is a sting type static pressure probe constructed from 0.042" O.D. tubing. It has a rounded nose and three pressure taps located at a distance ℓ = 10d from the front end. It is described in Figure (29).

Results of the free stream calibration show that the measured pressure coefficient is 0.0075 independent of velocity.

Next, the probe was tried inside the boundary layer, with its axis parallel to the floor. The results (Figure (30)) show erratic

variations across the layer, but the changes about the average value of $Cp_m = 0.0055$ do not exceed $\Delta Cp_m = \pm 0.002$. This range of variation is tolerable in use.

From what was described above, it is clear that the needle static probe gave the best performance by being less sensitive than the other two probes to turbulence and proximity of the wall.

The final test for this probe was to find its sensitivity to inclination of the flow. This was done for angles of attack of $+5^\circ$ and -5°. The results of this test are shown in Figure (30). We observe from the plots the same unpredicted variation across the boundary layer as in the zero angle of attack case. The average values of pressure coefficient are:

θ	Cp_m
-5	.003
0	.0055
+5	.008

The scatter, in all cases, is ± 0.0002 about the average. But the differences between the averages and the scatter are small enough to permit the use of this probe in the present test.

Results

The surveys were obtained at the standard four stations for the two models with T = 0.5". The needle probe was aligned with its measuring holes at the desired station at an angle which is the average between the local wall slope and free stream direction. By so doing, it is assured that the relative angle between the probe and the local flow does not exceed 4.5°.

The results, normalized to a form of static pressure coefficient, are shown in Figure (31) for the two models. The following observations are made:

(i) For the two models and the two stations where $Cp_w = 0$, the static pressure remains nearly zero over the entire layer, reaching a value of -0.01 or less in the free stream.

(ii) WW1: At the trough station a layer of constant static pressure 0.15" in height is observed. Proceeding the static pressure declines until above h = 0.55" it decays exponentially. At the crest, the layer of constant static pressure is 0.05" thick, followed almost immediately by exponential decay.

(iii) WW2: No tendency to form a layer of constant static pressure near the wall is observed for this model. Static pressure curves decay exponentially above 0.35" distance from the wall at the trough and 0.25" distance from the wall at the crest.

Because of the observed exponential form of the pressure curves away from the wall, a curve fit was obtained whose form was chosen from the uniform, inviscid solution for flow over a wavy surface. Corrections made for the actual reduced amplitude of the wall pressure and for the existence of a layer of constant pressure near the wall, yielding the function

$$Cp_s(y) = Cp_w \, e^{-\alpha(y-A)}$$

where $\alpha = 2\pi/\lambda$ and A is a parameter to be optimized for least square deviation. Only data points with $y > 0.5$" were included in the curve fitting. The results are shown together with the data in Figure (31). The values found for A are:

Model	STN	A in.
WW1	(2)	0.45
WW1	(4)	0.12
WW2	(2)	0.20
WW2	(4)	0.10

Note that the values of A are very close to the displacement thickness of the boundary layer at the same locations.

IV.5. Total Pressure Survey

In principle, knowing both the velocity and the static pressure distributions across the flow field, one can determine the total pressure using Bernouli's equation. Even so, it was decided to measure the total pressure because direct measurement is more accurate and can provide a check for the quality of the static pressure.

In order to get good resolution, a flat mouth Pitot tube was used with opening 0.010" high. Measurements were made with p_o as reference. The two models with T = 0.5", were surveyed, each at the standard four stations.

The analysis of the results of the total pressure survey are given in the next chapter. Here they are used to check the static pressure distributions discussed above.

Check of the Static Pressure Distribution

A non-dimensional form of Bernoulli's equation for a point in the flow field is

$$Cp_t = Cp_s + (\bar{U}/U_o)^2 \quad .$$

Therefore, a comparison is made between the direct measurement of Cp_t and the value calculated from the sum $Cp_s + (\bar{U}/U_o)^2$ (Sections IV. 4. and IV. 2.). Two typical plots are given in Figure (32). It is observed that the differences do not exceed 0. 025 out of 1. 0. All other cases show the same accuracy or better, and therefore are not shown.

IV. 6.. X-Array Probe Survey

Probes

The main purpose of using an X-array hot-wire probe is to measure Reynolds stresses and related quantities, i. e. mixing length and eddy viscosity.

DISA type 55A38 probes were used. The two sensors are 1. 2 mm long, 0. 005 mm diameter, Pt-platted tungsten wires, placed in an X-array. Two probes were used during the investigation. One, a standard 55A38, was used to survey the flat plate and WW1. For WW2 a special probe with bent prongs was built in order to allow measurement very close to the wall without exceeding the range of linearity. This special probe has the same sensors as the standard one and is shown in Figure (33).

The schematic of measurement is shown in Figure (34). Two channels, each containing DISA anemometer and linearizer are used for the two sensors. In addition, a DISA Random Signal Analyzer and Correlator is used to produce the sum and difference of the turbulence

signals. Two RMS units are used, in turns, to record four signals: $\tilde{E}_1$, $\tilde{E}_2$, $\tilde{E}_s = (E_1 \tilde{+} E_2)$, $E_d = (E_1 \tilde{-} E_2)$. Details about the utilization and calibration of the probes are presented in Appendix A.

If the calibration constants of the probes are defined by

$$E_1 = Au + Bv \quad ,$$

$$E_2 = Cu - Dv \quad ,$$

where E_1, E_2 are the linearized outputs in volts and u, v are the axial and normal velocity components in m/sec., then their results of the calibration gives ;

Probe: X-1

Calibration constants: A = 0.402 B = 0.556

C = 0.399 D = 0.423

Range of linearity: $\pm 23^\circ$,

Probe: X-S

Calibration constants: A = 0.462 B = 0.475

D = 0.457 D = 0.490

Range of linearity: $+23^\circ$, -20° .

Stations of Survey

Data presented above showed a strong modulation of the flow quantities over the wavy wall models. Therefore, it was decided to increase the number of stations of survey for the present measurement. The boundary layer was surveyed at eight stations, four of which are the standard stations, and the remaining four are interspersed between them. In this way, a more complete picture of the flow field, including

the distributions of the turbulent quantities is obtained.

Comparison with the Results of a Single Element Probe

Because of the tedious process of calibration of the X-array probes, the results are compared with those obtained by a single element probe (Section IV. 2.) in order to gain confidence in the accuracy of the present measurements. Five sample cases are shown in Figure (35). The first one is the flat plate case, and the other four are the standard stations of survey for WW1. The two velocity components, and the turbulent quantities U', V' and $\overline{u'v'}$ are shown on a log (y) scale as in Section IV.2. The following observations are made:

(i) Longitudinal velocity component, $\overline{U}$, and turbulence intensity, U', differ by no more than 5% of their maximum values from their counterparts $\overline{Q}$ and Q' measured with a single element probe. In spite of these small differences, the two curves always show the same trends.

(ii) Normal velocity component, $\overline{V}$, is practically zero in the case of the plain floor, and at the crest and trough stations of the wavy wall, as expected. At the downhill and uphill stations, $\overline{V}$ has negative and positive values respectively, that diminish toward the edge of the boundary layer. The ratio $\overline{V}/\overline{U}$ near the wall agrees with the local surface inclination.

(iii) For the case of the plain floor the Reynolds stress is constant near the wall with a value

$$\overline{u'v'}/\tfrac{1}{2}\rho U_o^2 = 0.00298 \quad .$$

This value is in good agreement with the wall shear coefficient $C_f = 0.00306$ found in Section III. 2. by fitting Cole's Law of the Wake to the velocity profiles.

Turbulent Intensities

The results of the measurements of the two turbulent intensities, U' and V', are presented in Figure (37). The distributions of the turbulence intensities and the shear stress that will be discussed in the following section, exhibit oscillations of damped amplitude superimposed on the reference flat plate boundary layer distributions. This wave phenomena will be related in Section V. 5. to the Rayleigh problem. Here, the important findings are summarized.

(i) At distances exceeding 1.2" for WW1 and 0.6" for WW2, above the line connecting the centers of the waves, the two turbulence intensities are practically independent of the station along the surface wave and are given by the reference case. The changes in these quantities are large near the wall and decay as the outer layer is approached. Qualitatively, the changes are the same for the two models, but it is apparent that the normal gradients in WW2 are larger than those in WW1.

(ii) In the vicinity of the trough, the normal distributions of V' increase with increasing y, reaching a peak for which $V'/U_o = 0.05$ at $y = 0.17$" for WW1 and $y = 0.12$" for WW2. With increasing y, the curves undershoot the reference curves and then merge into the unperturbed distributions. On the uphill slope of the models V' increases very close to the wall. This trend is strongest just behind the crest,

where a value $V'/U_o = 0.05$ is measured at the points closest to the wall. This local maximum again approaches the reference distribution in an oscillatory manner.

(iii) In the vicinity of the wall, the oscillatory behavior of U' is more pronounced than that of V'. The distributions reach a peak near the wall at the station just downstream of the crest. The maximum measured values are $U'/U_o = 0.130$ for WW2. Proceeding outward at the same station, the distributions decrease below the reference value, form a second peak and then merge into the reference distribution. Further downstream, on the downhill slope, the peak closest to the wall flattens somewhat and the intensity is reduced. At the trough, a flat maximum with $U'/U_o = 0.11$ is found at a distance $y = 0.25''$ for WW1 and $y = 0.16''$ for WW2.

Turbulent Shear Stress

The turbulent shear stress distributions given in Figure (38) show large variations across the layer as well as along the wall wave. The oscillatory nature of the normal distributions is apparent at all stations; the amplitude of oscillation about the reference curve being much larger than noted for the turbulent intensities in each case.

(i) As in the case of the turbulent intensities, the shear stress distribution is practically independent of longitudinal position at distances exceeding $1.2''$ for WW1 and $0.6''$ for WW2, above the mean surface line. Again, the two models show similar trends but the layer of strongest variations in C_τ is appreciably thinner in the case of WW2 than that of WW1.

(ii) The downhill slope of the wave is characterized by a layer of high shear stress near the wall, followed by a damped oscillatory behavior with increasing y. Just downstream of the crest, the maximum measured $C_\tau = 0.0072$ is found adjacent to the wall. Further downstream the layer thickens until at the trough it is 0.5" wide with a peak value $C_\tau = 0.005$. At the next station a rapid change takes place, i.e. the layer exhibits a reversed curvature forming an S shape distribution adjacent to the wall. This profile evolves on the uphill slope into a dip; i.e. $C_\tau \simeq 0$ close to the wall, followed by a shallow peak. At the crest, the dip begins to flatten, and it is followed by a rapid change from a dip to an overstress layer at STN ($4\frac{1}{2}$).

Mixing Length and Eddy Viscosity

The mixing length is defined by the equation

$$-\overline{u'v'} = \ell^2 \left(\frac{\partial \bar{U}}{\partial y}\right) \quad .$$

Hence, for the evaluation of ℓ, $\partial\bar{U}/\partial y$ must be computed from the data. In order to overcome the difficulty associated with differentiating experimental data, smoothing was introduced graphically for $y > 1$". In addition, in the vicinity of the crest the velocity profiles exhibit a flat maximum near the edge of the layer. Because the derivative vanishes there, causing unacceptable errors, this part of the data was ignored in the evaluation of the mixing length.

In order to determine the effect of curvature on the distribution of mixing length, Sawyer's[5] theory was used. The essentials of this theory, and an attempt to evaluate the empirical constant k are given in Appendix B. Sawyer's expression can be written as

$$\overline{u'v'} = \ell_s^2 \frac{\partial \overline{U}}{\partial y}\left(\frac{\partial \overline{U}}{\partial y} - k\frac{\overline{U}}{R}\right) \quad .$$

Since the results of Appendix B are not conclusive, the value k = 10 was chosen arbitrarily for computations. As will be explained in detail below, the correction for curvature is not large, therefore the choice of k is not critical. For the computations, local radii of curvature of the mean streamlines were evaluated graphically from Figure (41).

The results are shown in Figure (39), on which the following summary is based:

(i) The distribution of ℓ near the wall is linear, as in the case of the flat plate, for only part of the stations. For the others, mainly those in the vicinity of the crest, the function oscillates, showing different trends at different stations. Hence, there is some uncertainty in the evaluation of the slopes of the ℓ-vs-y curves near the wall. In spite of this uncertainty it is apparent that the slopes are appreciably larger in the vicinity of the crest than in the vicinity of the trough.

(ii) On the uphill slope of the wave, and at the crest, ℓ is nearly zero for $y < 0.08''$, reflecting the low shear stress in that zone.

(iii) The mixing length is modulated in the outer layer as well as in the vicinity of the wall. Typically, at the trough $\ell/\delta = 0.07$, while at the crest $\ell/\delta = 0.16$. Note that for the reference profile, a value $\ell/\delta = 0.10$ was found in the outer layer.

(iv) Sawyer's theory was applied at the crest and at the trough only, since for the remaining stations the wall curvature is small

enough to make the correction unimportant.

At the trough the slope of ℓ_s-vs-y near the wall is 15% larger than that of ℓ-vs-y, for the two models.

At the crest Sawyer's analysis can be applied only to the first two data points for WW1, because at all the other points it was found that $\partial\overline{U}/\partial y < k\,\overline{U}/R$, even for k = 5, thus predicting negative ℓ_s, which is meaningless.

Eddy viscosity is defined by the equation

$$-\overline{u'v'} = \epsilon \frac{\partial \overline{U}}{\partial y} \quad .$$

The results of the computation of eddy viscosity are presented in a non-dimensional form ϵ/ν-vs-y in Figure (40). The modulation of the eddy viscosity distributions, which is apparent near the wall and in the outer layer, is similar to the modulation of the mixing length. The values of $\epsilon/\nu = 140$ at the trough and $\epsilon/\nu = 300$ at the crest are found in the outer layer of WW1. For WW2, the values are $\epsilon/\nu = 230$ at the crest.

V. ANALYSIS OF THE RESULTS

V. 1. Boundary Layer Thicknesses, Shape Factor and Stream Lines

The common definitions of flat plate boundary layer thicknesses fail to describe the situation over a wavy wall. The reason is that u_e loses its meaning, since inviscid theory predicts velocity perturbations across the flow field. Definition of boundary layer thickness, δ, as the distance where u/u_e reaches a certain value (0.995, say) is not valid. Also, as will be discussed below, the velocity profiles do not obey the Law of the Wake and hence the technique used in Section III. 2. cannot be applied here to evaluate δ. Because of the lack of a better way, a definition based on the turbulence level was adopted for the present case. The turbulence level Q'/U_o, at $y = \delta$, for the reference profiles (Chapter III) was found from Figure (13), and for the wavy wall profiles δ is determined as the distance from the wall where turbulence level reaches the same value as the corresponding reference profiles. The results are summarized in the table on page 47. It is found that at the two slopes, boundary layer thickness is within 0.1" from the reference profile. At the crest, it is from 0.1" to 0.3" thinner, while at the trough 0.1" to 0.3" thicker.

As mentioned above, the usual definition of displacement thickness and momentum thickness do not describe properly the situation over a wavy wall, since u_e is not a constant. To account for this, u_e will be replaced by a reference velocity, u_r, which is the inviscid local velocity, modified for the fact that the actual wall pressure is lower than predicted by inviscid theory.

$$u_r = U_o(1 + \Delta u_w e^{-2\pi y/\lambda})$$

with $$\Delta u_w = \frac{Cp_w}{2} U_o$$

hence $$u_r = U_o\left(1 + \frac{Cp_w}{2} e^{-2\pi y/\lambda}\right) .$$

Here measured value of Cp_w (Section IV. 1.) is used rather than theoretical.

The displacement thickness and momentum thickness take the form

$$\delta^* = \int_o^\delta (u_r - u)dy/U_o$$

$$\theta = \int_o^\delta u(u_r - u)dy/U_o^2 .$$

The velocity profiles, as obtained by a single-wire probe (Section IV. 2), were integrated numerically to yield the location of the streamlines and the integral thicknesses defined above. The results, together with the form factor $H = \delta^*/\theta$, are summarized in the following tables. The same was done for data obtained by the X-array probe, for T = 0. 5".

WW 1

T	$\delta_{REF.}$	STN	δ	δ^*	θ	H
0.05	1.50	1	1.58	0.253	0.180	1.41
		2	1.82	0.401	0.243	1.65
		3	1.60	0.252	0.190	1.33
		4	1.43	0.217	0.190	1.14
0.25	2.43	1	2.40	0.298	0.219	1.36
		2	2.53	0.415	0.258	1.61
		3	2.40	0.306	0.234	1.31
		4	2.25	0.307	0.271	1.13
0.50	3.41	1	3.38	0.377	0.290	1.30
		2	3.70	0.467	0.308	1.52
		3	3.43	0.365	0.291	1.25
		4	3.10	0.364	0.327	1.11

WW2

T	$\delta_{REF.}$	STN	δ	δ^*	θ	H
0.25	1.96	1	2.00	0.266	0.192	1.39
		2	2.26	0.368	0.237	1.55
		3	2.03	0.275	0.210	1.31
		4	1.85	0.251	0.206	1.24
0.50	3.08	1	3.06	0.336	0.256	1.31
		2	3.26	0.454	0.313	1.45
		3	3.10	0.333	0.264	1.26
		4	2.80	0.302	0.258	1.19
0.75	3.70	1	3.70	0.466	0.354	1.32
		2	3.88	0.554	0.380	1.46
		3	3.74	0.455	0.357	1.28
		4	3.50	0.414	0.347	1.19

Boundary Layer Thicknesses and Shape Factor

(All dimensions are in inches)

The results are presented in Figure (40) where the shape of the streamlines and the boundary layer thicknesses are shown. The most important observations are:

(i) The shape of the streamlines can be traced for T = 0.5" only, because only in this case data exist for eight stations of survey. It is clearly seen that the amplitude of the streamlines decreases rapidly from that at the wall to almost zero at the edge of the boundary layer.

(ii) The amplitude of the displacement line is smaller than that of the wall itself, reflecting the appreciable changes in the shape of the velocity profiles along the wavy wall.

(iii) The line defining the edge of the boundary layer is practically straight for WW2 with all trip heights. For WW1, this line is practically straight for the thick boundary layer case (T = 0.75") only. For the other two cases, small amplitude is observed.

V.2. Conservation of Momentum

In Section IV.2. a check for two-dimensionality of the flow field was reported, based on a comparison of the centerline velocity profiles and those 4"off the centerline of the test stations. Here, an additional test is presented, based on the conservation of momentum along one surface wave. Noting that the contribution of the skin friction along one wave is small compared to the momentum flux in the boundary layer, i.e., that it is comparable with the experimental error involved in the measurements of velocity and pressure, therefore the skin friction ignored in the momentum balance.

The following contour is chosen as a control volume.

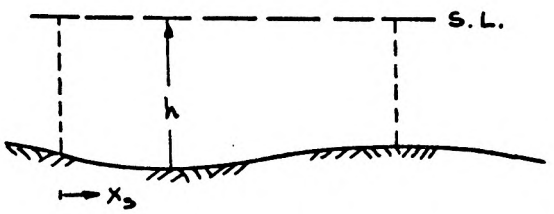

The upper bound is the streamline passing the edge of the boundary layer at STN(1). In section V. 1., it was shown that for T = 0.5" this streamline is nearly straight, and parallel to the line connecting the centers of the wall wave. Hence, there is no contribution to the x-momentum from this surface of the control volume.

The momentum balance is given by

$$\oint p \cdot dy = \oint \rho u \cdot u \, dy \quad .$$

Ignoring the differences between U and Q one finds

$$\tfrac{1}{2} \oint C_p \, dy = \oint (\bar{U}/U_o)^2 \, dy \quad .$$

Let:

$$I_1 = \int_o^h (\bar{U}/U_o)^2 \, dy; \; I_2 = \tfrac{1}{2} \int_o^h C_p \, dy; \; I_3 = \int_o^{x_s} C_{p_w} \, dy,$$

where h is the height defined in the sketch.

We will compare the sum $I_1 + I_2 + I_3$ at three stations with I_1 at STN(1).

WW1

STN	1	2	3	4
I_1	2.67	2.54	2.74	2.82
I_2	0	0.18	0	-0.19
I_3	0	-0.03	0	0.02
Σ	2.67	2.69	2.74	2.65

WW2

STN	1	2	3	4
I_1	2.44	2.41	2.56	2.49
I_2	0	0.08	0	-0.10
I_3	0	-0.02	0	0.01
Σ	2.44	2.47	2.56	2.40

The maximum deviations from the values at STN(1) do not exceed 4% and hence it is concluded that the flow is two-dimensional within the accuracy of the measurements.

V.3. Validity of Ludwig and Tillmann Skin Friction Law

The Ludwig and Tillmann skin friction law is one of the most commonly used in the study of turbulent boundary layers. This empirical law is based on measurements in boundary layers over flat plates. It relates the local skin friction to the form factor and Reynolds number based on momentum thickness by the equation

$$C_f = 0.246\, Re_\theta^{-0.268}\, 10^{-0.678H}$$

Since this is a local law, it is expected to be valid only for equilibrium flow. Nevertheless, it was decided to examine its

applicability to the present test conditions. The needed data (H and θ) were taken from the tables of the previous section. The results, normalized by the reference profiles skin friction coefficient, together with the measured values (Section IV. 3.) are presented in Figure (42).

Since only four data points are available along a surface wave, the comparison is not conclusive. Nevertheless, it is apparent that the Ludwig and Tillmann formula predicts properly the magnitude of the change in wall shear, but fails to predict the phase shift in the shear distribution, especially on the downhill slope of the wave.

V. 4. Law of the Wall

The widely used Coles'[9] Law of the Wall is given by the equation

$$\frac{u}{u_\tau} = C + \frac{1}{\kappa} \ln\left(\frac{y\, u_\tau}{\nu}\right)$$

with the constants $C = 5.0$ and $\kappa = 0.41$.

The foundation of this law is the functional and dimensional analysis given by Millikan.[17] It is based on the following observations for constant pressure boundary layer;

$$\frac{u-u_e}{u_\tau} = f\left(\frac{y}{\delta}\right) \qquad \text{velocity defect in outer layer ,}$$

$$\frac{u}{u_\tau} = g\left(\frac{u_\tau\, y}{\nu}\right) \qquad \text{velocity in the viscous layer .}$$

There exists a region of overlap, where the two expressions are valid. The equivalence of the velocity profiles given by $f(y/\delta)$ and by $g(y\, u_\tau/\nu)$ in this intermediate region generates the above mentioned law.

In the present situation, another length parameter (λ) exists and hence the functional analysis given above is not expected to be valid.

Nevertheless, the velocity profiles (Figures (19) and (36)) do show semilogarithmic sections at distances typically ranging from 0.3" to 1" of distance from the wall. In most cases, this semilogarithmic section can be traced without ambiguity, as shown by the slopes traced in Figure (36). Only in a few cases in WW1 this section is either so short or the waviness in the data is so large, that some uncertainty is caused in the determination of the slope. Note that within the range of distances from the wall, where the semilogarithmic section exists, the characteristic waviness in the distributions of C_τ is still apparent for WW1 and almost completely decayed for WW2. Indeed, most of the difficulties in the determination of the slopes are associated with WW1.

In the case of a flat plate, the von Kármán constant κ in the Law of the Wall is also the slope of the mixing length distribution near the wall. The existence of such relation for the present situation was examined.

Let the semilogarithmic portion of the velocity profiles be described by the equation

$$\frac{u}{u_\tau} = C^* + \frac{1}{\sigma} \ell n \left(\frac{y u_\tau}{\nu} \right) \quad .$$

The distribution of σ along the surface wave was determined from the measured velocity profiles and wall shear distribution and is summarized in Figure (43).

The mixing length distributions that were discussed in Section IV. 6. and presented in Figure (39) are linear near the wall for part of the stations of survey. Let such linear part in the ℓ-vs-y curves be given by

$$\ell = \sigma' y \quad .$$

Wherever possible, the slope σ' was measured and the result plotted in Figure (43), from which the following is observed:

(i) The agreement between σ based on velocity profiles and u_τ and σ' based on mixing length distribution is good.

(ii) The maximum value of σ is reached at the crest and is $\sigma = 0.95$ for WW1 and $\sigma = 0.66$ for WW2. The minimum is obtained at the trough and is $\sigma = 0.20$ for the two models.

(iii) For the two models, $\sigma = \kappa$ at, or close to, the inflection points of the surface wave.

V. 5. Analysis of Total Pressure and Total Velocity

The results of Section IV. 2. and IV. 6. show that most of the turbulent action (i. e. production, dissipation and conduction) take place in the wall layer. It is suggested, therefore, that the outer part of the layer be treated as inviscid. In order to check this assumption, the variation of the total pressure along streamlines is studied.

The stream function in the form ψ/U_o is found by integration of the velocity profiles of Section IV. 2. and the total pressure from the results of Section IV. 5. . Using proper interpolation, the variations of Cp_t as a function of ψ/U_o were evaluated for the four stations

of survey for each of the models. The results are shown in Figure (44). It is found that outside the wall layer the profiles are almost identical, with differences that do not exceed acceptable experimental error. In particular, there is no trend for the total pressure to decrease along streamlines.

This conclusion led to the analysis of the outer layer by using inviscid, non-uniform flow small perturbation technique. This analysis is given in Appendix B.

In the previous section it was noted that the Law of the Wall fails to apply in the present situation. The reason is the modulation of the slope factor σ along the surface wave caused by the distributions of static pressure. It was decided, therefore, to seek a presentation of an equivalent velocity which is preserved along the streamlines. Based on the findings discussed above, a total velocity, based on total pressure, was defined by

$$U^t = (\bar{U}^2 + 2(p_s - p_o)/\rho)^{\frac{1}{2}}$$

or

$$U^t = (2(p_t - p_o)/\rho)^{\frac{1}{2}} \quad .$$

Note that U^t is reduced to $\bar{U}$ where $p_s = p_o$, that is for the case of the flat plate and at STN(1) and STN(3).

Total velocity profiles were computed and Coles' Law of the Wake was fitted to them. The results are shown in Figure (46). It is found that, indeed, total velocity profiles obey the Law of the Wake at all four stations of survey. The parameters of similarity are summarized below. Note, however, that u_τ does not have the meaning of friction velocity, and serves only as a normalizing parameter.

Model	STN	u_τ m/sec	$\bar{\pi}$	δ in.
WW1	1	.61	.15	3.15
	2	.59	.30	3.26
	3	.60	.18	3.18
	4	.62	.03	3.00
WW2	1	.61	.16	2.81
	2	.59	.35	2.89
	3	.61	.12	2.94
	4	.63	.02	2.68

Note that compared to the reference profiles (Section III. 2.), u_τ is decreased at the trough and increased at the crest, while $\bar{\pi}$ is increased at the trough and decreased at the crest. This phenomena is caused by the stretching of streamtubes near the trough and their contraction near the crest.

The same finding can be seen by plotting the velocity and total velocity profiles on log-log chart. This presentation is aimed at examining the applicability of the power law to these profiles. The plots are shown in Figure (46) for the two models with T = 0.5". It is found, as before, that the two profiles at STN(1) and STN(3) are practically identical and obey the power law. At the other two stations, namely the crest and the trough, only total velocity profiles behave according to this law. The exponent n in the power law was found graphically and is:

$$\frac{U^t}{U_o} = \left(\frac{y}{\delta}\right)^{1/n} .$$

STN	n	
	WW1	WW2
1	8.6	7.5
2	6.9	6.3
3	7.9	8.2
4	9.2	8.6

V. 6. The Wall Layer

The distributions of turbulent shear stress and intensities near the wall (Section IV. 6.) show a wavy structure with amplitudes decreasing toward the edge of the boundary layer. This phenomenon resembles that of a flow near an oscillating flat plate known as Rayleigh problem (i. e. [18]). In the present problem the wall is stationary but the wall layer is subjected to alternating pressure, and must match its edge velocity to that of the outer layer. The analysis of the outer layer presented in Appendix B shows that the perturbations in velocity at a distance y = 0. 2" from the wall are $\Delta u = \pm 0.15\ U_o$. This alternating matching condition induces the wavy structure of the turbulence quantities.

In Section IV. 6. it was mentioned that the wave phenomenon is practically decayed at distances above the wall of 1. 2" for WW1 and 0. 6" for WW2.

The laminar rayleigh problem predicts no perturbation in shear stress at the wall for phase angles $\phi_1 = \pi/4$ and $\phi_2 = 5\pi/4$. Assuming that in the turbulent case there is no additional phase shift due to delay in the formation of turbulent quantities, these locations

correspond approximately to STN ($1\frac{1}{2}$) and STN ($3\frac{1}{2}$) respectively. Half wave length of the shear wave near the wall was measured at these stations as the distance from the wall of the intersection between the reference and the local shear stress profiles. The average values found are

$$\text{WW1: } L_{\frac{1}{2}} = 0.21 \quad ,$$

$$\text{WW2: } L_{\frac{1}{2}} = 0.33 \quad .$$

In some of the stations the wave form is pronounced away from the wall and the wave length can be evaluated without sacrifice in accuracy. The average values measured outside the layer of formation of the first wave are

$$\text{WW1: } L_{\frac{1}{2}} = 0.55 \quad ,$$

$$\text{WW2: } L_{\frac{1}{2}} = 0.35 \quad .$$

The predicted half wave length for the Rayleigh problem[18] is

$$K_{\frac{1}{2}} = 2\pi \sqrt{\nu/2n} \quad ,$$

where n is the angular velocity of oscillation. In the present problem n is replaced by $2\pi U_o/\lambda$ and ν is replaced by ϵ measured in the outer layer of the reference profiles. The results are

$$\text{WW1: } K_{\frac{1}{2}} = 0.49 \quad ,$$

$$\text{WW2: } K_{\frac{1}{2}} = 0.34 \quad .$$

The agreement between the measured and the predicted values is good. Note also that near the wall $L_{\frac{1}{2}}$ is smaller than away from the wall,

since the local ϵ is relatively low.

Associated with the alternating velocity that induces the wave phenomena in the wall layer is alternating longitudinal pressure gradient. Clauser's[19] β parameter is intended solely to characterize the equilibrium boundary layers. Nevertheless, its local extreme values were evaluated in order to demonstrate the strength of the pressure gradients.

$$\beta = \frac{\delta^* \, dp/dx}{\tau_w} \quad .$$

For the present case, dp/dx is replaced by dp_w/dx. All the local quantities are measured values. The results are:

$$\text{WW1: } \beta_{max} = 14.0, \quad \beta_{min} = -12.4 \quad ,$$

$$\text{WW2: } \beta_{max} = 31.4, \quad \beta_{min} = -24.0 \quad .$$

These values can cause appreciable changes in the shape factor H for equilibrium flow. Actually, as the table in Section V. 1. indicates, the changes do not exceed $\pm$ 0. 25 in H.

In Section IV. 6. it was shown that the trends in the changes in the distributions of u' and v' are similar to the changes in the distributions in C_τ. However, near the wall the relative changes in the turbulent shear stress are much larger than those of the velocities. Typically C_τ changes by 100% with respect to the flat plate values near the wall, while U' changes by $\pm$ 20% only. It is concluded therefore that the changes in velocity intensities is not a necessary condition for change in shear stress. This can be accomplished by change in correlation factor which, according to the findings is a rapid process.

V.7. Turbulent Shear Models for Flow Over Wavy Boundary

One of the major objectives of the present investigation was to examine the validity of the assumptions and models currently used in the computation of turbulent boundary layers in the case of a wavy boundary. In the present section, a comparison is made between some of the models and the findings of the experiment. As in the introduction, this survey is based on the proceedings of AFOSR-IFP-Stanford Conference.[1]

Mixing Length and Eddy Viscosity Model

Cebesi-Smith Model

In the wall layer this model assumes

$$\ell = K_1 y (1-\exp(-y/A'))$$

where $K_1 = 0.40$ and $A' = 26\nu(\tau_w/\rho+y\, dp/dx/\rho)^{\frac{1}{2}}$. This model approaches $\ell = K_1 y$ at distances from the wall larger than the thickness of the viscous layer.

In the outer layer the model assumes

$$\epsilon = K_2 U_o \delta^*$$

with $K_2 = 0.0168$.

In Section IV.6. it was shown that the slope of the mixing length distributions near the wall varies appreciably along the surface wave. Therefore the inner model does not apply. The outer model predicts eddy viscosity which is proportional to δ^*. Actually the present situation is reversed: ϵ is large at the crest where δ^*

decreased and small in the trough where δ^* increased.

Energy Methods

Bradshaw-Ferris Model

This model relates the turbulent shear stress to the turbulent energy by the equation

$$\overline{u'v'} = 0.15\,\overline{q^2} \quad ,$$

which can be written in the following non-dimensional form

$$C_\tau = 0.30\,\overline{q^2}/U_o^2 \quad .$$

Qualitatively, it was observed that the changes in C_τ are appreciably larger and more rapid than the changes in U' and V'. Therefore, proportionality is not expected between C_τ and $\overline{q^2}$ as assumed by the model. To demonstrate this, the measured values of C_τ are plotted vs $\overline{q^2}$ in Figure (47). Note that since $\overline{w'^2}$ was not measured in the present test, $\overline{q^2}$ is approximated by the sum $\overline{u'^2} + 2\,\overline{v'^2}$. Figure (47) shows that indeed near the wall the deviation between the model and the actual measurements is appreciable.

Note, however, that one aspect of this model seems to prevail in the outer layer; namely $\overline{u'v'}$ is converted without appreciable variations, even though the velocity profiles change measurably.

Mellor-Herring Second Method

This model relates the eddy viscosity to the mean turbulent energy. In the wall layer:

$$\frac{\epsilon}{\nu} = \frac{\chi^2}{550 + \chi/0.16} \quad \text{where} \quad \chi = \frac{y\overline{(q'^2)}^{\frac{1}{2}}}{\nu} \ .$$

For the outer layer the model gives

$$\frac{\epsilon}{\nu} = 0.029\ \frac{\Omega}{\nu} \quad \text{where} \quad \Omega = \int_0^\infty q'\, dy \ .$$

The validity of the inner part of the model was checked by plotting the measured values of ϵ/ν vs χ. This presentation is shown in Figure (48) from which the following is observed: near the wall, the uphill and downhill stations give ϵ/ν distribution which deviate appreciably from that predicted by the model, but at larger distances from the wall they approach the model. On the other hand, the trough and crest stations give ϵ/ν distribution which is close to the model near the wall, but deviate from it appreciably away from the wall.

The changes in Ω along the wall wave to not exceed $\pm$ 5%, since the changes in q' distributions are restricted to the vicinity of the wall. On the other hand, the changes in the distributions of ϵ/ν in the outer layer are as much as $\pm$ 50% of the reference value. Hence, this model does not apply in the present case.

Hence, within the accuracy of the measurements, shear stress is constant along streamlines. Therefore, the modulation of the mixing length and the eddy viscosity in the outer layer are caused solely by the changes in $\partial\bar{U}/\partial y$. In view of the facts that total velocity is conserved along streamlines and that total velocity profiles obey Coles' Law of the Wake, it was decided to examine the behavior of mixing length and eddy viscosity based on this quantity and defined by the expressions;

$$\overline{u'v'} = \ell^{t^2} (\partial U^t/\partial y)^2 \quad ,$$

$$\overline{u'v'} = \epsilon^t \, \partial U^t/\partial y \quad .$$

The derivative $\partial U^t/\partial y$ was evaluated from results of total pressure survey, using the same way as discussed in Section IV. 6. . Since U^t is based on total pressure survey, ℓ^t and ϵ^t were evaluated only at the four basic stations of survey.

The distributions of ℓ^t for the two models are presented in Figure (49). It is observed that, indeed, the curves corresponding to the four stations are reduced to the distribution of ℓ for the reference profile. Note in particular that this observation is equally true near the wall and in the outer layer. The slope of the ℓ^t-vs-y curves near the wall is 0.41 as expected. In the outer layer the value $\ell^t/\delta = 0.10$ is found, which is larger by 11% from the value $\ell/\delta = 0.09$ commonly quoted in the literature.

The distributions of ϵ^t are given in Figure (50). In this case the differences between the four stations are larger than in the case of ℓ^t, but they are much smaller than the differences between the

distributions of ϵ.

The slope of the curves near the wall agrees with that predicted by the Mellor-Herring first model which gives

$$\epsilon = \kappa u_\tau y \quad ,$$

and are 11% lower than predicted by Lees[20] model, which is given by

$$\epsilon = 0.018 U_o y \quad .$$

VI. SUMMARY AND CONCLUSIONS

VI. 1. Effect of the Ratio λ/δ

One of the main goals of the present study was to explore the importance of the ratio of wave length to boundary layer thickness on the flow field. The measurements of wall pressure, velocity profiles and turbulence level and wall shear did not indicate any strong trend or phenomena related to this parameter. Furthermore, survey of the turbulence intensities and shear stress, using an X-array probe, showed that changes in these quantities take place in a wall layer, which is very thin compared with δ.

VI. 2. The Outer Layer

The measurements with a Pitot probe show that in the outer part of the boundary layer the total pressureis almost conserved along streamlines. Based on this finding, the outer layer was analyzed by applying inviscid, non-uniform small perturbation method which gave good agreement with the measured velocity.

It was found that the velocity profiles in the vicinity of the crest and the trough do not obey Coles' Law of the Wall, because of mismatch between the actual and the required slopes of the semi-logarithmic section of the profiles. However, total velocity profiles that are defined by

$$U^t = (\overline{U}^2 + 2(p-p_o/\rho)^{\frac{1}{2}}$$

do obey the Law of the Wake.

The static pressure in the outer part of the boundary layer decays exponentially according to the modified result of uniform inviscid theory given by

$$p_s - p_o = (p_w - p_o)e^{-2\pi(y-A)/\lambda} \quad ,$$

where $(p_w - p_o)$ is the actual access wall pressure and A is of the order of the displacement thickness of the boundary layer.

VI. 3. The Wall Layer

The inner part of the boundary layer is characterized by very strong variations in turbulence intensities and shear stress. The changes in normal distributions of these quantities are oscillatory with amplitude decaying exponentially toward the edge of the layer. This nature of the modulation of the shear stress distributions resembles qualitatively the flow field of the Rayleigh problem, i. e. flow near an oscillating flat plate. On the downhill slope of the wall the first half wave of the perturbation shear wave forms a layer of high shear stress near the wall, while on the uphill slope a layer of near zero shear stress is formed near the wall.

The direct effect of the wall curvature, as predicted by Sawyer's theory, was found small. The flow field is affected mainly by the alternating static pressure near the wall, which is an indirect consequence of the wall shape. An appreciable phase shift was found in the distribution of skin friction. The changes in shear stress are very rapid and appreciably larger than the corresponding changes in turbulence intensities.

VI. 4. Model for Turbulent Shear Stress

The results of the present study were compared with three models for shear stress frequently used in the computation of turbulent boundary layers (Cebeci-Smith, Mellor-Herring second methods, Bradshaw-Ferris). It was found that because of the rapid changes in stress distribution near the wall and the modulation of mixing length and eddy viscosity in the outer layer, none of the above mentioned models described the situation over the wavy wall models.

However, it was discovered that if mixing length and eddy viscosity are based on total velocity, i.e.

$$\ell^t = \frac{\overline{(u'v')}^{\frac{1}{2}}}{\frac{\partial U^t}{\partial y}} \quad \text{and} \quad \epsilon^t = \frac{\overline{u'v'}}{\frac{\partial U^t}{\partial y}}$$

then the distribution curves are identical with the corresponding curves obtained for flat plate boundary layer.

VI. 5. Suggestion for Further Research

On the basis of the results and conclusions of the present experiment, several related investigations are suggested, aimed at better understanding of turbulent boundary layer over a wavy boundary and the origin of cross-hatching ablation.

1. Extension of the range of geometrical parameters (a/λ and λ/δ) to include the asymptotic short and long wave lengths.

2. Experimental investigation of turbulent boundary layer over a wavy wall in supersonic speeds. Because of the different phase shift in pressure distribution, the net effect of curvature and pressure gradient may be different than in the present case.

3. Further research is needed to study the three-dimensional effects associated with flow over wavy boundaries. The existence of streamwise counterrotating vortices in turbulent boundary layers is well established now. Their strength is expected to be amplified on the concave portion of the surface wave because of Taylor-Göertler instability. The alternate growth and decay of such vortices will generate lateral distribution of flow quantities. The present test did not intend to explore such phenomena. However, it is believed that further research in this direction will contribute to the understanding of turbulent shear stress.

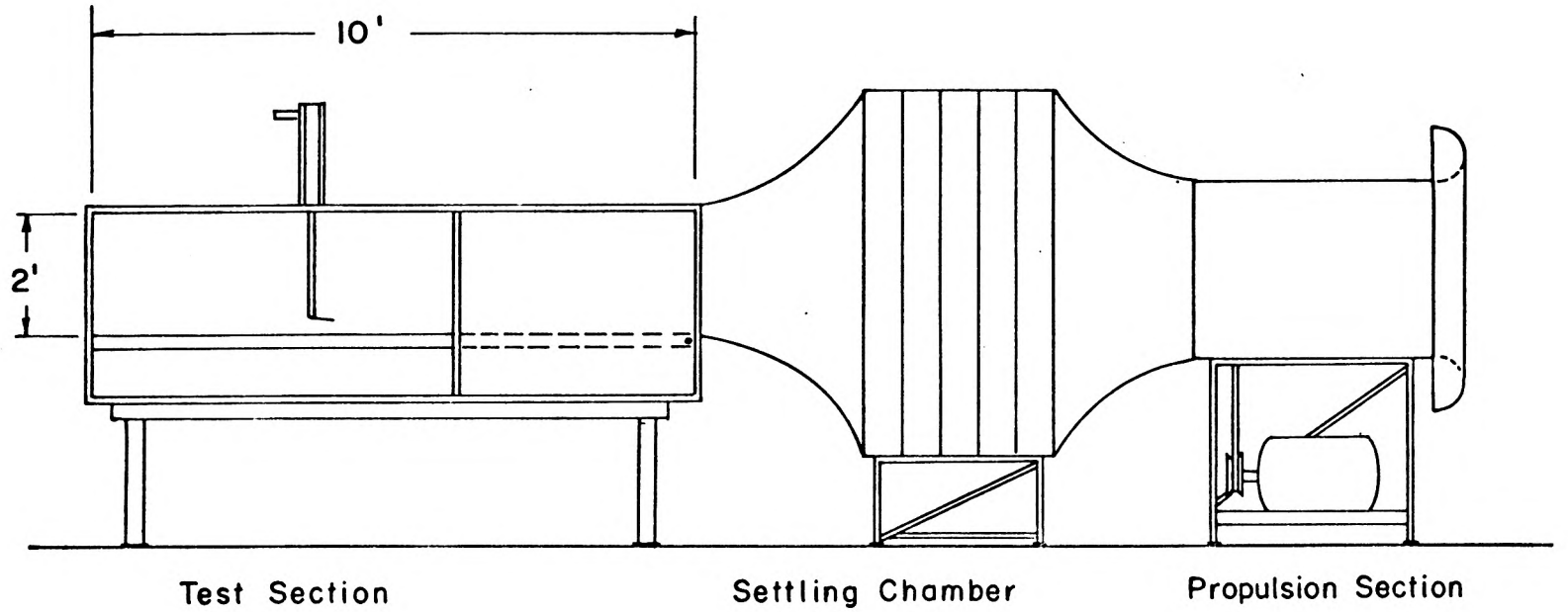

FIG. 1 WIND TUNNEL - GENERAL VIEW

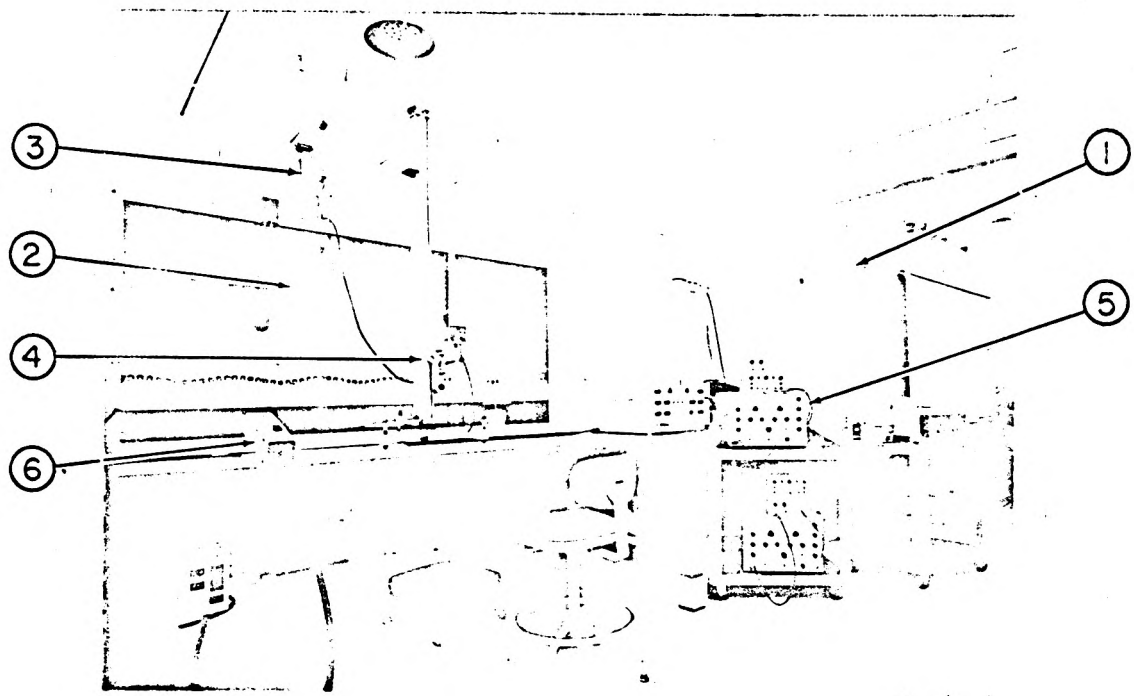

1. Settling chamber
2. Test section
3. Traverse mechanism
4. Cathetometer
5. Hot-wire equipment (DISA)
6. Speed controller

FIG. 2 EXPERIMENTAL SET- UP

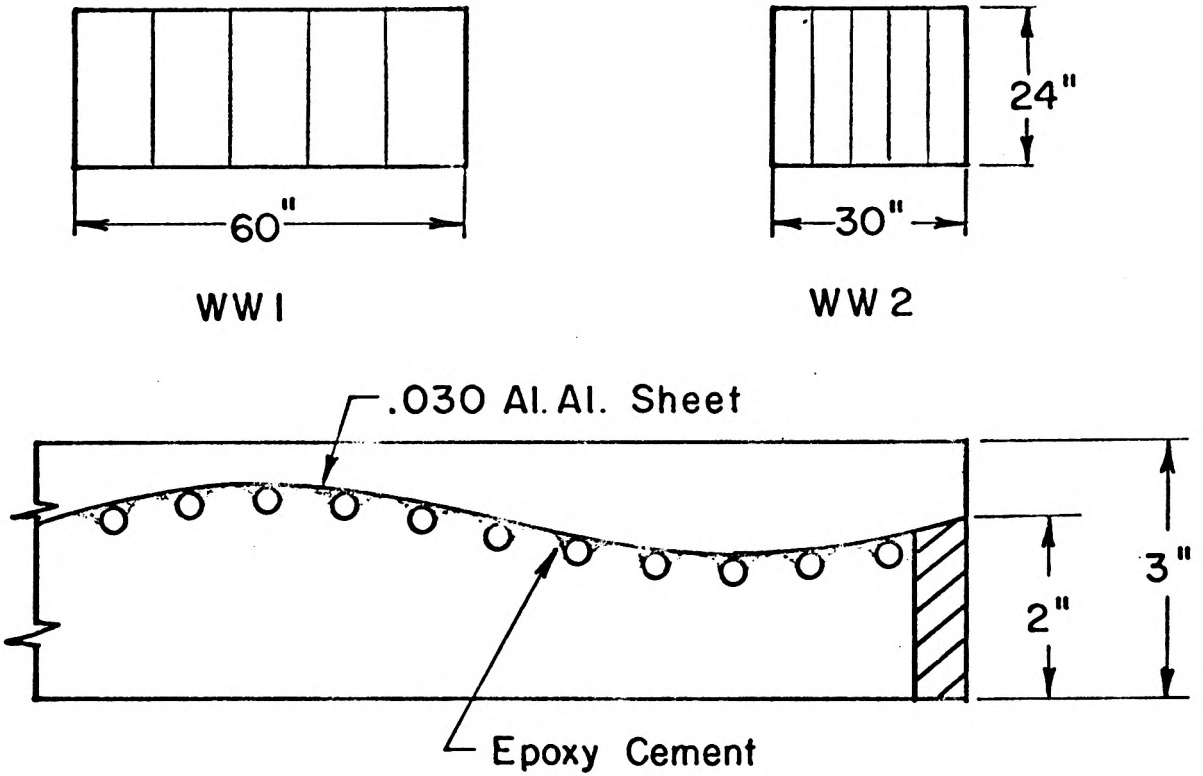

FIG. 3 WAVY WALL MODELS - DETAILS OF CONSTRUCTION

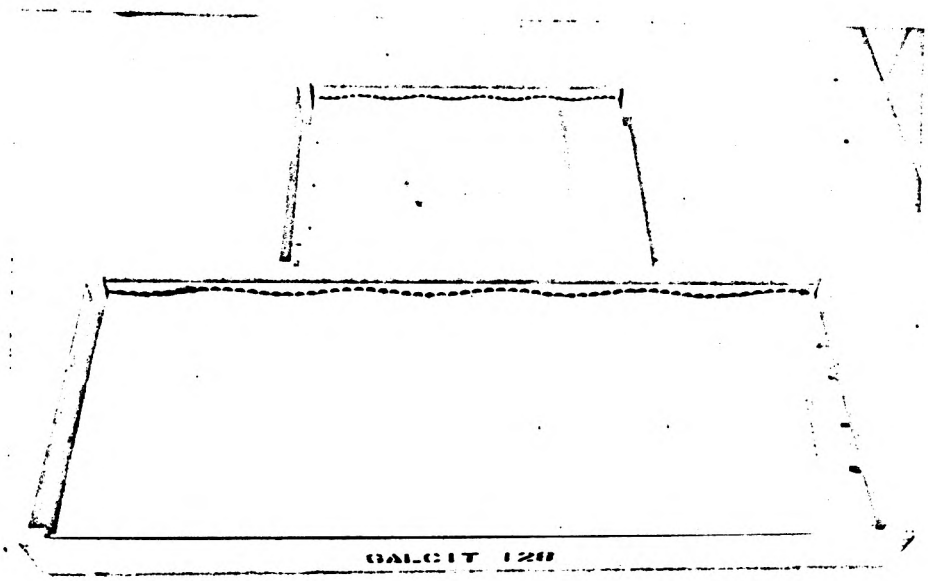

Front : WW 1
Rear : WW2

FIG. 4 WAVY WALL MODELS

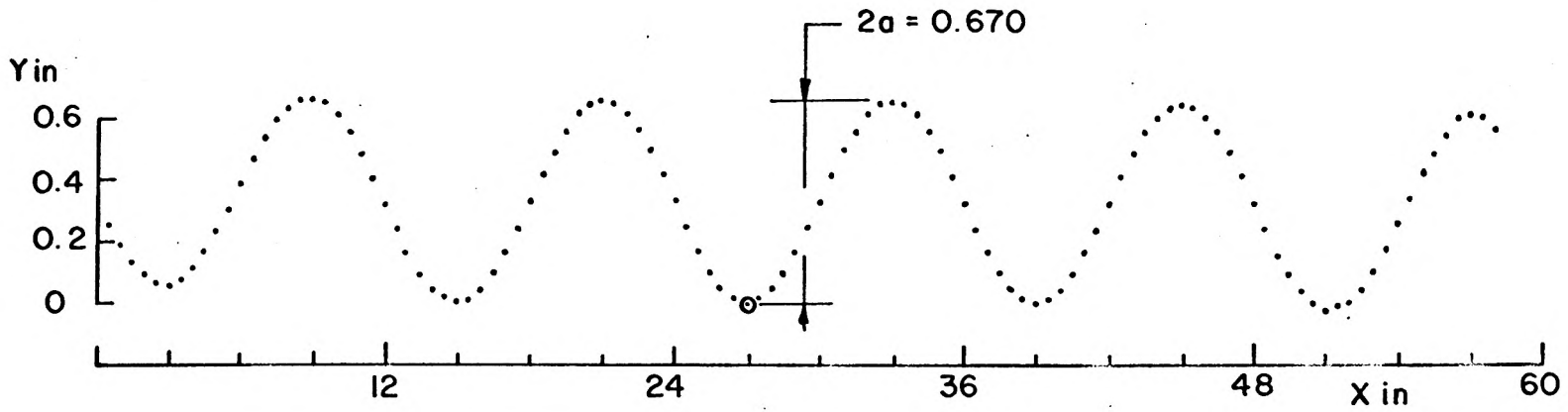

FIG. 5a SHAPE OF WAVY WALL I
MEASURED ALONG ℄

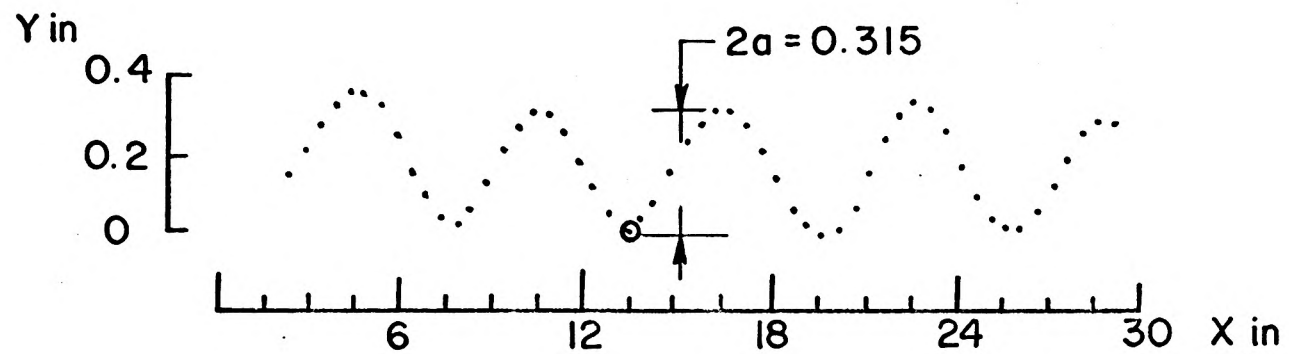

FIG. 5 b SHAPE OF WAVY WALL 2
MEASURED ALONG ℄

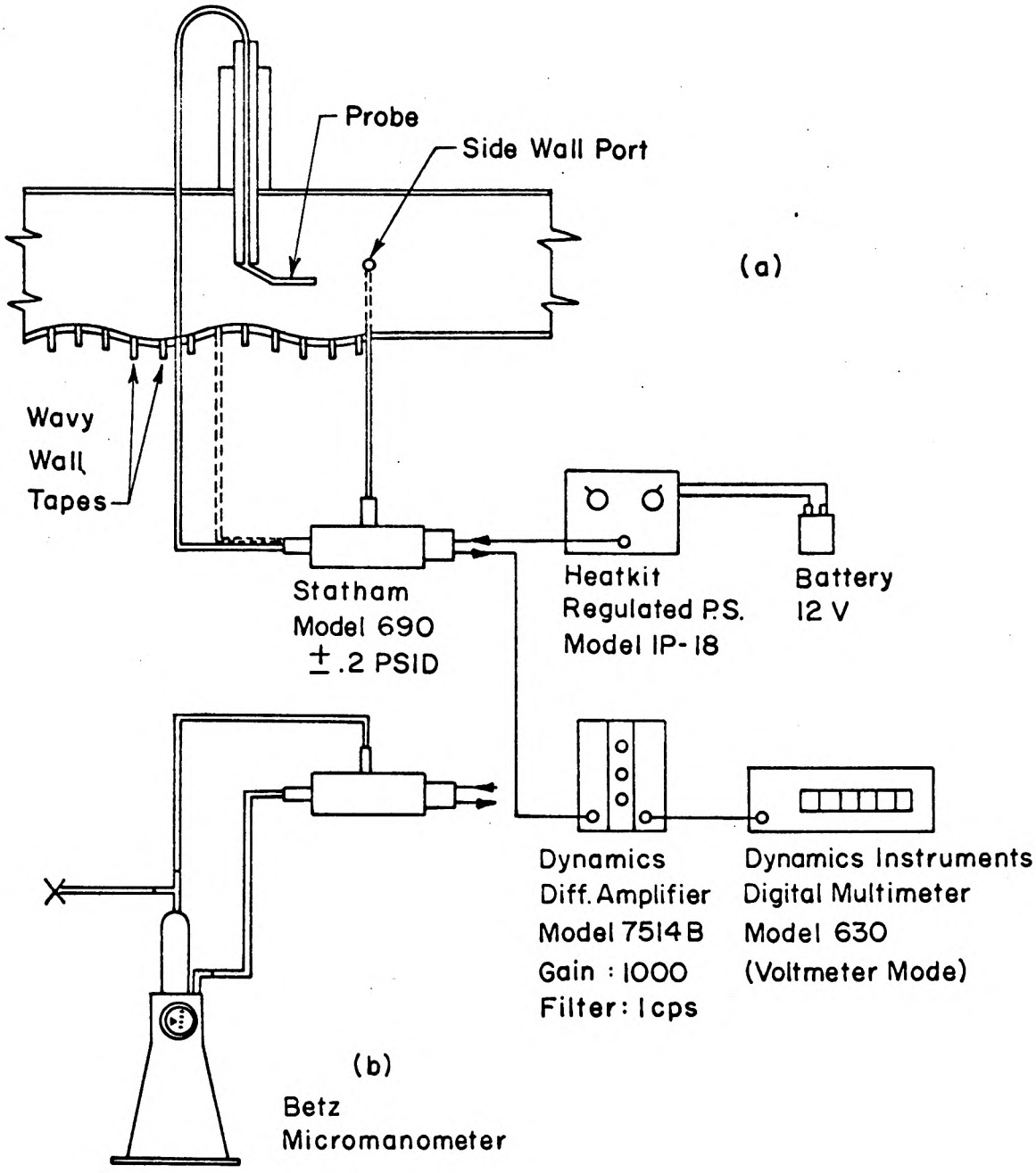

FIG. 6 MEASUREMENT OF PRESSURES
(a) Schematic Of Set-Up
(b) Calibration Of Transducer

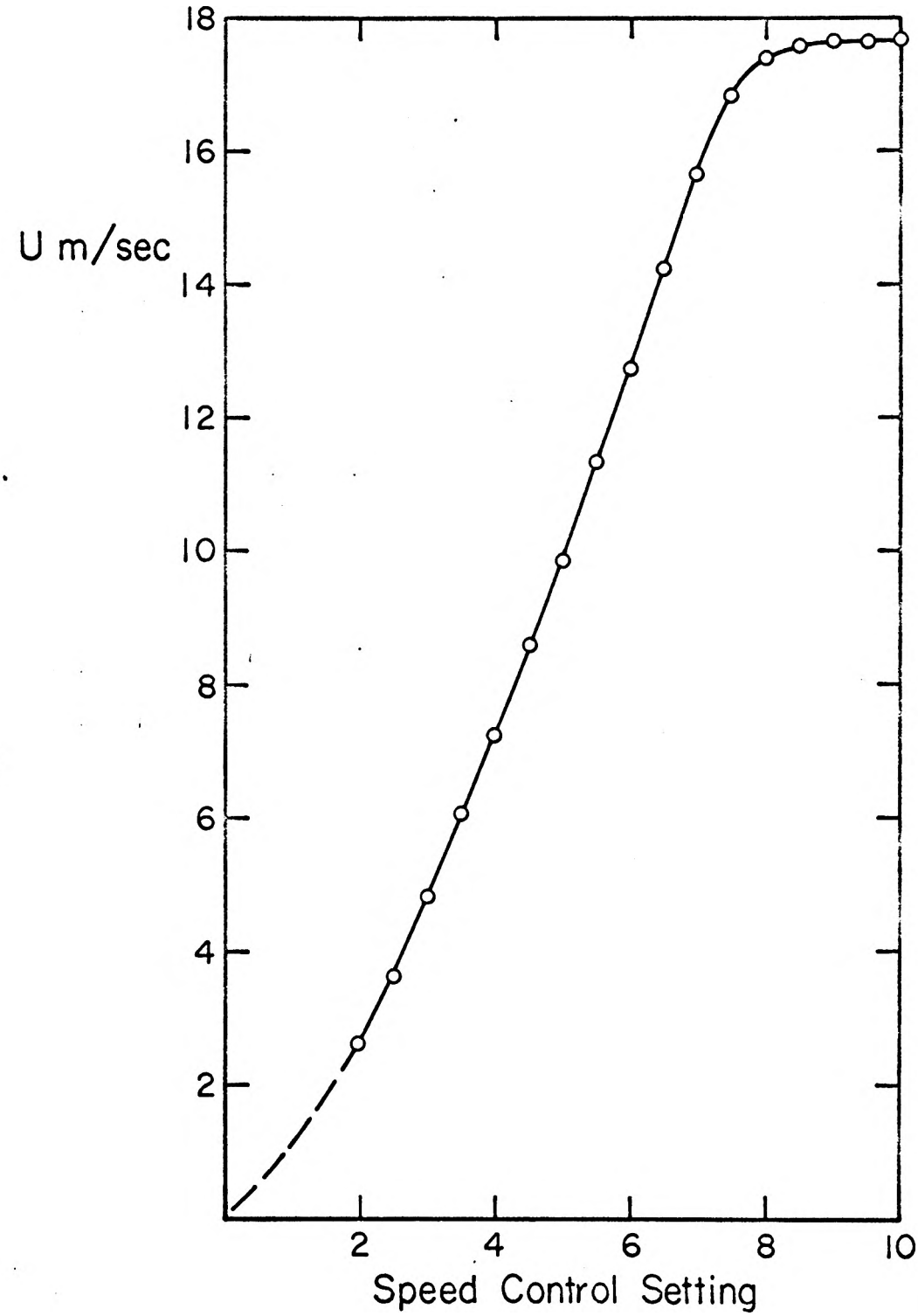

FIG. 7 CALIBRATION OF AIRSPEED AT THE CENTER OF THE TEST SECTION

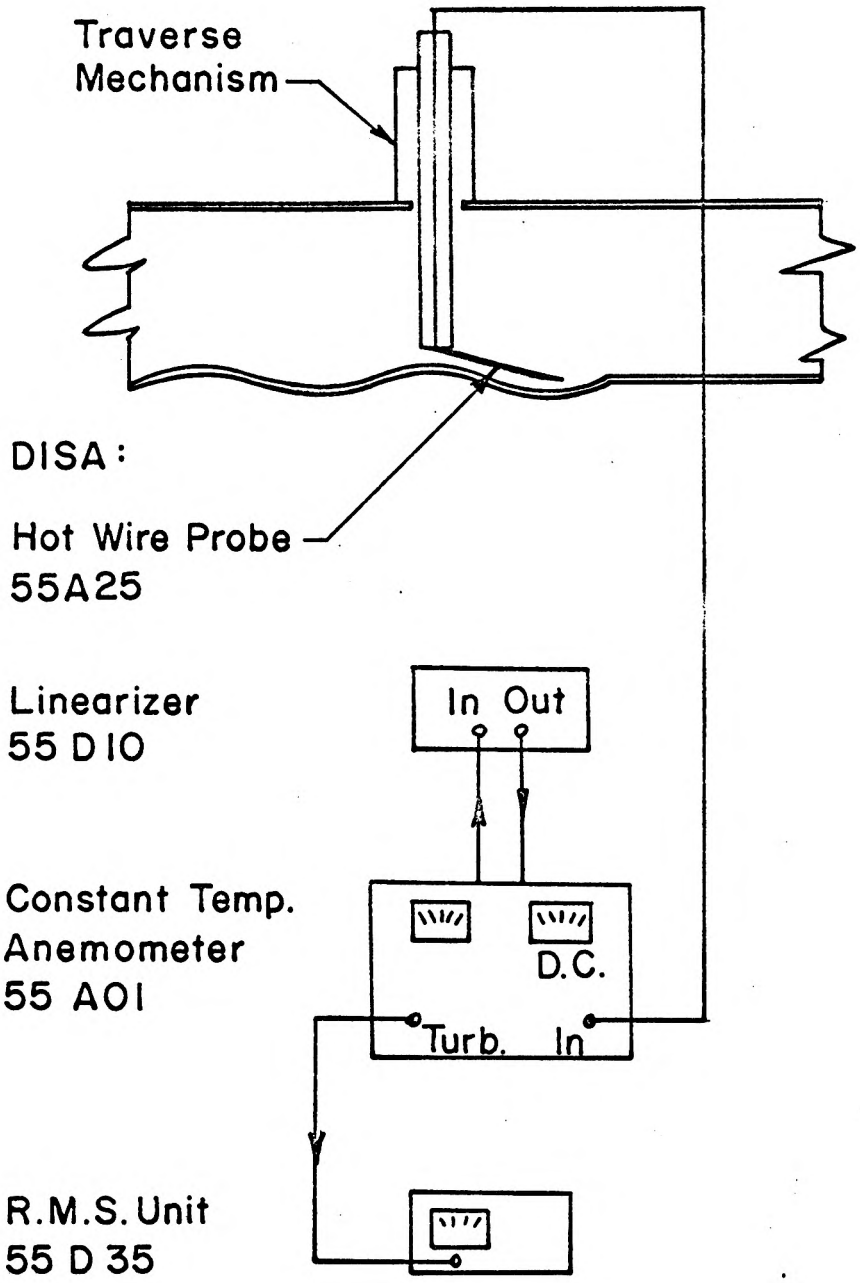

FIG. 8 MEASUREMENT OF BOUNDARY LAYER PROFILE AND TURBULENCE LEVEL USING SINGLE ELEMENT HOT-WIRE PROBE

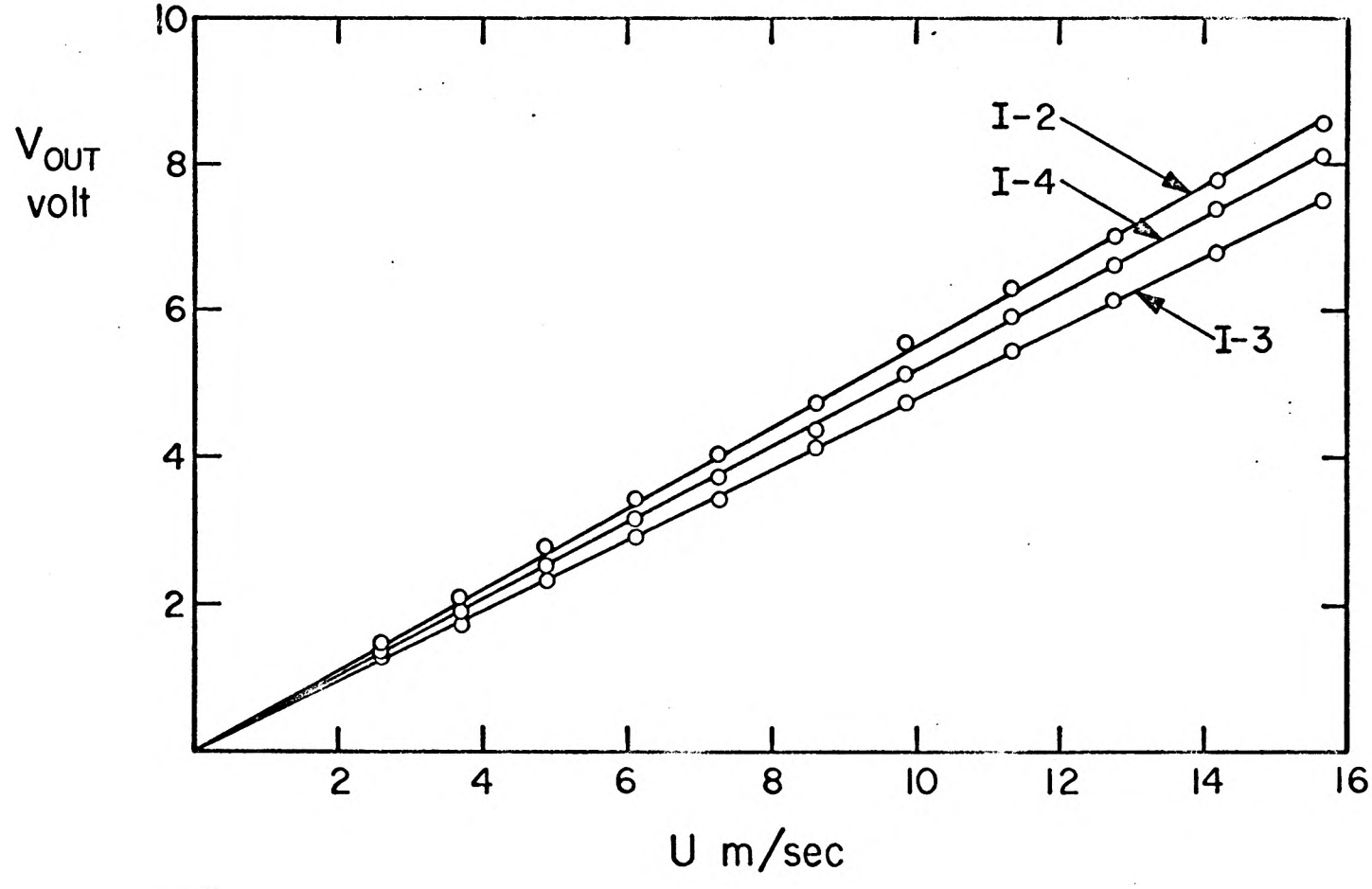

FIG. 9 CALIBRATION OF SINGLE ELEMENT HOT WIRE PROBES

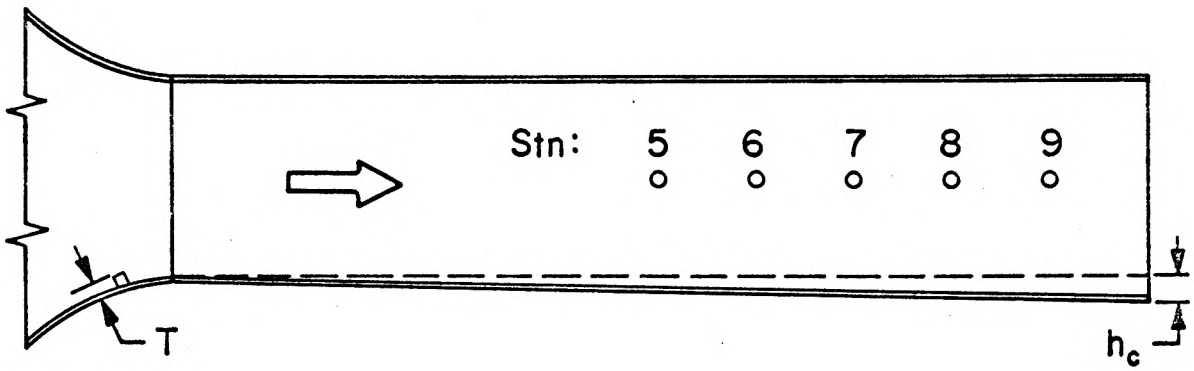

a. LOCATION OF STATIC PRESSURE PORTS

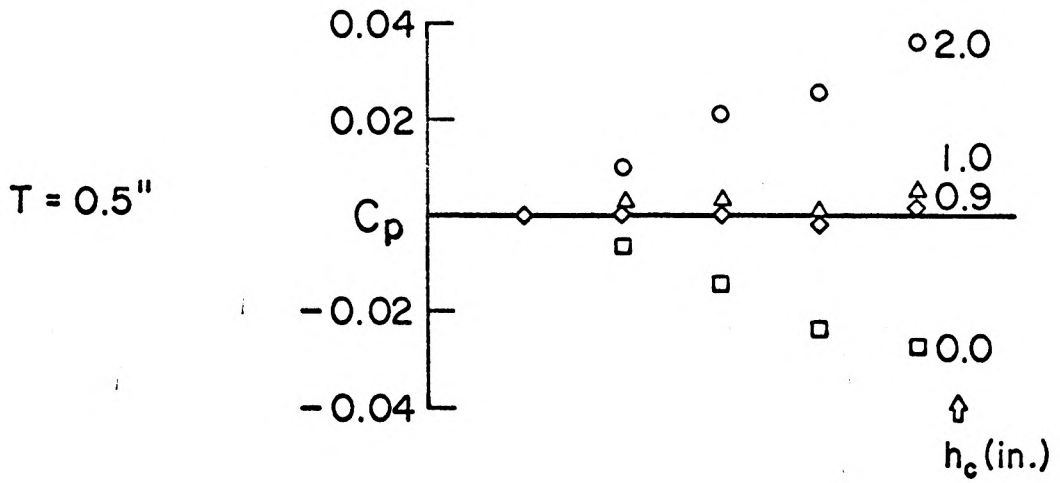

b. SIDE WALL PRESSURE DISTRIBUTION

FIG. 10 COMPENSATION FOR BOUNDARY LAYER GROWTH

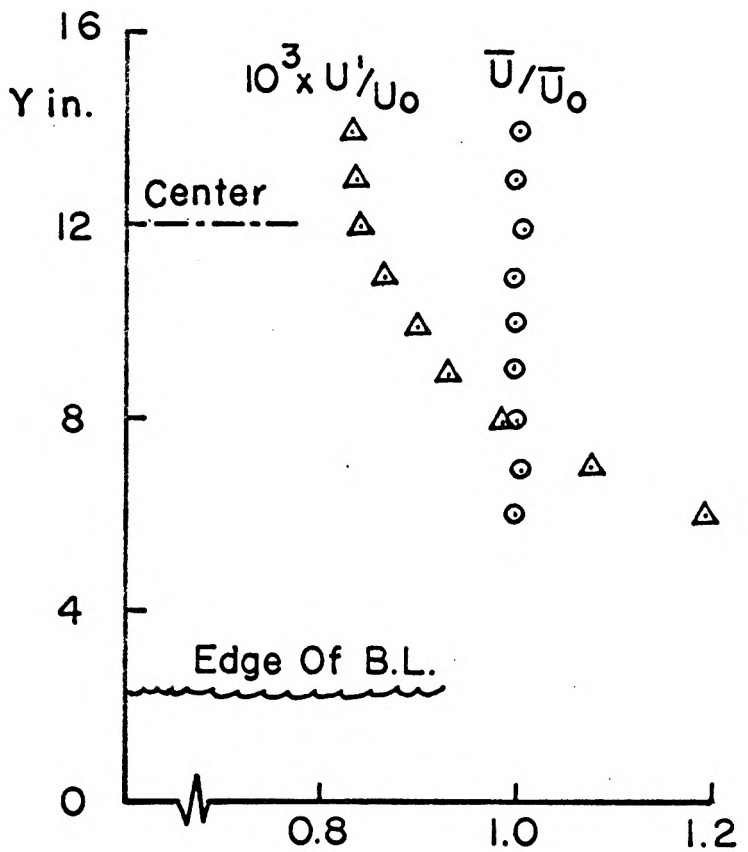

FIG. 11 AVERAGE VELOCITY AND FREE STREAM TURBULENCE IN THE TEST SECTION

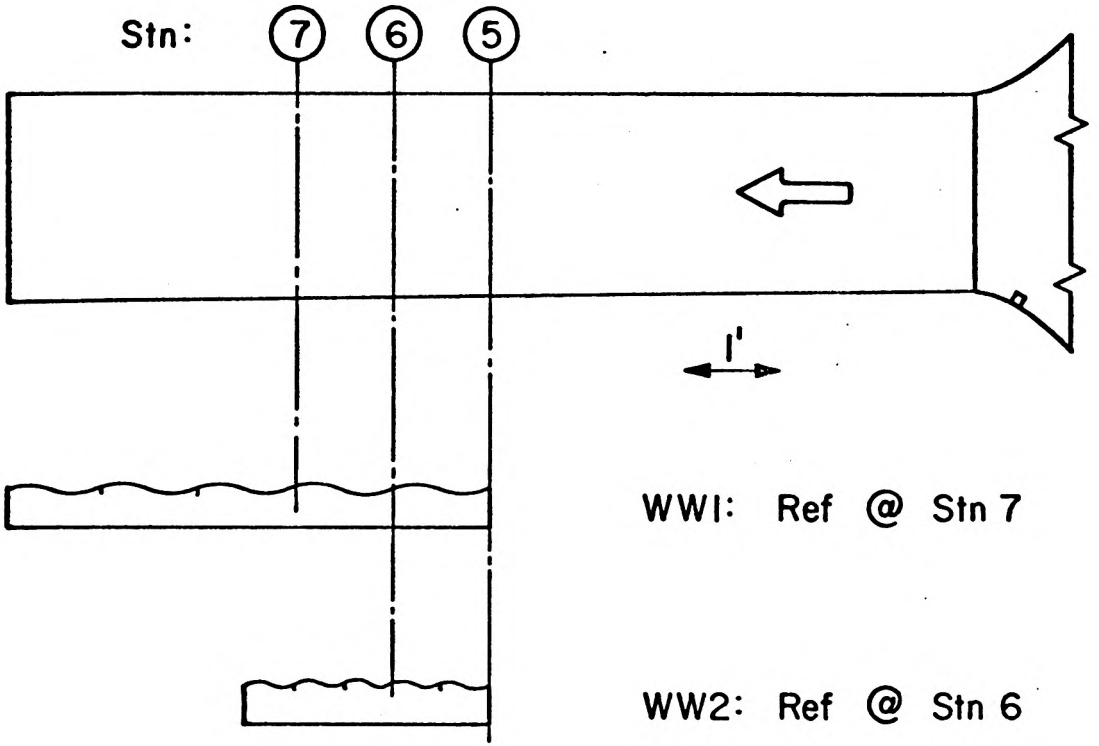

FIG. 12 LOCATION OF THE TWO MODELS AND THE CORRESPONDING REFERENCE PROFILES IN THE TEST SECTION

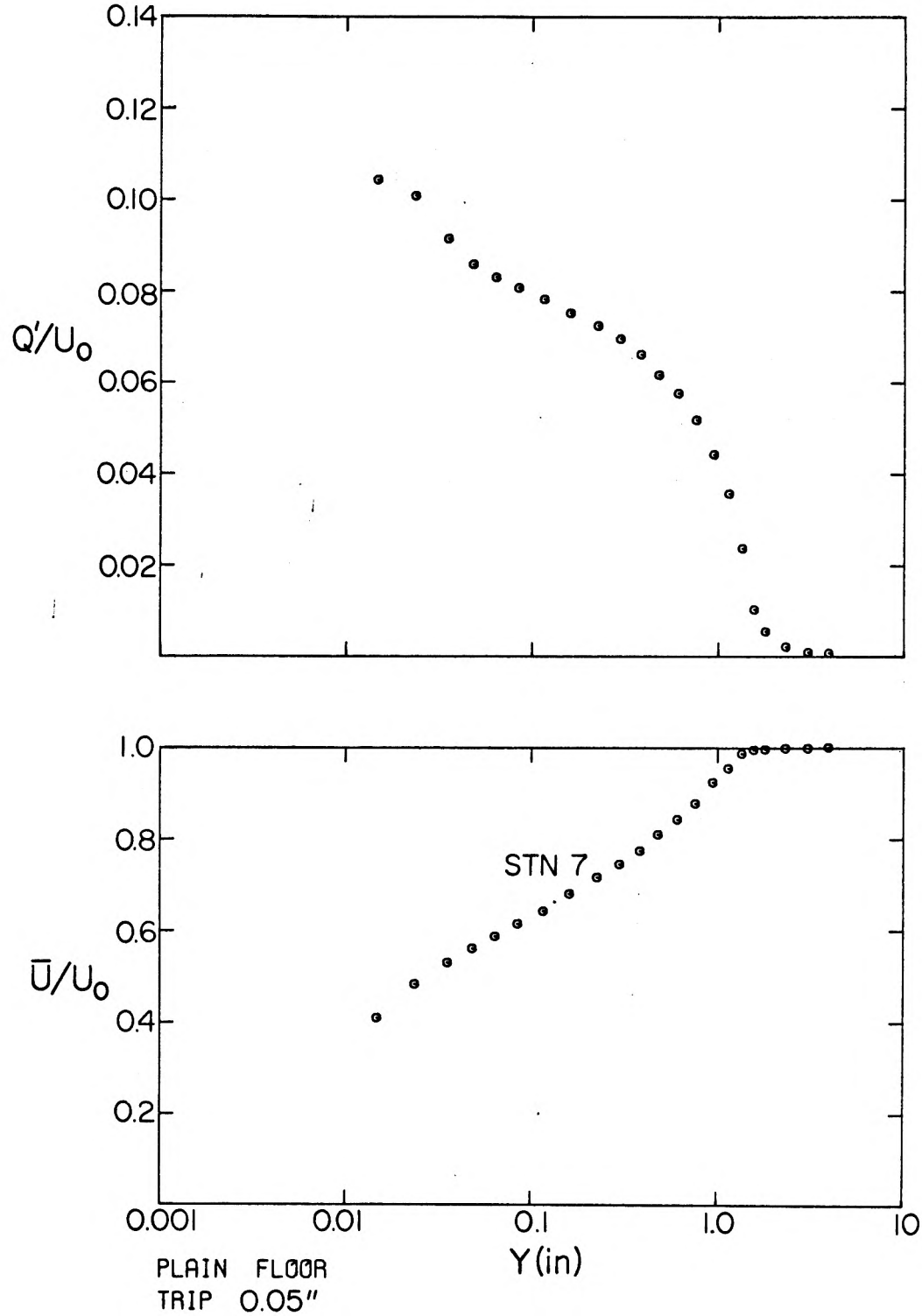

FIG. 13a REFERENCE VELOCITY AND TURBULENCE LEVEL PROFILES

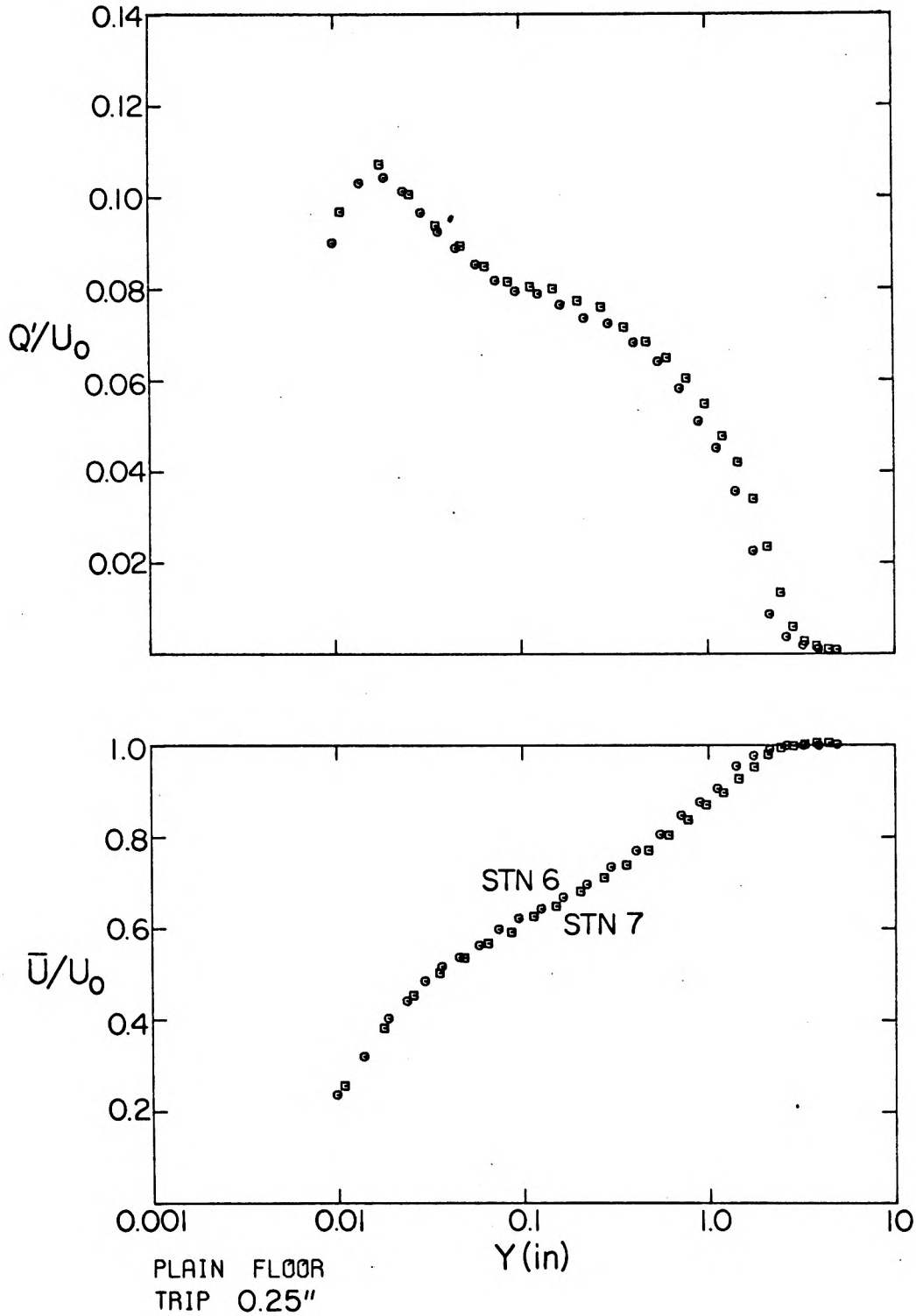

FIG. 13b REFERENCE VELOCITY AND TURBULENCE LEVEL PROFILES

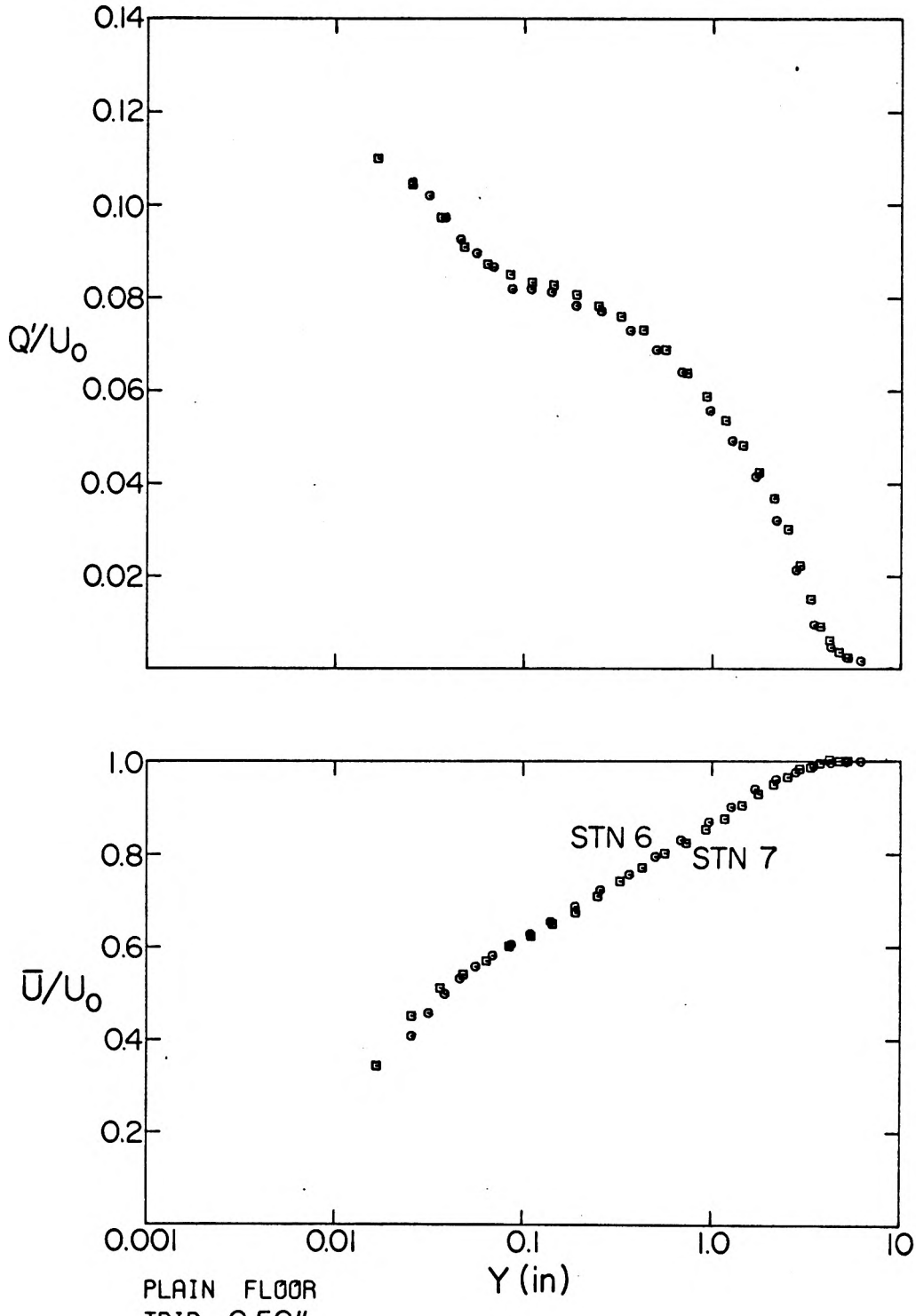

FIG.13c REFERENCE VELOCITY AND TURBULENCE LEVEL PROFILES

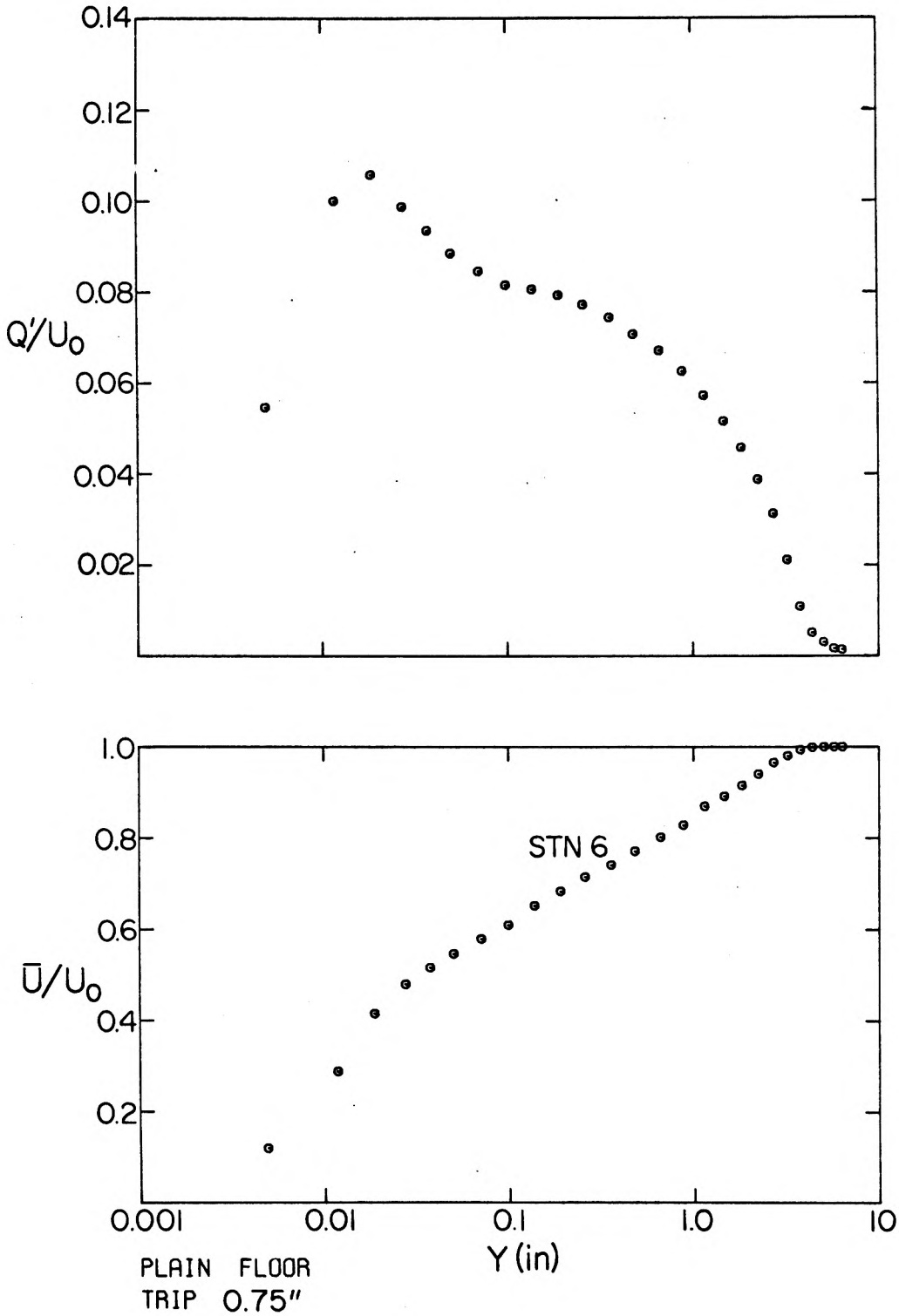

FIG. 13d REFERENCE VELOCITY AND TURBULENCE LEVEL PROFILES

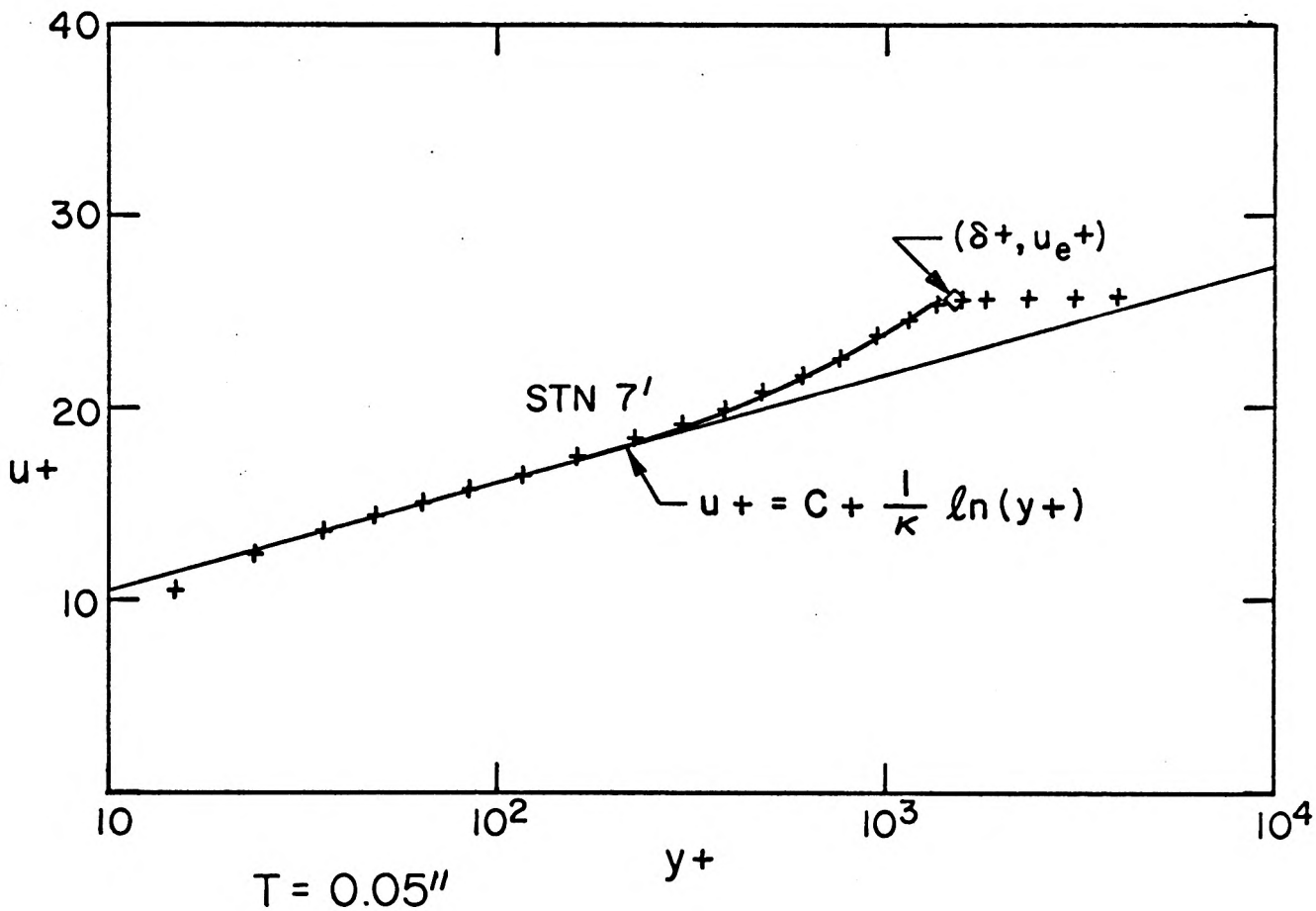

FIG. 14a REFERENCE PROFILES REDUCED TO SIMILARITY COORDINATES

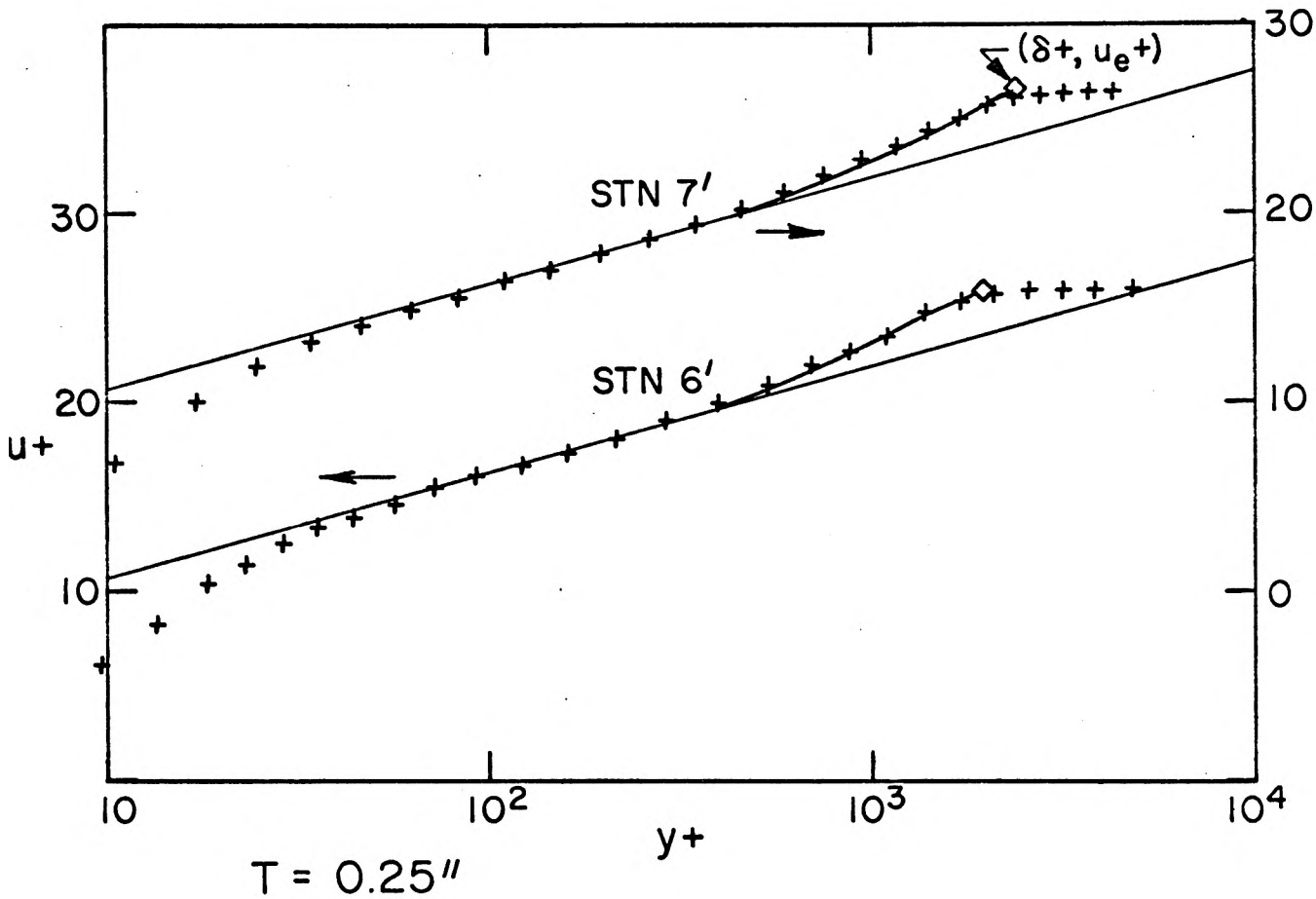

FIG. 14b REFERENCE PROFILES REDUCED TO SIMILARITY COORDINATES

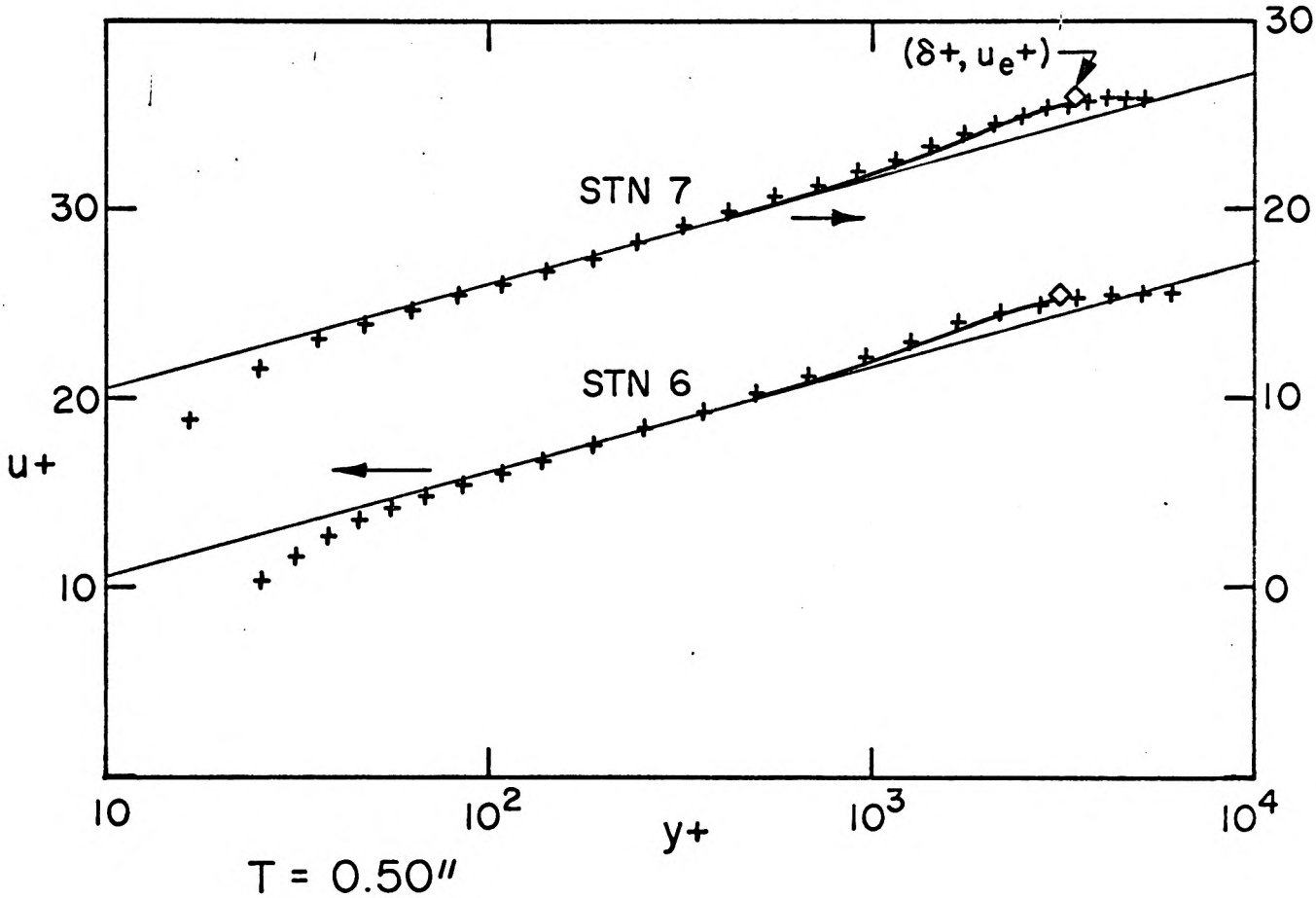

FIG.14c REFERENCE PROFILES REDUCED TO SIMILARITY COORDINATES

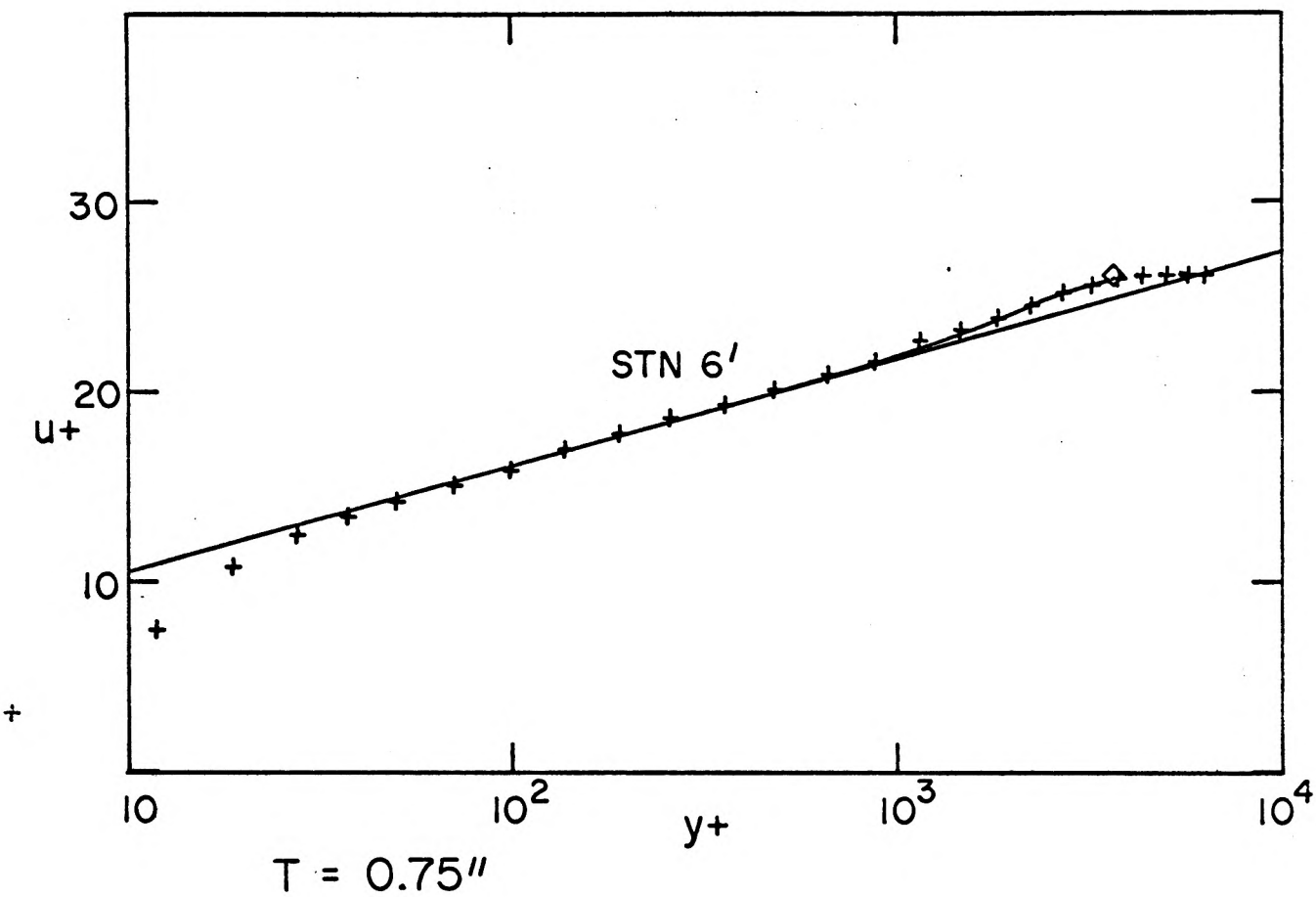

FIG. 14d REFERENCE PROFILES REDUCED TO SIMILARITY COORDINATES

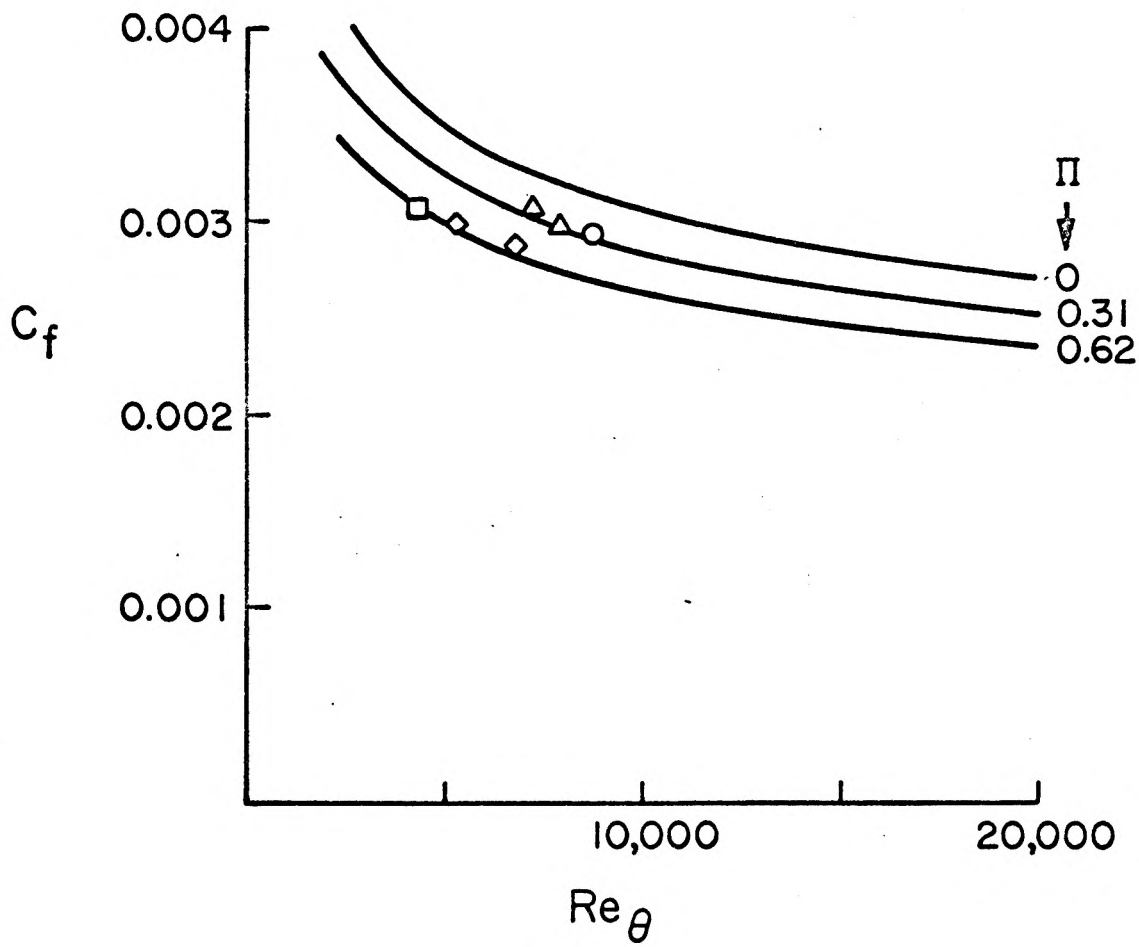

PRESENT TEST, REF. PROFILES:

SYM.	$T_{in.}$	STN 6		STN 7	
		δ	Π	δ	Π
□	0.05			1.50	.59
◇	0.25	1.96	.51	2.43	.51
△	0.50	3.08	.22	3.41	.23
○	0.75	3.70	.23		

FIG. 15 COMPARISON BETWEEN MEASURED WALL FRICTION COEFFICIENT AND LUDWIG AND TILLMAN FRICTION LAW.

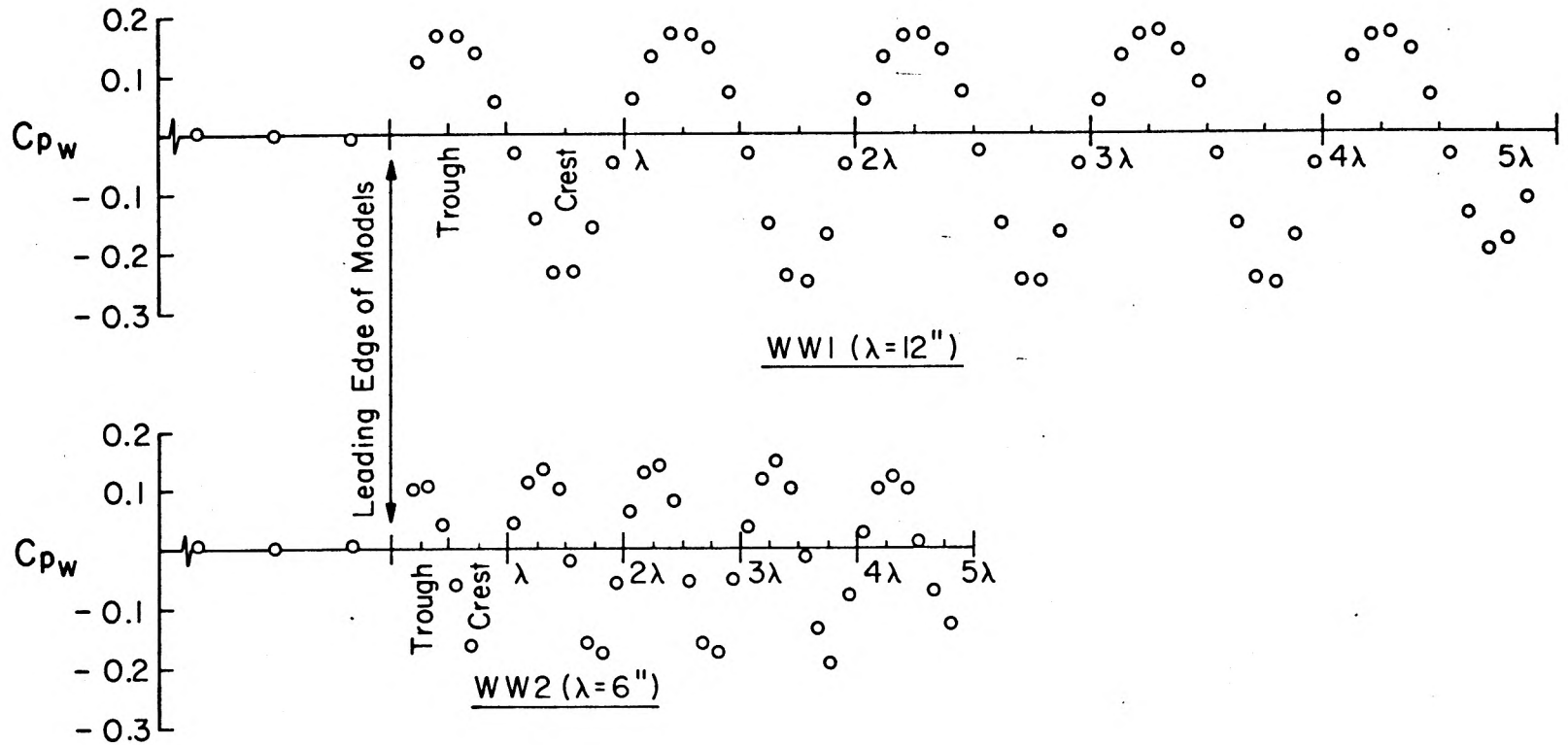

FIG. 16 SURFACE PRESSURE DISTRIBUTION ALONG WAVY WALL MODELS (TRIP=0.5")

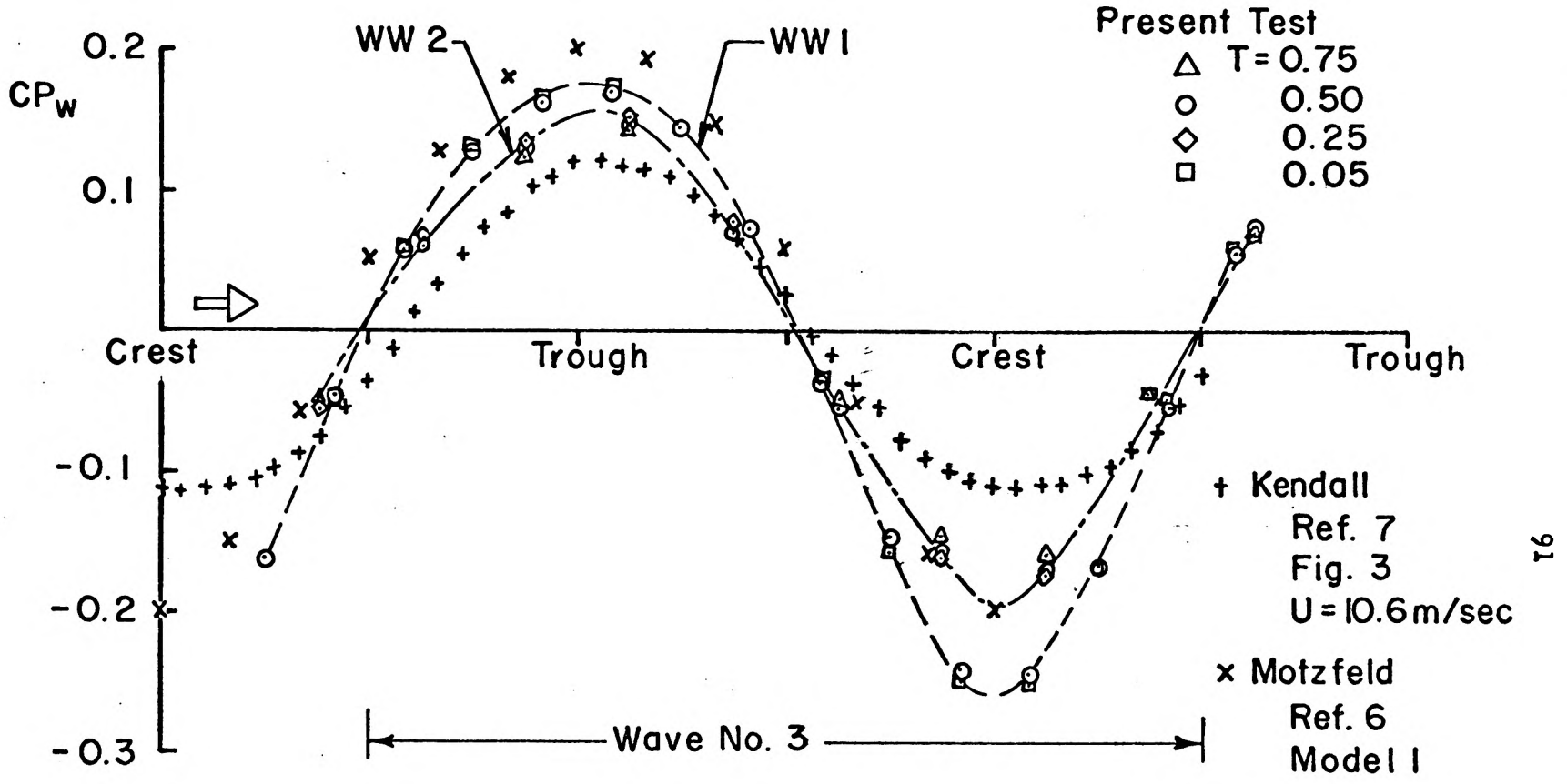

FIG. 17 COMPARISON OF SURFACE PRESSURE DISTRIBUTION FOR ALL THE CASES

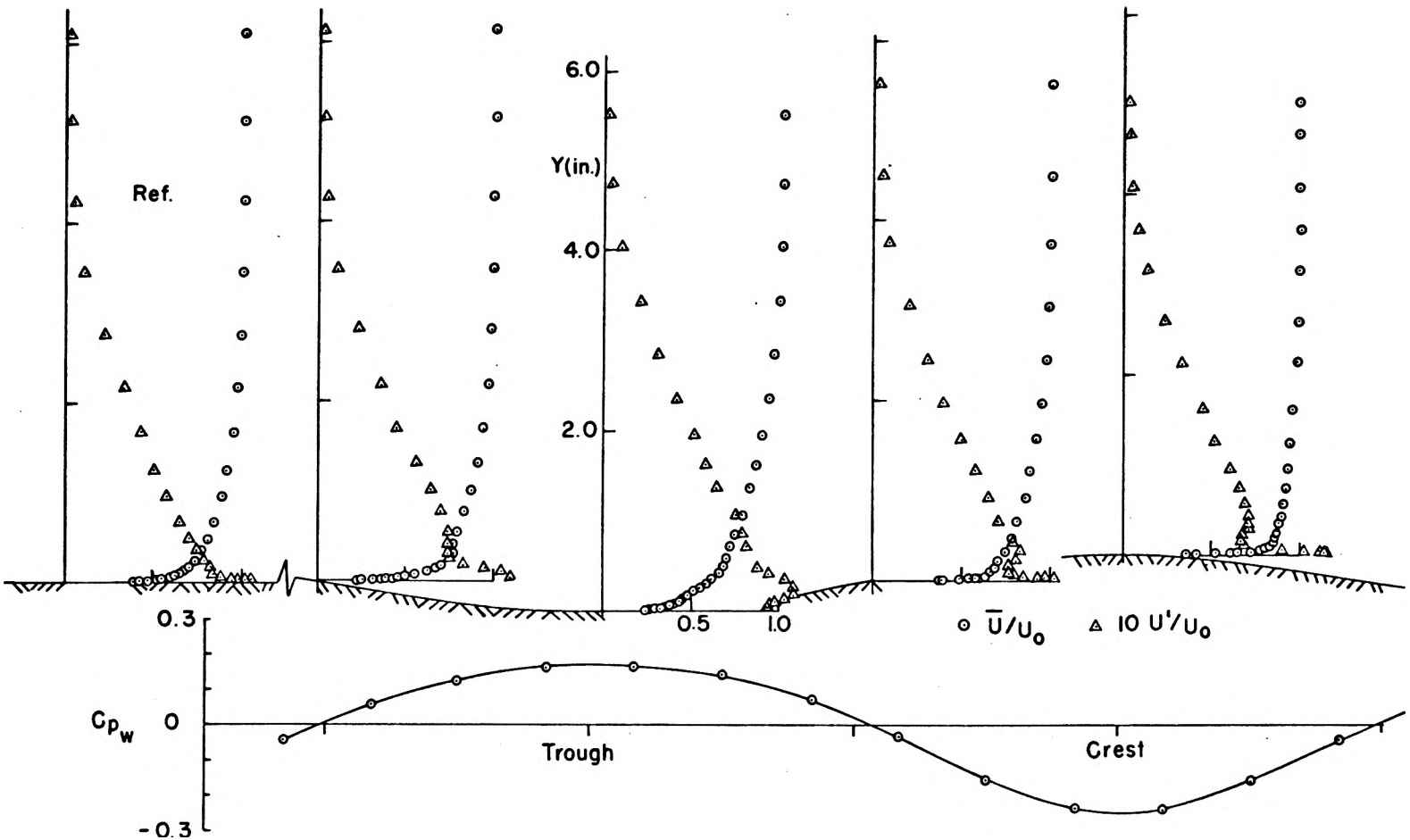

FIG.18a PRESSURE COEFFICIENT DISTRIBUTION, AVERAGE VELOCITY AND FLUCTUATION LEVEL AT FOUR SURVEY STATIONS ALONG WAVE NO. 3 MODEL: WWI TRIP: 0.50 in.

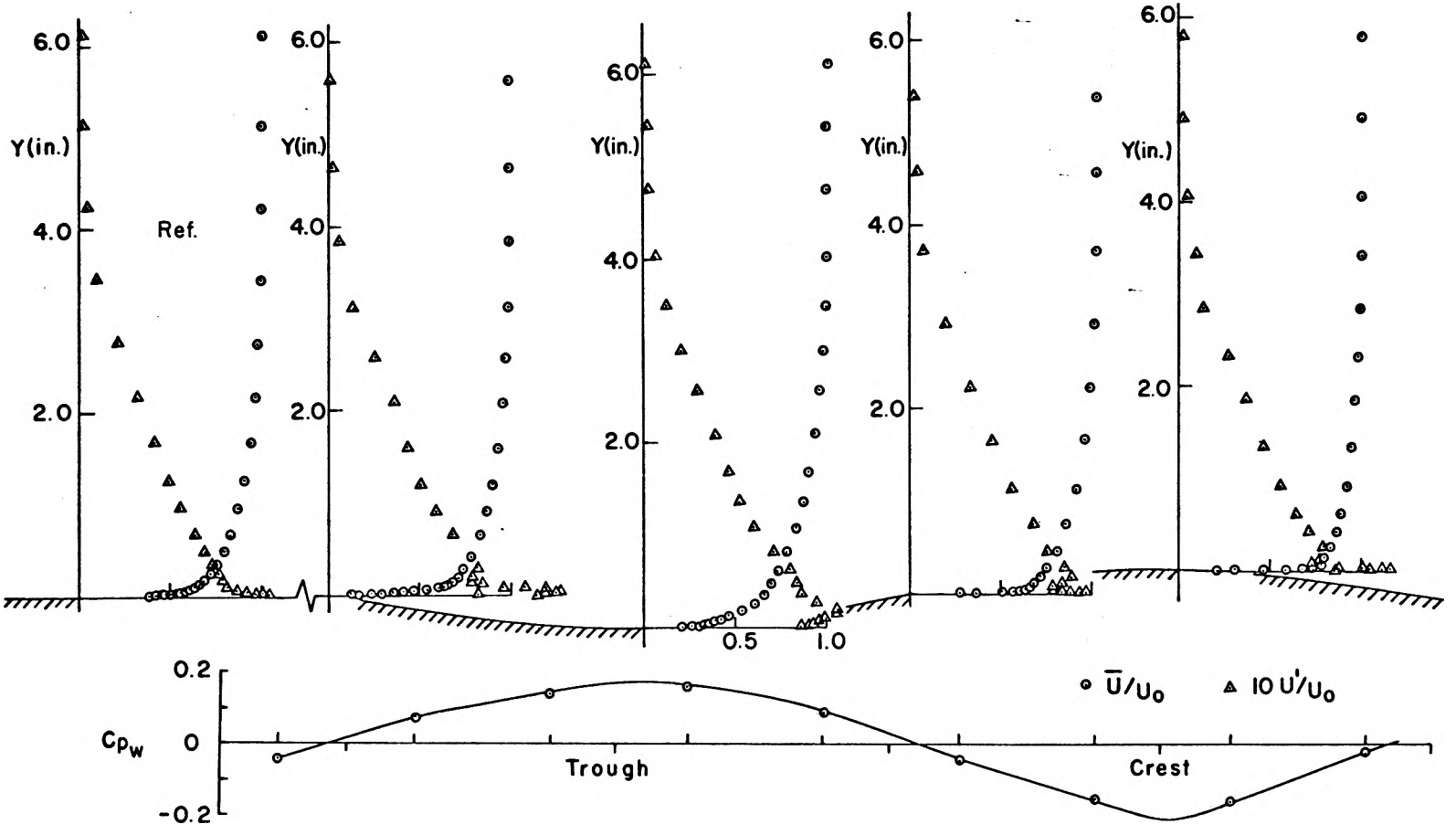

FIG. 18b PRESSURE COEFFICIENT DISTRIBUTION, AVERAGE VELOCITY AND FLUCTUATION LEVEL AT FOUR SURVEY STATIONS ALONG WAVE NO. 3 MODEL : WW2 TRIP : 0.50 in.

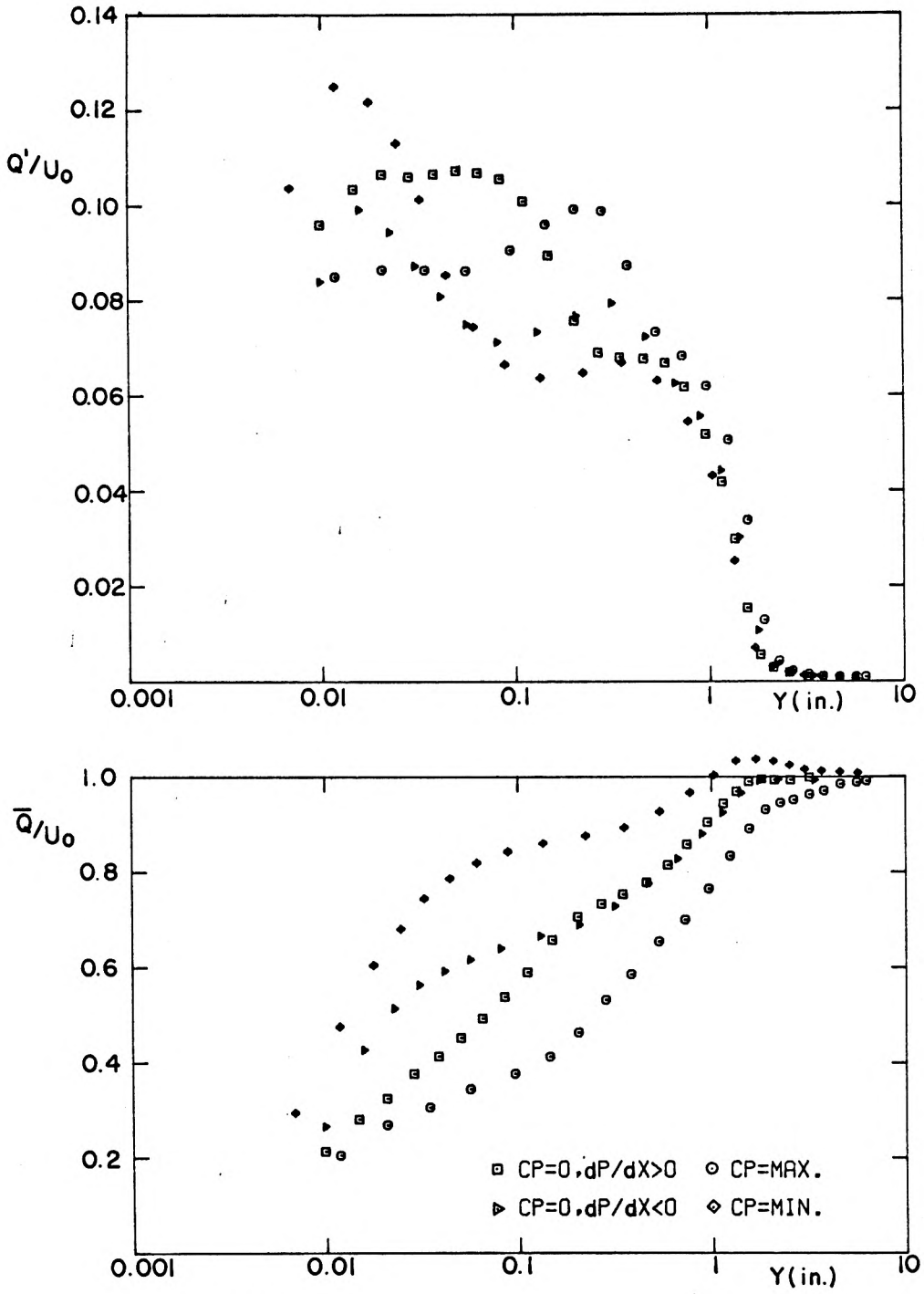

MODEL WW 1
TRIP 0.05

FIG. 19a AVERAGE VELOCITY AND TURBULENCE LEVEL DISTRIBUTION IN THE BOUNDARY LAYER

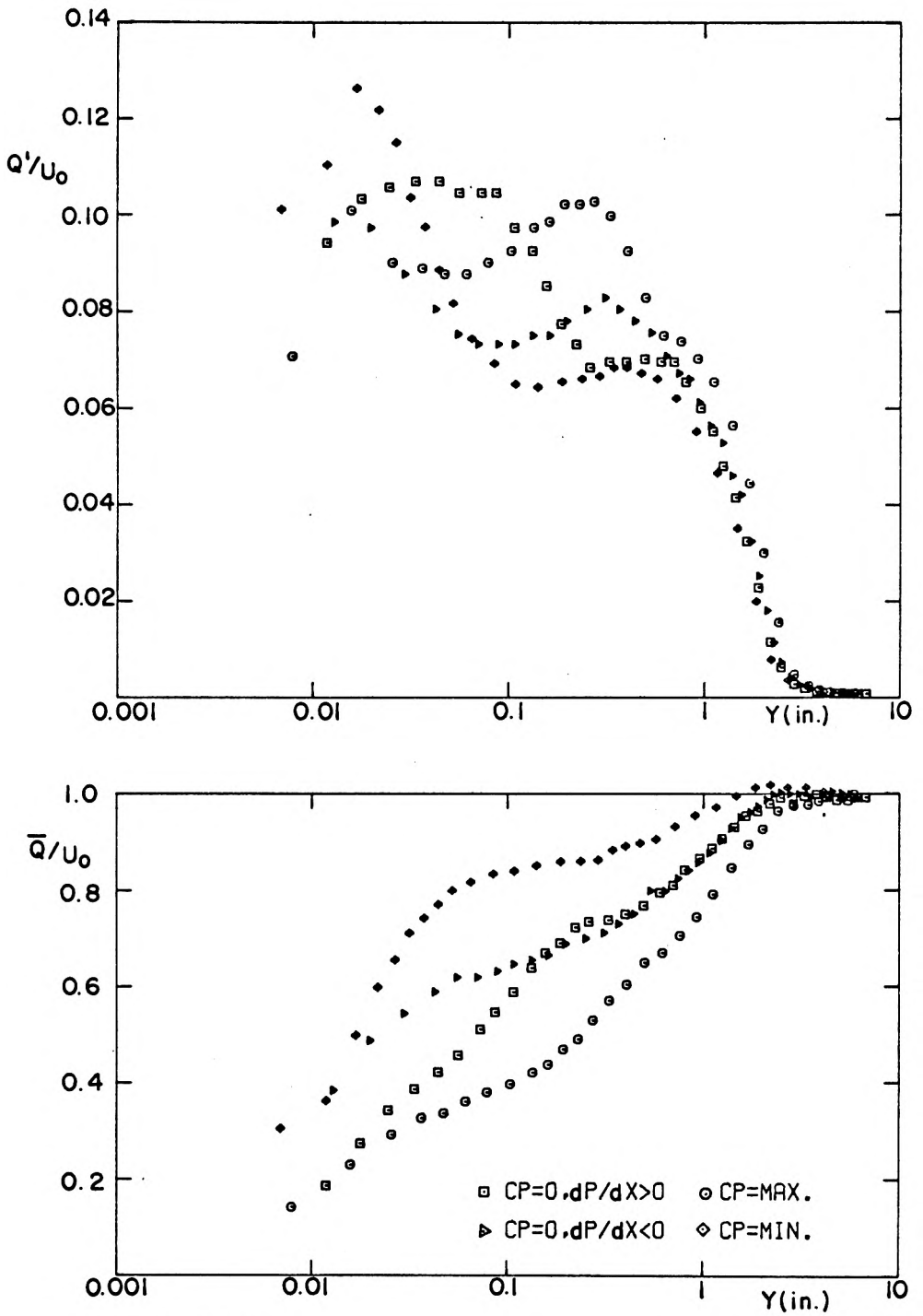

MODEL WW I
TRIP 0.25

FIG. 19 b AVERAGE VELOCITY AND TURBULENCE LEVEL DISTRIBUTION IN THE BOUNDARY LAYER

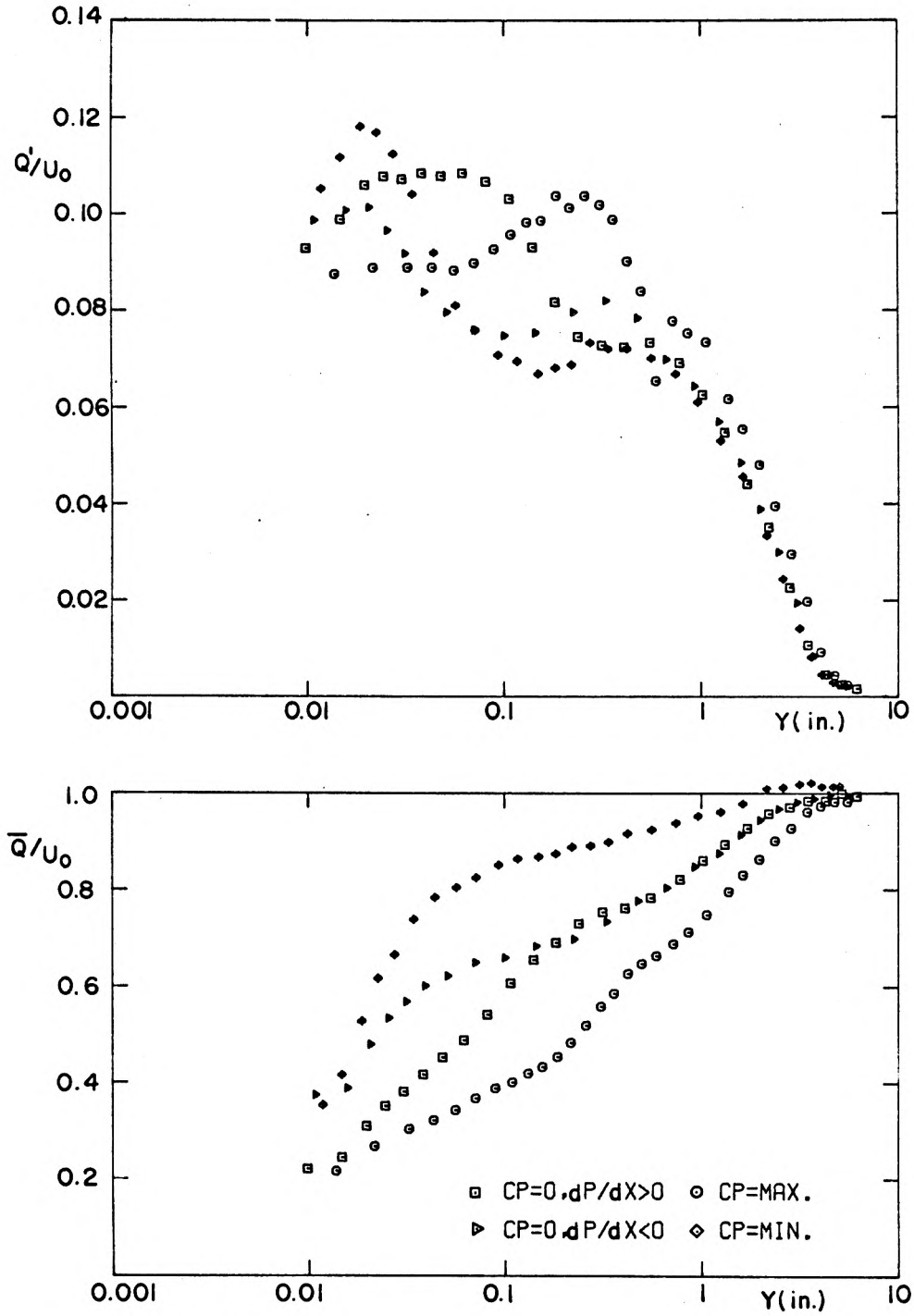

FIG. 19c AVERAGE VELOCITY AND TURBULENCE LEVEL DISTRIBUTION IN THE BOUNDARY LAYER

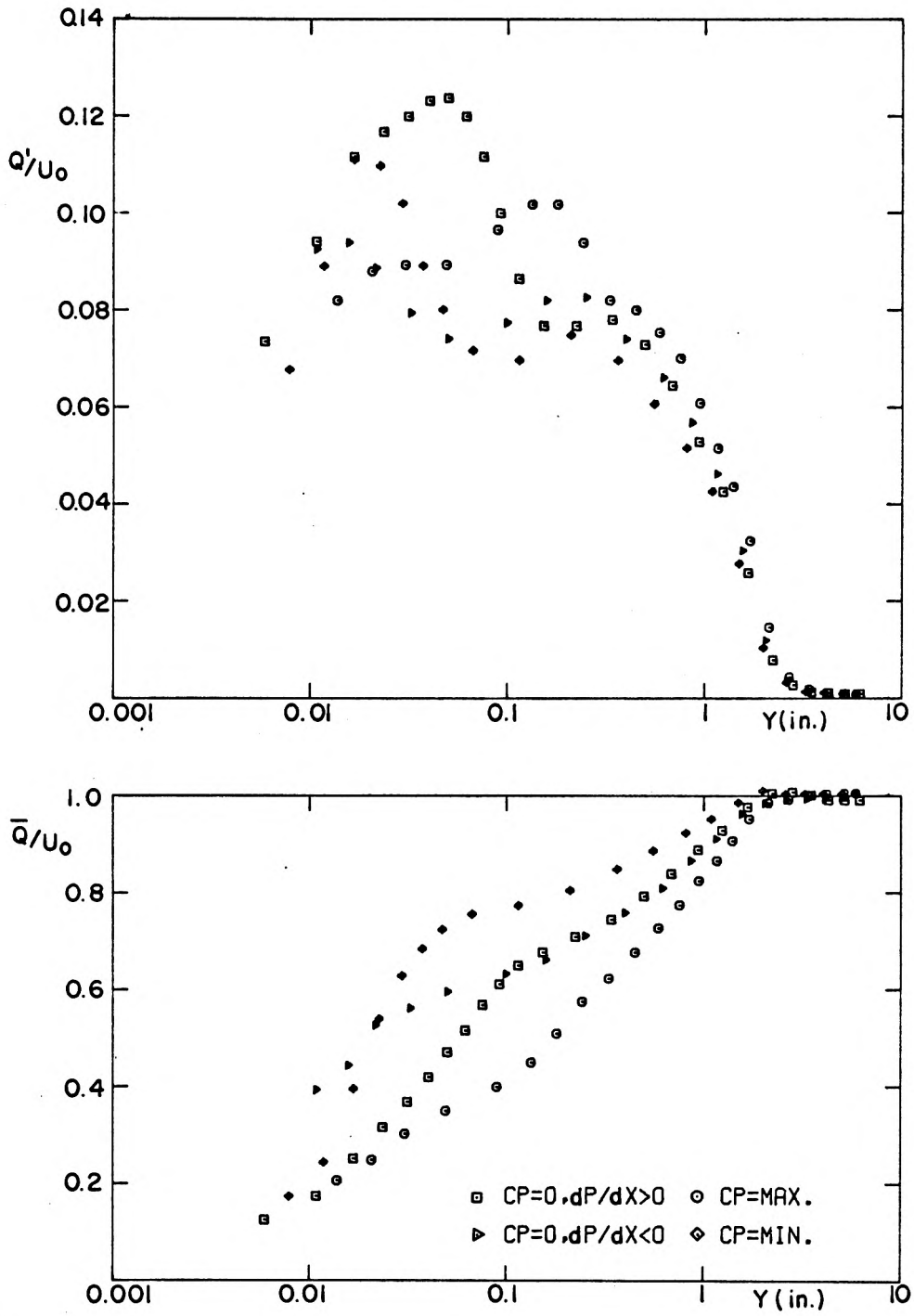

MODEL W W 2
TRIP 0.25

FIG. 19d AVERAGE VELOCITY AND TURBULENCE LEVEL DISTRIBUTION IN THE BOUNDARY LAYER

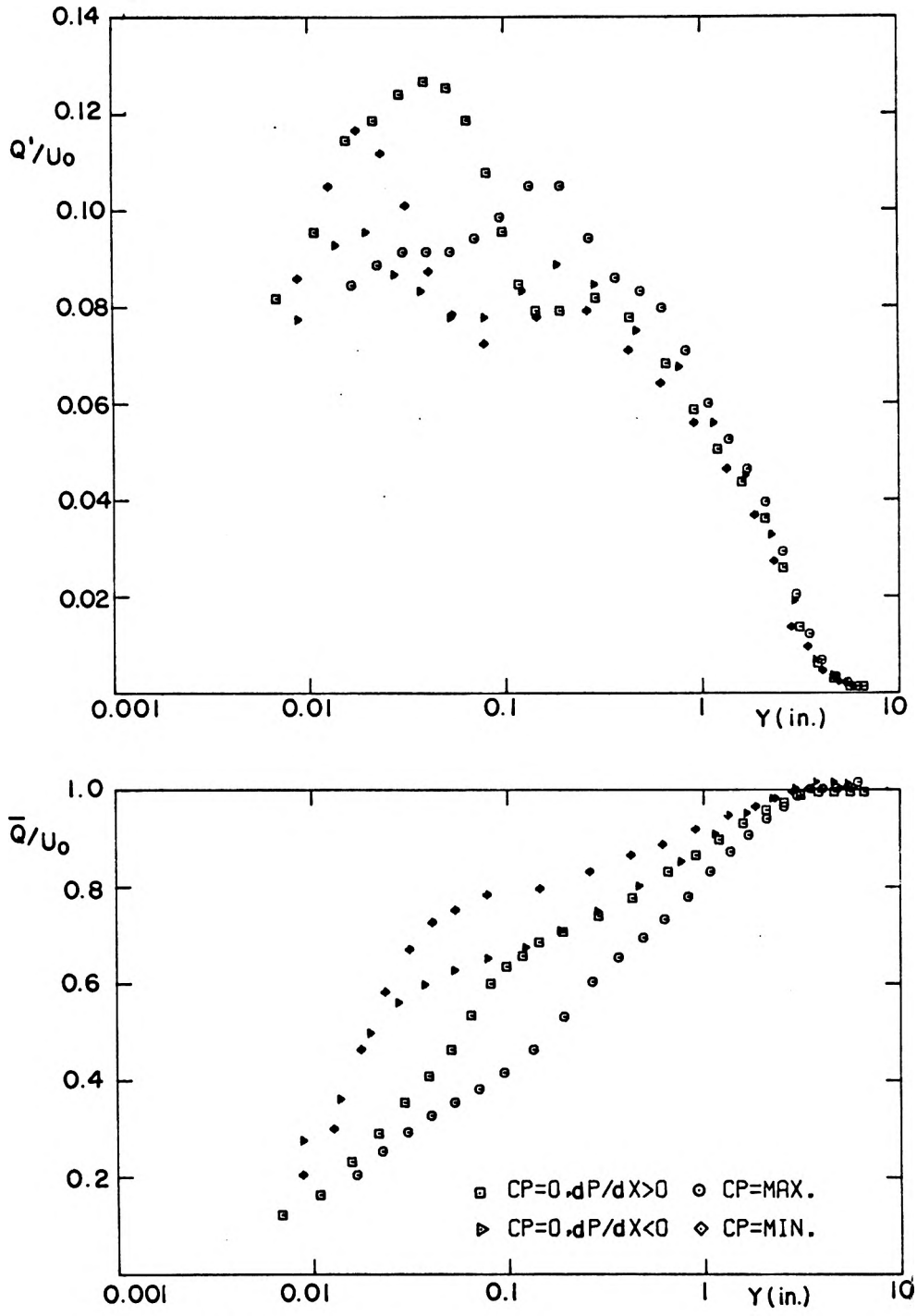

MODEL WW 2
TRIP 0.50

FIG. 19e AVERAGE VELOCITY AND TURBULENCE LEVEL DISTRIBUTION IN THE BOUNDARY LAYER

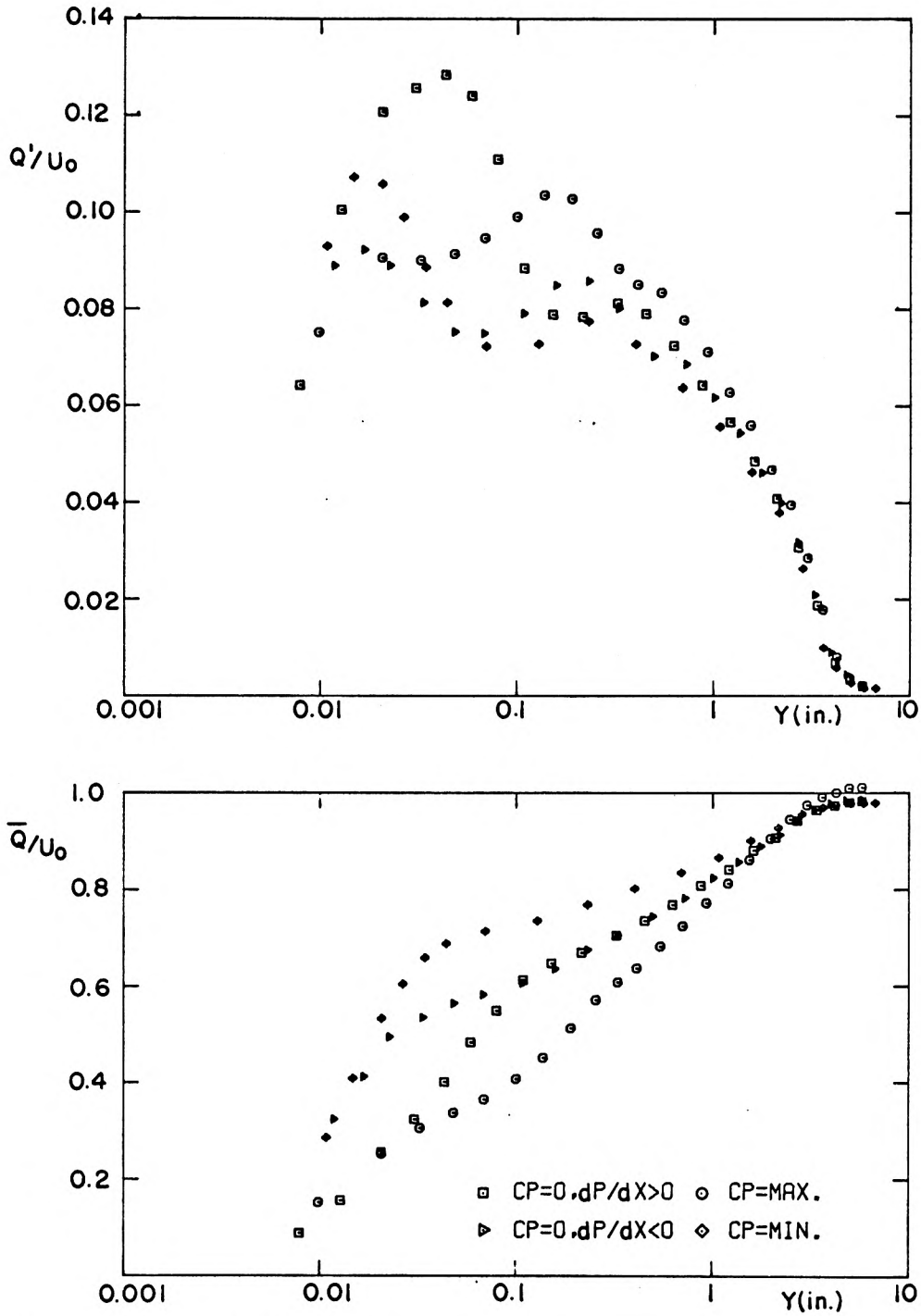

MODEL WW 2
TRIP 0.75

FIG. 19f AVERAGE VELOCITY AND TURBULENCE LEVEL DISTRIBUTION IN THE BOUNDARY LAYER

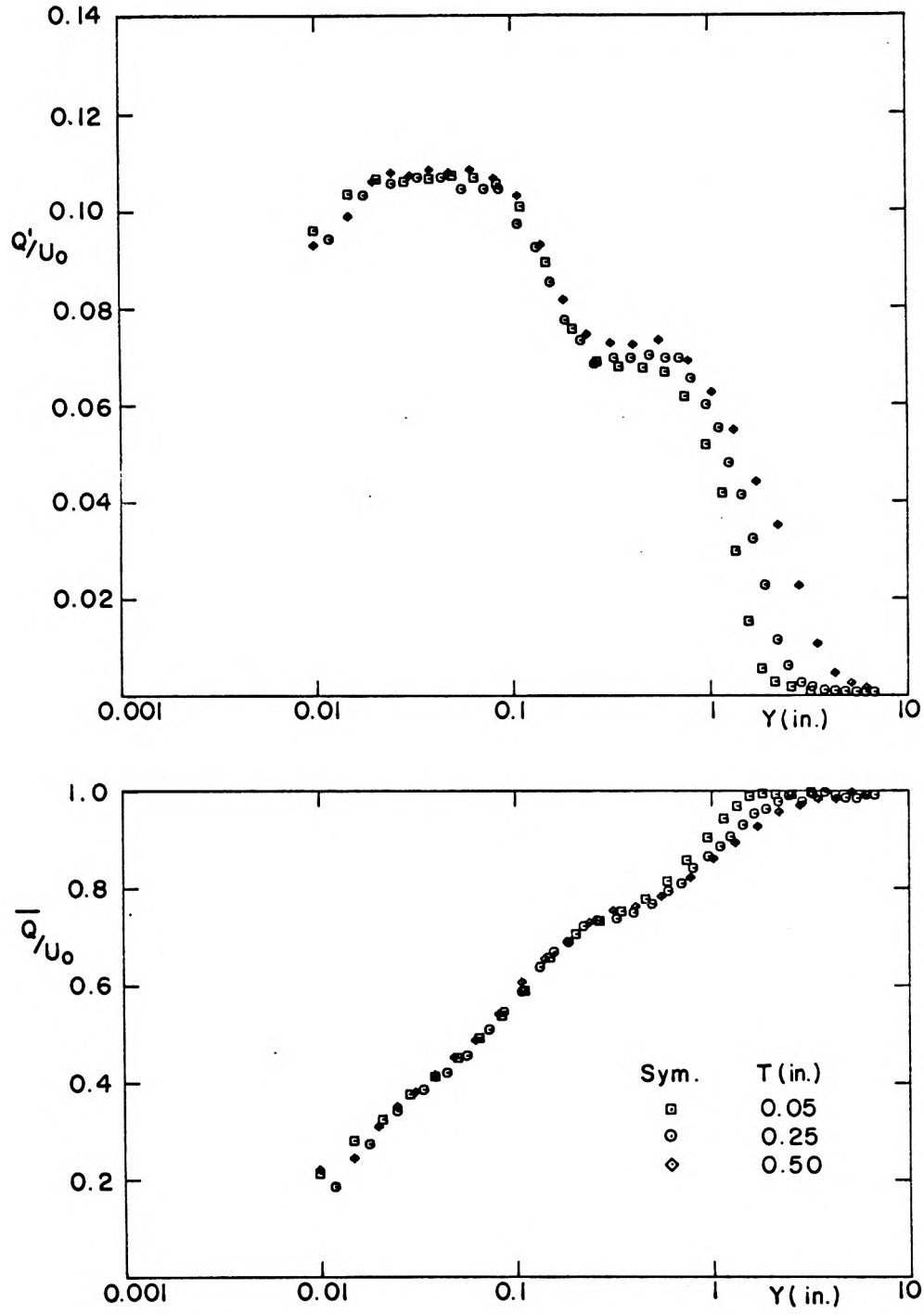

MODEL WW I
STATION 0F SURVEY CP = 0, dP/dx > 0

FIG. 20a EFFECT 0F B.L. TRIP HEIGHT 0N AVERAGE VELOCITY AND TURBULENCE LEVEL

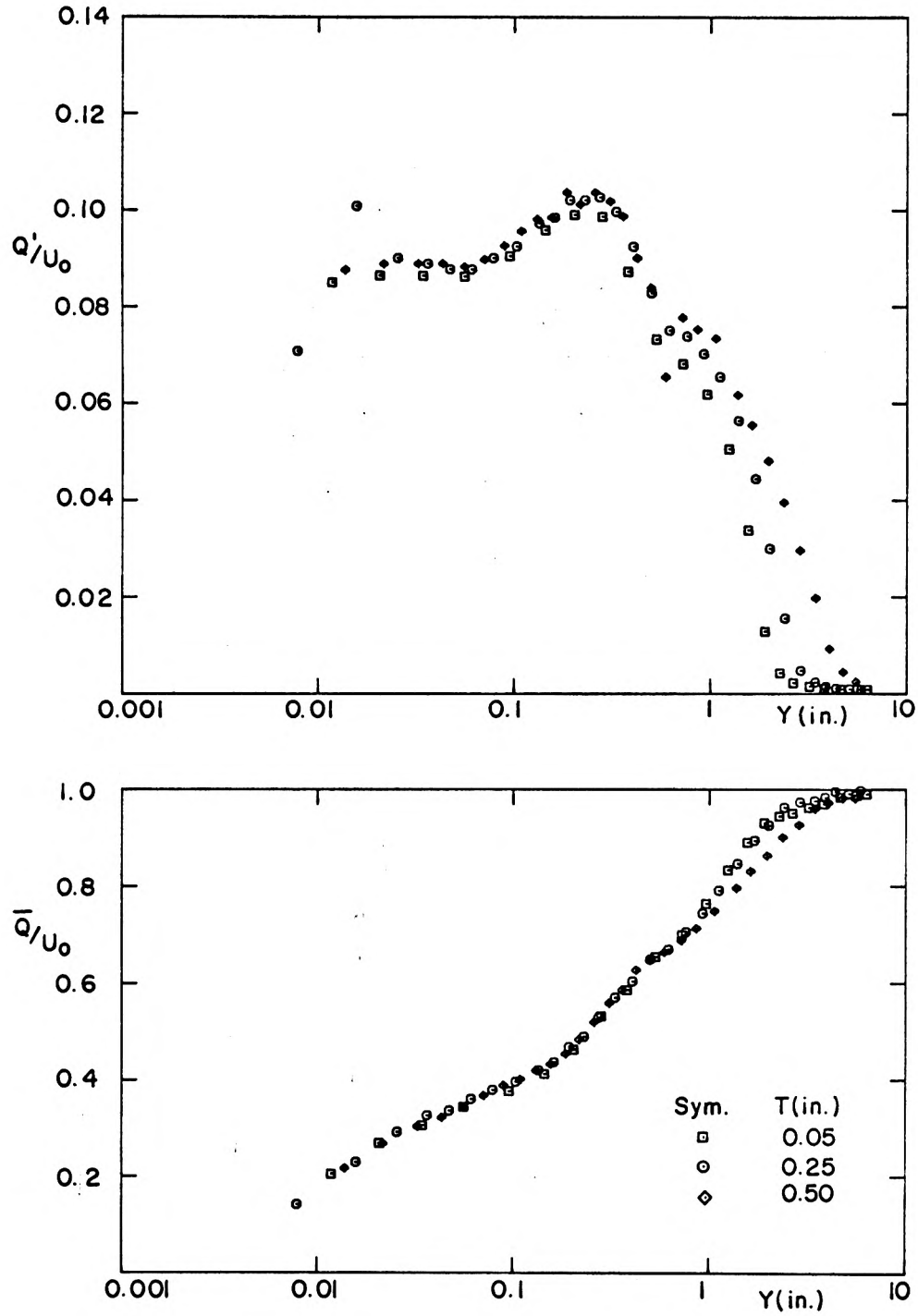

MODEL WW I
STATION OF SURVEY CP = MAX.

FIG.20b EFFECT OF B.L. TRIP HEIGHT ON AVERAGE VELOCITY AND TURBULENCE LEVEL

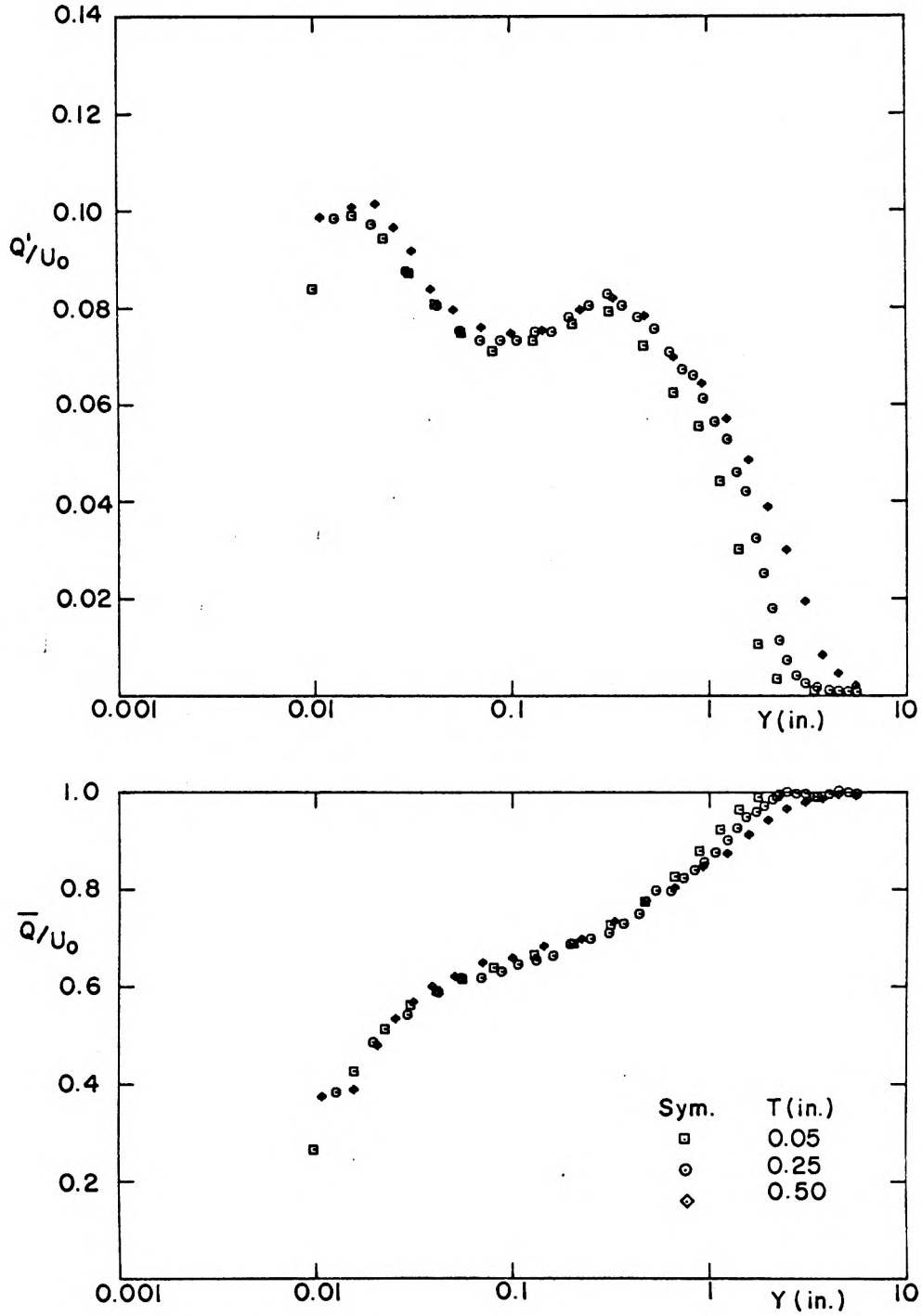

MODEL WW I
STATION 0F SURVEY CP = 0, dP/dx < 0

FIG.20c EFFECT 0F B.L. TRIP HEIGHT 0N AVERAGE VELOCITY AND TURBULENCE LEVEL

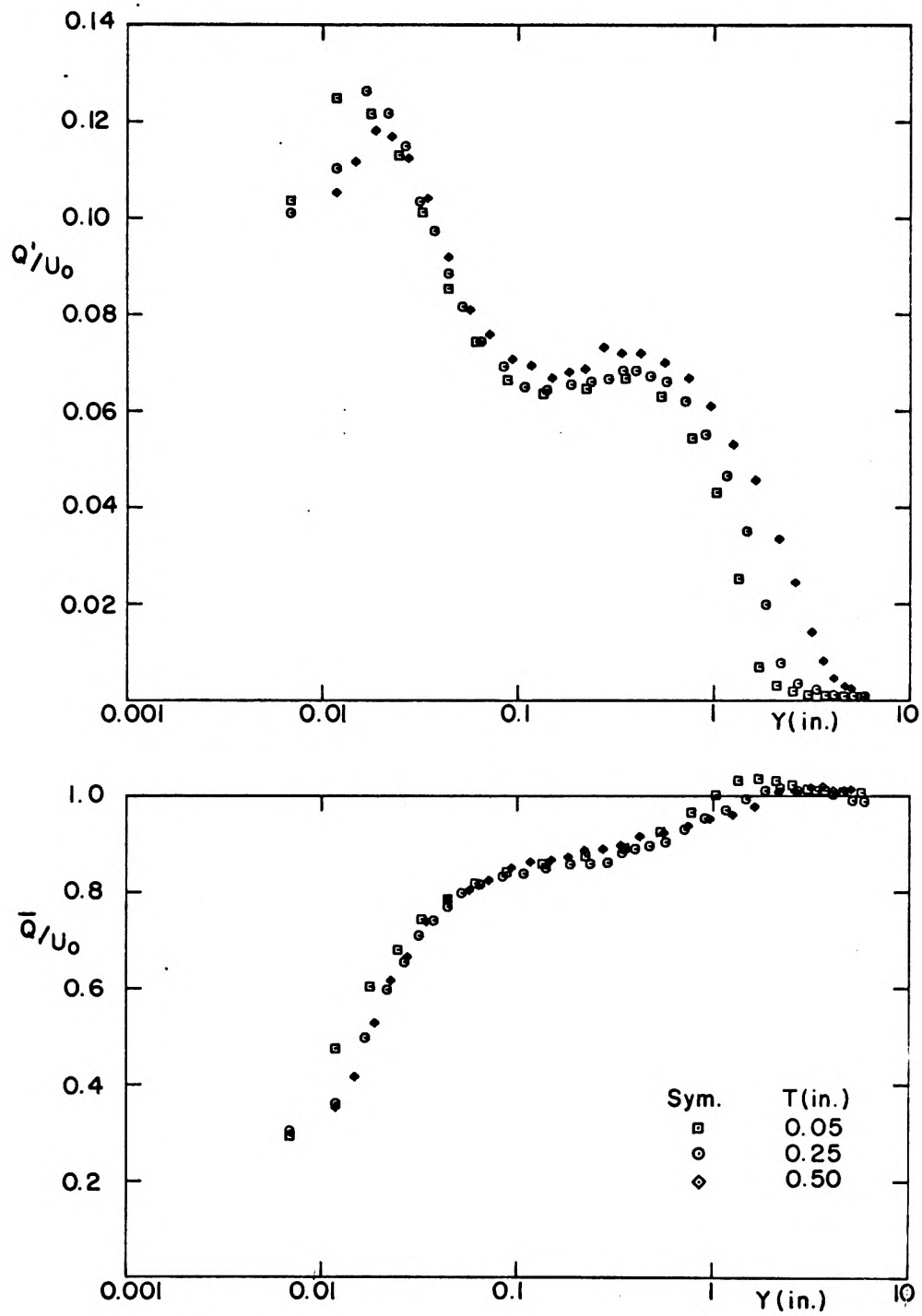

MODEL WWI
STATION OF SURVEY CP = MIN.

FIG.20d EFFECT OF B.L. TRIP HEIGHT ON AVERAGE VELOCITY AND TURBULENCE LEVEL

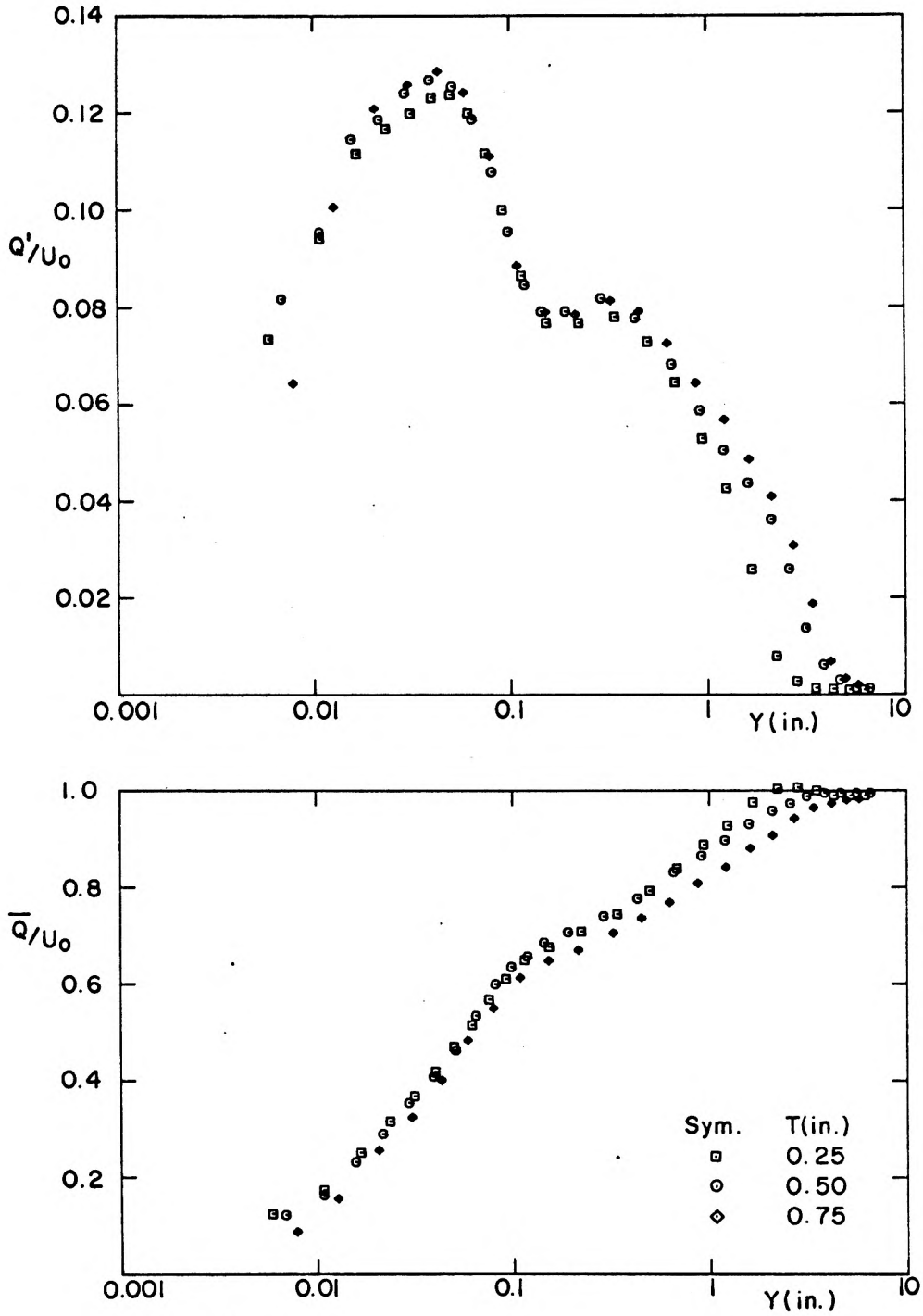

MODEL WW 2
STATION 0F SURVEY CP = 0, dP/dx > 0

FIG.20e EFFECT 0F B.L. TRIP HEIGHT 0N AVERAGE VELOCITY AND TURBULENCE LEVEL

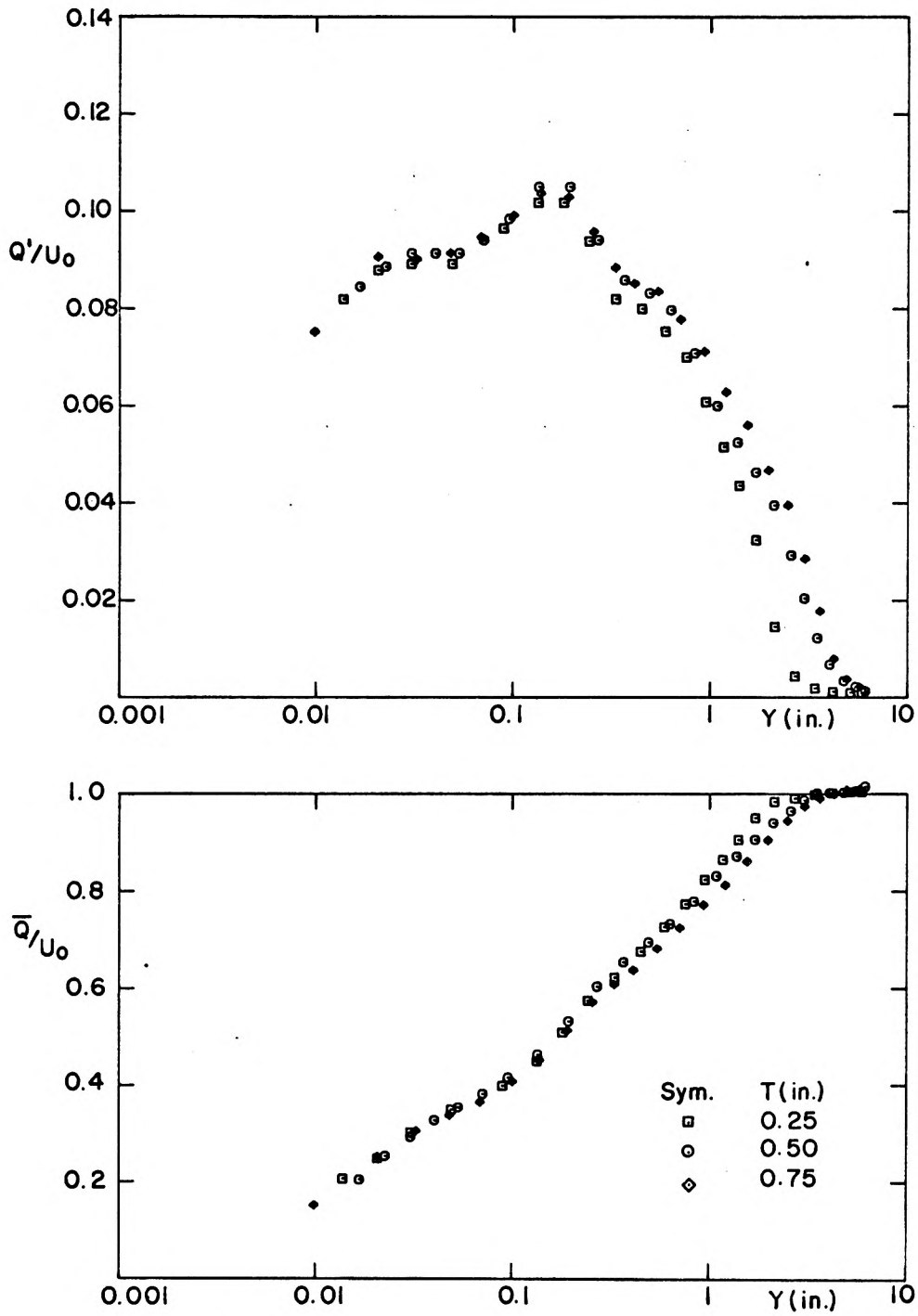

MODEL WW 2
STATION OF SURVEY CP= MAX.

FIG.20f EFFECT OF B.L. TRIP HEIGHT ON AVERAGE VELOCITY AND TURBULENCE LEVEL

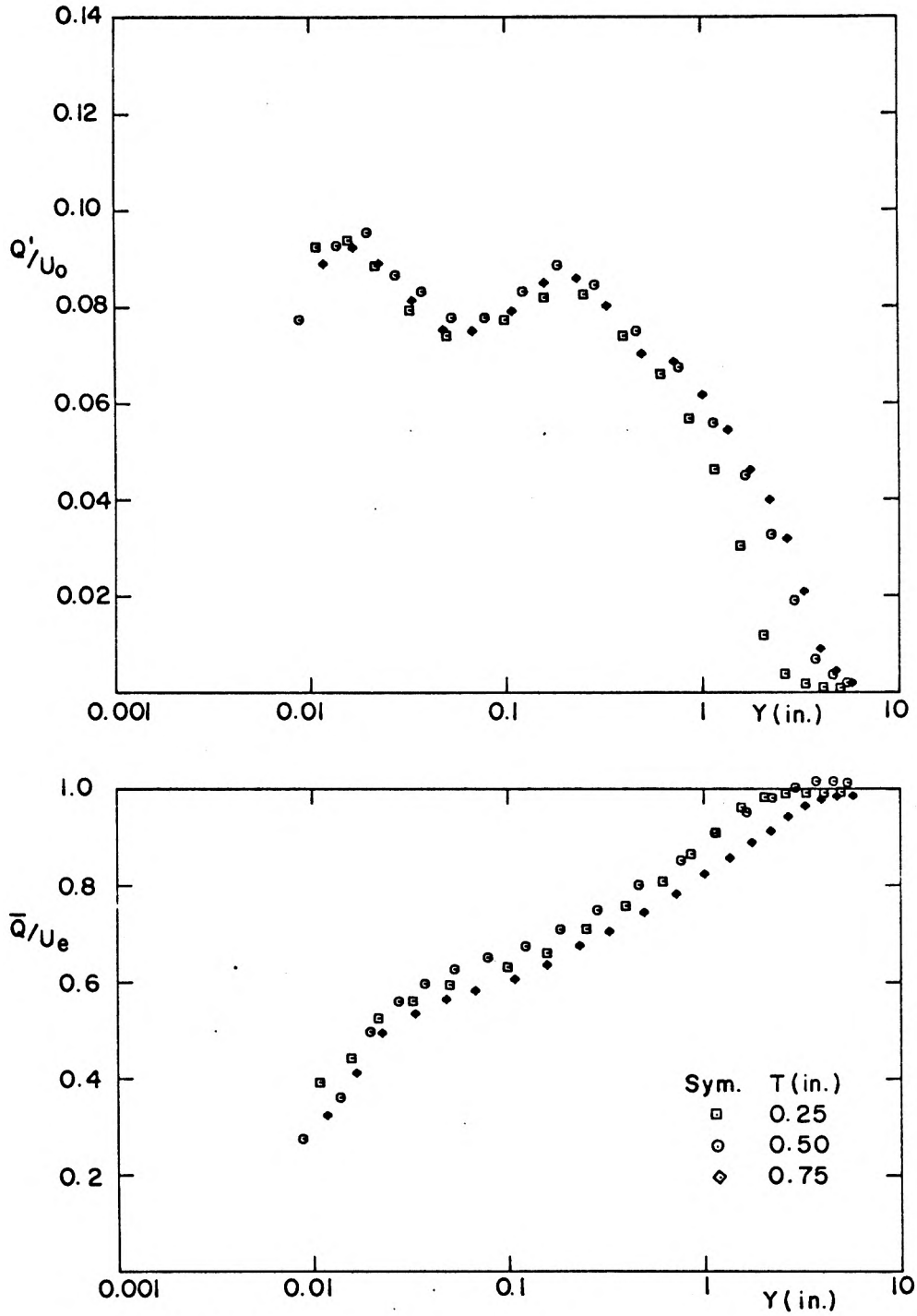

MODEL WW 2
STATION OF SURVEY CP = 0, dP/dx < 0

FIG.20g EFFECT OF B.L. TRIP HEIGHT ON AVERAGE VELOCITY AND TURBULENCE LEVEL

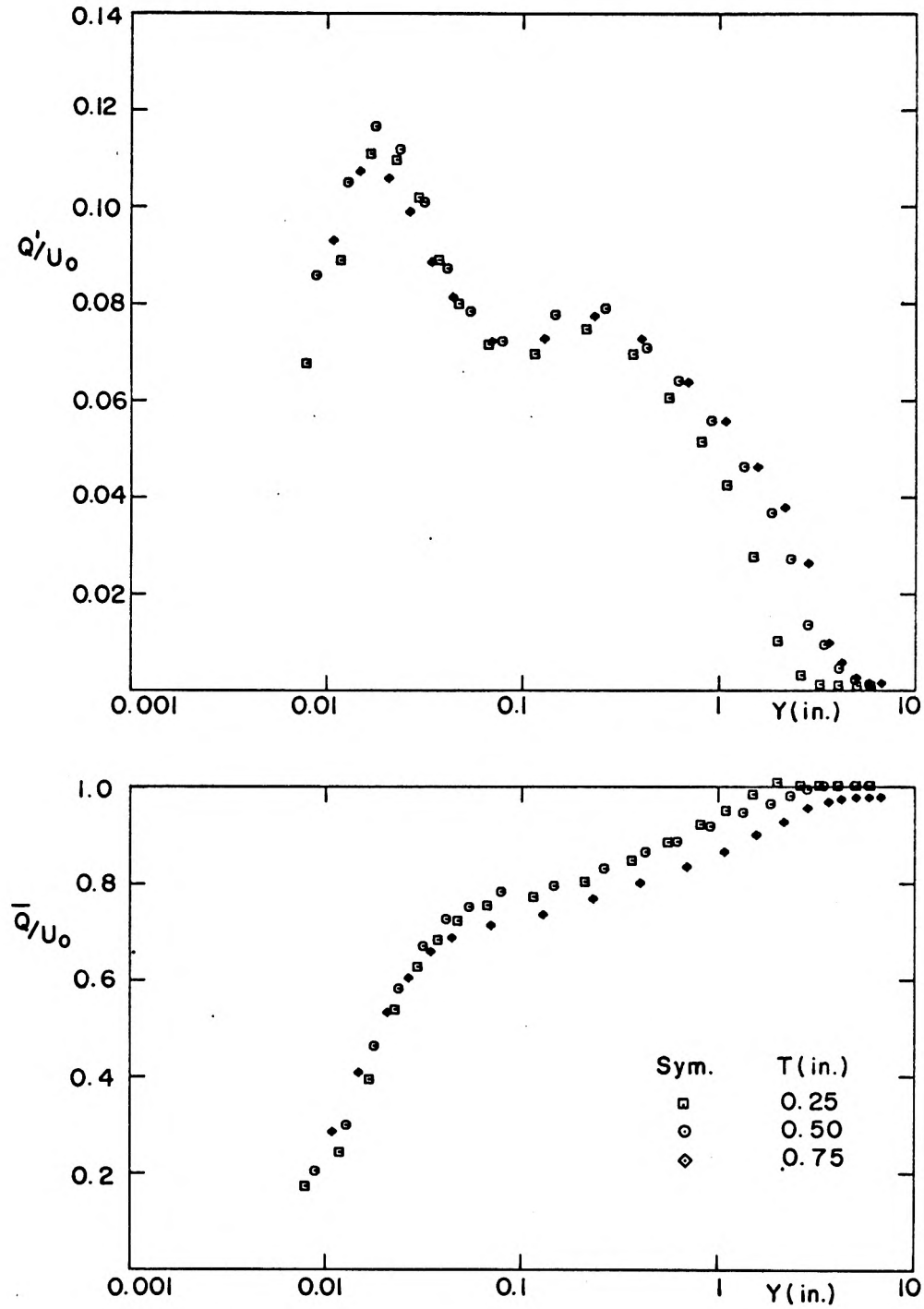

MODEL WW 2
STATION 0F SURVEY CP = MIN.

FIG.20h EFFECT 0F B.L. TRIP HEIGHT 0N AVERAGE VELOCITY AND TURBULENCE LEVEL

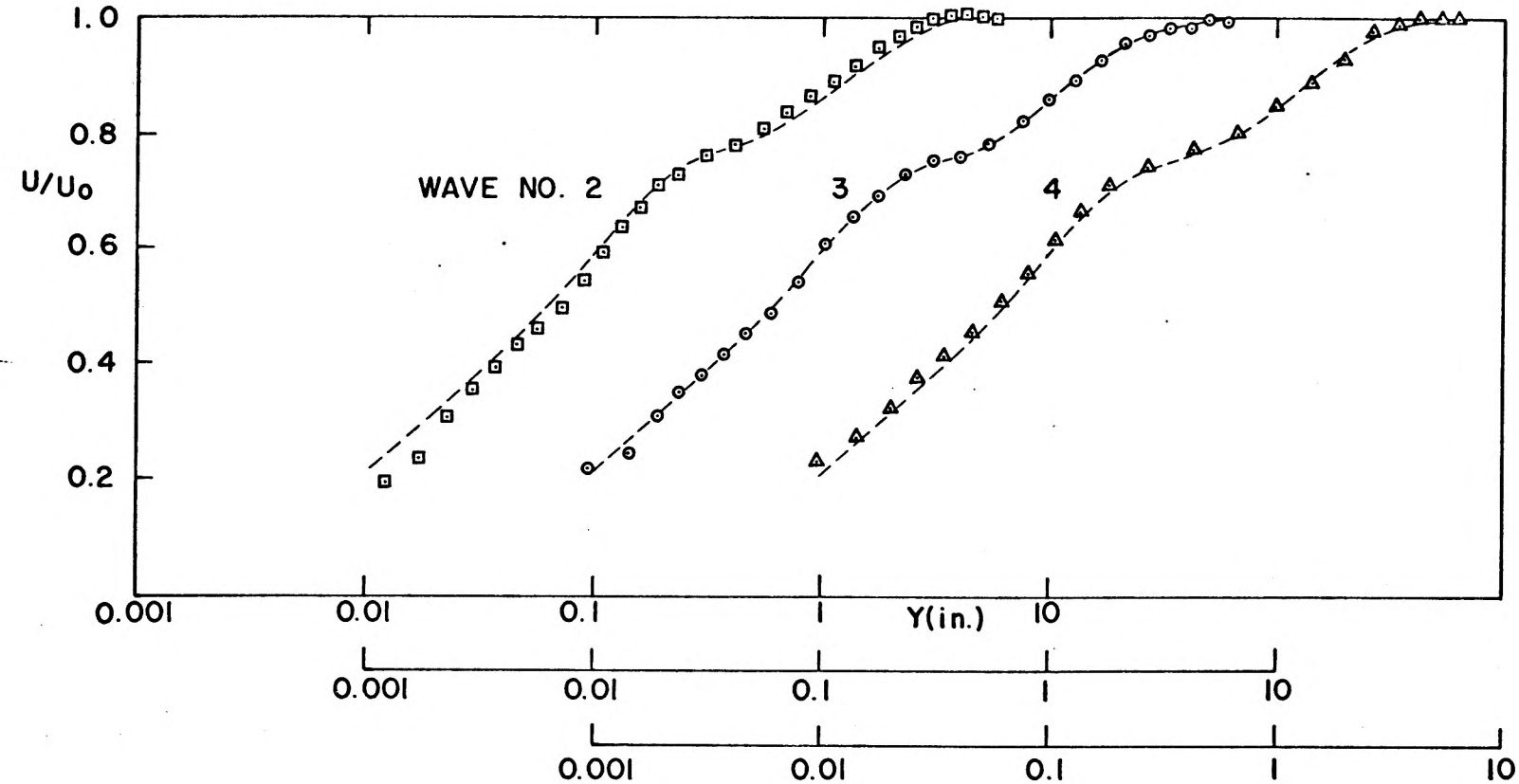

FIG.21a DEVELOPMENT OF VELOCITY PROFILE ALONG THE WAVY WALL
STATION OF SURVEY : CP = 0, dP/dx > 0

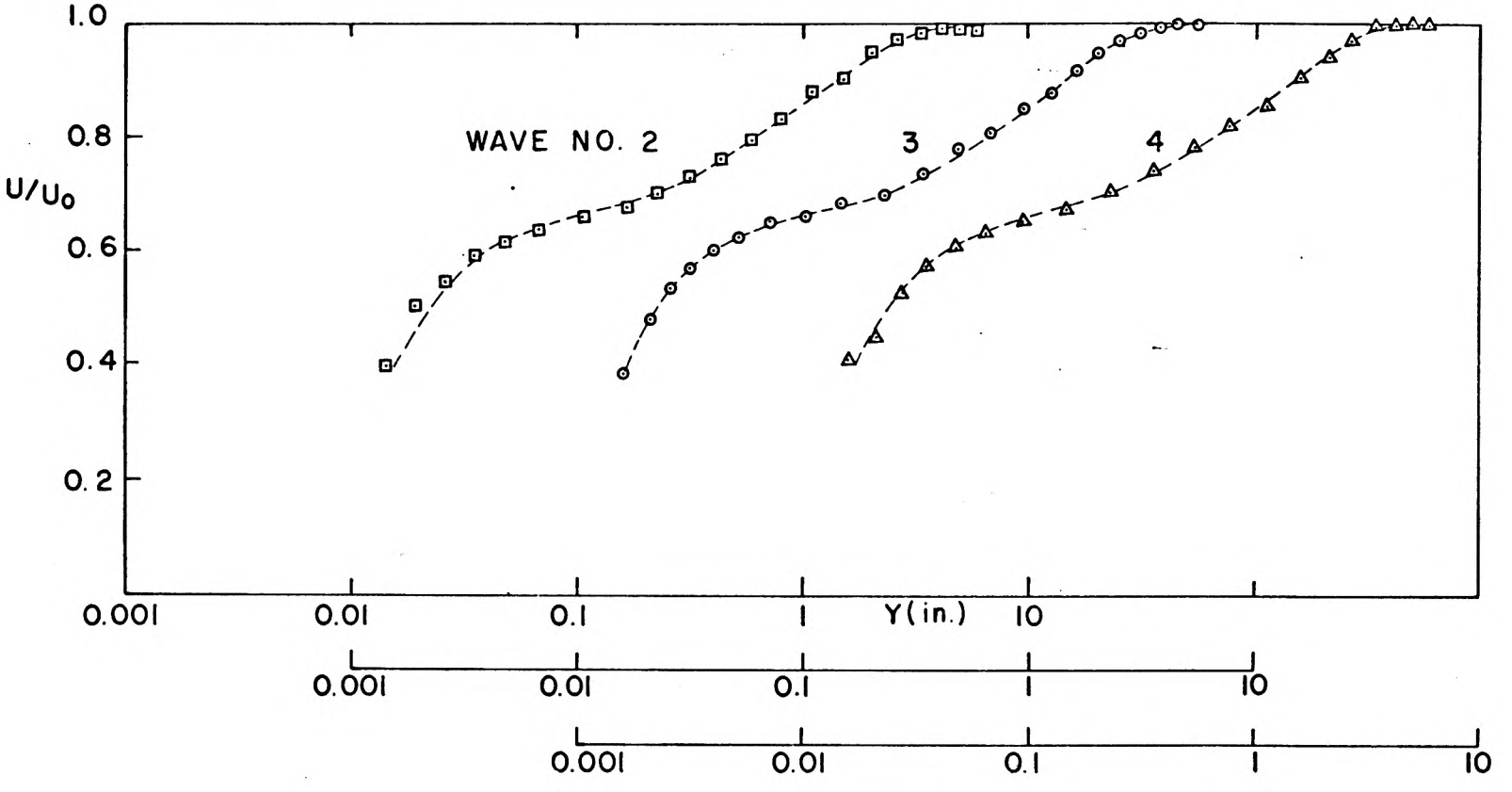

FIG. 21b DEVELOPMENT OF VELOCITY PROFILE ALONG THE WAVY WALL
STATION OF SURVEY: CP = 0, dP/dx < 0

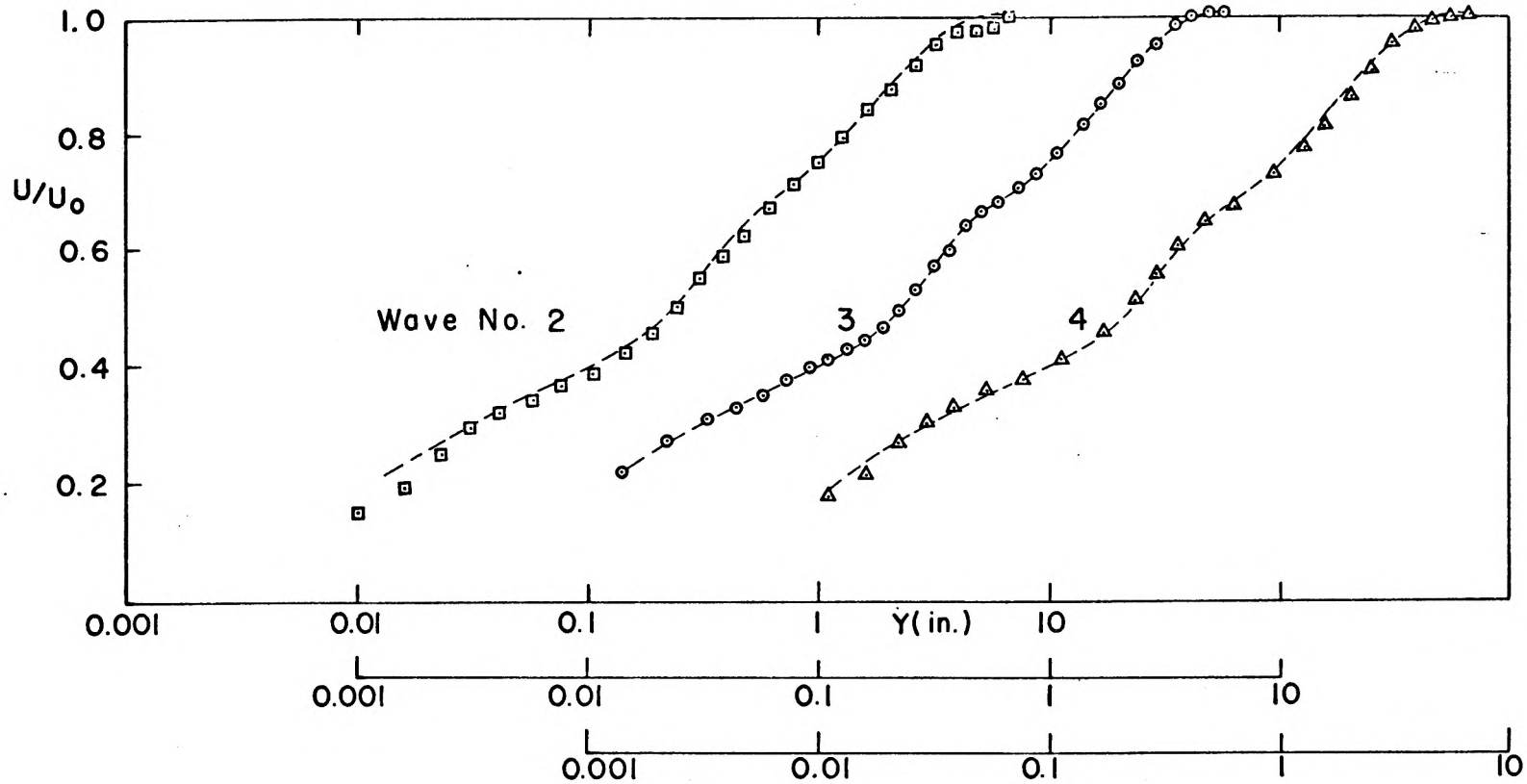

FIG. 21 c DEVELOPMENT OF VELOCITY PROFILE ALONG THE WAVY WALL
STATION OF SURVEY: CP = MAX.

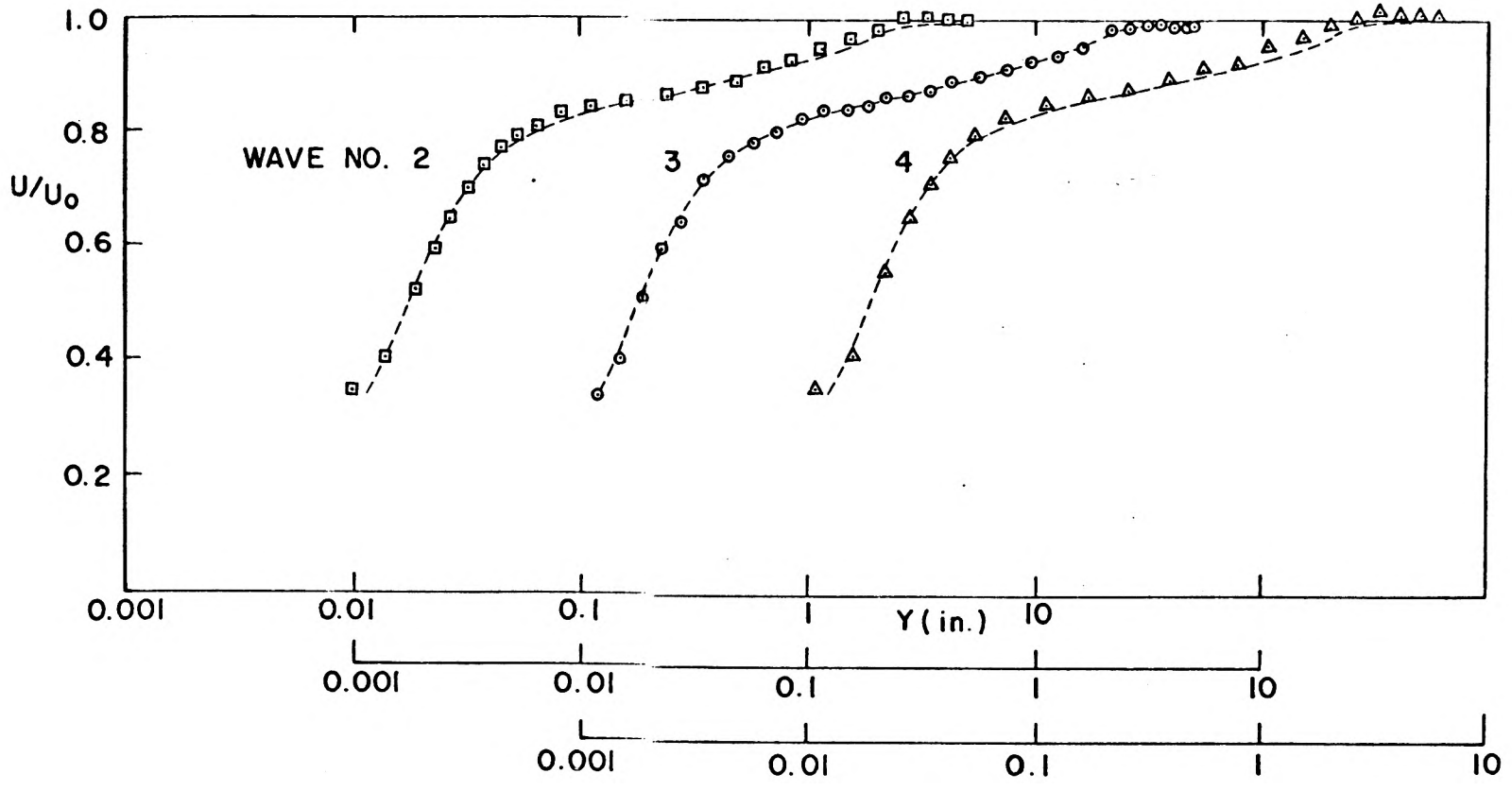

FIG. 21 d DEVELOPMENT OF VELOCITY PROFILE ALONG THE WAVY WALL
STATION OF SURVEY : CP = MIN.

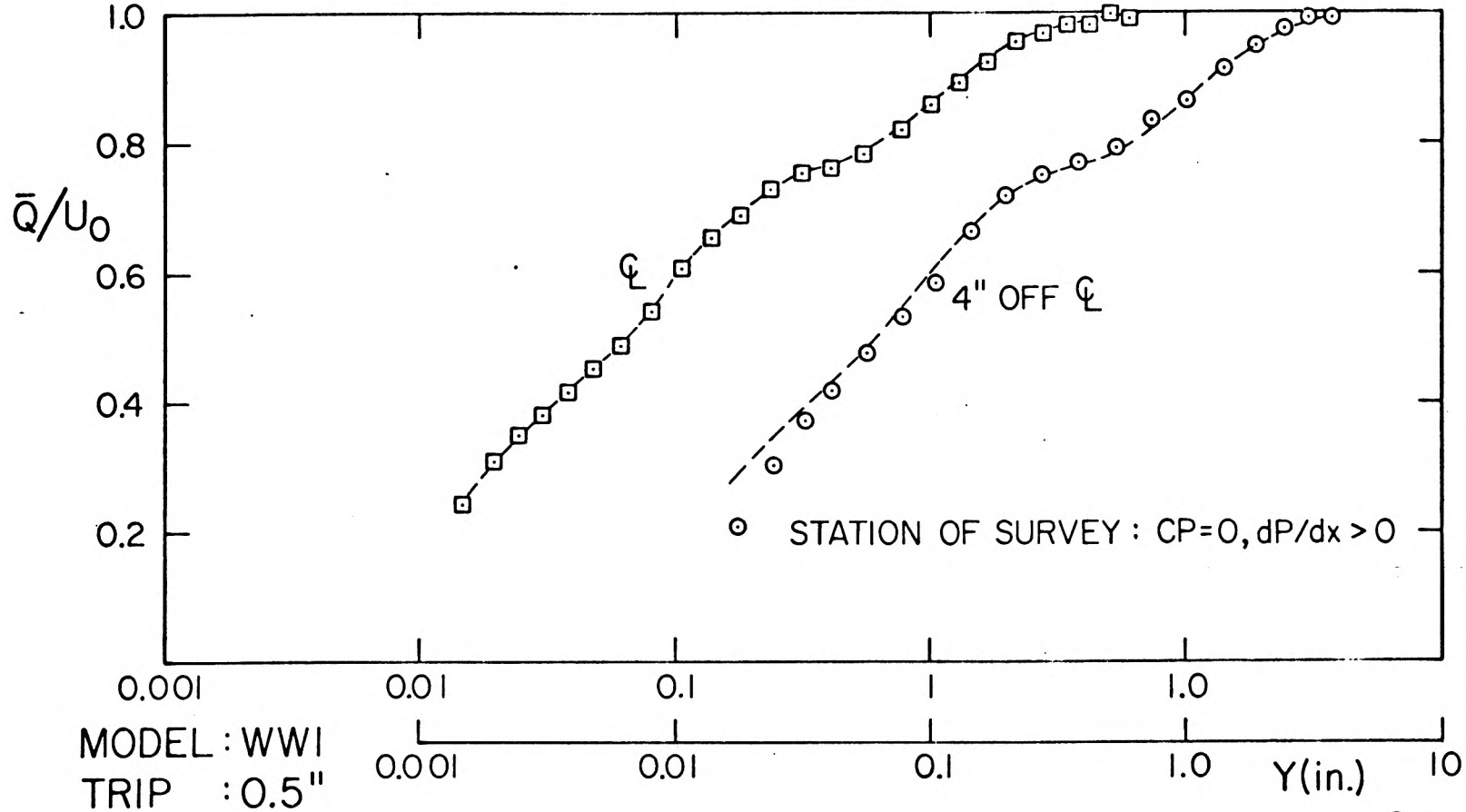

FIG. 22a TEST FOR TWO-DIMENSIONALITY OF THE FLOW OVER THE WAVY WALL

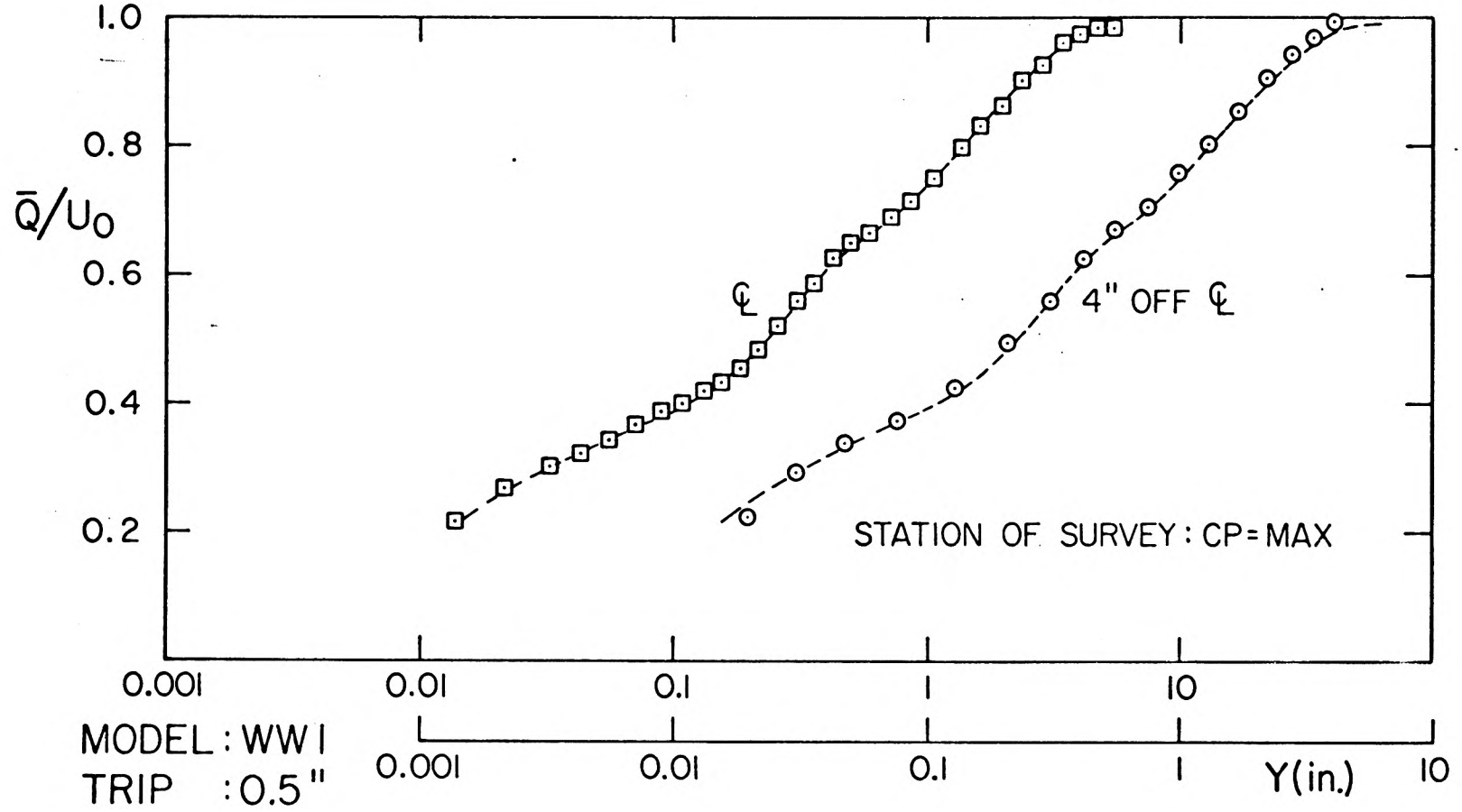

FIG. 22b TEST FOR TWO-DIMENSIONALITY OF THE FLOW OVER THE WAVY WALL

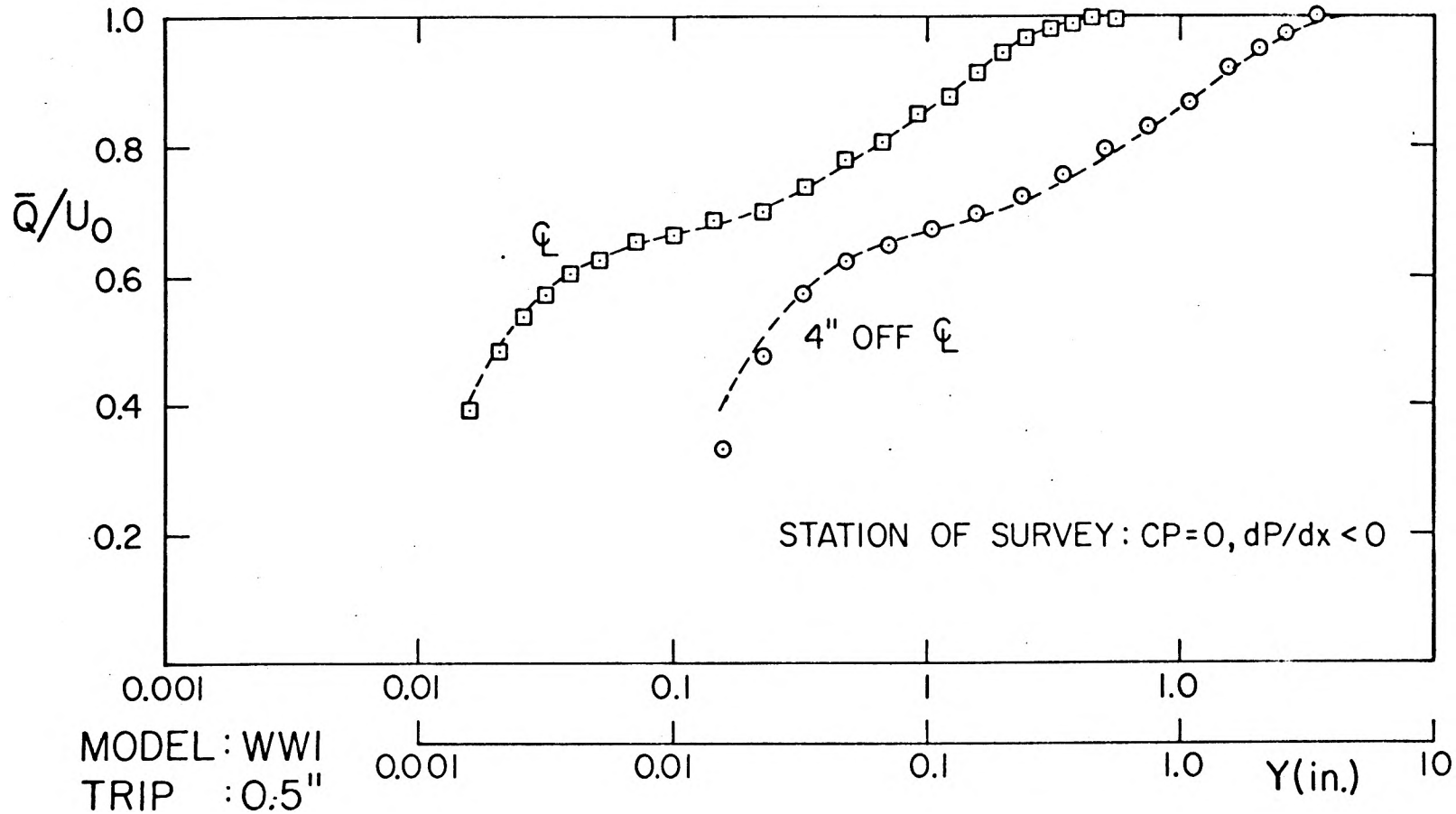

FIG.22c TEST FOR TWO-DIMENSIONALITY OF THE FLOW OVER THE WAVY WALL

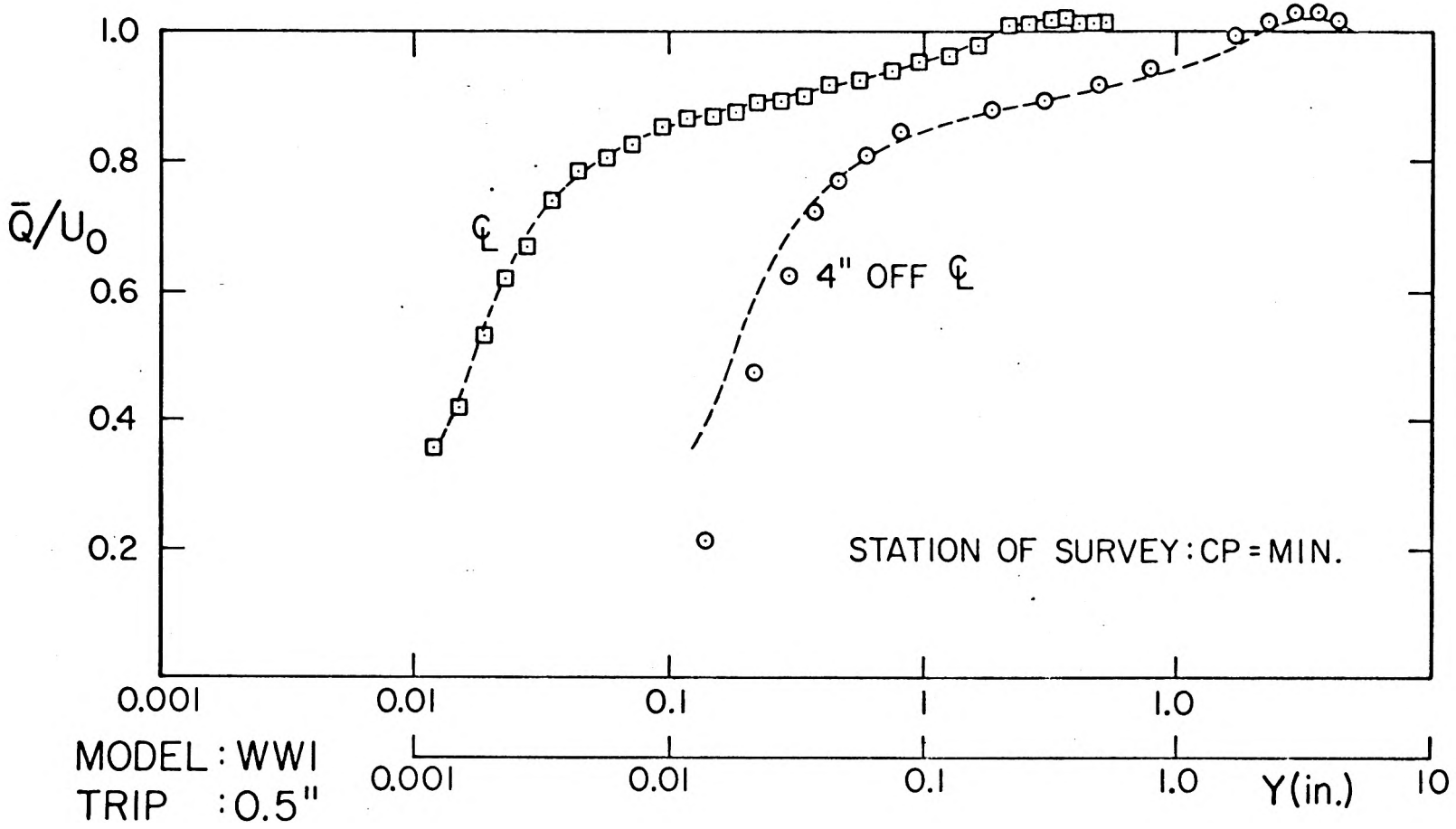

FIG.22d TEST FOR TWO-DIMENSIONALITY OF THE FLOW OVER THE WAVY WALL

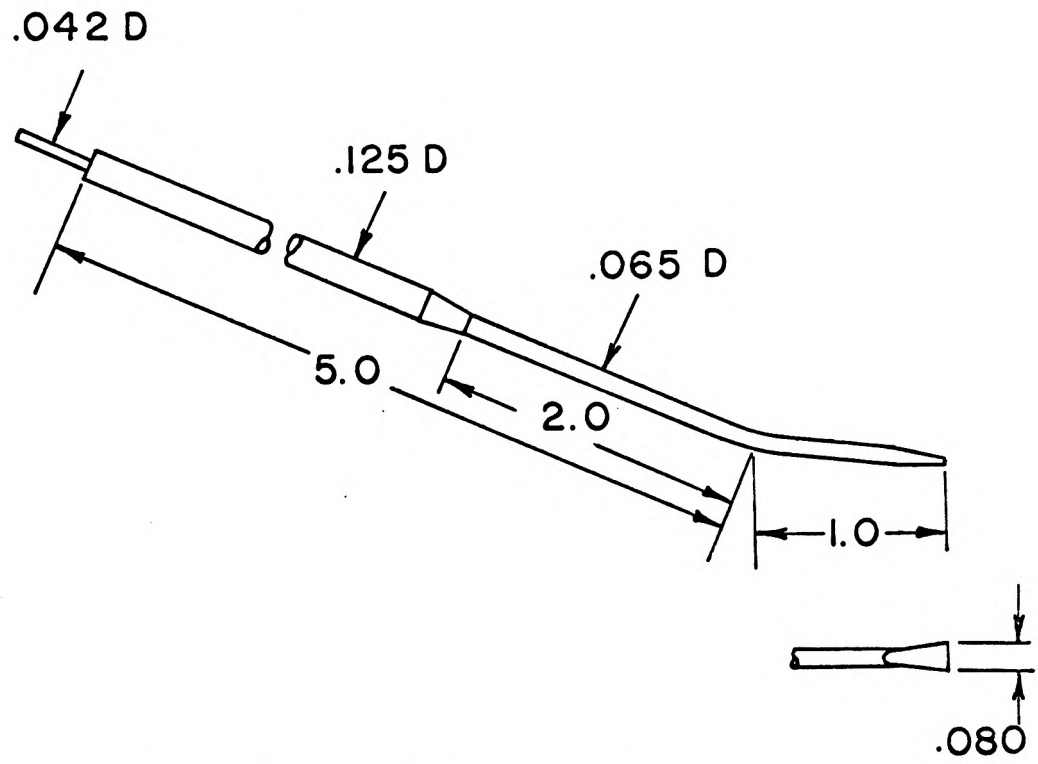

a. General Dimensions Of Probe

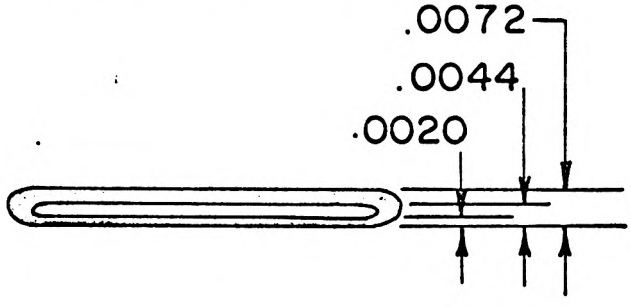

b. Front End View (25:1)

FIG. 23 PRESTON TUBE PROBE

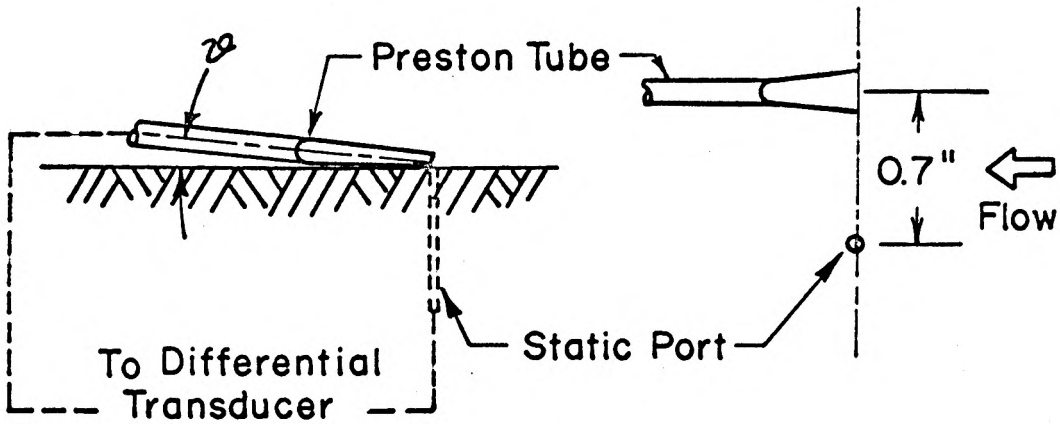

c. Method Of Measurement

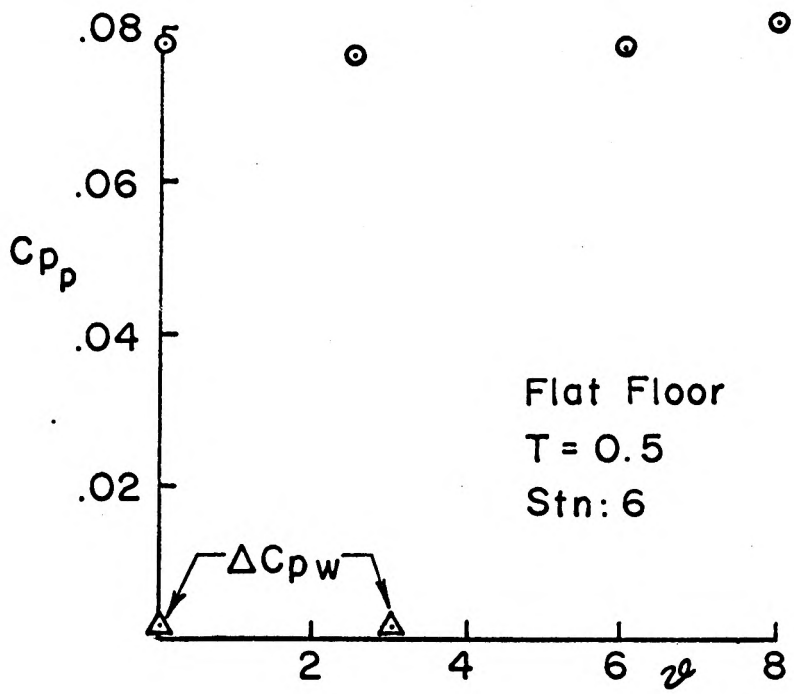

d. Sensitivity To Inclination Angle

FIG. 23 PRESTON TUBE PROBE (CON'T.)

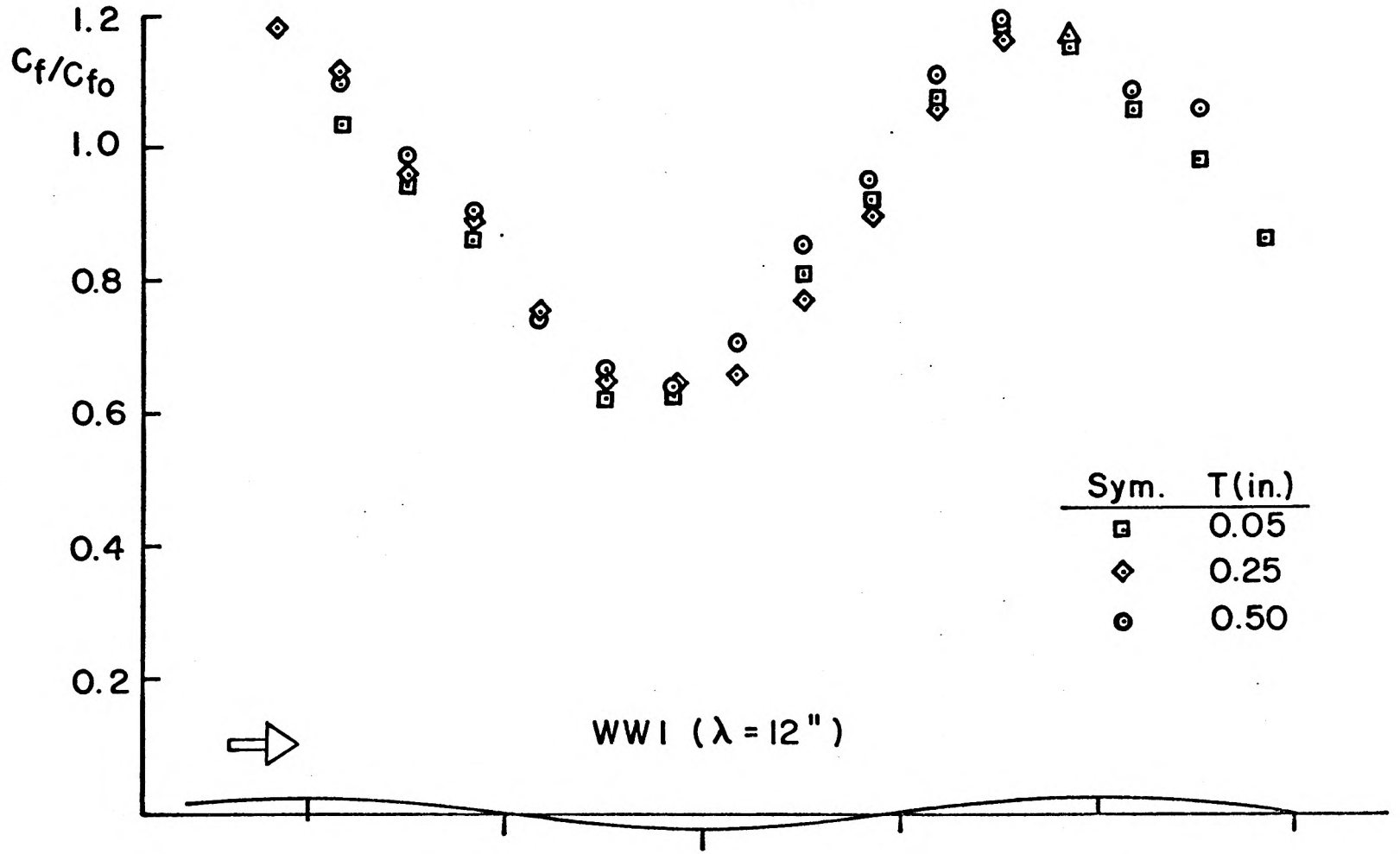

FIG. 24a WALL SHEAR DISTRIBUTION

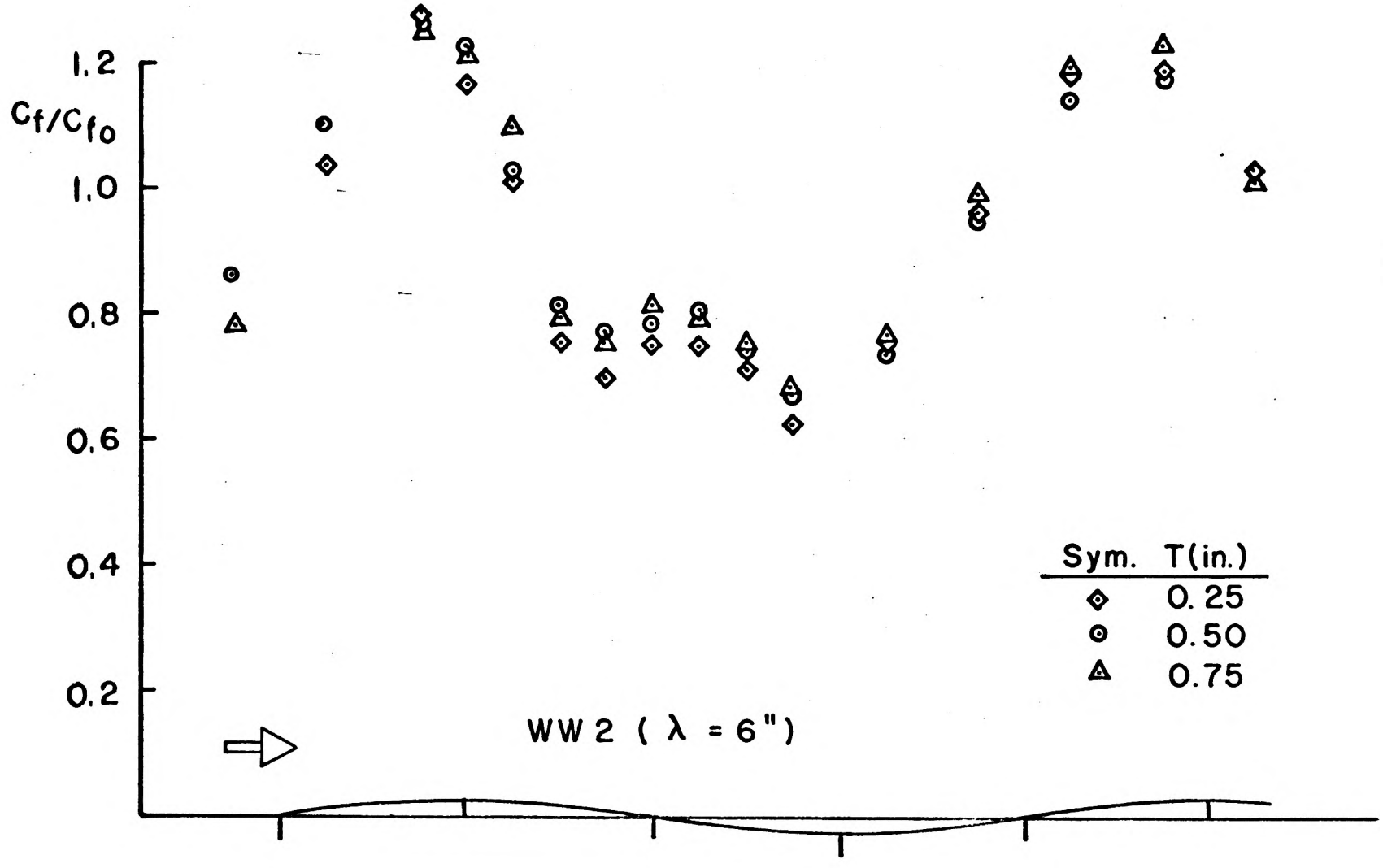

FIG. 24b WALL SHEAR DISTRIBUTION

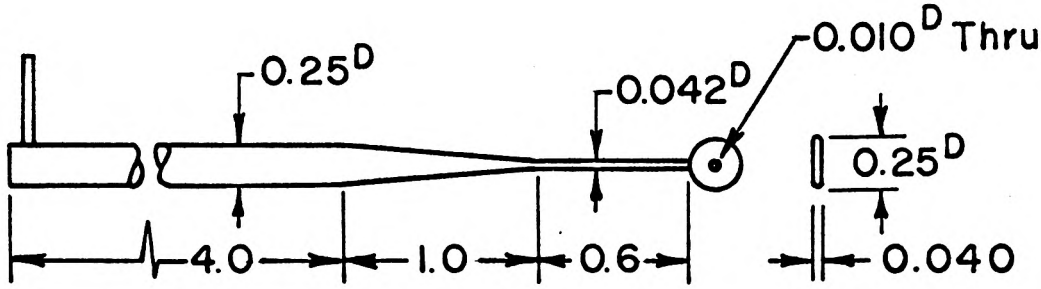

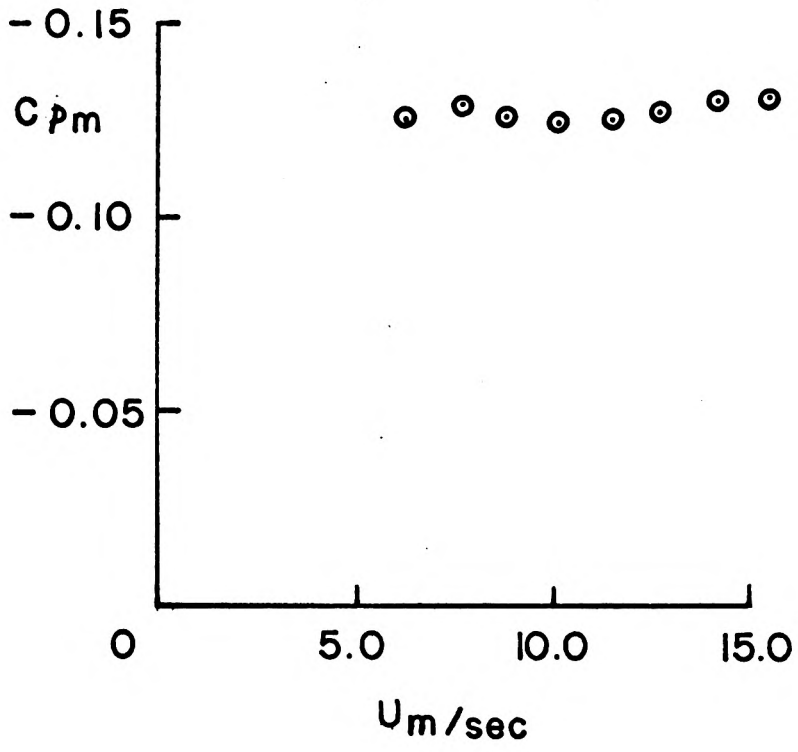

FIG. 25 DISC PROBE AND ITS CALIBRATION IN FREE STREAM

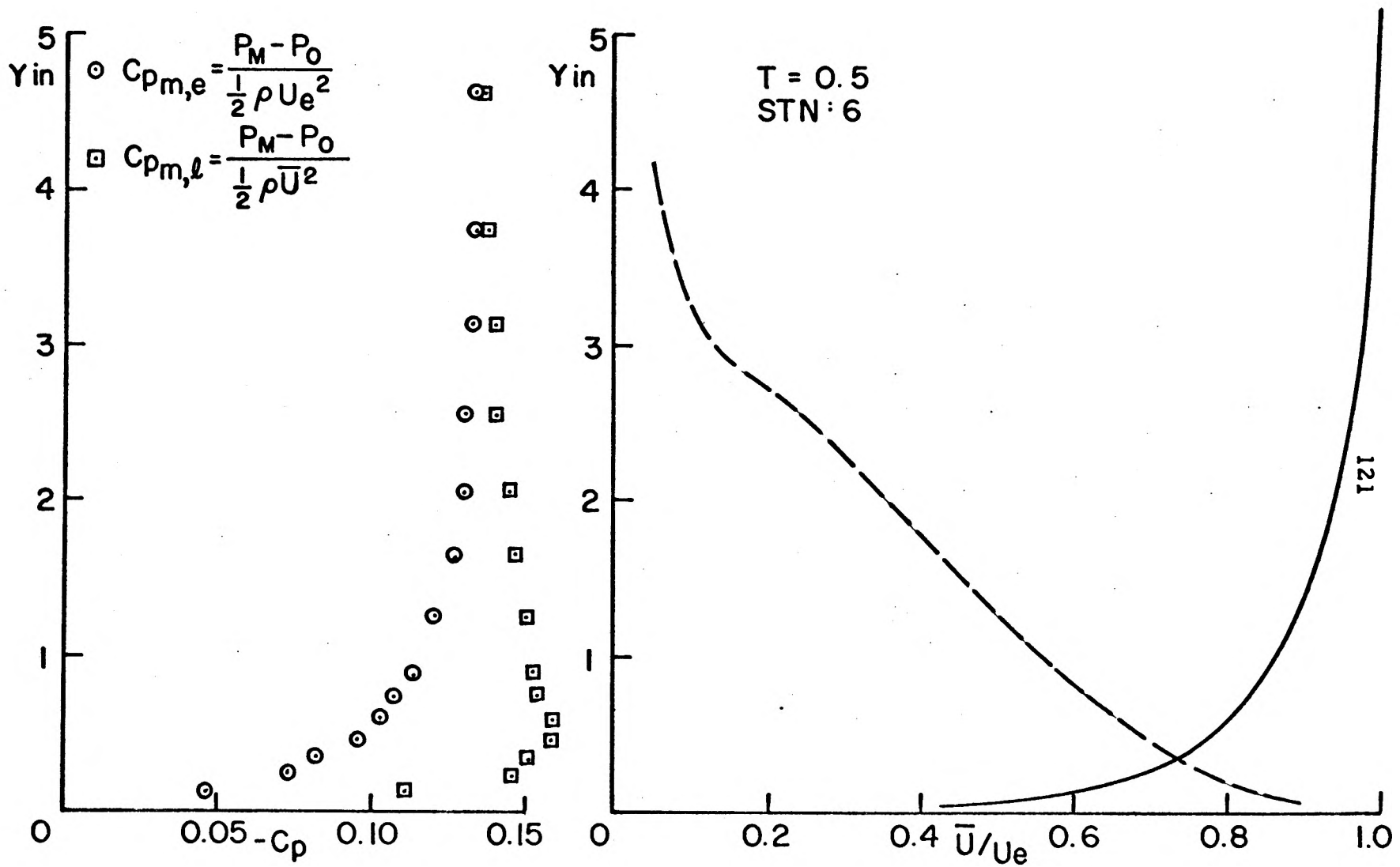

FIG. 26 CALIBRATION OF DISC PROBE IN BOUNDARY LAYER

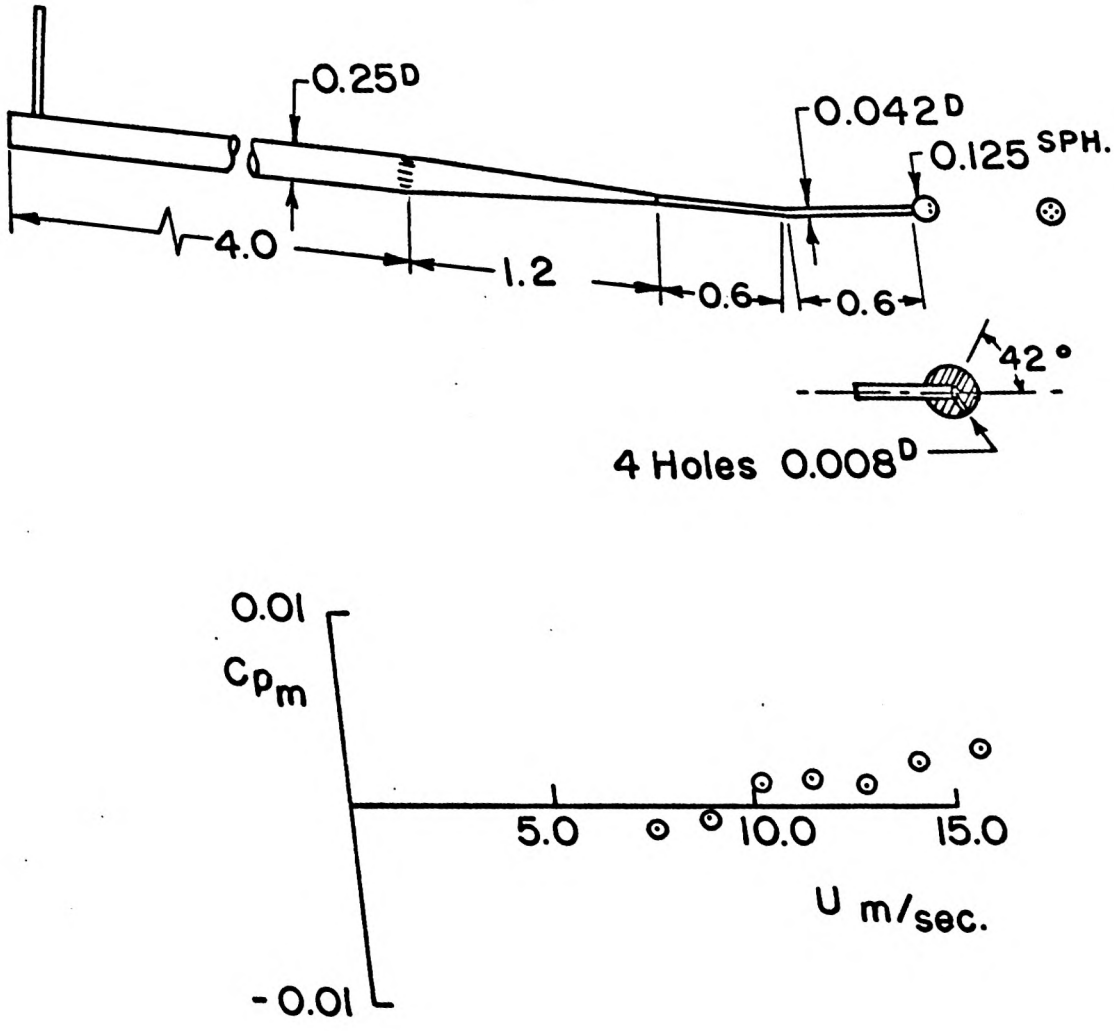

FIG. 27 SPHERE PROBE AND ITS CALIBRATION IN FREE STREAM

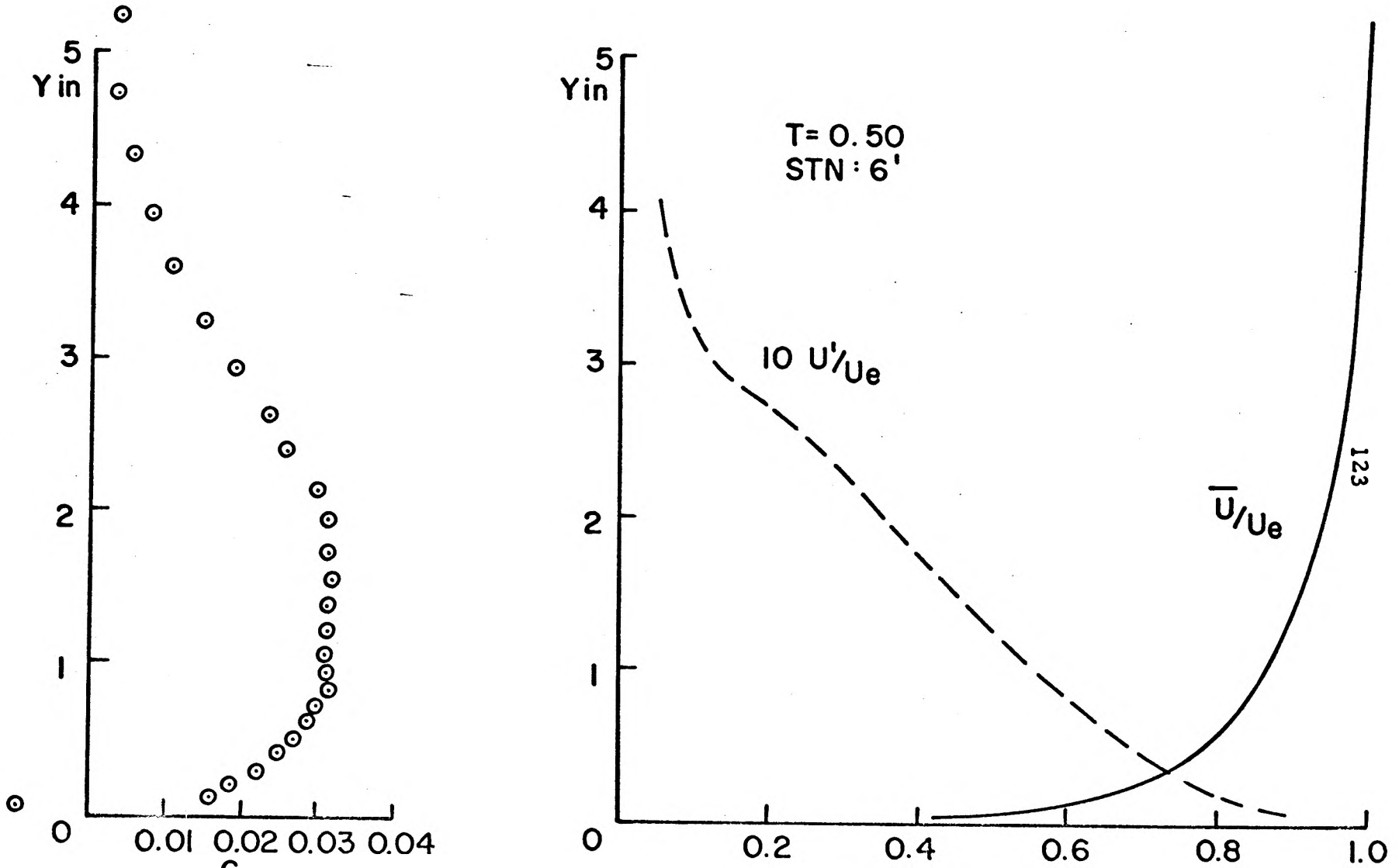

FIG.28 CALIBRATION OF SPHERE PROBE IN BOUNDARY LAYER

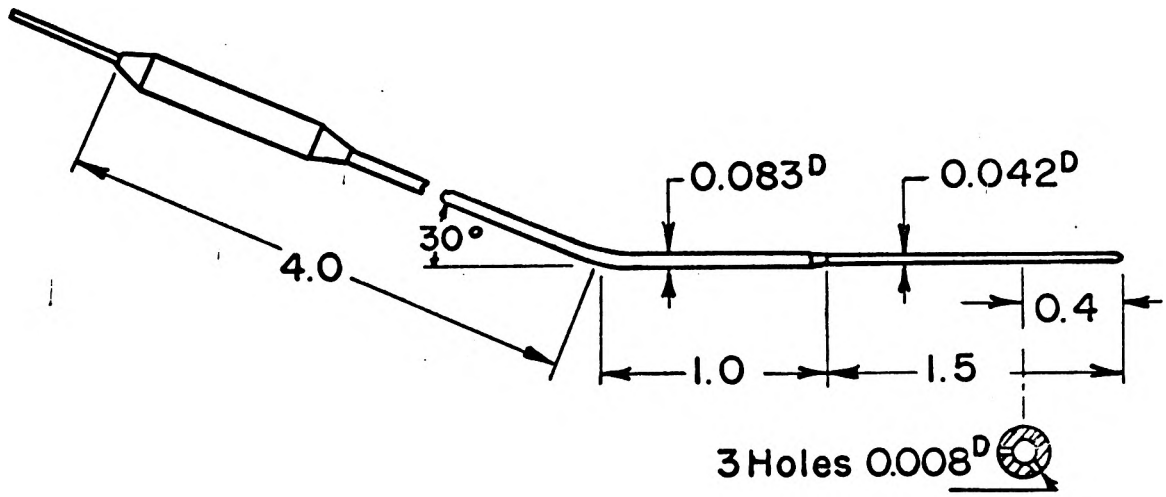

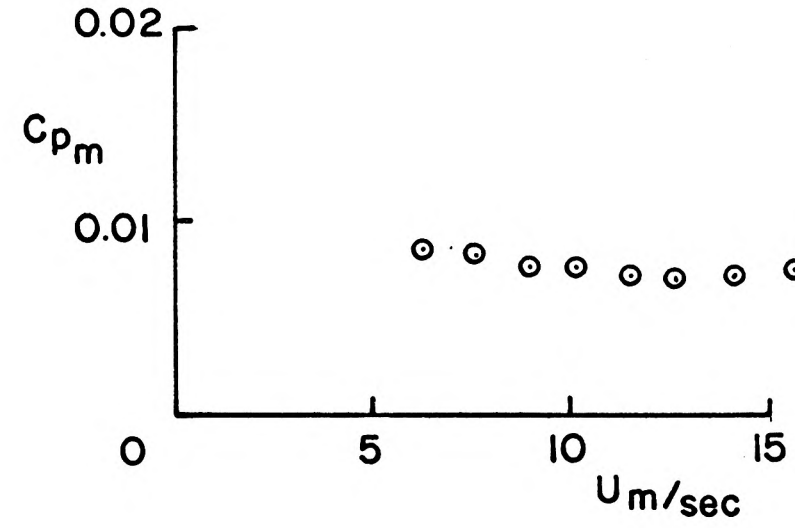

FIG. 29 NEEDLE PROBE AND ITS CALIBRATION IN FREE STREAM

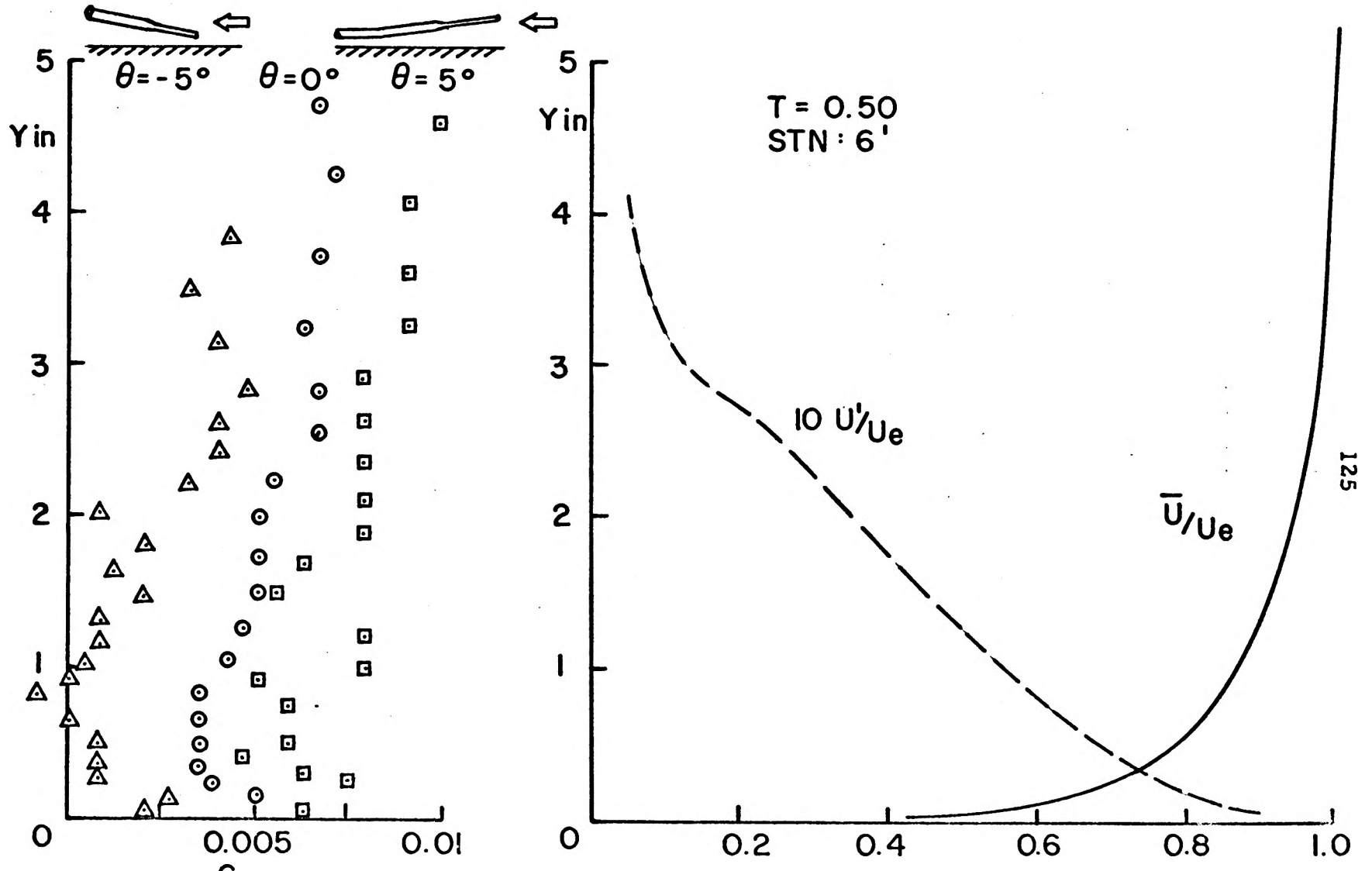

FIG. 30 CALIBRATION OF STATIC PROBE IN BOUNDARY LAYER

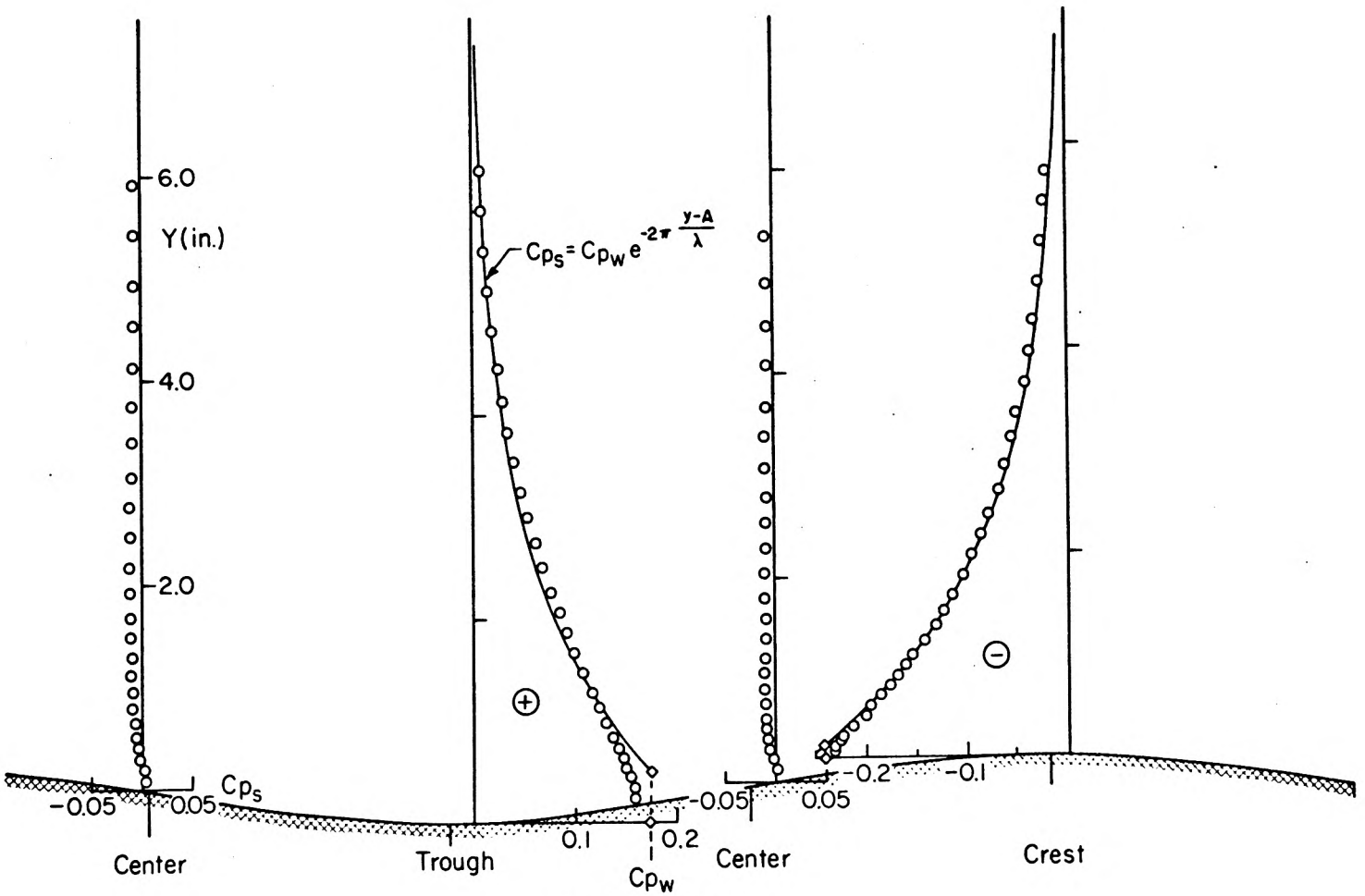

MODEL : WWI
TRIP : 0.5"

FIG. 31a STATIC PRESSURE DISTRIBUTION

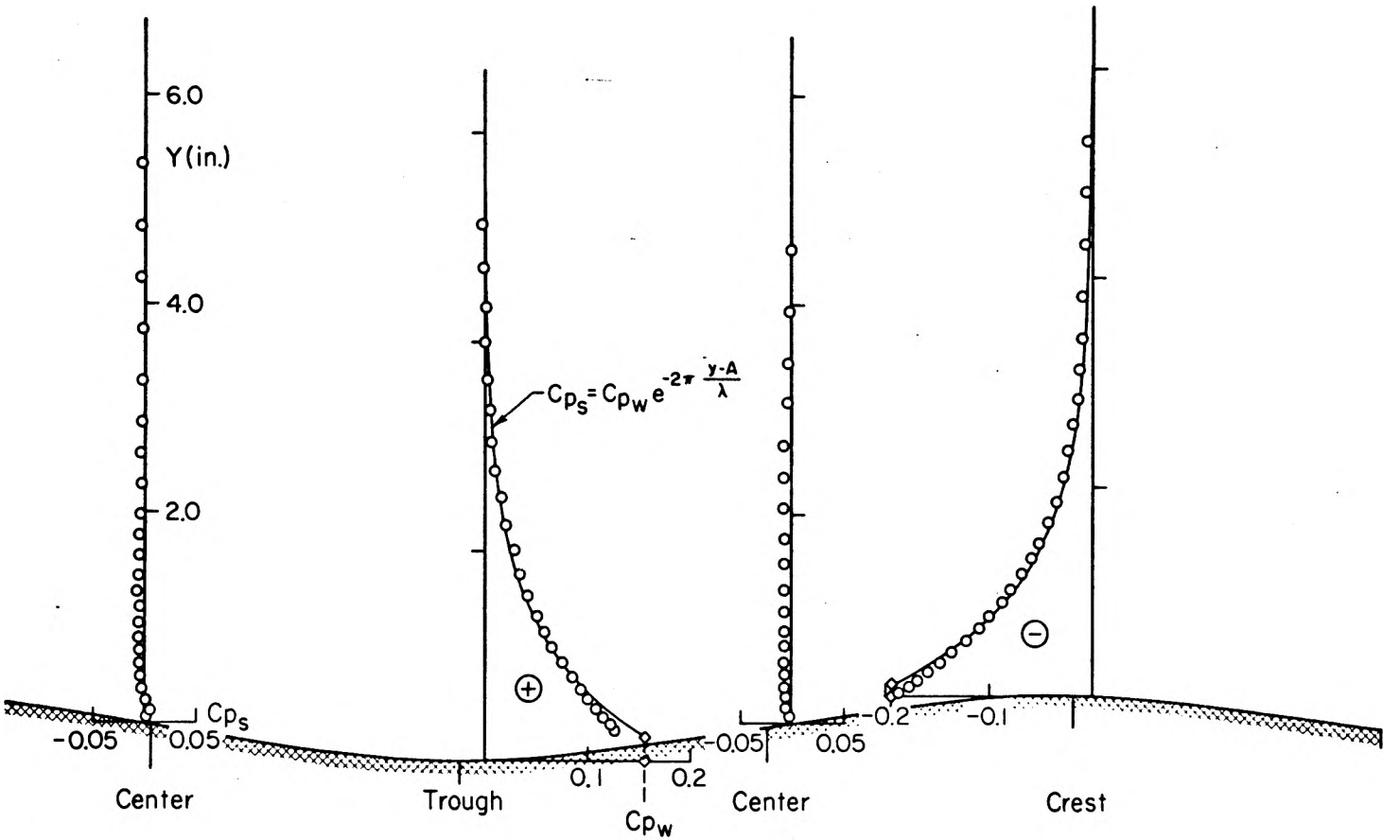

MODEL : WW2
TRIP : 0.5"

FIG. 31 b STATIC PRESSURE DISTRIBUTION

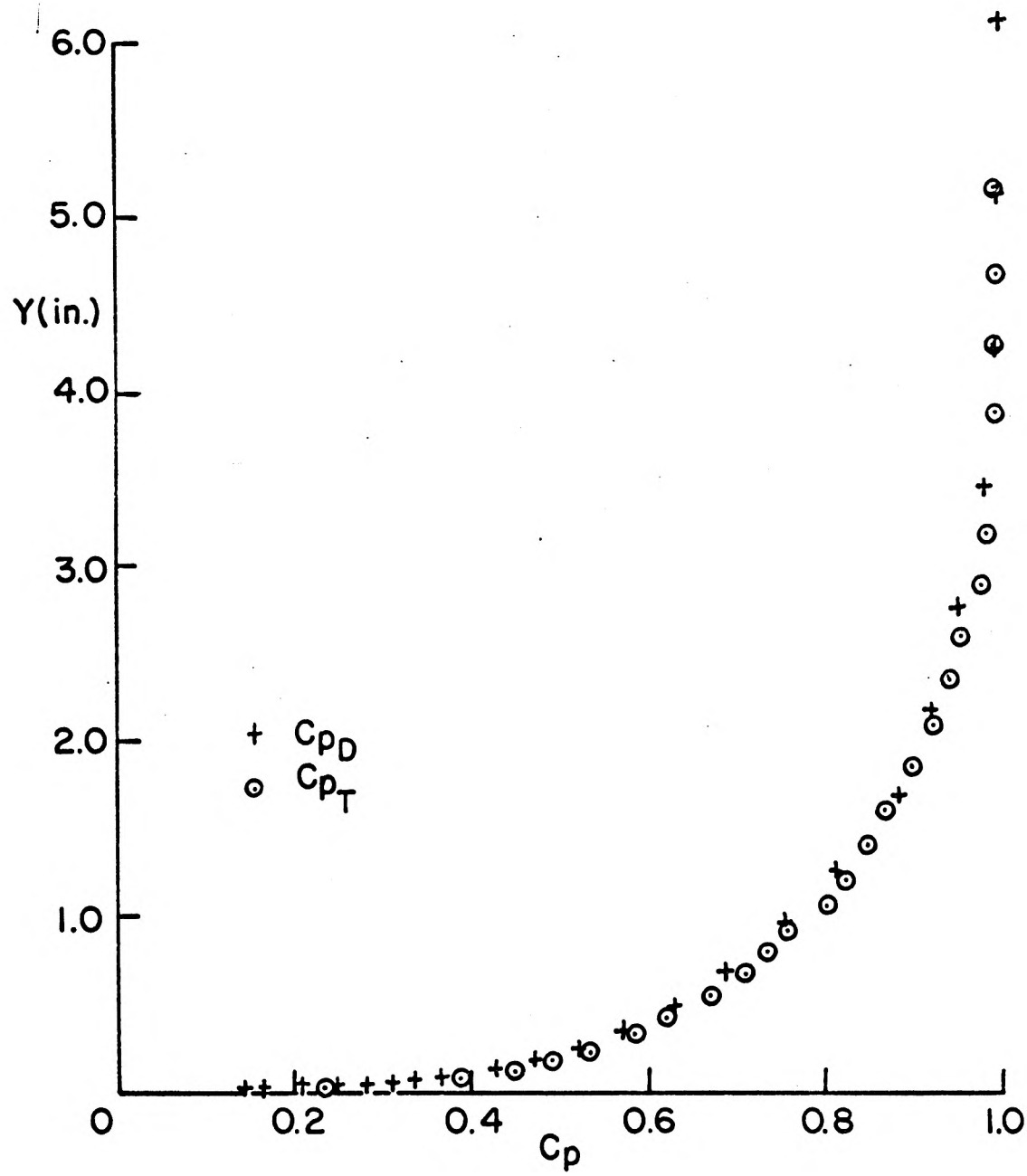

FIG. 32a COMPARISON OF DIRECT AND INDIRECT MEASUREMENT OF TOTAL PRESSURE COEFFICIENT

FLAT PLATE STN. 6' T= 0.50 in.

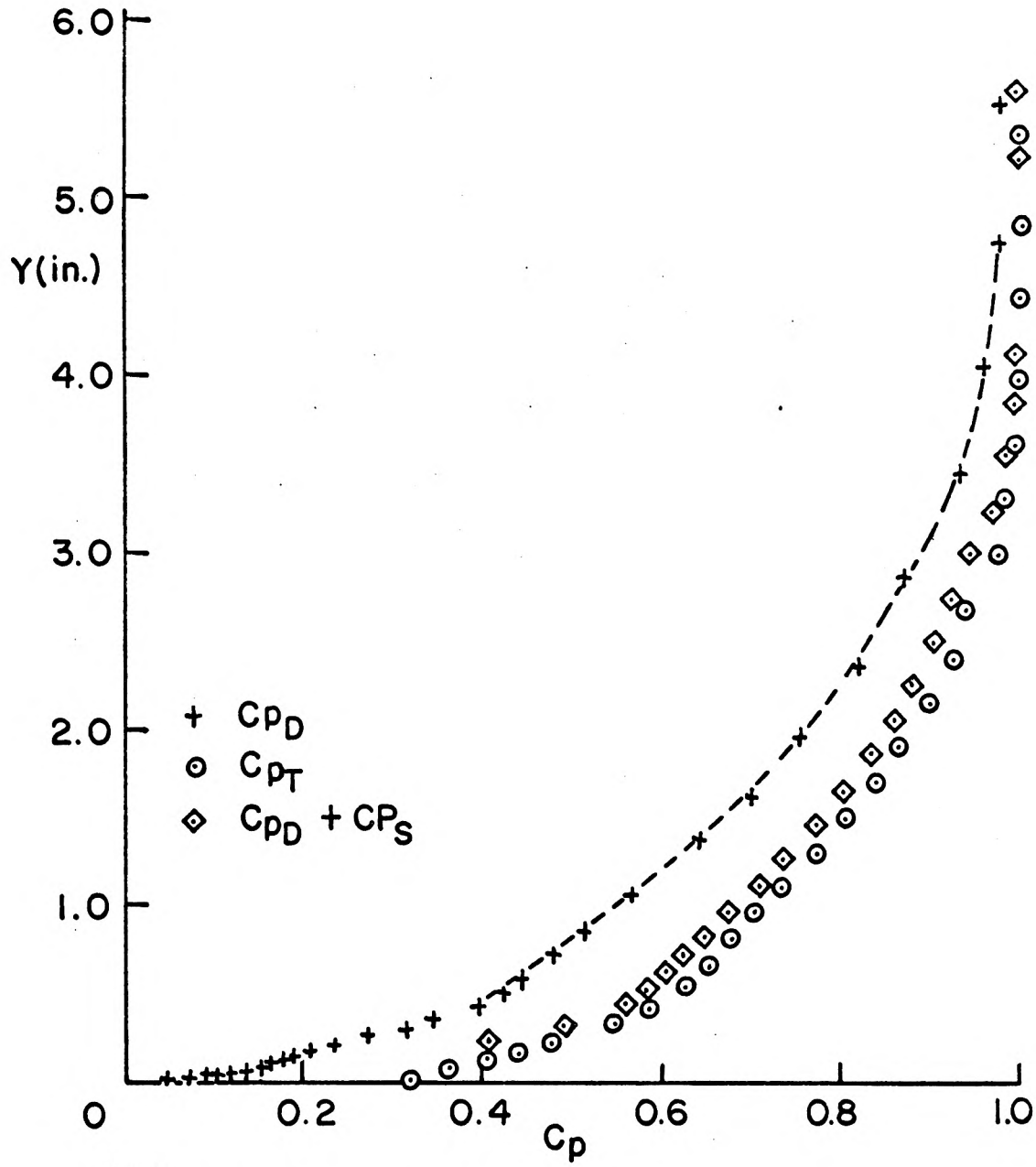

FIG. 32b COMPARISON OF DIRECT AND INDIRECT MEASUREMENT OF TOTAL PRESSURE COEFFICIENT

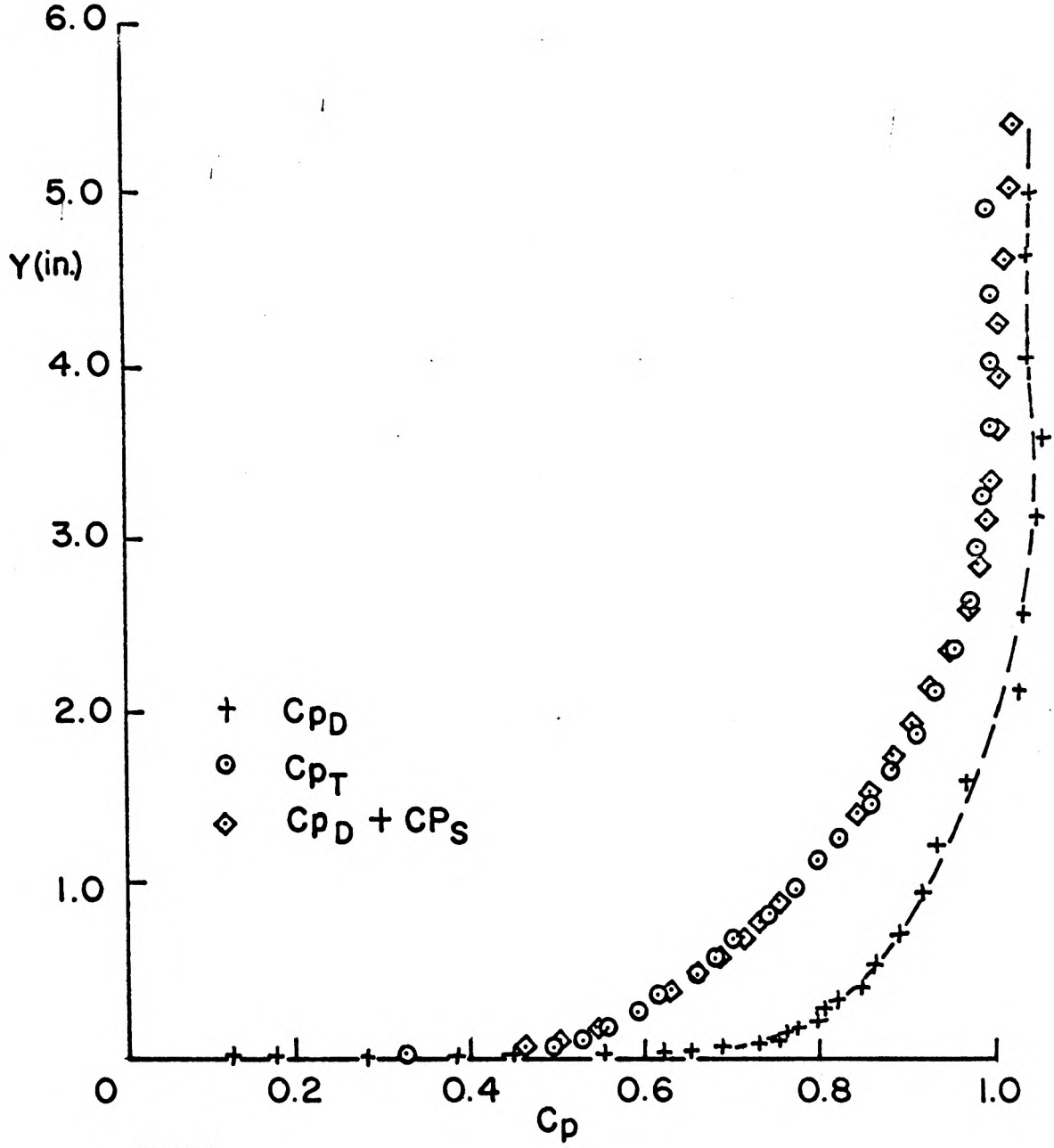

FIG. 32c COMPARISON OF DIRECT AND INDIRECT MEASUREMENT OF TOTAL PRESSURE COEFFICIENT

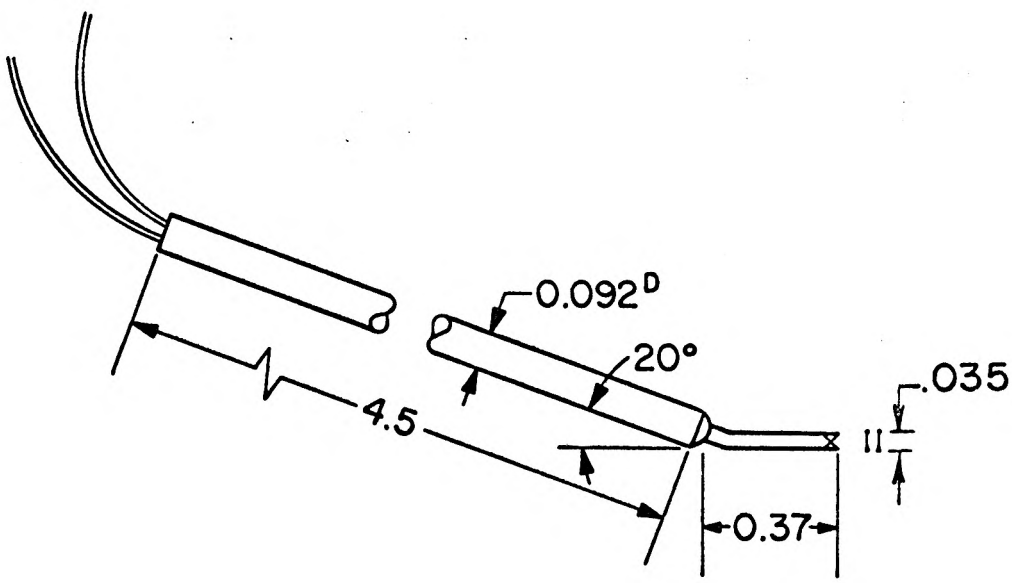

FIG. 33 SPECIAL X-ARRAY HOT WIRE PROBE
(MODIFIED DISA MODEL 55A38)

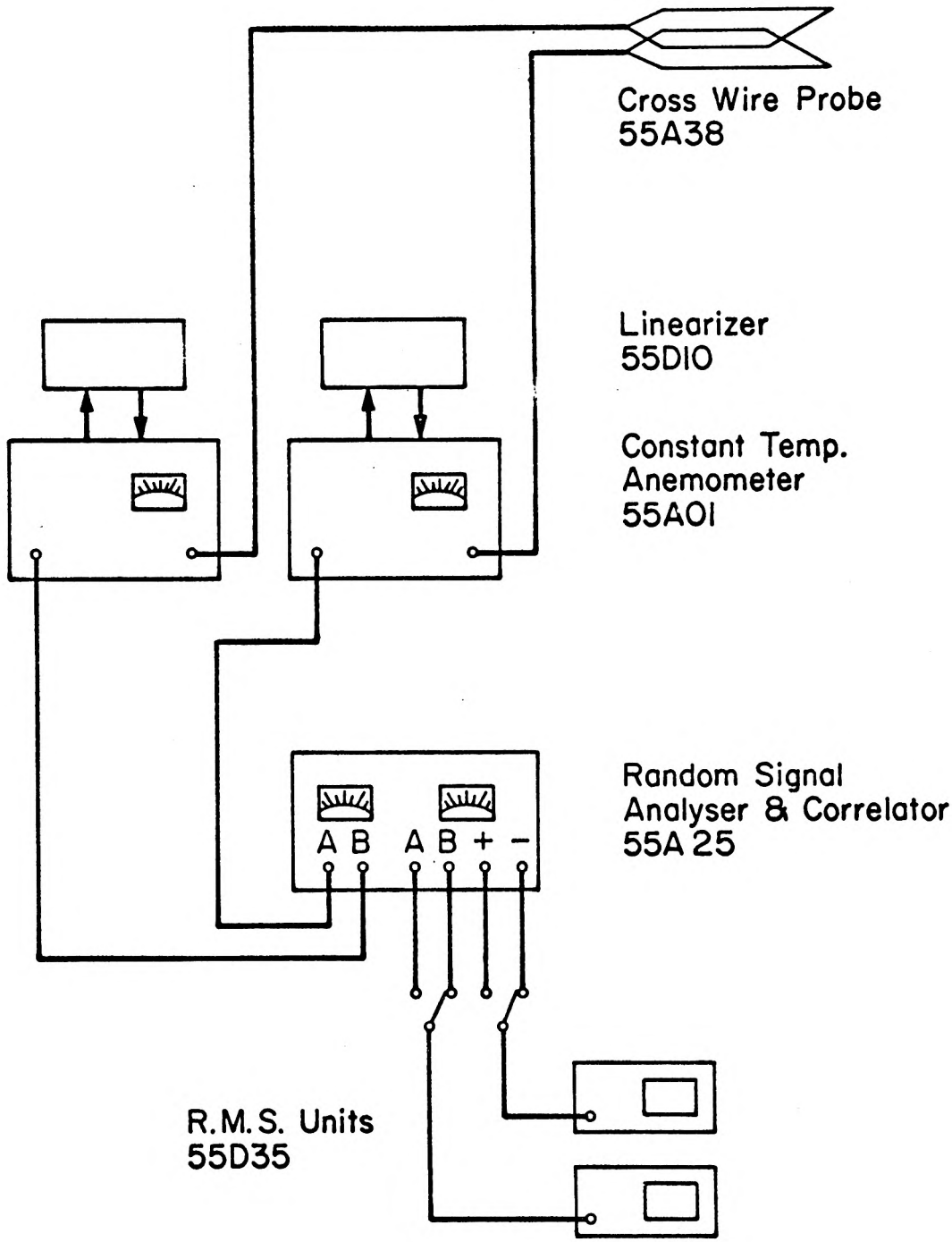

FIG. 34 MEASUREMENT OF TURBULENT INTENSITIES AND REYNOLDS STRESSES USING X-ARRAY HOT WIRE PROBE

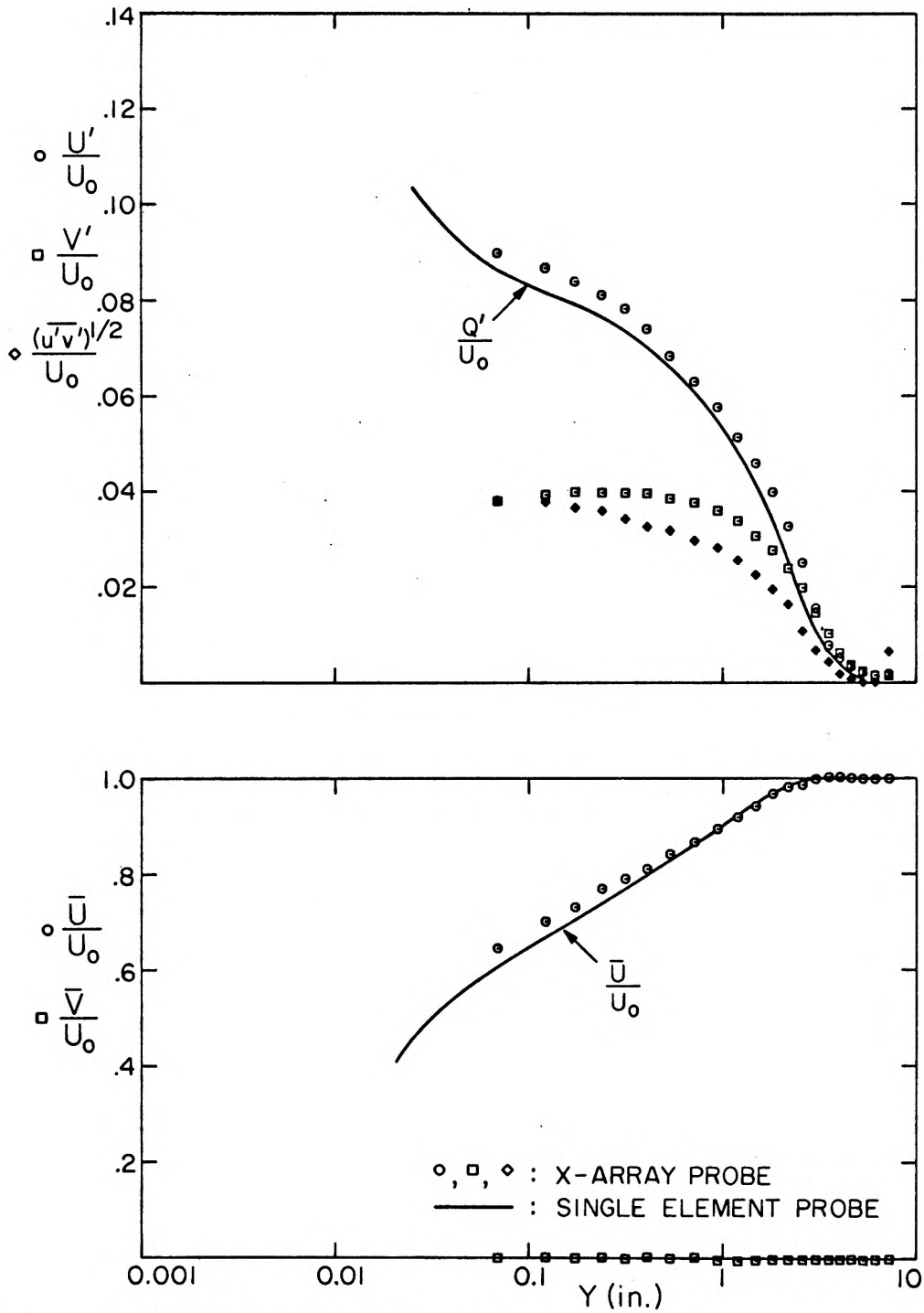

MODEL: PLAIN FLOOR
STATION OF SURVEY: 6'

FIG.35a VELOCITY COMPONENTS , TURBULENCE INTENSITIES AND REYNOLDS STRESS DISTRIBUTION

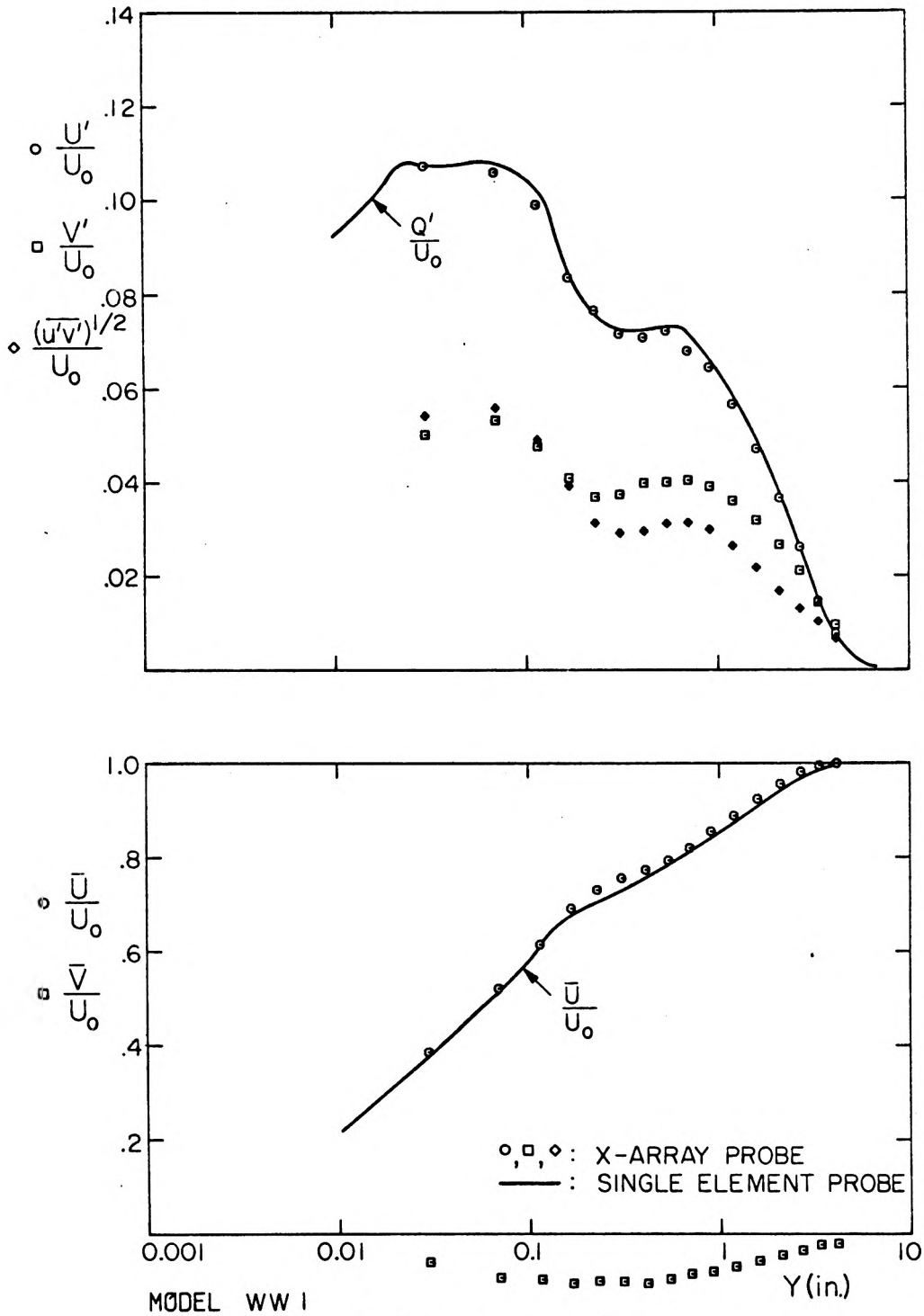

FIG.35b VELOCITY COMPONENTS , TURBULENCE INTENSITIES AND REYNOLDS STRESS DISTRIBUTION

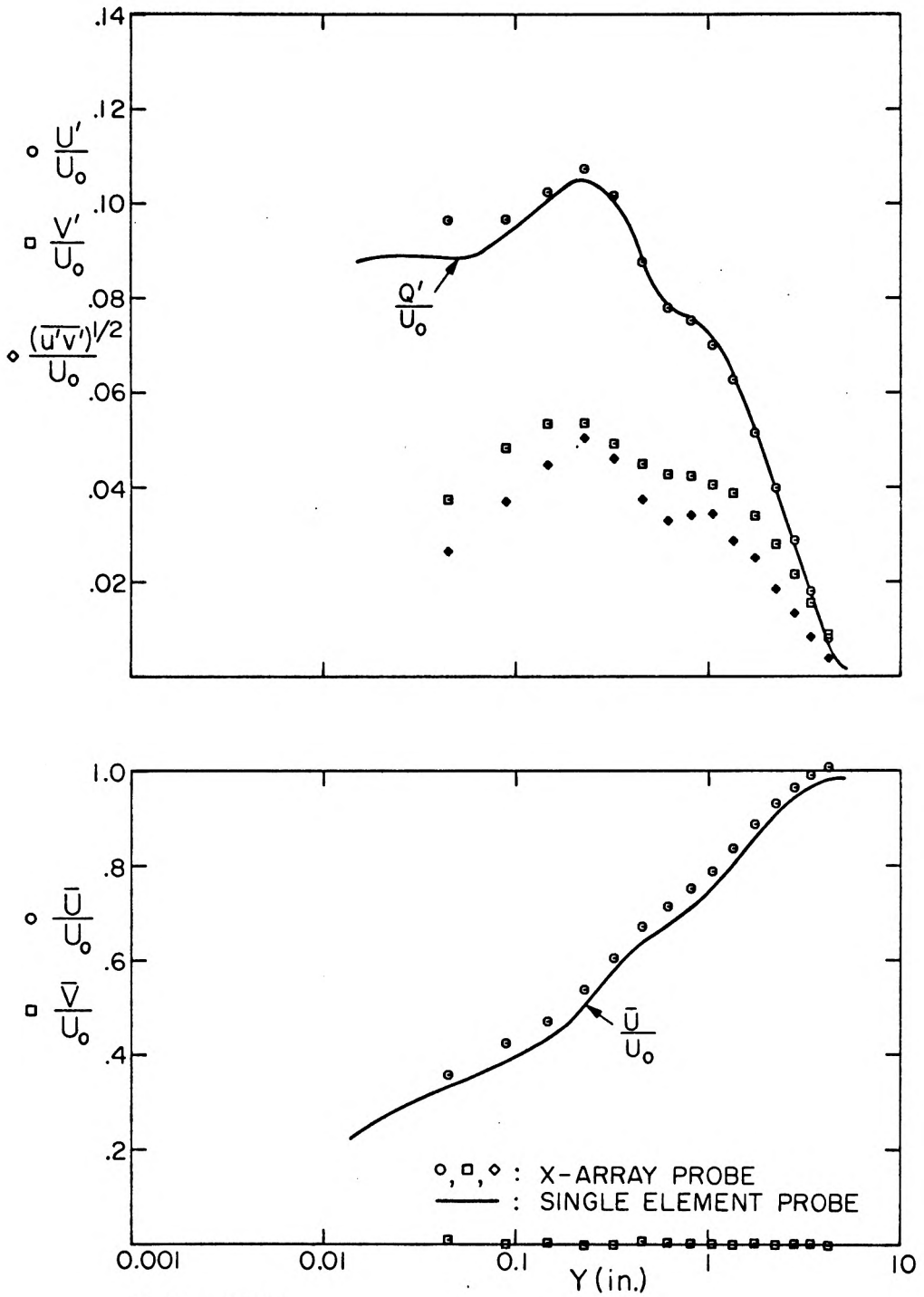

MODEL: WW I
STATION OF SURVEY: CP = MAX.

FIG.35c VELOCITY COMPONENTS , TURBULENCE INTENSITIES AND REYNOLDS STRESS DISTRIBUTION

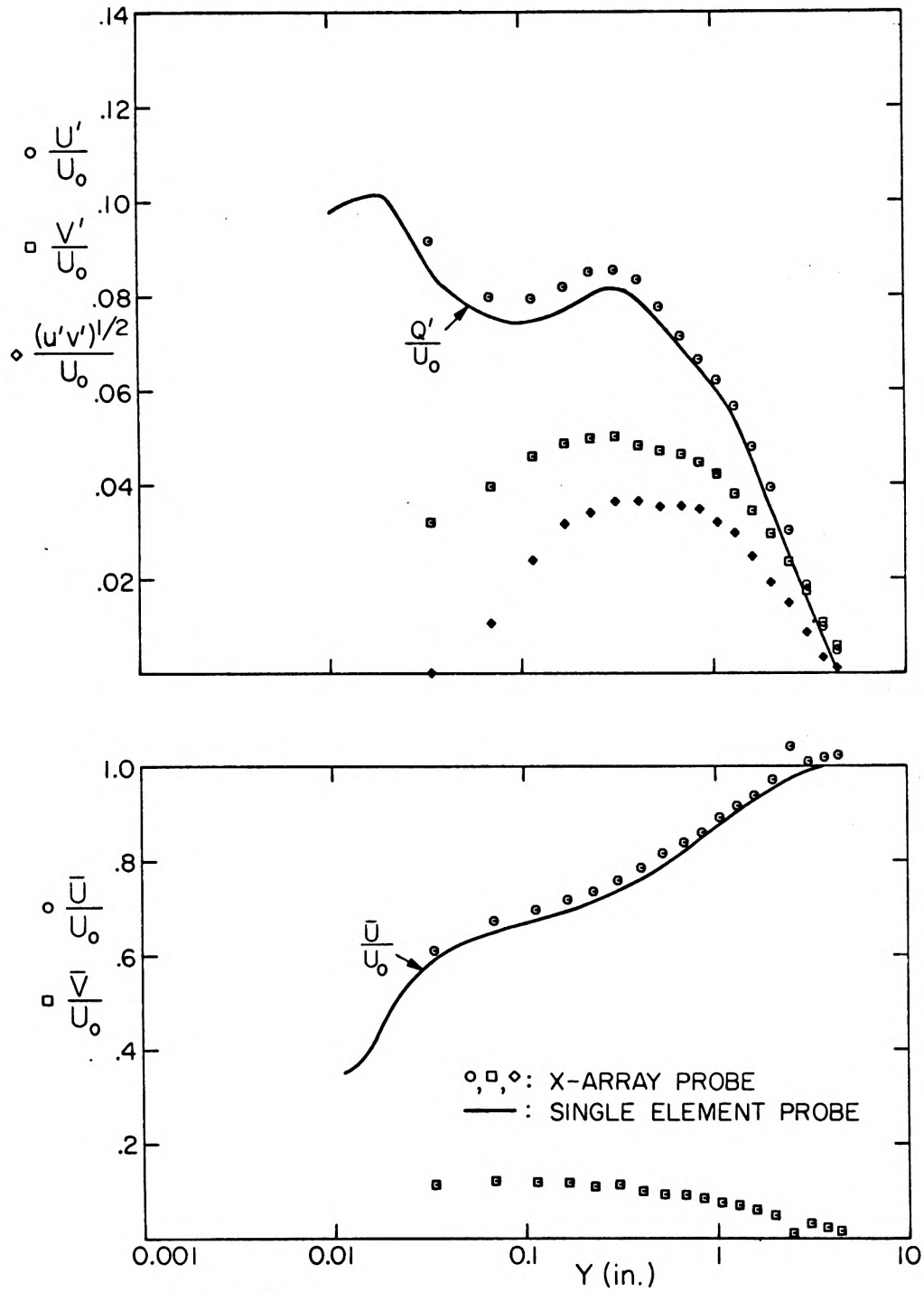

MODEL: WW I
STATION OF SURVEY: CP = 0, dP/dX < 0

FIG.35d VELOCITY COMPONENTS , TURBULENCE INTENSITIES AND REYNOLDS STRESS DISTRIBUTION

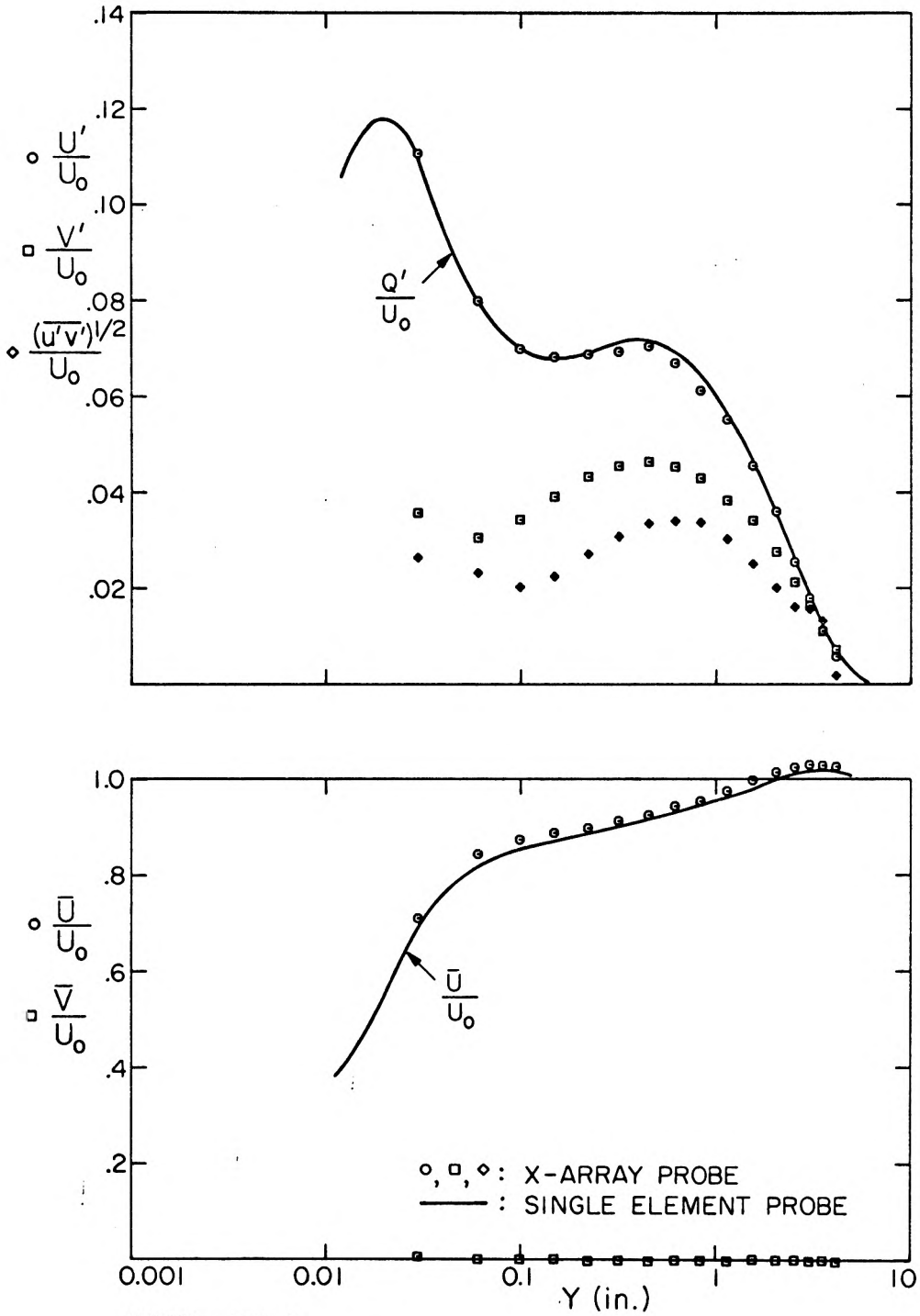

MODEL: WW I
STATION OF SURVEY: CP = MIN.

FIG.35e VELOCITY COMPONENTS , TURBULENCE INTENSITIES AND REYNOLDS STRESS DISTRIBUTION

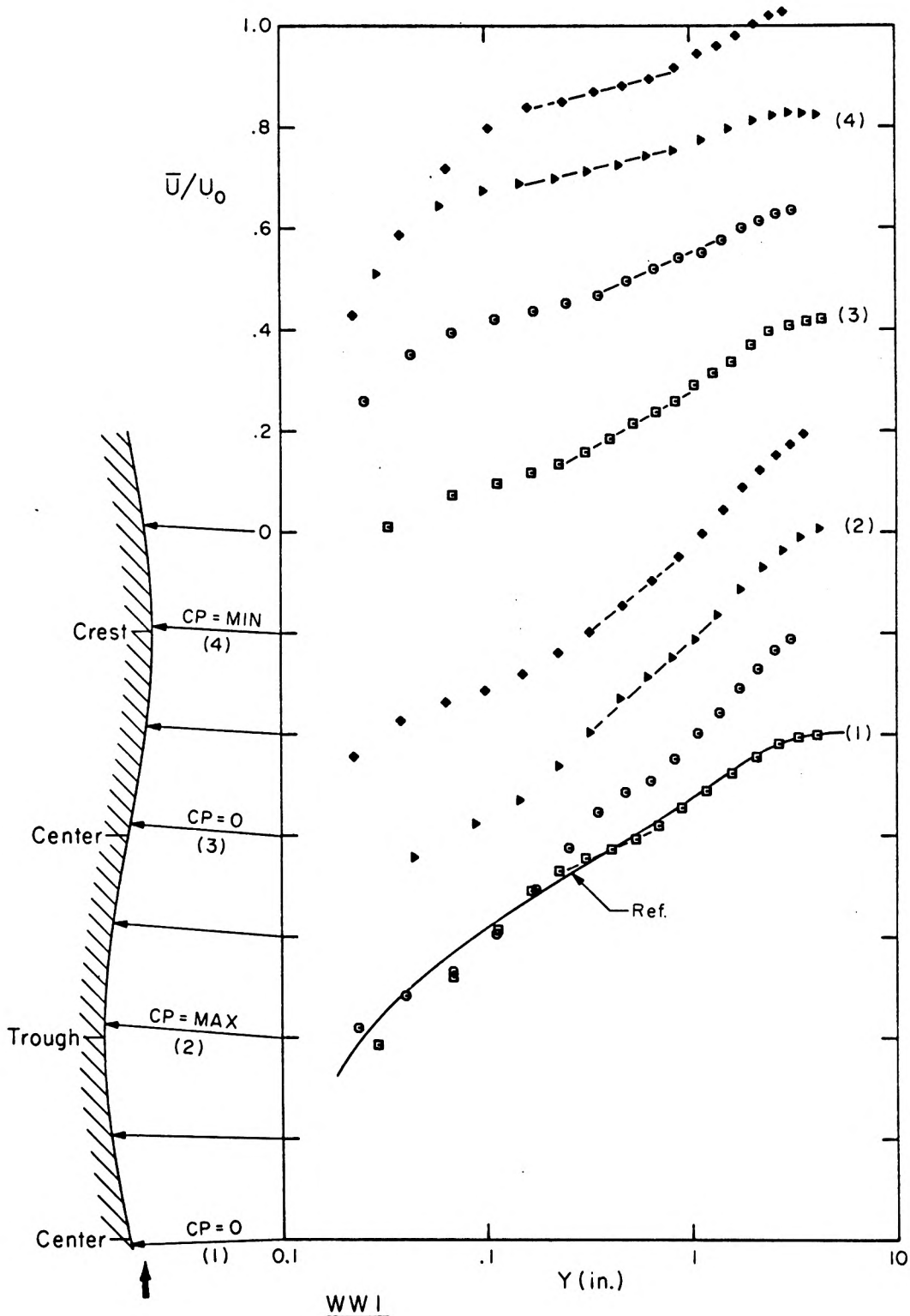

Fig.36a DEVELOPMENT OF AVERAGE VELOCITY PROFILES

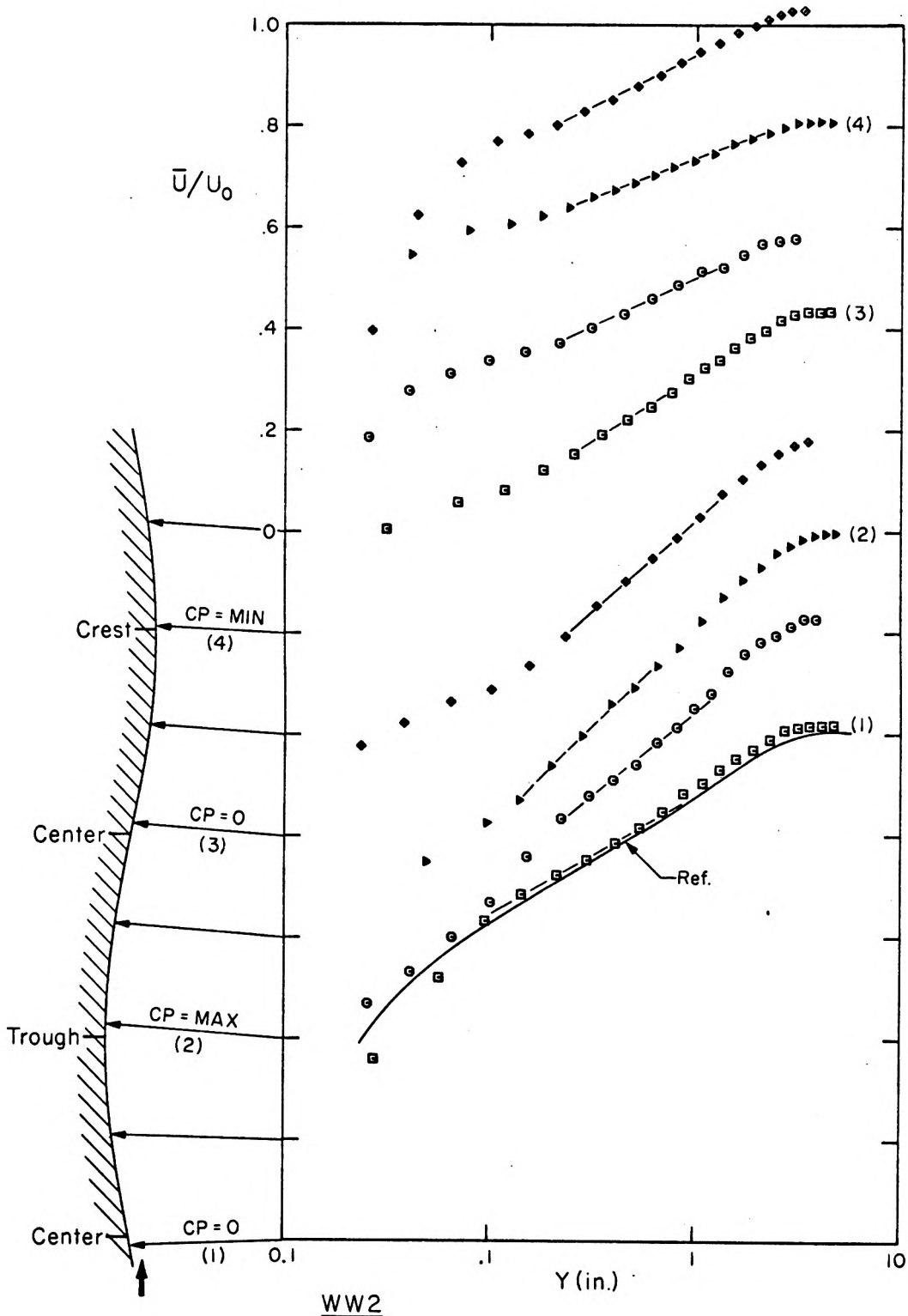

Fig.36b DEVELOPMENT OF AVERAGE VELOCITY PROFILES

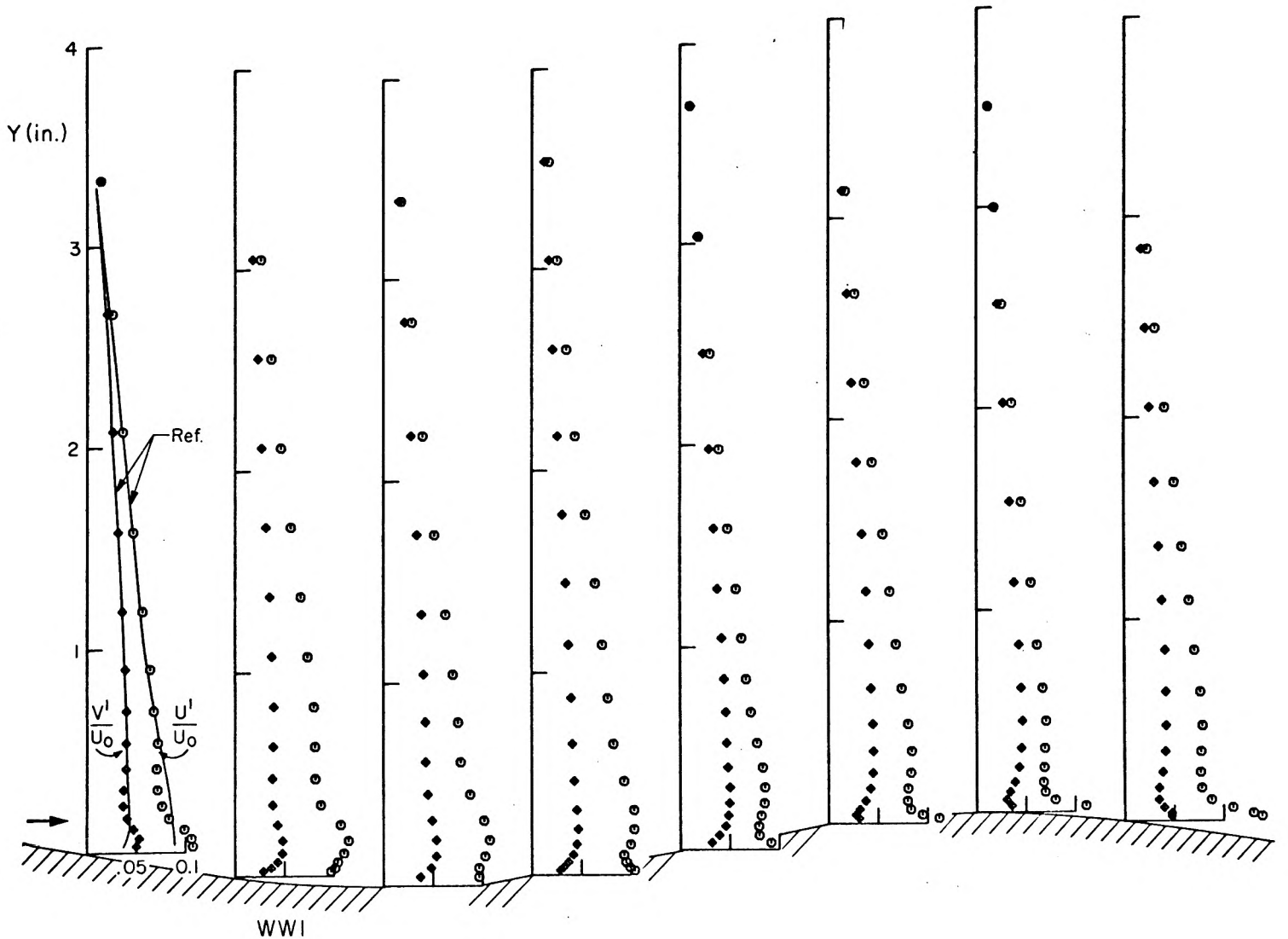

Fig37aTURBULENCE INTENSITIES DISTRIBUTION

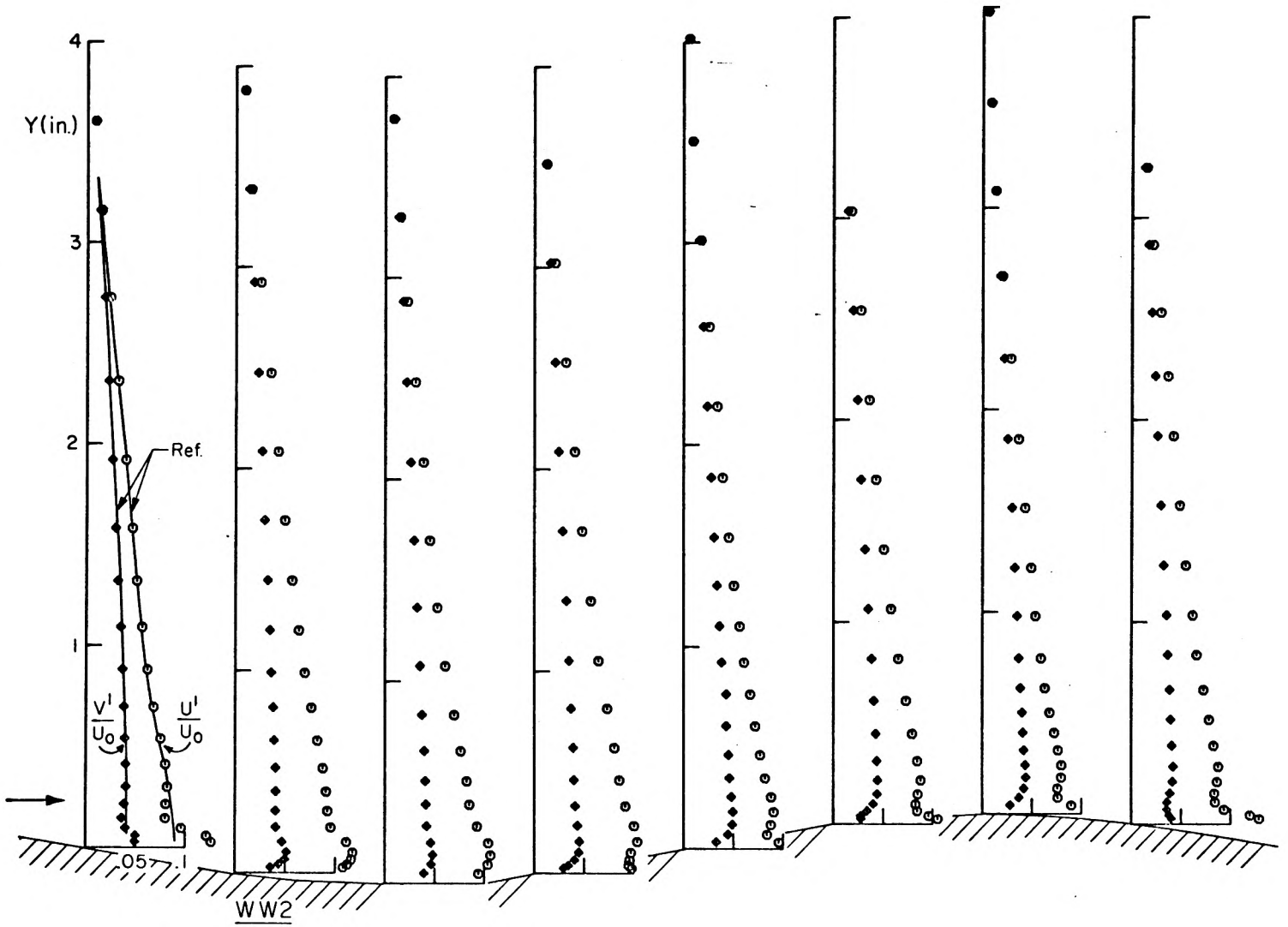

Fig37bTURBULENCE INTENSITIES DISTRIBUTION

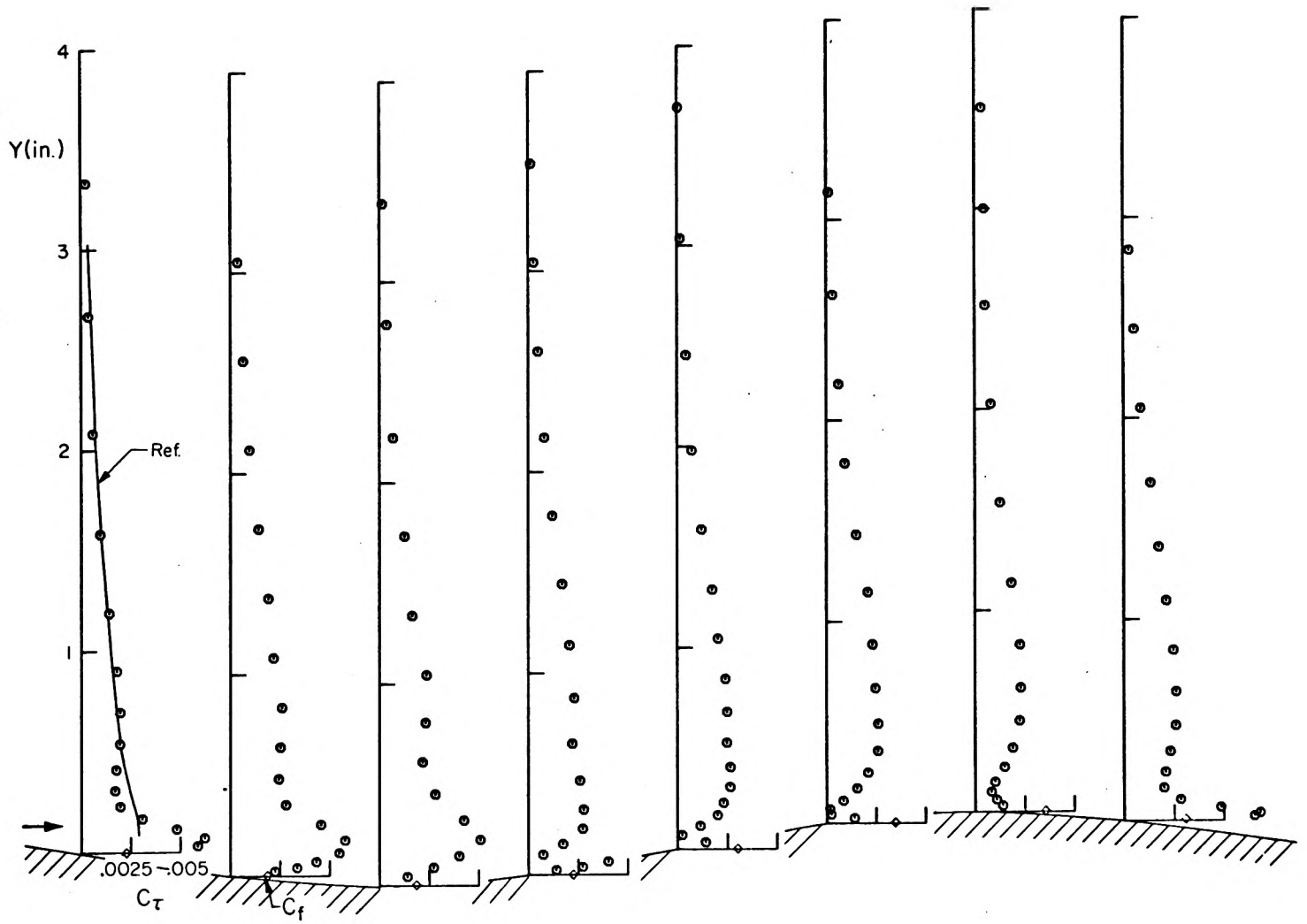

WWI

Fig. 38a TURBULENT SHEAR STRESS COEFFICIENT DISTRIBUTION

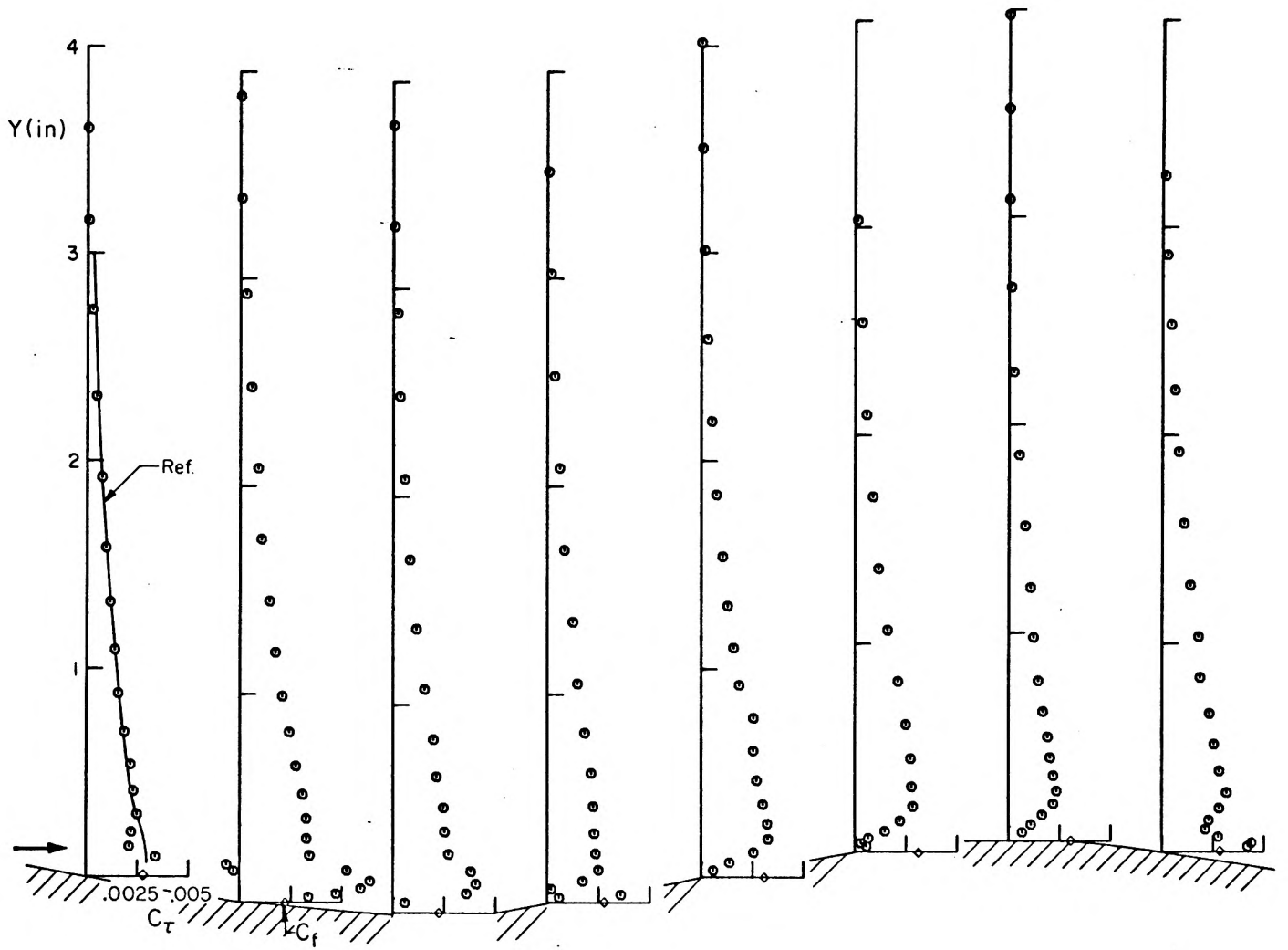

Fig.38bTURBULENT SHEAR STRESS COEFFICIENT DISTRIBUTION

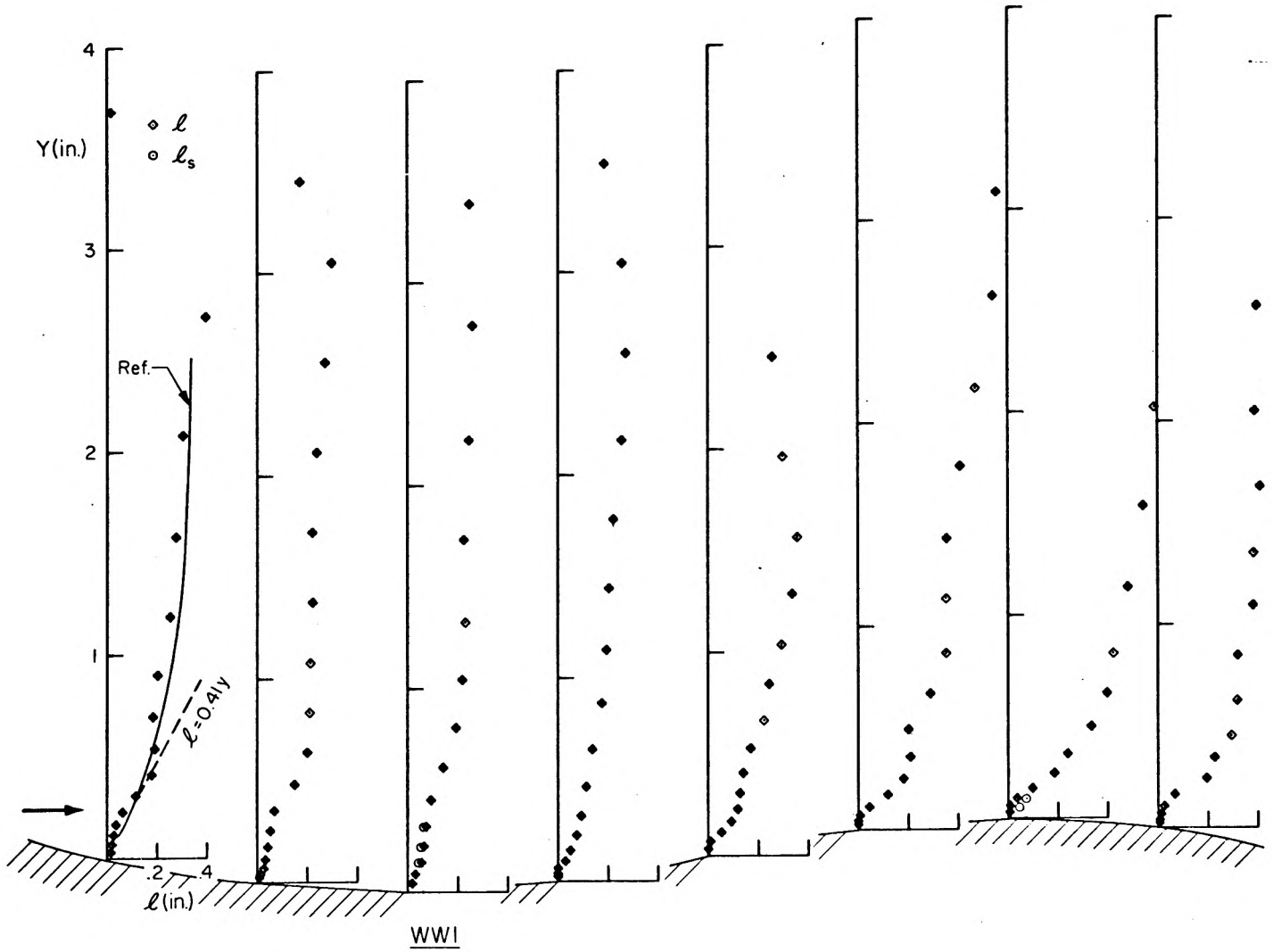

Fig.39a MIXING LENGTH DISTRIBUTION

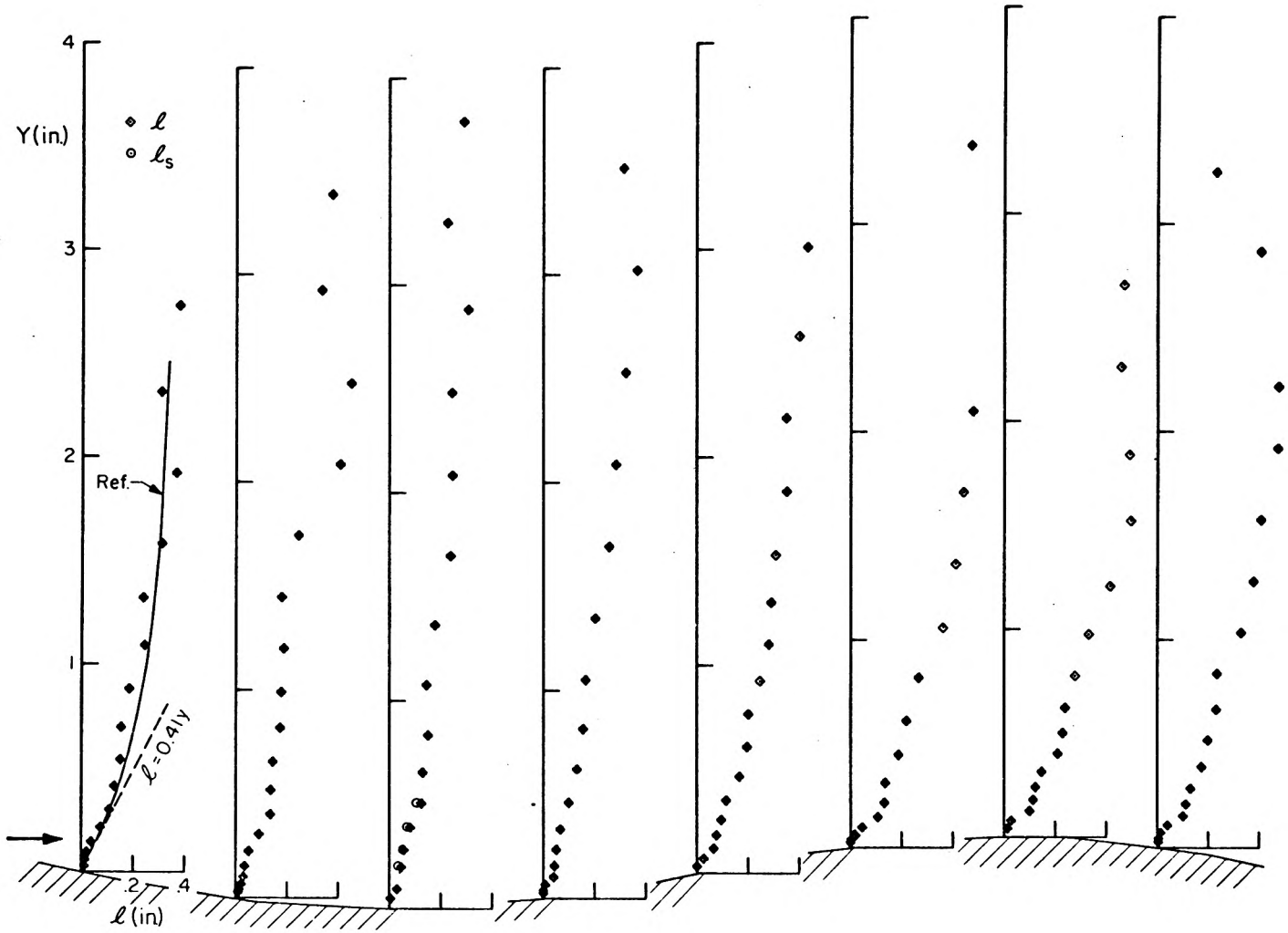

Fig.39b MIXING LENGTH DISTRIBUTION

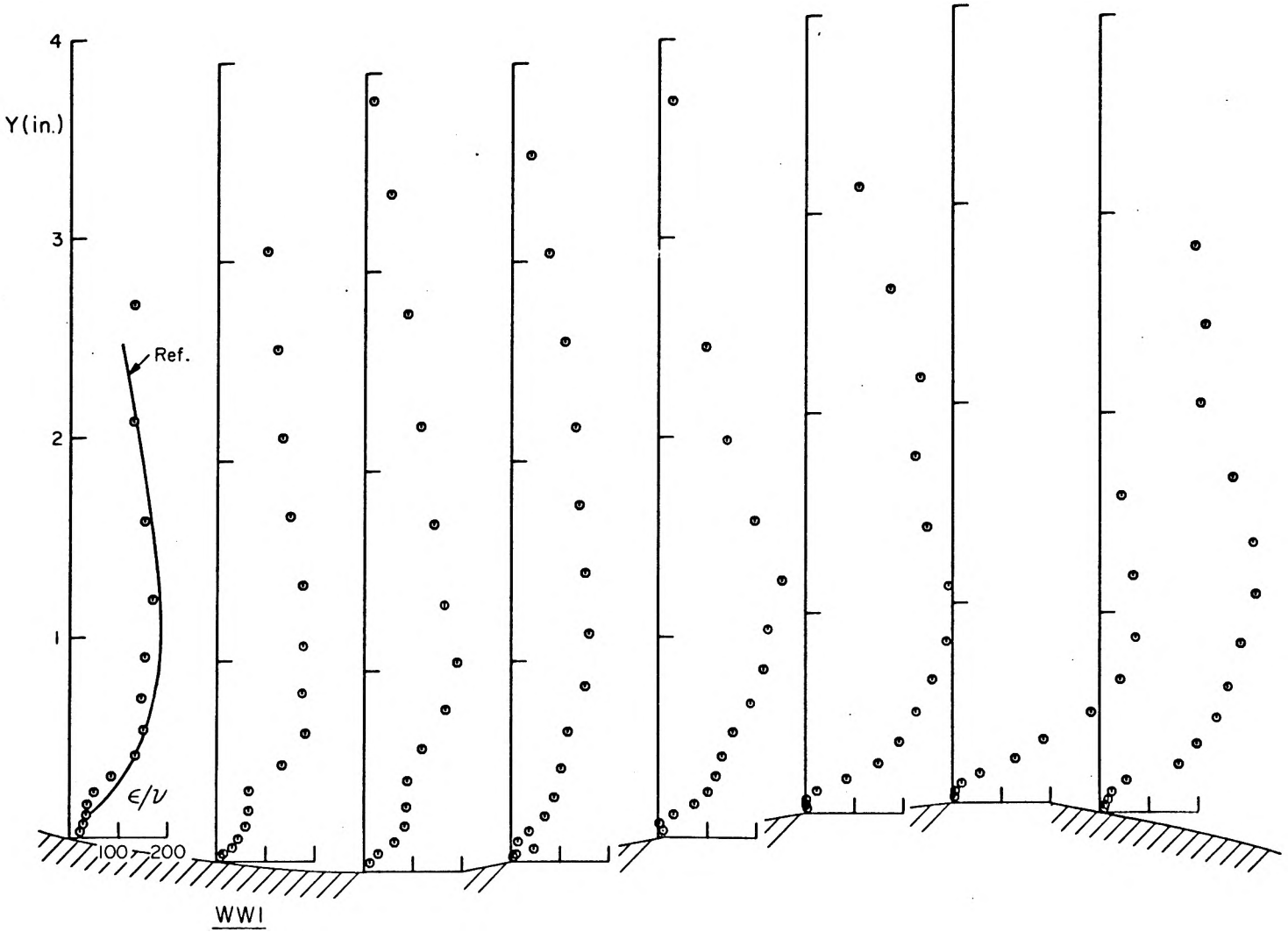

Fig 40a EDDY VISCOSITY DISTRIBUTION

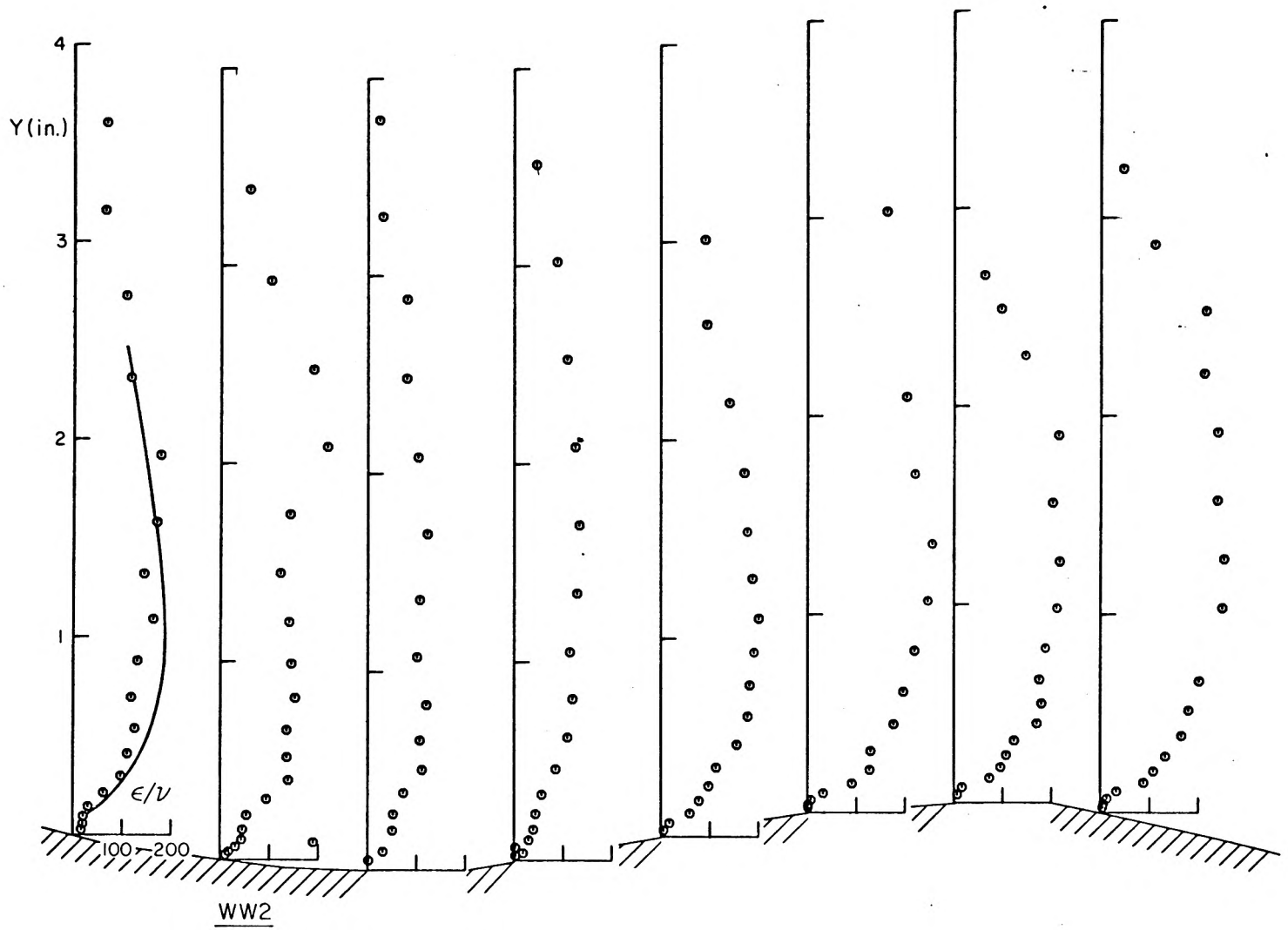

Fig.40bEDDY VISCOSITY DISTRIBUTION

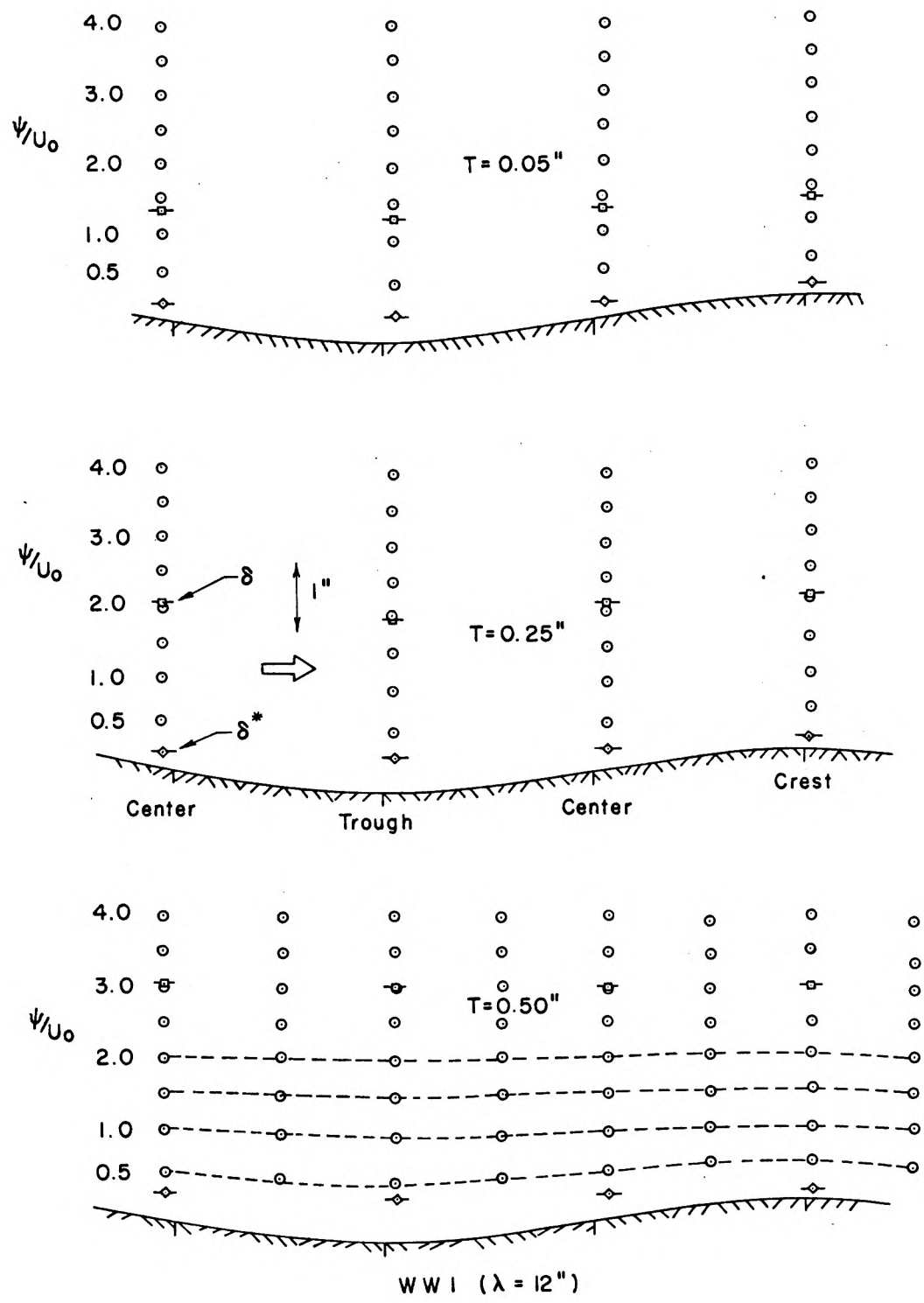

FIG.41a HEIGHT OF STREAMLINES ABOVE SURFACE AND BOUNDARY LAYER THICKNESSES

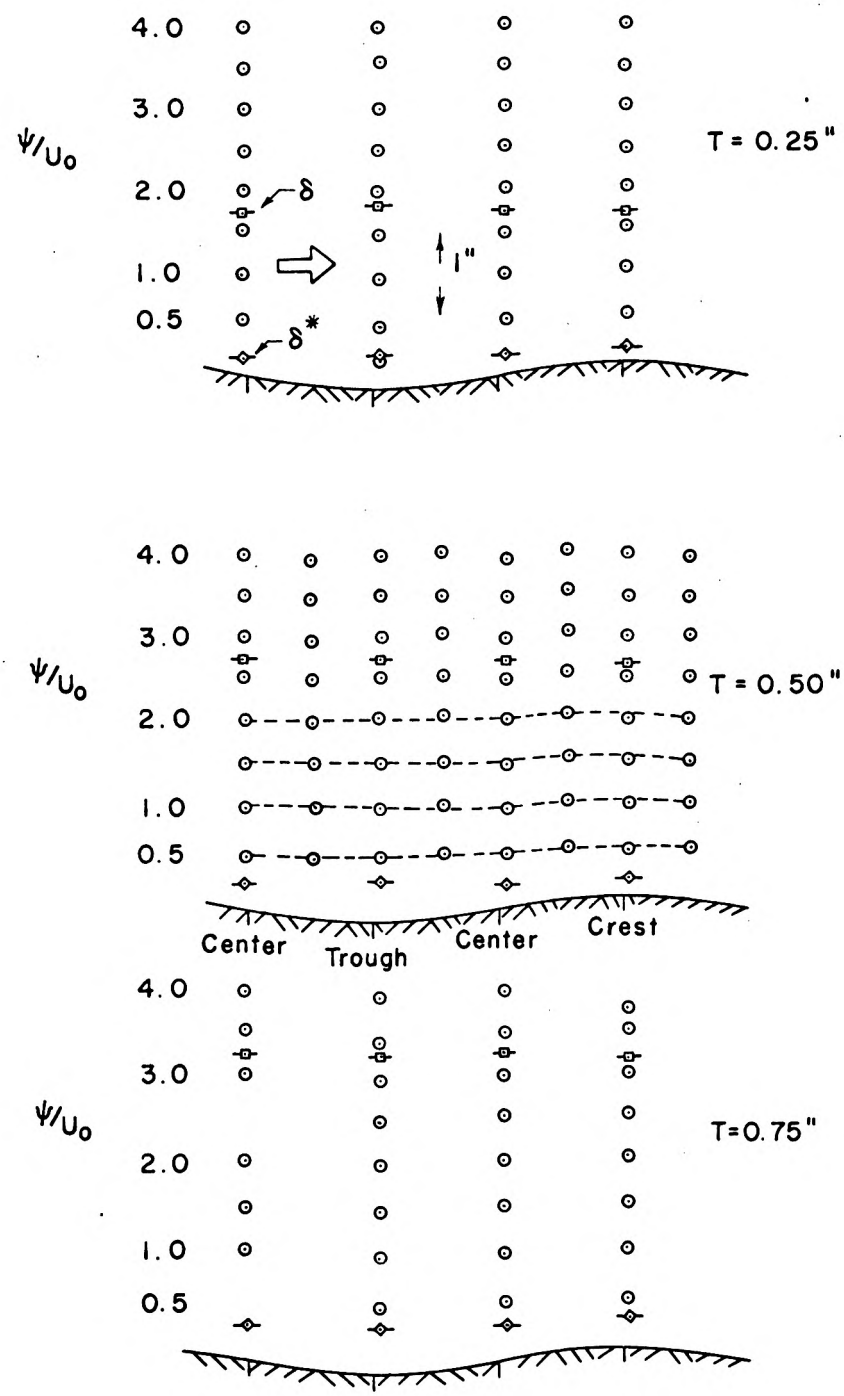

WW 2 (λ = 6")

FIG.41b HEIGHT OF STREAMLINES ABOVE SURFACE AND BOUNDARY LAYER THICKNESSES

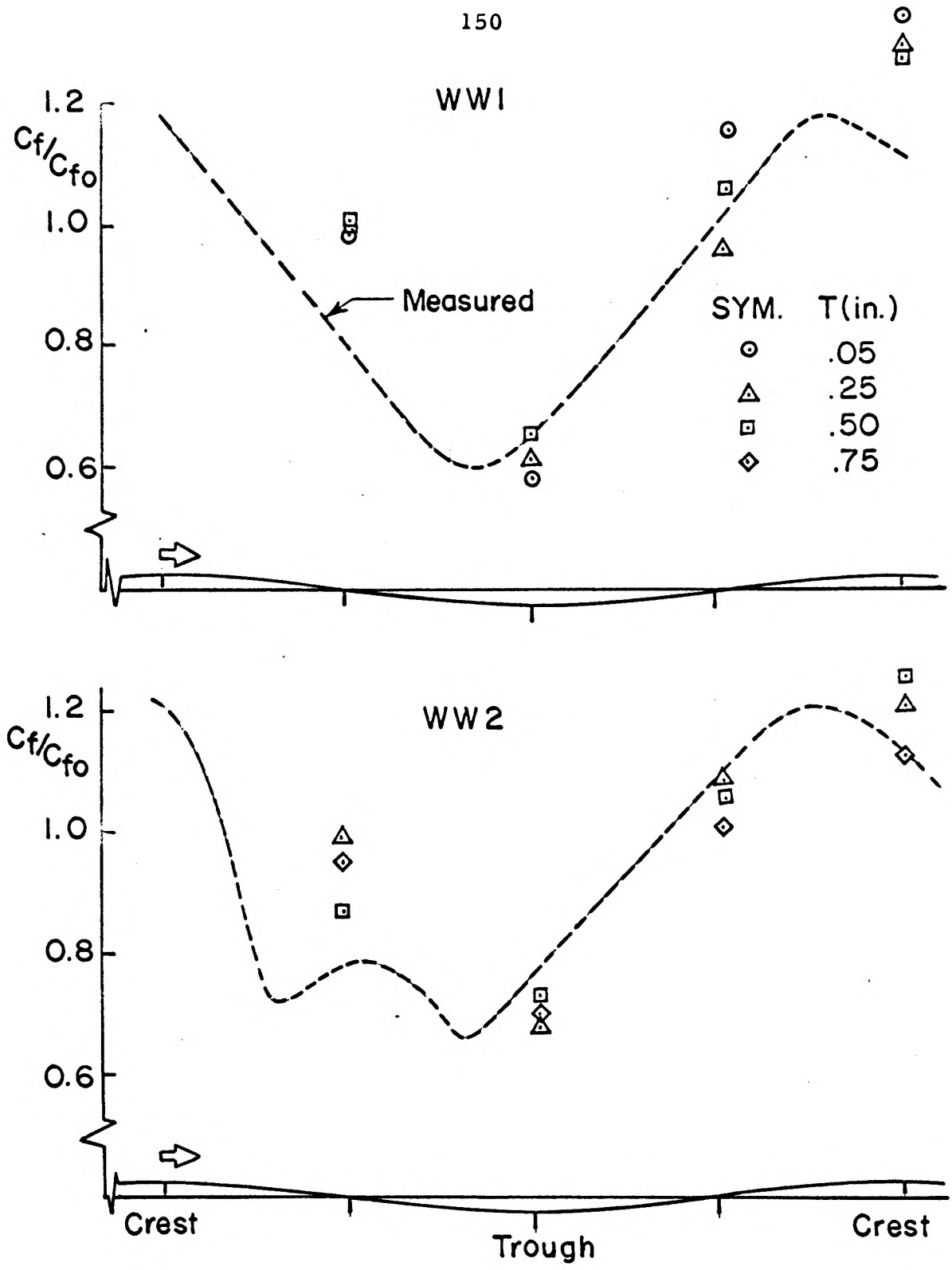

FIG. 42 COMPARISON BETWEEN MEASURED SKIN FRICTION DISTRIBUTION AND PREDICTION BY LUDWIG AND TILLMANN LAW

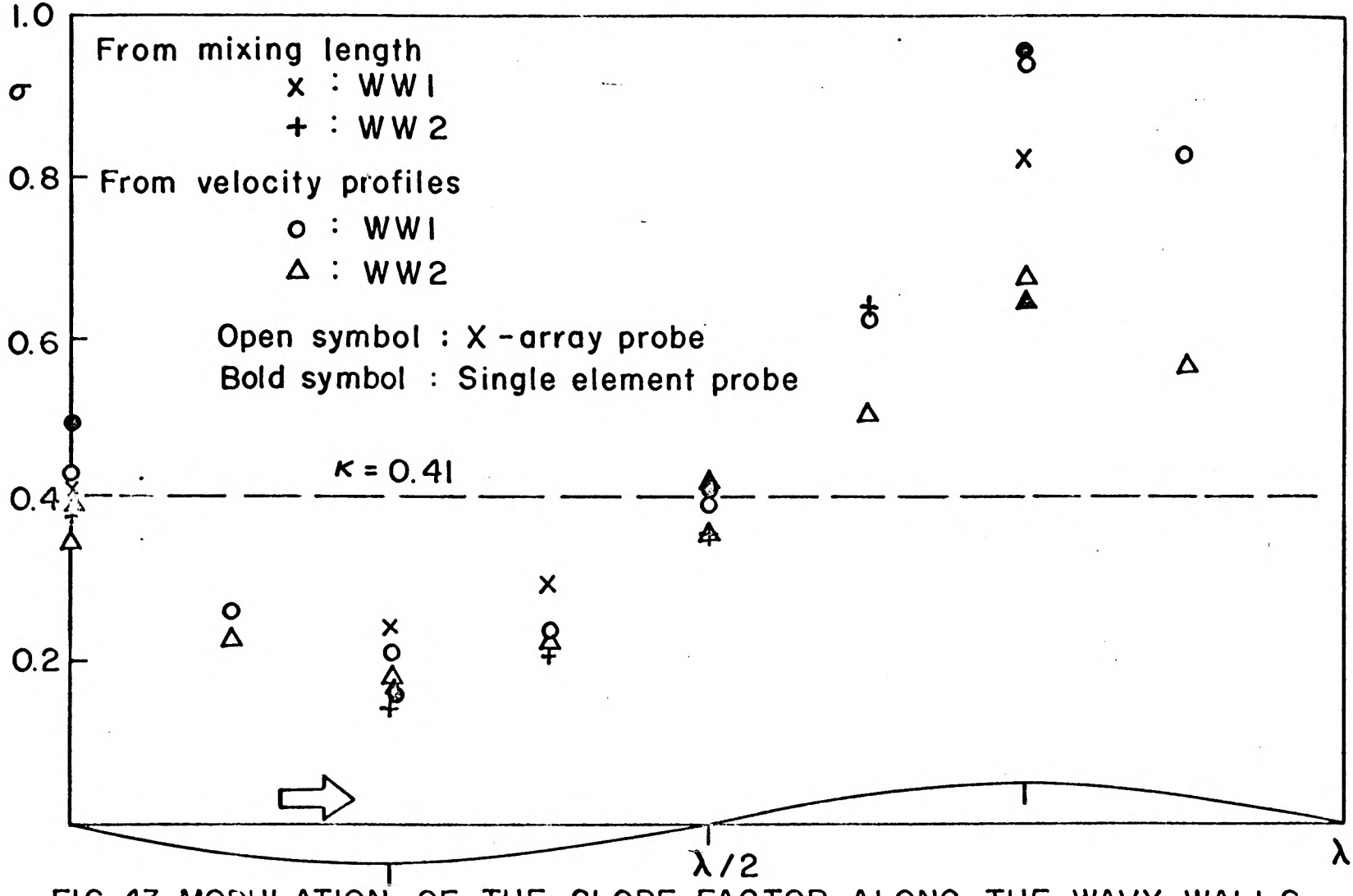

FIG. 43 MODULATION OF THE SLOPE FACTOR ALONG THE WAVY WALLS

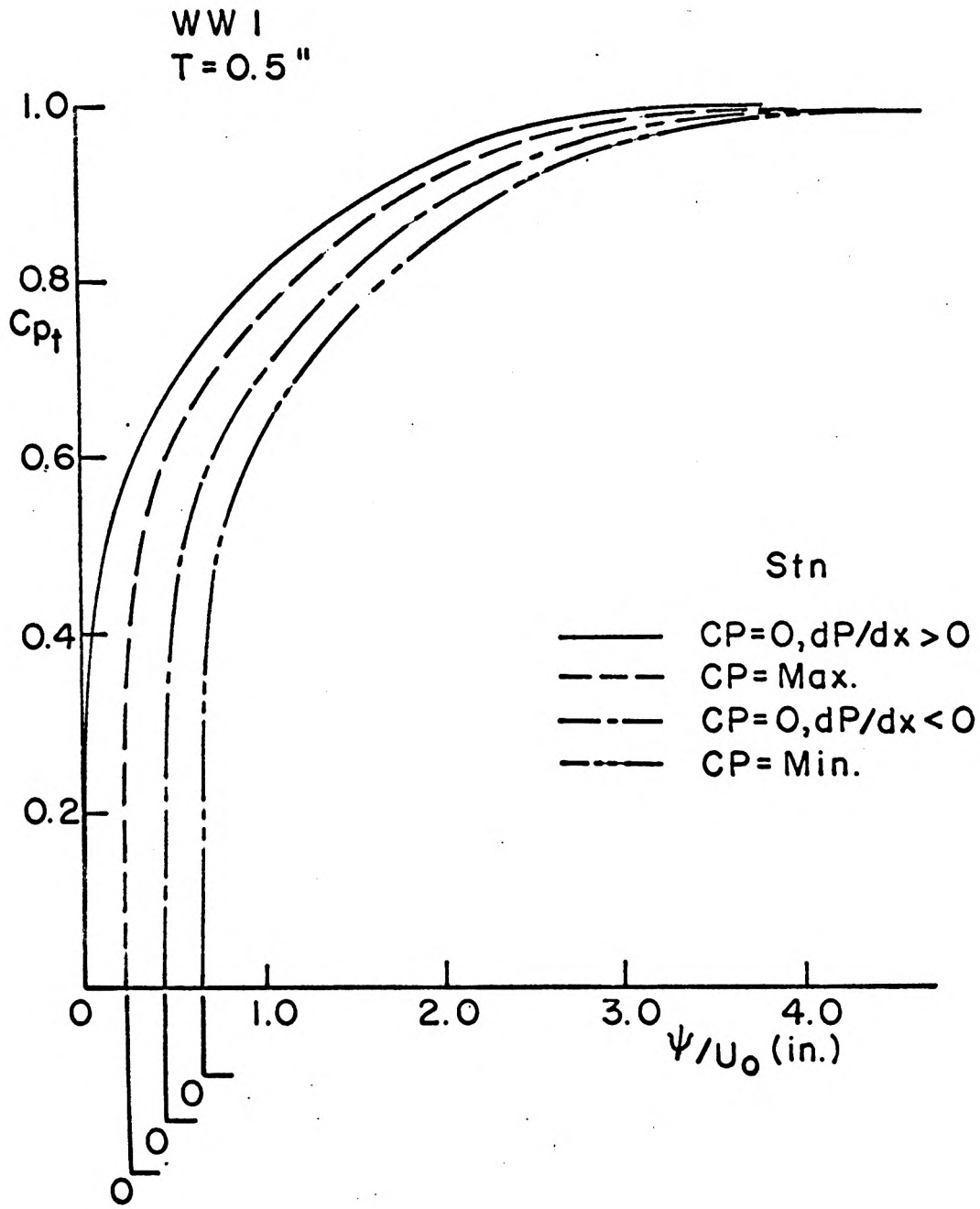

FIG.44a DEPENDENCE OF TOTAL PRESSURE UPON STREAMLINE

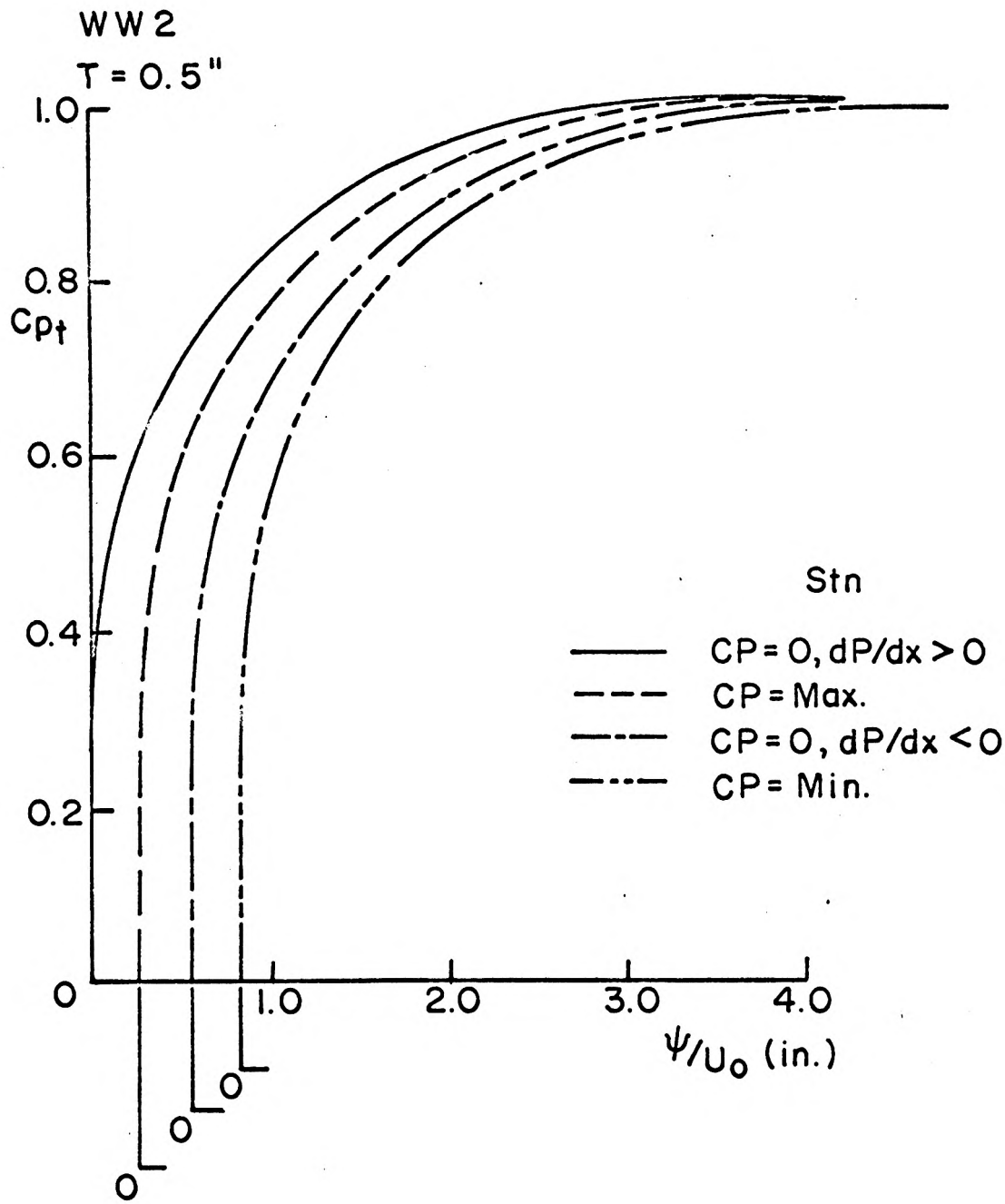

FIG.44b DEPENDENCE OF TOTAL PRESSURE UPON STREAMLINE

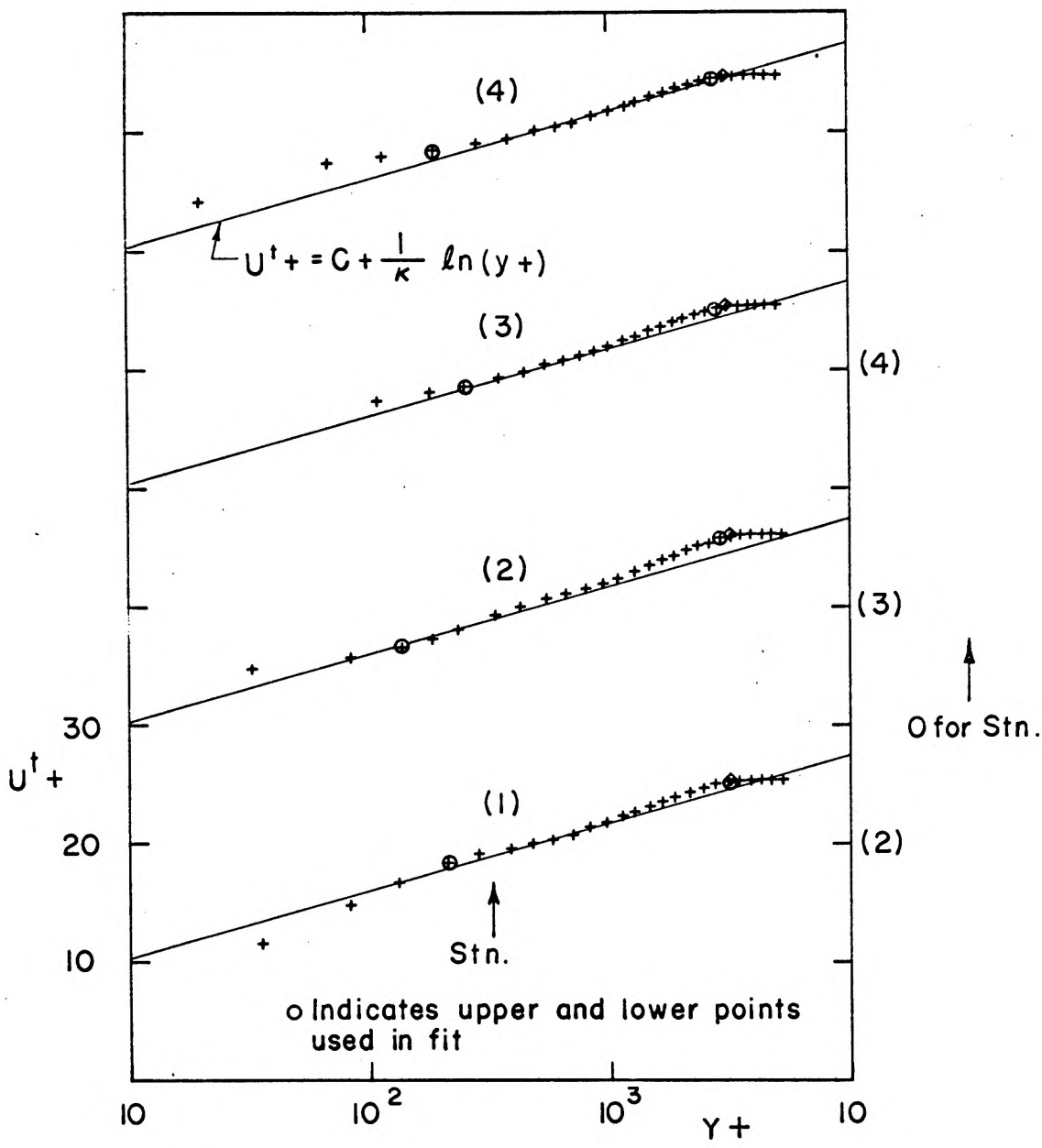

MODEL: WW I
TRIP: 0.5"

FIG.45a LAW OF THE WAKE FITTED TO TOTAL VELOCITY PROFILES

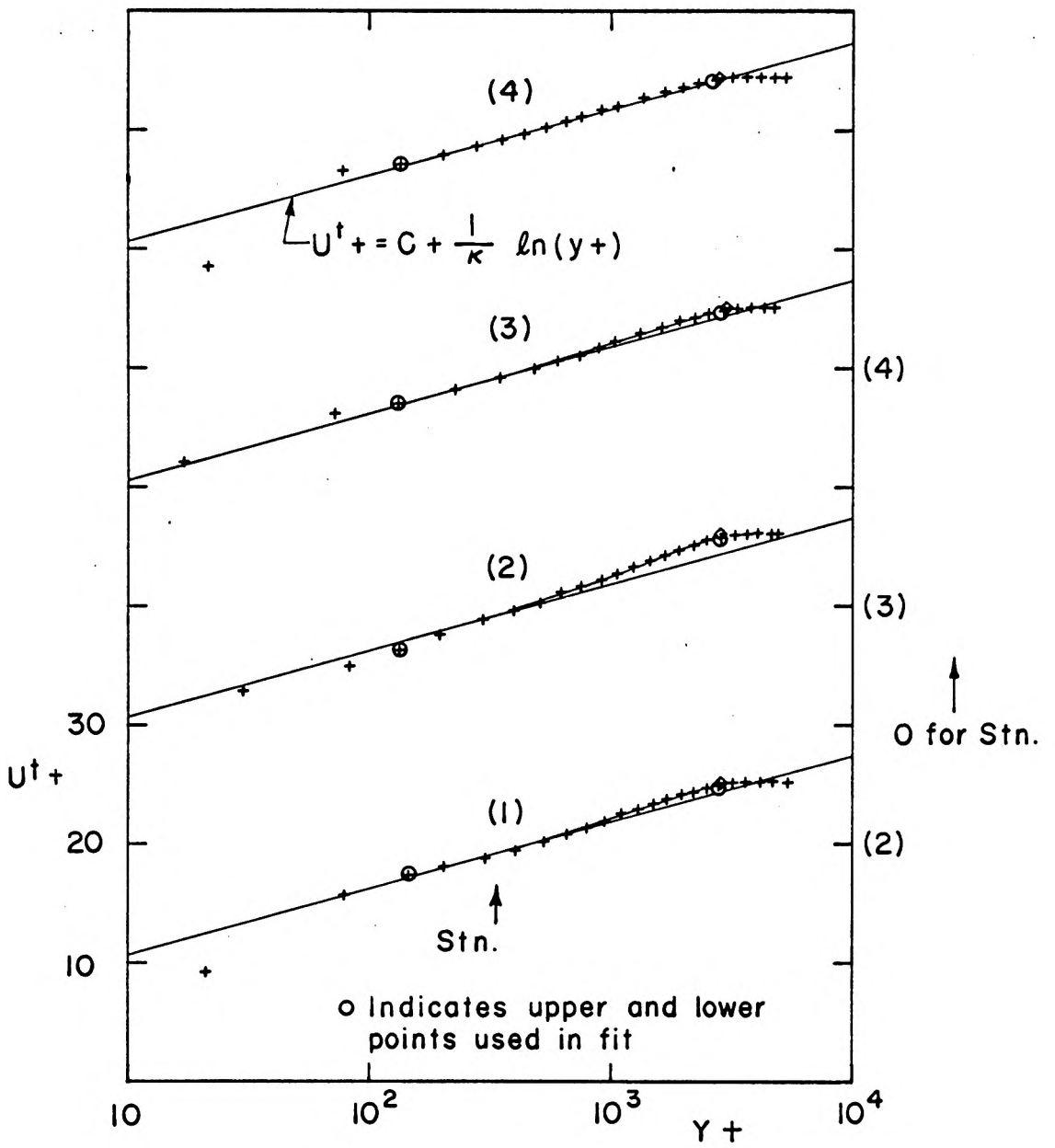

MODEL: WW 2
TRIP: 0.5"

FIG.45b LAW OF THE WAKE FITTED TO TOTAL VELOCITY PROFILES

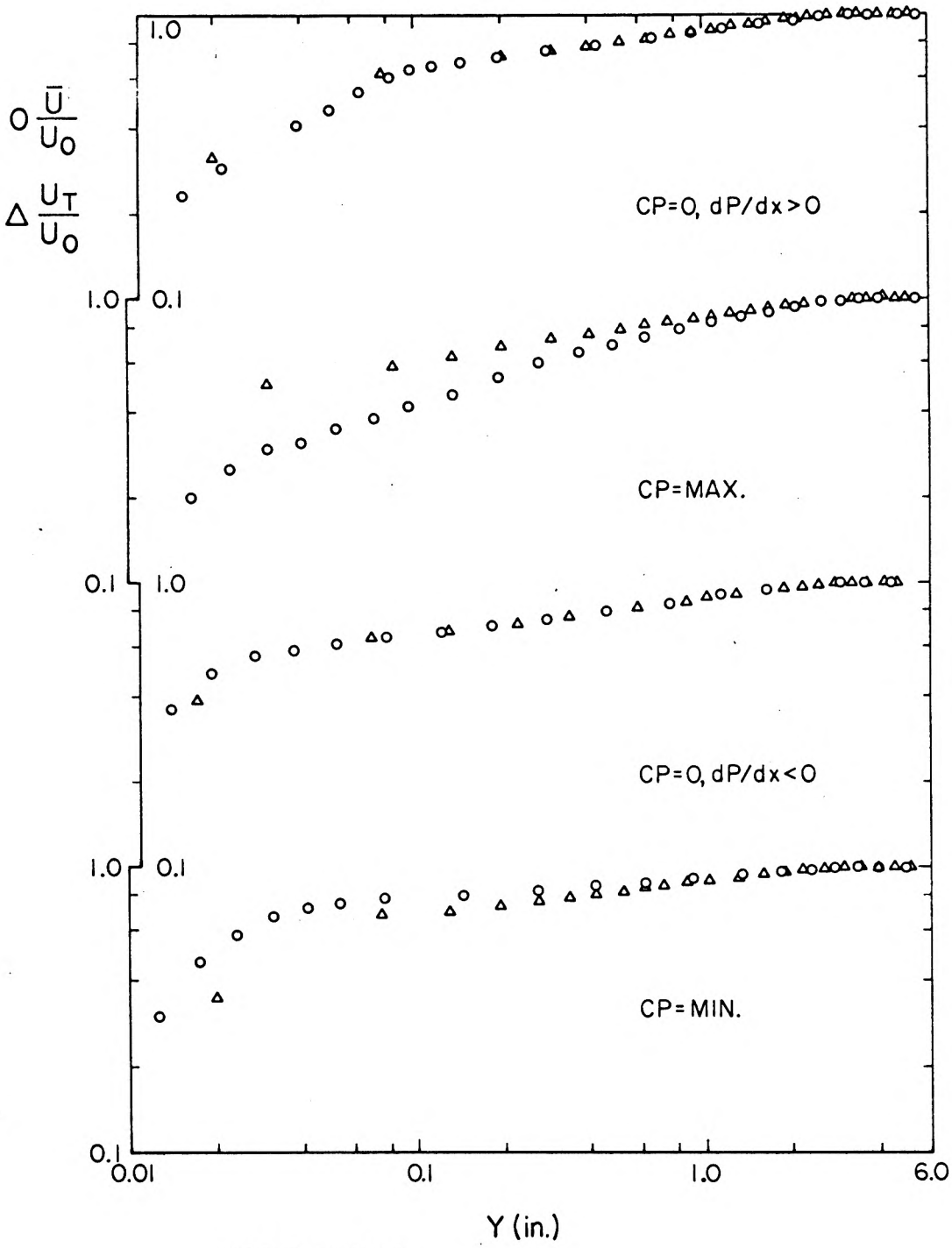

MODEL: WW I
TRIP : 0.5"

FIG. 46a LOG-LOG PRESENTATION OF VELOCITY AND TOTAL VELOCITY

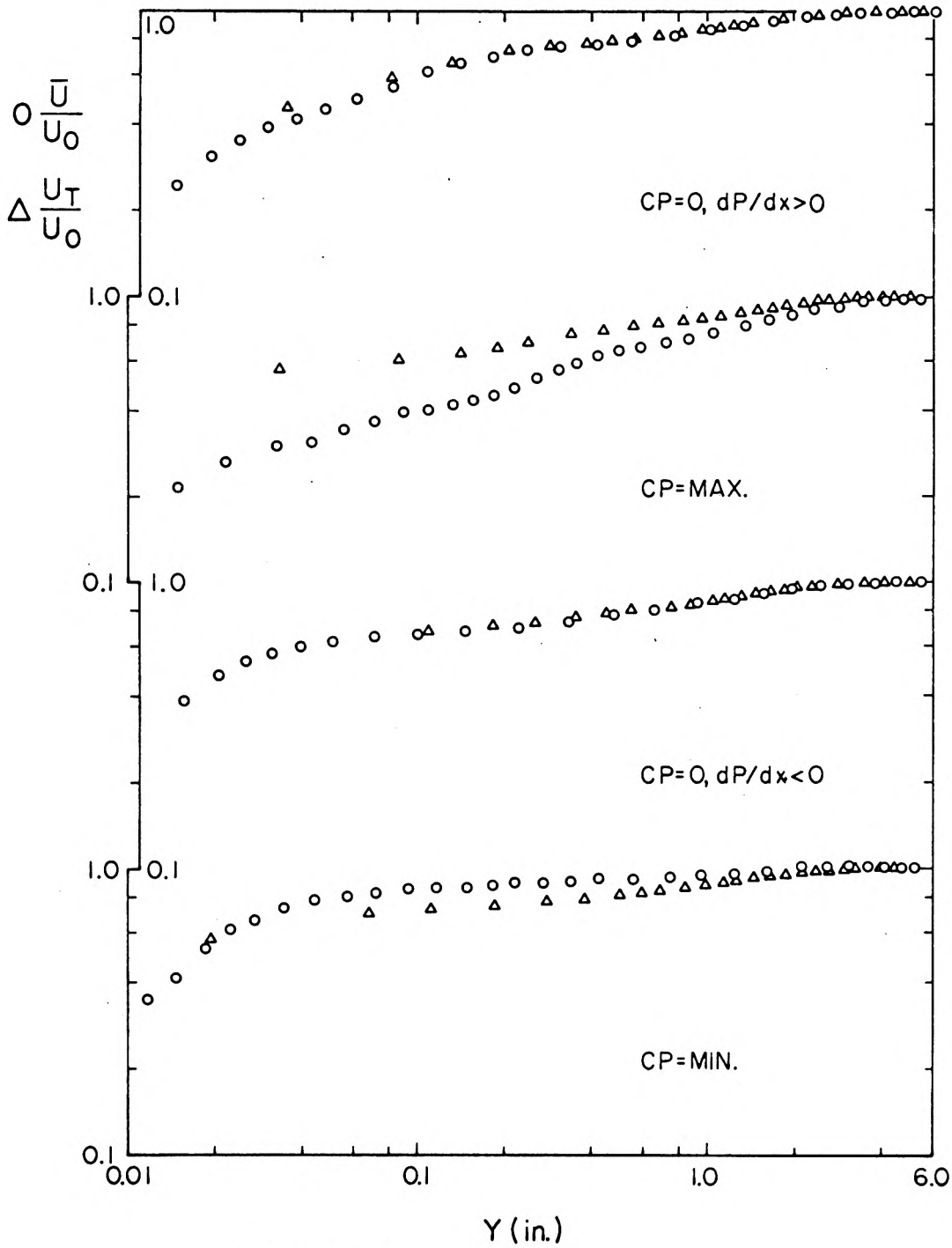

FIG.46b: LOG-LOG PRESENTATION OF VELOCITY AND TOTAL VELOCITY

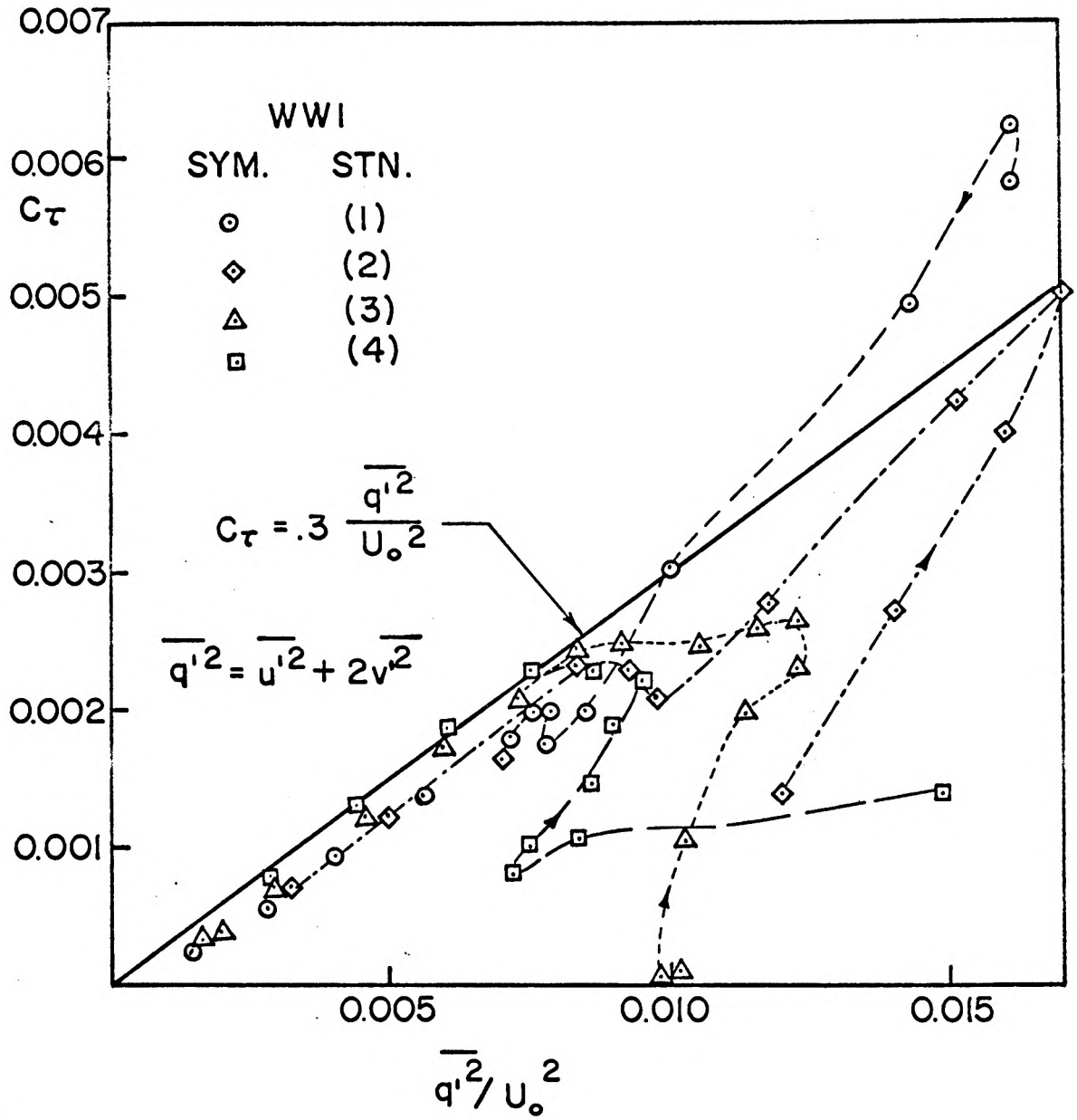

FIG. 47 COMPARISON BETWEEN MEASURED SHEAR STRESS COEFFICIENT AND BRADSHAW-FERRIS MODEL

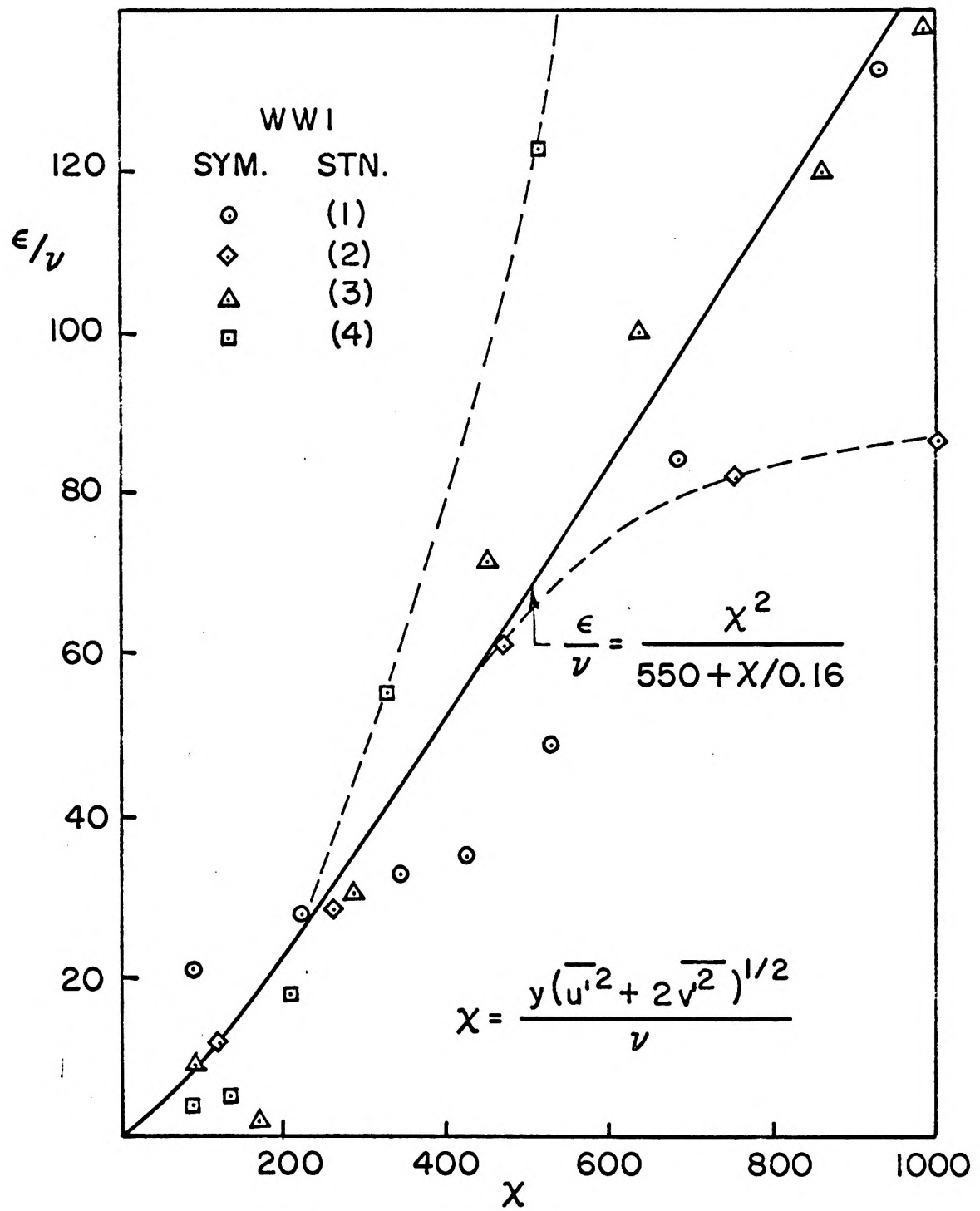

FIG. 48 COMPARISON BETWEEN MEASURED EDDY VISCOSITY AND MELLOR-HERRING MODEL

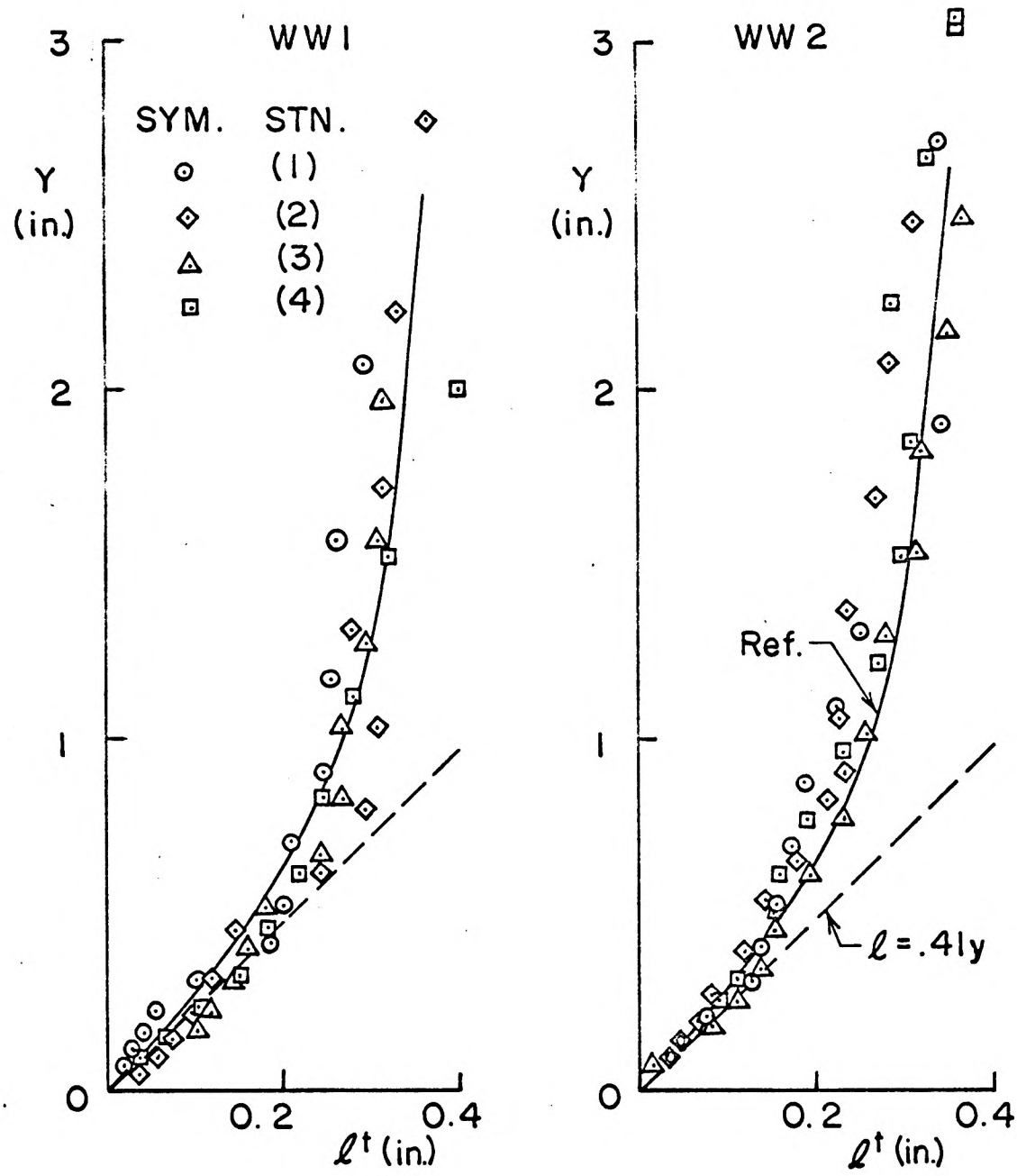

FIG.49 DISTRIBUTION OF MIXING LENGTH BASED ON TOTAL VELOCITY

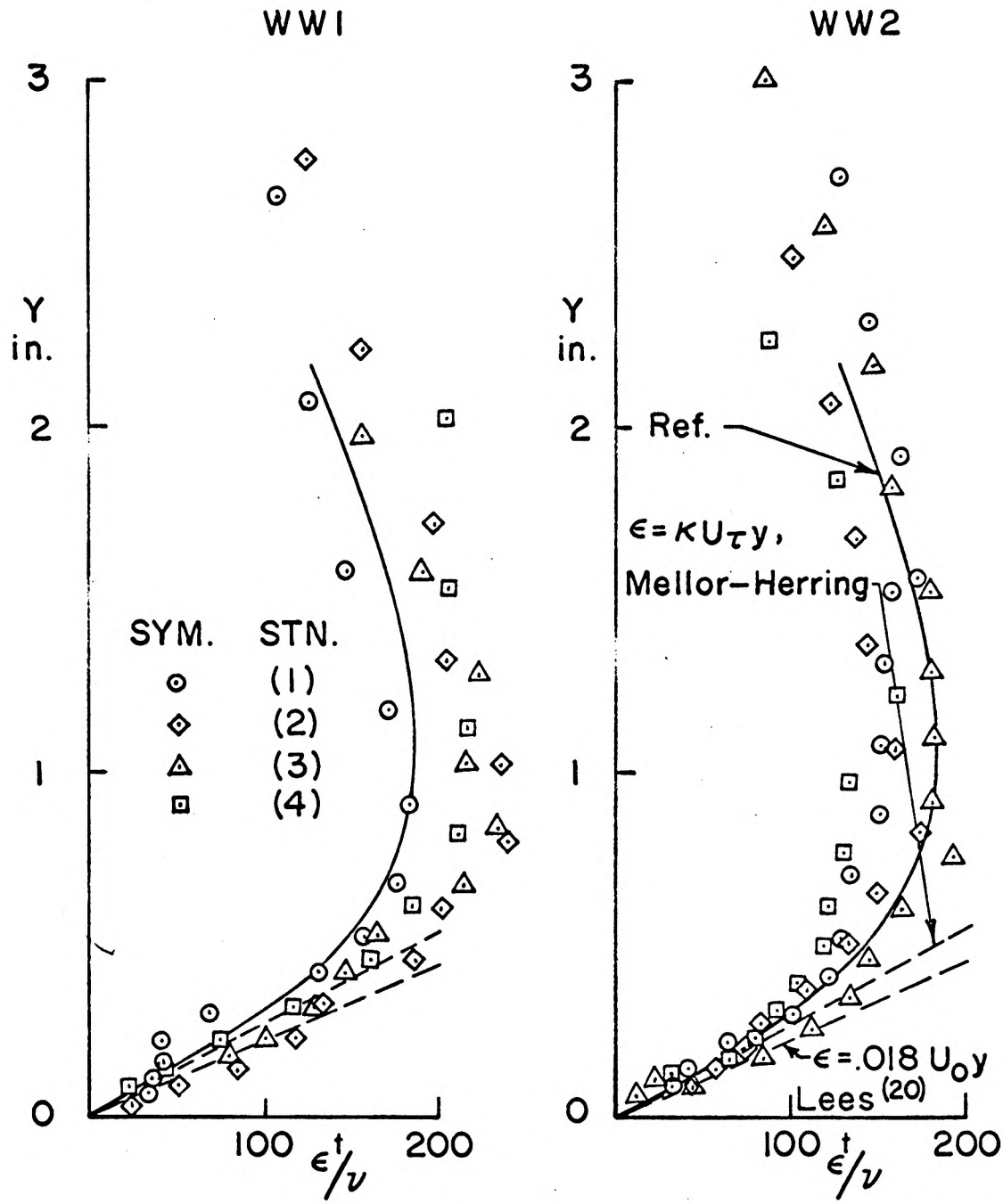

FIG. 50 DISTRIBUTION OF EDDY VISCOSITY BASED ON TOTAL VELOCITY

APPENDIX A

Calibration and Data Reduction of X-Array Hot-Wire Probes

A. 1. Measurement and Data Reduction

The schematic of the measurement of turbulent quantities was described in Figure (34). Within the range of linearity, the linearized outputs of the two sensors are related to the axial (u) and normal (v) velocity component by:

$$\left.\begin{aligned} E_1 &= Au + Bv \quad , \\ E_2 &= Cu - Dv \quad , \end{aligned}\right\} \quad \text{A-1}$$

where A, B, C and D are calibration constants, to be determined experimentally.

The D. C. components of the output are read from the meters belonging to the anemometers. They are related to the average velocity components by:

$$\left.\begin{aligned} \overline{E_1} &= A\bar{u} + B\bar{v} \quad , \\ \overline{E_2} &= C\bar{u} - D\bar{v} \quad . \end{aligned}\right\} \quad \text{A-2}$$

System A-2 can be solved for $\bar{u}$, $\bar{v}$.

Since we are interested in three turbulent quantities, $\overline{u'^2}$, $\overline{v'^2}$ and $\overline{u'v'}$, it is not sufficient to measure the R. M. S. outputs of the two sensors as was done for a single element probe. In order to gain another equation, the sum and difference of the two turbulent signals are generated by a random signal analyses and correlator.

By definition, the squared RMS values of the two output signals, their sum, and their difference are given by:

$$\left.\begin{aligned}
(E_1')^2 &= \overline{(A\tilde{u} + B\tilde{v})^2} \quad , \\
(E_2')^2 &= \overline{(C\tilde{u} - D\tilde{v})^2} \quad , \\
(E_s')^2 &= \overline{[(A+C)\tilde{u} + (B-D)\tilde{v}]^2} \quad , \\
(E_d')^2 &= \overline{[(A-C)\tilde{u} + (B+D)\tilde{v}]^2} \quad .
\end{aligned}\right\} \text{A-3}$$

By rearranging the right hand side of A-3 we find the redundant system:

$$\left.\begin{aligned}
(E_1')^2 &= A^2\,\overline{u'^2} + B^2\,\overline{v'^2} + 2AB\,\overline{u'v'} \quad , \\
(E_2')^2 &= C^2\,\overline{u'^2} + D^2\,\overline{v'^2} - 2CD\,\overline{u'v'} \quad , \\
(E_s')^2 &= (A+C)^2\,\overline{u'^2} + (B-D)^2\,\overline{v'^2} + 2(A+C)(B-D)\,\overline{u'v'} \quad , \\
(E_d')^2 &= (A-C)^2\,\overline{u'^2} + (B+D)^2\,\overline{v'^2} + 2(A+C)(B-D)\,\overline{u'v'} \quad .
\end{aligned}\right\} \text{A-4}$$

To eliminate one equation, we subtract the second equation from the first, and use the difference together with the third and the fourth equations. This yields a system that, for the ideal probe (A=B=C=D), has a diagonal form:

$$\left.\begin{aligned}
(E_s')^2 &= (A+C)^2\,\overline{u'^2} + (B-D)^2\,\overline{v'^2} + 2(A+C)(B-D)\,\overline{u'v'} \quad , \\
(E_d')^2 &= (A-C)^2\,\overline{u'^2} + (B-D)^2\,\overline{v'^2} + 2(A-C)(B+D)\,\overline{u'v'} \quad , \\
(E_1')^2 - (E_2')^2 &= (A-C)^2\,\overline{u'^2} + (B^2-D^2)\,\overline{v'^2} + 2(AB+CD)\,\overline{u'v'} \quad ,
\end{aligned}\right\} \text{A-5}$$

where E_1', E_2' and E_s', E_d' are measured and recorded by two R.M.S.

units that are connected to the output terminals of the random signal analyzer. Then system A-5 can be solved for the three turbulent quantities.

A.2. Calibration of X-Array Probes

If the probe is mounted at an angle ϑ to the axis of the test section, at its center, the axial and normal velocity components become:

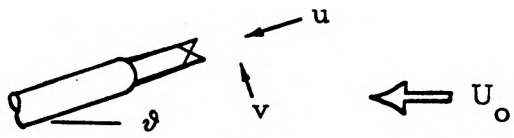

$$u = U_o \cos \vartheta$$

$$v = U_o \sin \vartheta$$

Substituting these values into equations A-1, the output voltages are related to U_o and ϑ by

$$E_1 = U_o(A \cos \vartheta + B \sin \vartheta) \quad ,$$

$$E_2 = U_o(C \cos \vartheta + D \sin \vartheta) \quad .$$

For several angles of incidence, within the range $\pm 30^\circ$, the velocity was changed using the speed control setting and the linearized hot wire output was recorded for the two channels. The results are shown in Figure (A1) for one of the probes used. The slopes of the calibration, μ_1 and μ_2, were measured, and are related to the calibration constants and the angle of incidence by;

$$\mu_1(\vartheta) = A \cos \vartheta + B \sin \vartheta \quad ,$$

$$\mu_2(\vartheta) = C \cos \vartheta - D \sin \vartheta \quad ,$$

which can be written as;

$$\frac{\mu_1(\vartheta)}{\cos\vartheta} = A + B \operatorname{tg}\vartheta \quad ,$$

$$\frac{\mu_2(\vartheta)}{\cos\vartheta} = C - D \operatorname{tg}\vartheta \quad .$$

To determine the constants, $\mu_1(\vartheta)/\cos\vartheta$ and $\mu_2(\vartheta)/\cos\vartheta$ were plotted vs. tg ϑ in Figure (A2). The intersection of the curves with the axis $\vartheta = 0$, and their slopes, yield the desired constants. Also, the range of linearity can be found from the curves in Figure (A2).

The results are:

Probe	X-1	X-S
A	0.402	0.462
B	0.556	0.475
C	0.399	0.457
D	0.423	0.490
Limit of Linearity upper	$+23^o$	$+23^o$
Limit of Linearity lower	-23^o	-20^o

Another factor to be considered when using X-Array probes at large inclination angles is the noise produced by vortices, shedding from its prongs. To evaluate this factor, the turbulence output from the two sensors was recorded for the maximum speed used during the calibration. The results are shown in Figure (A3), from which it is seen that within the range of linearity, this noise is admissible.

A. 3. Transformation of Coordinates

The Analysis given in the previous two sections was done in coordinate system attached to the probe. Actually, the probe was aligned with its prongs only approximately parallel to the local slope of the wall. Therefore transformation of coordinates is needed for consistent presentation of the data. For rotation of coordinates, we have

$$u^{*} = u\cos\alpha + v\sin\alpha \quad ,$$

$$v^{*} = -u\sin\alpha + v\cos\alpha \quad .$$

Using these relations one finds:

$$\overline{u^{*,2}} = \overline{u'^{2}}\cos^{2}\alpha + \overline{v'^{2}}\sin^{2}\alpha + \overline{u'v'}\sin 2\alpha$$

$$\overline{v^{*,2}} = \overline{u'^{2}}\sin^{2}\alpha + \overline{v'^{2}}\cos^{2}\alpha + \overline{u'v'}\sin 2\alpha$$

$$\overline{u^{*}v^{*}} = \overline{u'v'}\cos 2\alpha + \tfrac{1}{2}\left(\overline{u'^{2}} - \overline{v'^{2}}\right)\sin 2\alpha \quad .$$

The data presented below is given in free stream coordinates.

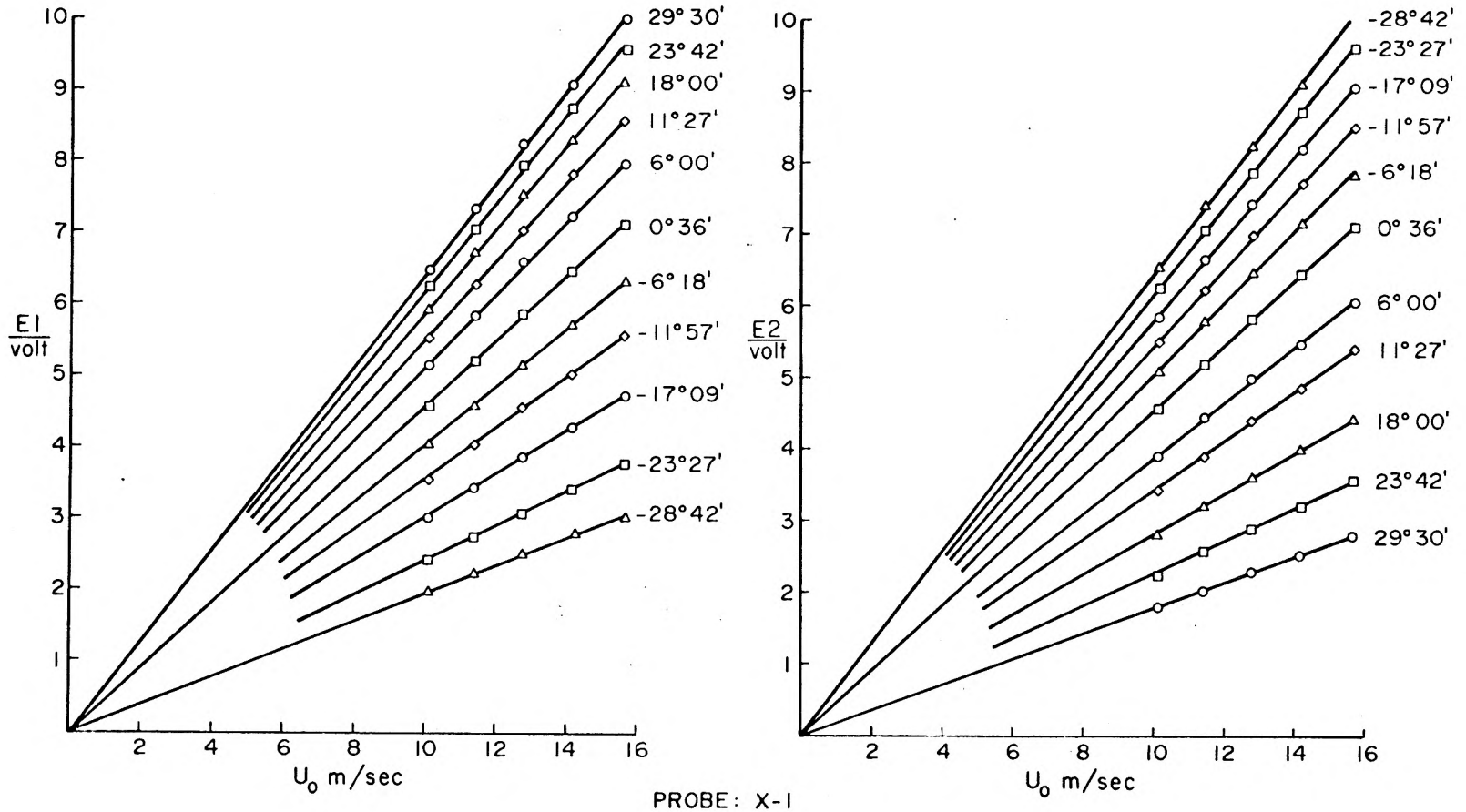

PROBE: X-1

Fig. A 1 CALIBRATION OF X-PROBE-DEPENDANCE OF OUTPUT UPON VELOCITY

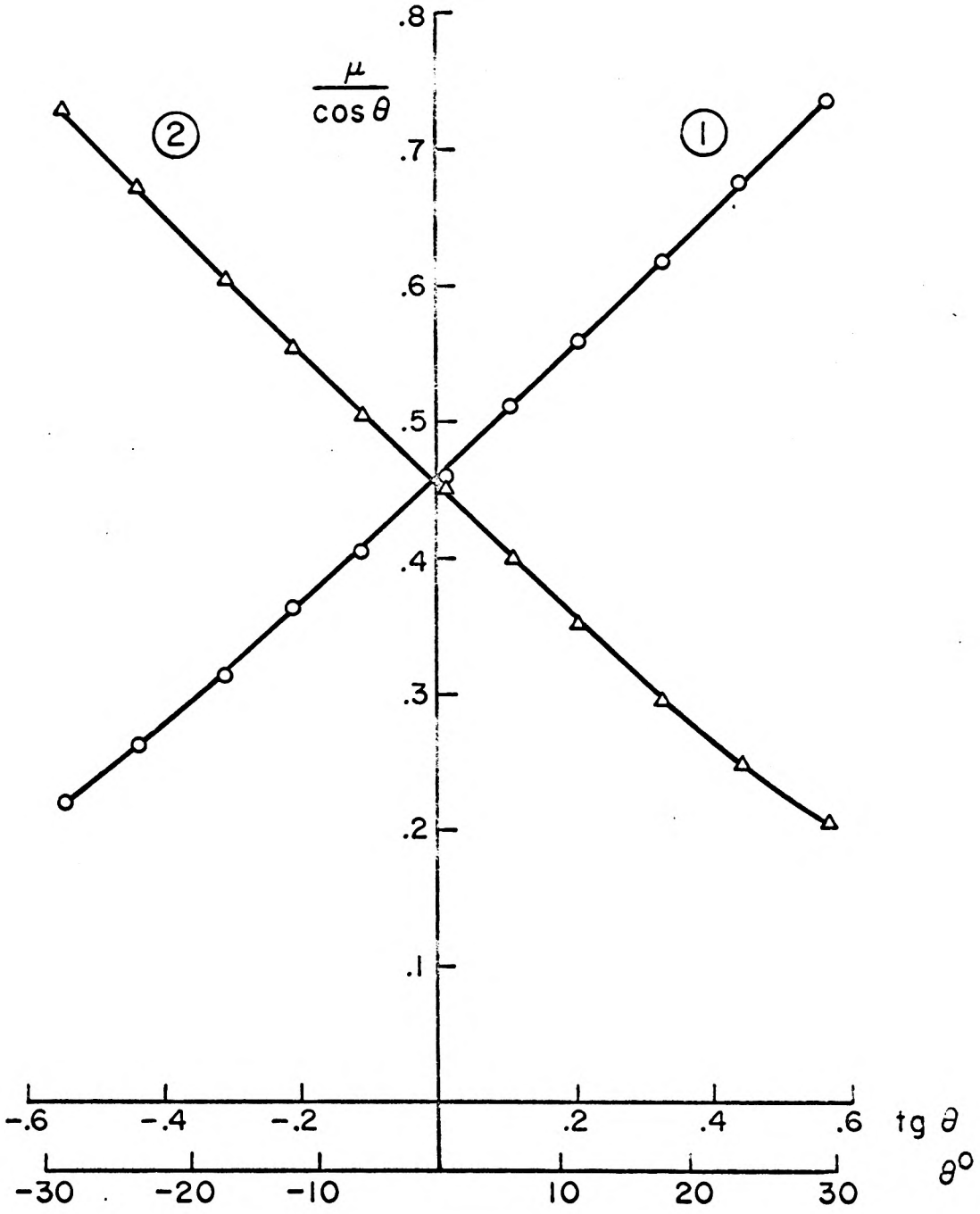

PROBE : X - 1

Fig.A2 CALIBRATION OF X-PROBE-
DEPENDANCE OF OUTPUT UPON ANGLE

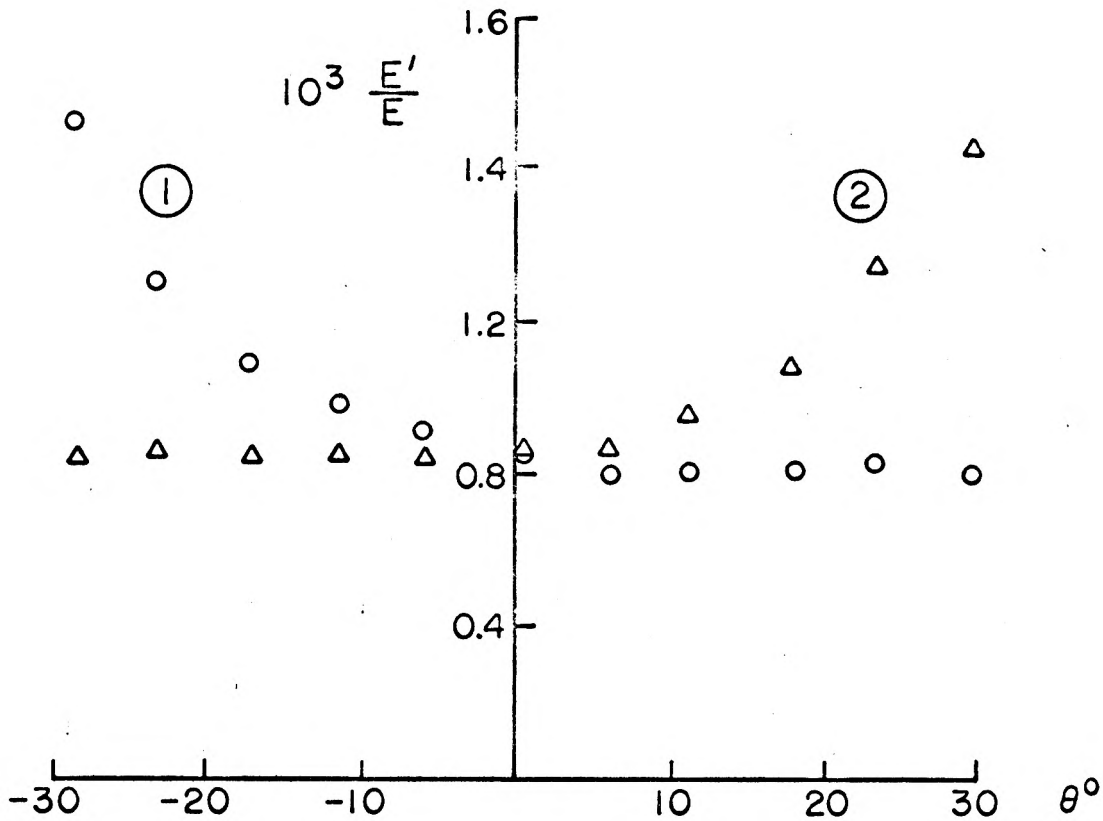

PROBE: X-1

Fig.A3 CALIBRATION OF X-PROBE-NOISE DUE TO PRONG INTERFERANCE

APPENDIX B

Curvature Effect on Mixing Length

Sawyer's[5] theory of the effect of curvature on the mixing length was used in Section IV. 6. for the evaluation of the mixing length distribution. In the present appendix, the principle of this theory is recalled and the results of the application of the theory to curved channel flow are presented, because of the resemblance of this flow to the boundary layer flow through their mutual dependence on the Law of the Wake.

According to mixing length theory, the turbulent mixing process is characterized by the speed U' and the length ℓ. In curved flow, the fluid experiences a deceleration U'^2/ℓ which is of order $\ell(\partial\overline{U}/\partial y)^2$ and a centrifugal acceleration $[U(y-\ell)^2 - U(y)^2]/R = -2\ell\,\overline{U}(\partial\overline{U}/\partial y)/R$. Hence, the ratio of the mixing length for a flow with curvature to that of a similar flow without curvature is given by

$$\frac{\ell}{\ell_s} = 1 - \frac{k}{2}\,\frac{U/R}{\partial\overline{U}/\partial y} \quad ,$$

where k is a constant to be determined experimentally. The turbulent shear, expressed in terms of zero curvature mixing length is

$$\frac{\tau}{\rho} = \ell_s^2\,\frac{\partial\overline{U}}{\partial y}\left(\frac{\partial U}{\partial y} - k\,\frac{U}{R}\right) \quad .$$

Sawyer used this expression to analyze two types of turbulent flows. For the first, a reattaching curved jet,[5] he found that k = 5 gave best agreement between experiment and theory. For the second flow, a wall jet,[21] k = 3 gave the best results.

In the present study, the results of the measurements of the mixing length distributions obtained by Watendorf[3] and Eskinazi,[4] in the fully developed portion of a curved channel were reduced to those of a straight channel by using the above expression with different values of k.

The results are summarized below for the two listed flows

Reference	Watendorf	Eskinazi
width of channel	5 cm	5"
inner radius	20 cm	25"
average speed	27 m/sec.	30 m/sec.
turbulent shear	computed based on measured wall shear	measured by cross-wire probe
k for best fit	7	15

The results are shown in Figures (B1, B2). It is found that the theory predicts the mixing length distribution in both cases but with different values of the parameter k. Since only two cases were analyzed, no conclusions can be drawn about the range of the parameter k or about the factors affecting it. However, as mentioned in Section IV. 6., it was found that in the present experiment the curvature effect is not large and therefore the knowledge of the parameter k is not critical.

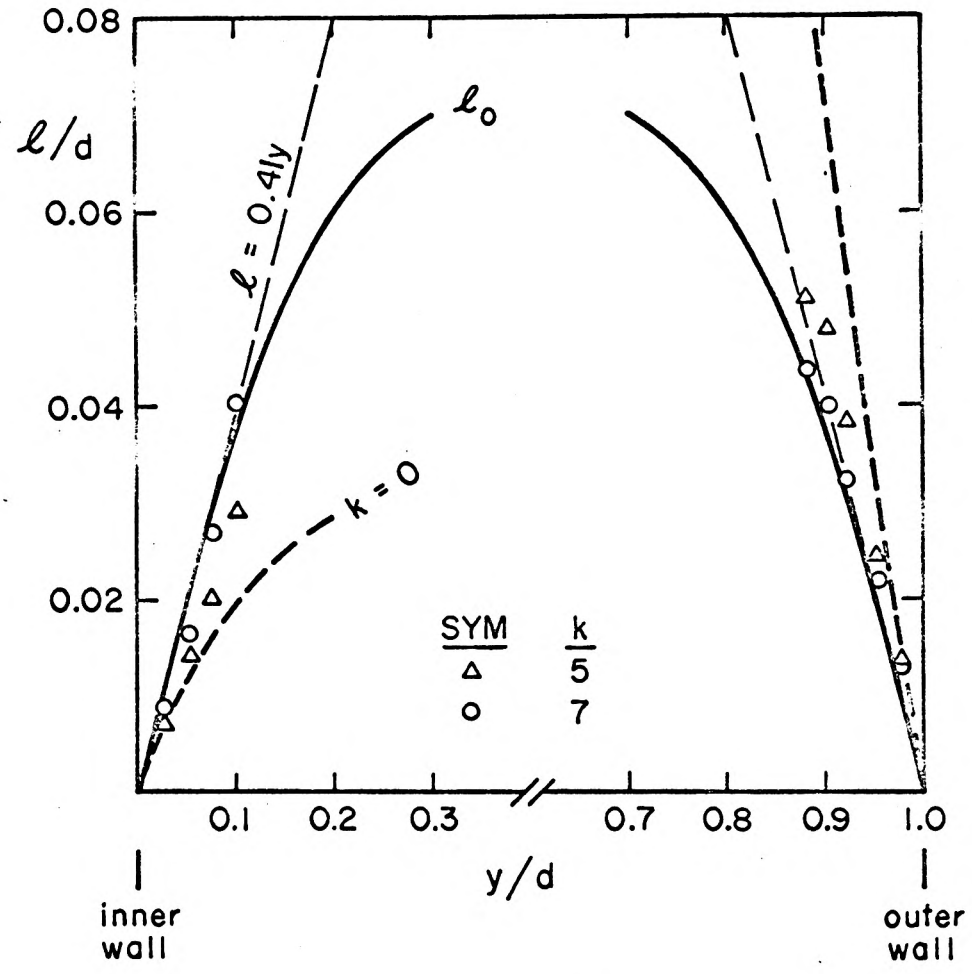

REF: WATTENDORF (3)

Fig. B1a ANALYSIS OF CURVED CHANNEL MIXING LENGTH DISTRIBUTION USING SAWYER'S THEORY

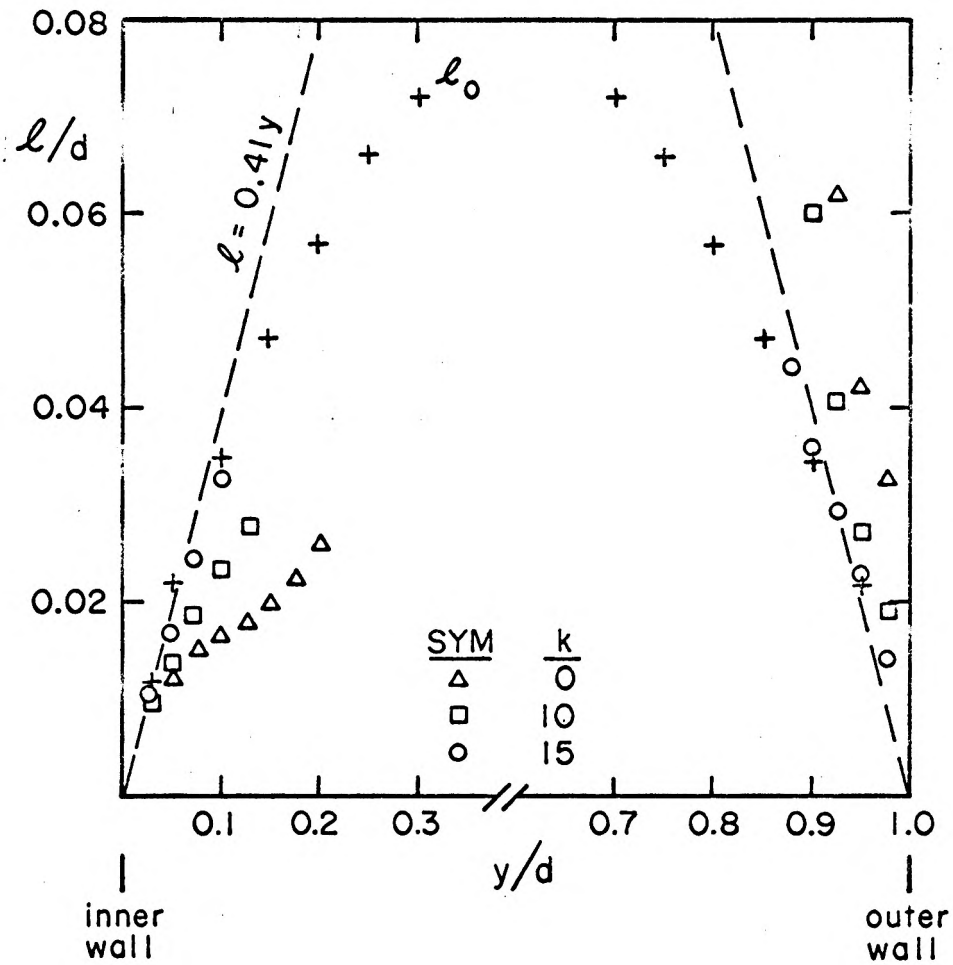

REF. ESKINASI [4]

Fig.B1b ANALYSIS OF CURVED CHANNEL MIXING LENGTH DISTRIBUTION USING SAWYER'S THEORY

APPENDIX C

Inviscid, Small Perturbation Analysis of Non-Uniform Flow Over a Wavy Wall

The results of the analysis of total pressure distribution (Section V.3), show that the flow outside the wall layer can be considered inviscid. This conclusion motivated the present analysis of the outer layer as inviscid, but non-uniform flow over a wavy surface. By its nature this analysis will not predict wall shear.

The basic equations of motion are expressed in a cartesian coordinate system, with the x-axis taken along the centers of the surface waves:

$$u \frac{\partial u}{\partial x} + v \frac{\partial u}{\partial y} = - \frac{1}{\rho} \frac{\partial p}{\partial x} \quad ,$$

$$u \frac{\partial v}{\partial x} + v \frac{\partial v}{\partial y} = - \frac{1}{\rho} \frac{\partial p}{\partial y} \quad ,$$

$$\frac{\partial u}{\partial x} + \frac{\partial v}{\partial y} = 0 \quad .$$

Let the wall surface be given by

$$y_s = a \sin(\alpha x) \quad , \qquad \text{with} \quad \alpha = 2\pi/\lambda \quad ,$$

so that the slope is

$$\frac{dy_s}{dx} = \epsilon \cos(\alpha x) \quad , \qquad \text{with} \quad \epsilon = 2\pi a/\lambda \quad .$$

We seek asymptotic solution for small ϵ in the form

$$u = u_o + \epsilon u_1 + \ldots . \quad ,$$

$$v = v_o + \epsilon v_1 + \ldots . \quad ,$$

$$p = p_o + \epsilon p_1 + \ldots . \quad .$$

The boundary conditions are

$$v_1(x, 0) = U_o \cos(\alpha x) \quad ,$$

$$v_o(x, 0) = v_2(x, 0) = \ldots = 0 \quad ,$$

where U_o is the unperturbed velocity away from the wall.

Substituting the series expansion into the system of equations, and collecting terms of like power in ϵ, the resulting 0^{th} order system takes the form:

$$u_o \frac{\partial u_o}{\partial x} + v_o \frac{\partial u_o}{\partial y} = - \frac{1}{\rho} \frac{\partial p_o}{\partial x} \quad ,$$

$$u_o \frac{\partial v_o}{\partial x} + v_o \frac{\partial v_o}{\partial y} = - \frac{1}{\rho} \frac{\partial p_o}{\partial y} \quad ,$$

$$\frac{\partial u_o}{\partial x} + \frac{\partial v_o}{\partial y} = 0 \quad .$$

Mathematically, any parallel flow, $u_o(y)$, will satisfy this system. But, in order to model for the physical situation, Coles' Law of the Wake will be used for these computations:

$$u_o(y) = u_\tau \left[C + \frac{1}{\kappa} \ell n \left(\frac{y\, u_\tau}{\nu} \right) + \frac{2\Pi}{\kappa} \sin^2 \left(\frac{\pi}{2} \frac{y}{\delta} \right) \right] \quad .$$

This law applies outside the viscous layer, that is for $y\, u_\tau / \nu > 70$. It cannot be extended to $y = 0$ because of the logarithmic singularity, and hence it will be assumed that u_o = constant for $y < y_w$, where the value of y_w will be discussed below in connection with the actual computations.

The complete first order system is:

$$u_o \frac{\partial u_1}{\partial x} + \frac{\partial u_o}{\partial x} u_1 + v_o \frac{\partial u_1}{\partial y} + \frac{\partial u_o}{\partial y} v_1 = - \frac{1}{\rho} \frac{\partial p_1}{\partial x} \quad ,$$

$$u_o \frac{\partial v_1}{\partial x} + \frac{\partial u_o}{\partial x} v_1 + v_o \frac{\partial u_1}{\partial y} + \frac{\partial v_o}{\partial y} v_1 = - \frac{1}{\rho} \frac{\partial p_1}{\partial y} \quad ,$$

$$\frac{\partial u_1}{\partial x} + \frac{\partial u_1}{\partial y} = 0 \quad .$$

Since $v_o = 0$, $p_o = 0$, and $\partial u_o / \partial x = 0$, this system takes the form;

$$u_o \frac{\partial u_1}{\partial x} + \frac{\partial u_o}{\partial y} v_1 = - \frac{1}{\rho} \frac{\partial p_1}{\partial x} \quad ,$$

$$u_o \frac{\partial v_1}{\partial x} = - \frac{1}{\rho} \frac{\partial p_1}{\partial y} \quad ,$$

$$\frac{\partial u_1}{\partial x} + \frac{\partial v_1}{\partial y} = 0 \quad .$$

Because of the boundary condition on $v_1(x, 0)$, the solution is expected to take the following form;

$$u_1 = \hat{u}(y) \sin(\alpha x) \quad ,$$

$$v_1 = \hat{v}(y) \cos(\alpha x) \quad ,$$

$$p_1/\rho = \hat{p}(y) \sin(\alpha x) \quad .$$

The resulting system is then

$$\alpha u_o \hat{u} + \frac{du_o}{dy} \hat{v} = - \alpha \hat{p} \quad ,$$

$$- \alpha u_o \hat{v} = - \hat{p}' \quad ,$$

$$\alpha \hat{u} + \hat{v}' = 0 \quad .$$

By algebraic manipulations, $\hat{v}$ can be isolated from the system giving

$$\hat{v}'' - \left(\frac{u_o''}{u_o} + \alpha^2\right)\hat{v} = 0,$$

with the boundary condition

$$\hat{v}(0) = U_o \quad .$$

The other two unknown functions, $\hat{p}$ and $\hat{u}$, are related to $\hat{v}$ by integration and differentiation respectively.

The differential equation for $\hat{v}$ does not have a simple solution. It can either be integrated numerically or solved by perturbation techniques. The latter technique is selected because it shows in an analytical form the importance of the functions and constants involved.

The asymptotic solution of the differential equation for $\hat{v}$ is based on the fact that in the outer layer $u_o''/u_o << \alpha^2$. To demonstrate this fact the unperturbed profile, u_o, is rewritten in terms of the velocity defect, giving

$$u_o = U_o - u_\tau\left[\frac{1}{\kappa}\ell n\left(\frac{y}{\delta}\right) + \frac{2\Pi}{\kappa}\cos^2\left(\frac{\pi}{2}\frac{y}{\delta}\right)\right] \quad .$$

The friction velocity u_τ is small compared with U_o. Therefore, the smallness parameter for the present expansion is chosen to be

$$\mu = u_\tau/U_o \quad .$$

For the outer layer, the ratio u_o''/u_o becomes

$$\frac{u_o''}{u_o} = \frac{\mu\left[-\frac{1}{\kappa y^2} + \frac{\pi^2 \overline{\pi}}{\kappa \delta^2} \cos\left(\pi \frac{y}{\delta}\right)\right]}{1 - \mu\left[\frac{1}{\kappa} \ell n\left(\frac{y}{\delta}\right) + \frac{2\overline{\pi}}{\kappa} \cos^2\left(\frac{\pi}{2} \frac{y}{\delta}\right)\right]} \quad .$$

Hence, to $0(\mu)$, $u_o''/u_o = u_o''/U_o$.

Therefore, we seek a solution for $\hat{v}$ of the form

$$\hat{v} = \overline{v}_o + \mu \overline{v}_1 + \ldots \quad .$$

The 0^{th} order solution is obtained for $\mu = 0$. This case corresponds to $u_o = U_o$, that is uniform, unperturbed flow. The associated equation is

$$\overline{v}_o'' - \alpha^2 \overline{v}_o = 0 \quad ,$$

which yields the solution

$$\overline{v}_o = U_o e^{-\alpha y} \quad .$$

This is exactly the result obtained by linearized potential theory.[8]

The differential equation for $\overline{v}_1$ is

$$\overline{v}_1'' - \alpha^2 \overline{v}_1 = \overline{v}_o \frac{u_o''}{u_\tau}$$

$$= \frac{1}{\mu} e^{-\alpha y} u_o'' \quad .$$

Using the method of variation of parameters, the solution of this equation is

$$2 \alpha \mu v_1 = -(u_o' + C_o)e^{-\alpha y} + e^{\alpha y} \int_{y_o}^{y} e^{-2d\eta} u_o''(\eta) d\eta \quad .$$

The boundary conditions on $\bar{v}_1$,

$$\bar{v}_1(0) = 0$$

and $$\bar{v}_1(y \to \infty) = 0 \quad ,$$

are used to evaluate the constants of integration, C_o and y_o. The results are

$$y_o = y_w$$

and

$$C_o = - \int_{y_w}^{\delta} e^{-2\alpha\eta} \, u_o''(\eta) d\eta \quad .$$

The solution for $\hat{v}$ (to order $\epsilon\mu$) is

$$\hat{v} = U_o e^{-\alpha y} - \frac{1}{2\alpha} e^{-\alpha y} (u_o' + C_o) + \frac{1}{2\alpha} e^{\alpha y} \int_{\sigma}^{y} e^{-2\alpha\eta} \, u_o''(\eta) d\eta \quad .$$

The streamwise component of the velocity is evaluated from the equations

$$\hat{u} = - \frac{1}{\alpha} \hat{v}' \quad ,$$

$$u_1 = \hat{u} \cos(\alpha x) \quad ,$$

yielding the result

$$u_1 = \left\{ U_o e^{-\alpha y} - \frac{1}{2\alpha} e^{-\alpha y} (u_o' + C_o) - \frac{1}{2\alpha} e^{\alpha y} \int_{\sigma}^{y} e^{-2\alpha\eta} \, u_o''(\eta) \, d\eta \right\} \cos(\alpha x) \, .$$

This result is used to evaluate the wall pressure, by using the linearized pressure coefficient

$$Cp_w = -2 \frac{u(o)}{U_o} \quad .$$

The velocity perturbation for $y \to 0$ is given by

$$u_1(0) = \left(U_o - \frac{C_o}{\alpha}\right) \cos(\alpha x) \quad , \quad \text{and}$$

the associated wall pressure coefficient ($\epsilon = 2\pi a/\lambda$) becomes

$$Cp_w = 4\pi \frac{a}{\lambda} \left(1 - \frac{C_o}{U_o \alpha}\right) \cos(\alpha x) \quad .$$

The integrals in the above expression for u_1 were evaluated numerically, for values of y_w ranging from 0.1" up to 0.4". It was found that, for $y_w < 0.15"$, the results were out of the expected range. The reason is that for these low values of y_w, u_o'' reaches very large values, thus violating the assumption of small a perturbation. Results of the computations, together with the measured velocity profiles at STN (2) and (4) are presented in Figure (C1), for the two models. The main observations are summarized below:

(i) For WW1, the first approximation for u_1, with $y_w = 0.2"$, is about 65% of the 0^{th} approximation. For increasing y_w, the difference between the two approximations diminishes. Agreement with measurements is good at the two stations for $y > 0.3"$.

(ii) For WW2, the differences between the 0^{th} and 1st approximations are very small for $y_w > 0.2"$. The agreement with the experimental data is very good for $y > 0.25"$.

Finally, the wall pressure coefficient was evaluated using the values of C_o discussed above. The results are summarized below and compared with the measured values of Section IV.1.

Model	Cp_w (analysis)			Cp_w (meas.)
	$C_o = 0$	$y_w = 0.2''$	$y_w = 0.3''$	
WW1	0.350	.140	.234	+0.175 -0.255
WW2	0.328	.256	.292	+0.155 -0.195

It must be noted here that the present analysis predicts a sinusoidal distribution of wall pressure, while the measurements (Section IV. 1.) show deviations from sinusoidal distribution. Also note that the analysis predicts the wall pressure much better than the linearized uniform flow theory ($C_o = 0$).

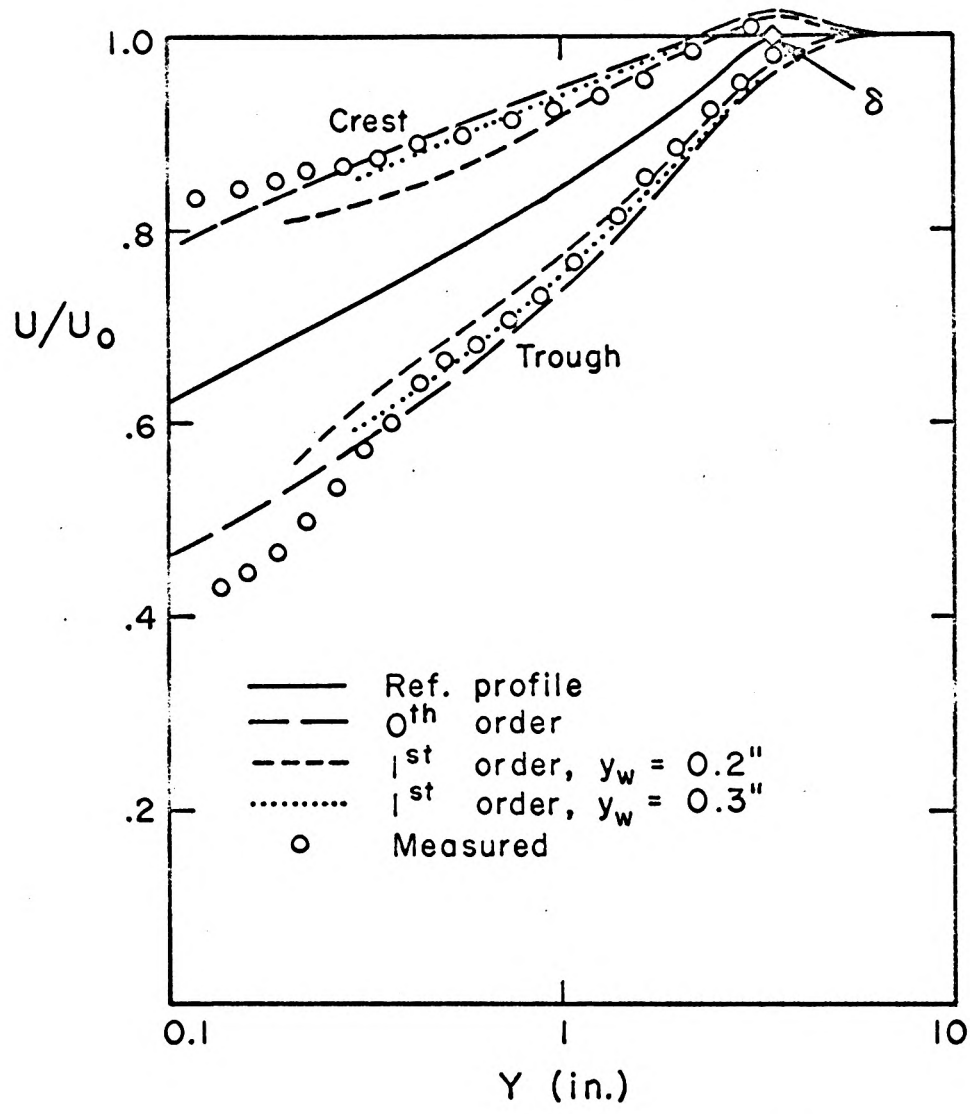

WW I

Fig.C1a COMPARISON BETWEEN INVISCID, SMALL PERTURBATION ANALYSIS OF THE OUTER LAYER AND MEASUREMENT

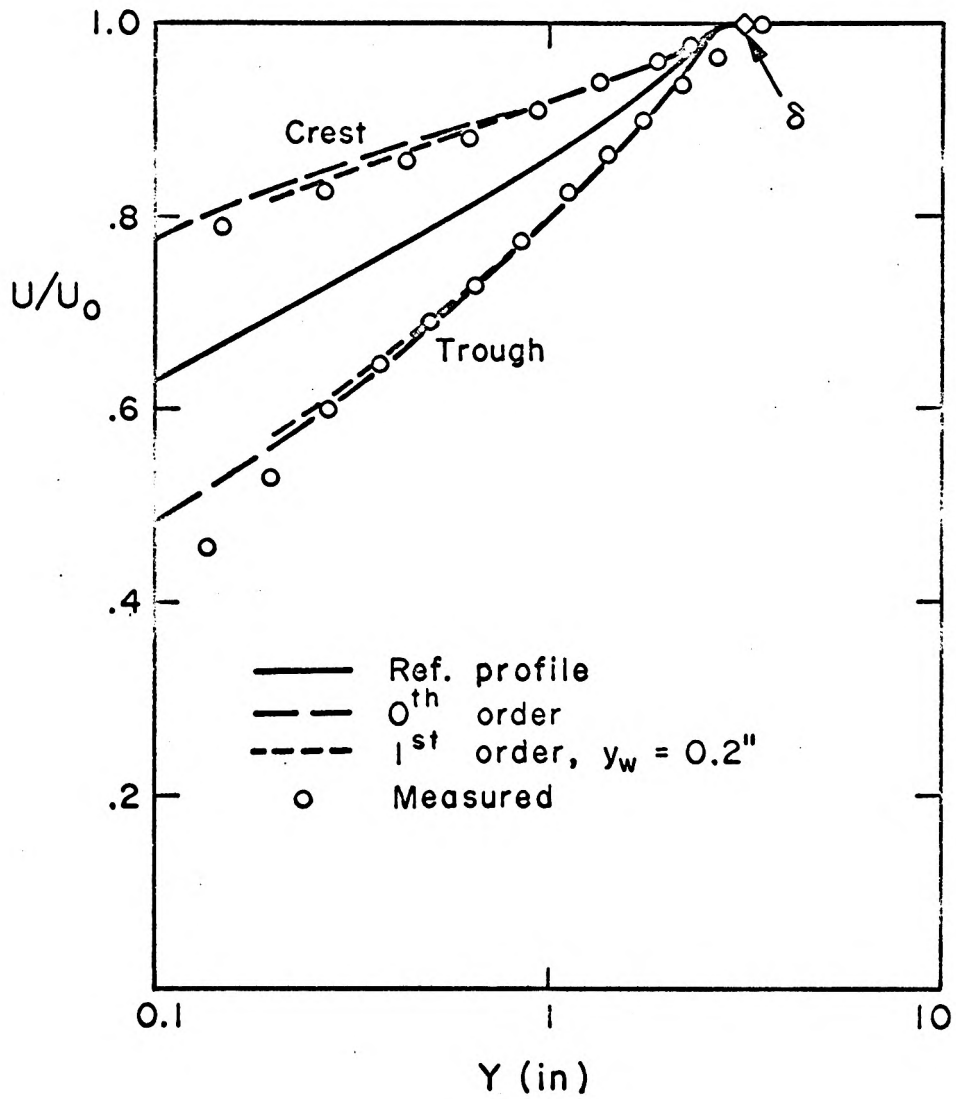

WW2

Fig.C1b COMPARISON BETWEEN INVISCID, SMALL PERTURBATION ANALYSIS OF THE OUTER LAYER AND MEASUREMENT

APPENDIX D

Analysis of the Wall Layer

In Section V. 6. a qualitative description of the wall layer was given by relating it to the Rayleigh problem. Here, a more rigorous analysis is presented, in order to demonstrate the controlling factors. The present analysis, unlike that of Appendix C must include viscosity.

The analysis will be performed in orthogonal curvilinear coordinate system whose x-axis is in the direction of the wall and the y-axis being perpendicular to it. The basic equations of motion, simplified to the boundary layer approximation (cf. chapter VII of [18] and Chapter 3 of [22] are:

$$u\frac{\partial u}{\partial x} + v\frac{\partial u}{\partial y} + \frac{uv}{R} = -\frac{1}{\rho}\frac{\partial \rho}{\partial x} + \nu\frac{\partial^2 u}{\partial y^2} + \frac{1}{\rho}\frac{\partial \tau}{\partial y} + \frac{2}{\rho}\frac{\tau}{R} \quad ,$$

$$\frac{u^2}{R} = -\frac{1}{\rho}\frac{\partial \rho}{\partial y} \quad ,$$

$$\frac{\partial u}{\partial x} + \frac{\partial v}{\partial y} + \frac{v}{R} = 0$$

with $\tau = \rho(\overline{u'v'})$ being the Reynolds shear stress.

The boundary conditions at the wall are

$$u(x, 0) = 0 \quad ,$$

$$v(x, 0) = 0 \quad .$$

For a surface given by

$$y_s = a \sin(\alpha x) \quad , \qquad \text{with} \quad \alpha = 2\pi/\lambda \quad ,$$

the radius of curvature is given approximately by

$$R(x) = 1/y_s''(x) \quad ,$$

so that

$$1/R(x) = -\varepsilon\,\alpha \sin(\alpha x) \quad , \qquad \text{with} \quad \varepsilon = 2\pi\, a/\lambda \quad .$$

As in Appendix C, we seek a solution for small ε in the form

$$u = u_o + \varepsilon\, u_1 + \ldots . \quad ,$$

$$v = v_o + \varepsilon\, v_1 + \ldots . \quad ,$$

$$p = p_o + \varepsilon\, p_1 + \ldots . \quad ,$$

$$\tau = \tau_o + \varepsilon\, \tau_1 + \ldots . \quad .$$

Substituting the series expansion into the system of equation and collecting terms of like powers in ε, one finds the following O^{th} order system:

$$u_o \frac{\partial u_o}{\partial x} + v_o \frac{\partial u_o}{\partial y} = -\frac{1}{\rho}\frac{\partial p_o}{\partial x} + \nu \frac{\partial^2 u_o}{\partial y^2} + \frac{1}{\rho}\frac{\partial \tau_o}{\partial y} \quad ,$$

$$\frac{\partial p_o}{\partial y} = 0 \quad ,$$

$$\frac{\partial u_o}{\partial x_o} + \frac{\partial v_o}{\partial y} = 0 \quad ,$$

which describes the development of the turbulent boundary layer on a flat plate. This system will not be solved in the usual way with an additional relation for the dependence of τ_o upon flow conditions. Instead, a standard presentation of flat plate boundary layer with Coles' Law of the Wake as outer part will be used.

The 1st order system for $v_o = 0$, $p_o = 0$ and $\partial u_o/\partial x = 0$ becomes:

$$u_o \frac{\partial u_1}{\partial x} + \frac{\partial u_o}{\partial y} v_1 = - \frac{1}{\rho} \frac{\partial p_1}{\partial x} + \nu \frac{\partial^2 u_1}{\partial y^2} + \frac{1}{\rho} \frac{\partial \tau_1}{\partial y} + \frac{2\alpha}{\rho} \tau_o \sin(\alpha x),$$

$$\alpha u_o^2 \sin(\alpha x) = - \frac{1}{\rho} \frac{\partial p_1}{\partial y} ,$$

$$\frac{\partial u_1}{\partial x} + \frac{\partial v_1}{\partial y} = 0 .$$

Further simplification of the x-momentum equation can be obtained if the analysis is restricted to a thin wall layer in which viscous terms are important. The thickness, δ_w, of such layer can be evaluated by order of magnitude analysis of the leading convective and viscous terms in the x-momentum equation. To do so, the eddy viscosity models of Mellor-Herring[1] will be used.

$$U_\infty \frac{u_1}{\lambda} \sim \epsilon \frac{u_1}{\delta w^2} , \quad \text{so that}$$

$$\delta_w^2 \sim \frac{\lambda \epsilon}{U_\infty} .$$

For the outer model:

$$\epsilon = K_2 U_\infty \delta^* \quad \text{with } K_2 = 0.016 ,$$

$$\delta_w \sim (\lambda \delta^*)^{\frac{1}{2}} .$$

For the inner model:

$$\epsilon = \kappa u_\tau y ,$$

$$\delta_w \sim \frac{u_\tau}{U_\infty} \lambda .$$

Both models show that for the actual cases $\delta_w/\delta < 1$.

From the continuity equation, the normal velocity v_1 at the edge of this layer, is of order

$$v_1 \sim U_\infty \delta_w/\lambda \quad .$$

Comparison of the order of magnitude of the two convective terms shows

$$u_o \frac{\partial u_1}{\partial x} \sim U_\infty \frac{U_1}{\lambda} \quad ,$$

$$\frac{\partial u_o}{\partial y} v_1 \sim \frac{U_\infty}{\delta} \frac{U_1 \delta_w}{\lambda} \quad ,$$

that is the first term is the dominant.

Also, comparison of the two contributions of the turbulent shear stresses, on the right hand side of the equation gives

$$\frac{\partial \tau_1}{\partial y} \sim \frac{\tau_1}{\delta_w} \quad ,$$

$$\alpha \tau_o \sim \frac{\tau_o}{\lambda} \quad ,$$

which shows that the first term dominates.

Then, the simplified x-momentum equation takes the form

$$u_o \frac{\partial u_1}{\partial x} = -\frac{1}{\rho} \frac{\partial p_1}{\partial x} + \nu \frac{\partial^2 u_1}{\partial y^2} + \frac{1}{\rho} \frac{\partial \tau_1}{\partial y} \quad .$$

In order to find out about the nature of the solution, a model equation has been devised by Kubota. The following further approximations are introduced in order to derive an equation that can be treated analytically.

(i) The molecular viscosity is ignored.

(ii) The unperturbed velocity u_o in the convective term is replaced by U_∞ (Oseen approximation).

To this approximation, the pressure is constant across the wall layer. Hence

$$\frac{1}{\rho}\frac{\partial p}{\partial x} = \frac{1}{2} U_\infty^2 \frac{d\, Cp_w}{dx}$$

$$= \frac{1}{2} U_\infty P \alpha \sin(\alpha x) \quad ,$$

where P is the amplitude of Cp_w.

Using eddy viscosity model for the turbulent shear stress, the model equation becomes:

$$U_\infty \frac{\partial u_1}{\partial x} = \frac{1}{2} U_\infty^2 P \alpha \sin(\alpha x) + \frac{\partial}{\partial y} \left(\epsilon \frac{\partial u_1}{\partial y}\right) \quad .$$

First, the outer eddy viscosity will be used. The model equation takes the linear form

$$\frac{\partial u_1}{\partial x} = \frac{1}{2} U_\infty P \alpha \sin(\alpha x) + K_2 \delta^* \frac{\partial^2 u_1}{\partial y^2} \quad .$$

If we seek a solution of the form

$$u_1 = \hat{u}\, e^{i\alpha x} \quad ,$$

the equation becomes

$$i\alpha \hat{u} = \frac{i}{2} U_\infty P \alpha + K_2 \delta^* \hat{u}'' \quad .$$

A particular solution is given by

$$\hat{u}_p = \frac{1}{2} \overline{U}_\infty P \quad ,$$

so that the equation for the complementary solution is

$$\hat{u}_c'' = \frac{i\alpha}{K_2 \delta^*} \hat{u}_c = 0 \quad ,$$

with the solution

$$\hat{u}_c = A \exp\left(- \frac{1+i}{\sqrt{2}} \frac{y}{H} \right)$$

with $H = (K_2 \lambda \delta^* / 2\pi)^{\frac{1}{2}}$, which is the same wave length as given in Section V. 6. by direct analogy with the Rayleigh problem.
Note that this solution is oscillatory with an exponentially decaying amplitude.

Next, using the inner model for eddy viscosity, the model equation becomes

$$i\alpha U_\infty \hat{u} = -\frac{i}{2} U_\infty^2 P \alpha + \kappa u_\tau \frac{d}{dy}\left(y \frac{d\hat{u}}{dy}\right) \quad .$$

A particular solution exists as before, and the equation for the complementary solution is

$$\frac{d}{dy}\left(y \frac{d\hat{u}_c}{dy}\right) - i \frac{\alpha U_\infty}{\kappa u_\tau} \hat{u}_c = 0 \quad .$$

This equation can be reduced to Kelvin's equation (Section 9. 9. of [23]) by the transformation

$$\eta = 2 \left(\frac{\alpha U_\infty}{\kappa u_\tau} y\right)^{\frac{1}{2}} \quad ,$$

giving the equation

$$\eta^2 \frac{d^2 \hat{u}_c}{d\eta^2} + \eta \frac{d\hat{u}}{d\eta} - i\eta^2 \hat{u}_c = 0 \quad ,$$

whose bounded solution as $\eta \to \infty$ is

$$\hat{u}_c = A(\ker(\eta) + i\,\mathrm{kei}(\eta)) \quad .$$

Then, the complete solution is:

$$u_1 = -\frac{1}{2} U_\infty P \cos(\alpha x) + A(\ker(\eta).\cos(\alpha x) - \mathrm{kei}(\eta)\sin(\alpha x)) \quad .$$

Note that the asymptotic behavior of $\hat{u}_c$ (Section 9.11. of [23]), for large values of η is

$$\hat{u}_c \sim A\left(\frac{\pi}{2\eta}\right)^{\frac{1}{2}} \exp\left(-\frac{1+i}{\sqrt{2}}\eta - \frac{\pi}{8}\right) \quad .$$

As before, this solution is oscillatory, with decaying amplitude. However, as was shown in the evaluation of the thickness of the wall layer, the present wave length is different from the one based on the outer model and is given by $H = \kappa u_\tau \lambda / 8\pi U_\infty$.

The function $\ker(\eta)$ is singular at $\eta = 0$, which predicts unbounded $\hat{u}_c$ near the wall. This is a result of ignoring the kinematic viscosity which is important in the sublayer. Although it can be shown that the shear stress distribution near the wall is bounded, the accuracy is not expected to be satisfactory.

REFERENCES

1. Kline, S. J. et. al. (ed.): "Computation of Turbulent Boundary Layers - 1968, δ Proceedings, AFOSR-IFP - Stanford Conference, Published by Dept. of Mech. Eng., Stanford University, 1969.

2. Laganelli, A. L., Nestler, D. E.: "Surface Ablation Pattern: A Phenomenology Study," AIAA J., vol. 7, no. 7, July 1969.

3. Wattendorf, F. L.: "A Study of the Effect of Curvature on Fully Developed Turbulent Flow," Proceedings of the Royal Society of London, Series A, Vol. CXLVIII, 1935.

4. Eskinazi, S.: "An Investigation of Fully Developed Turbulent Flow in a Curved Channel," The Johns Hopkins University, Mech. Eng. Dept., Report I-20, 1954.

5. Sawyer, R. A.: "Two-Dimensional Reattaching Jet Flows Including the Effects of Curvature on Entrainment," J. F. M., vol. 17, part 4, 1963.

6. Motzfeld, H.: "Die Turbulente Strömung on Wellign Wänden," Z. A. M. M., vol. 17, No. 4, August 1937.

7. Kendall, J. M.: "The Turbulent Boundary Layer Over a Wall with Progressive Surface Waves," J. F. M., vol. 41, part 2, 1970.

8. Shapiro, A.: "The Dynamics and Thermodynamics of Compressible Fluid Flow," Ronald Press, 1953.

9. Coles, D.: "The Young Person's Guide to the Data," A Survey Lecture Prepared for the 1968 AFOSR-IFP-Stanford Conference on Computation of Turbulent Boundary Layers.

10. Ludwieg, H. and Tillmann, W.: "Investigation of the Wall-Shearing Stress in Turbulent Boundary Layer," NACA TM 1285, May 1958.

11. Patel, V. C.: "Calibration of the Preston Tube and Limitations on its Use in Pressure Gradient," J. F. M., vol. 23, part 1, pp. 185-208, 1965.

12. Hsu, E. Y.: "The Measurement of Local Turbulent Skin Friction by Means of Surface Pitot Tubes," David Taylor Model Basin Report 957, 1955.

13. Bradshaw, B. A., and Gregory, M. A.: "The Determination of Local Turbulent Skin Friction from Observation in the Viscous Sub-Layer," R. & M. No. 3202, 1961.

References (Cont'd)

14. Preston, N. A.: "The Determination of Turbulent Skin Friction by Means of Pitot Tubes," J. of the Royal Aero. Soc., vol. 58, no. 110, Feb. 1954.

15. Bryer, D. W., Walshe, D. E., and Garner, H. C.: "Pressure Probes Selected for Three-Dimensional Flow Measurement," R. & M. 3037, 1958.

16. Höerner, S. F.: "Fluid Dynamics Drag," Author's Publication, 1965.

17. Millikan, C. B.: "A Critical Discussion of Turbulent Flows in Channels and Circular Tubes," Proceedings of the Fifth International Congress of Appl. Mech., 1938.

18. Schlichting, H.: "Boundary Layer Theory," McGraw-Hill, 1962.

19. Clauser, F. H.: "Turbulent Boundary Layers in Adverse Pressure Gradient," J. Aero. Sci., 21, 1954.

20. Lees, L.: "Turbulent Boundary Layer with Small Skin Friction," SAMSO TR-70-97, 1970.

21. Sawyer, R. A.: "Turbulent Wall Jets on Logarithmic Spiral Surfaces," The Aero. Quarterly, Vol. XVII, part 3, 1966.

22. Nakaguchi, H.: "Jet Along a Curved Wall," T. Moriya Memorial Seminar for Aerodynamics, R. M. No. 4, University of Tokyo, 1961.

23. National Bureau of Standards, "Handbook of Mathematical Functions," Appl. Math. Series, 55.

Unclassified

Security Classification

DOCUMENT CONTROL DATA - R&D

(Security classification of title, body of abstract and indexing annotation must be entered when the overall report is classified)

1. ORIGINATING ACTIVITY *(Corporate author)*

California Institute of Technology
Pasadena, California 91109

2a. REPORT SECURITY CLASSIFICATION

Unclassified

2b. GROUP

3. REPORT TITLE

Stability Theory for Cross Hatching, Part II. An Experiment on Turbulent Boundary Layer over Wavy Wall

4. DESCRIPTIVE NOTES *(Type of report and inclusive dates)*

Scientific Final

5. AUTHOR(S) *(Last name, first name, initial)*

Lester Lees, Toshi Kubota, Asher Sigal

6. REPORT DATE	7a. TOTAL NO. OF PAGES	7b. NO. OF REFS
April 1972	208	23

8a. CONTRACT OR GRANT NO.	9a. ORIGINATOR'S REPORT NUMBER(S)
F04701-68-C-0151	
b. PROJECT NO.	
c.	9b. OTHER REPORT NO(S) *(Any other numbers that may be assigned this report)*
d.	

10. AVAILABILITY/LIMITATION NOTICES

Distribution limited to U.S. Government agencies only; test and evaluation 14 Feb. 72. Other request for this document must be referred to SAMSO (RSSE).

11. SUPPLEMENTARY NOTES	12. SPONSORING MILITARY ACTIVITY
	SPACE AND MISSILE SYSTEMS ORGANIZATION (AFSC) Norton Air Force Base, Calif. 92409

13. ABSTRACT

An experimental investigation of turbulent boundary layer flow over wavy surfaces was conducted at low speed. Two models with the ratio of the amplitude to the wave length $a/\lambda = 0.03$ and wave lengths $\lambda = 6"$ and $12"$ were tested in an open-circuit wind tunnel. The free stream velocity was 15.4 m/sec, giving Reynolds number $Re = 2.54 \times 10^4$ per inch. Boundary-layer thickness varied from $\delta = 1.5"$ to $\delta = 4.1"$ by means of boundary-layer trips of various height, in order to change the ratio λ / δ The following measurements were taken: wall pressure distribution, average pressures, and shear stress distribution across the layer.

Wall pressure perturbation is much lower than predicted by uniform, inviscid theory and is slightly non-symmetric. Wall stress distribution has a peak with $C_f/C_{fo} = 1.2$ upstream of the crest and a dip of $C_f/C_{fo} = 0.6$ upstream of the trough.

The turbulence intensities and shear stress distributions near the wall show oscillatory modulation superimposed on the reference flat plate profiles. The amplitude of the oscillations decays exponentially toward the edge of the layer, so that in the outer part of the layer the turbulence quantities are practically independent of the longitudinal position.

DD FORM 1 JAN 64 1473

Security Classification

14. KEY WORDS	LINK A		LINK B		LINK C	
	ROLE	WT	ROLE	WT	ROLE	WT
Turbulence, Boundary Layer, Wavy Wall						

INSTRUCTIONS

1. ORIGINATING ACTIVITY: Enter the name and address of the contractor, subcontractor, grantee, Department of Defense activity or other organization *(corporate author)* issuing the report.

2*a*. REPORT SECURITY CLASSIFICATION: Enter the overall security classification of the report. Indicate whether "Restricted Data" is included. Marking is to be in accordance with appropriate security regulations.

2*b*. GROUP: Automatic downgrading is specified in DoD Directive 5200.10 and Armed Forces Industrial Manual. Enter the group number. Also, when applicable, show that optional markings have been used for Group 3 and Group 4 as authorized.

3. REPORT TITLE: Enter the complete report title in all capital letters. Titles in all cases should be unclassified. If a meaningful title cannot be selected without classification, show title classification in all capitals in parenthesis immediately following the title.

4. DESCRIPTIVE NOTES: If appropriate, enter the type of report, e.g., interim, progress, summary, annual, or final. Give the inclusive dates when a specific reporting period is covered.

5. AUTHOR(S): Enter the name(s) of author(s) as shown on or in the report. Enter last name, first name, middle initial. If military, show rank and branch of service. The name of the principal author is an absolute minimum requirement.

6. REPORT DATE: Enter the date of the report as day, month, year; or month, year. If more than one date appears on the report, use date of publication.

7*a*. TOTAL NUMBER OF PAGES: The total page count should follow normal pagination procedures, i.e., enter the number of pages containing information.

7*b*. NUMBER OF REFERENCES: Enter the total number of references cited in the report.

8*a*. CONTRACT OR GRANT NUMBER: If appropriate, enter the applicable number of the contract or grant under which the report was written.

8*b*, 8*c*, & 8*d*. PROJECT NUMBER: Enter the appropriate military department identification, such as project number, subproject number, system numbers, task number, etc.

9*a*. ORIGINATOR'S REPORT NUMBER(S): Enter the official report number by which the document will be identified and controlled by the originating activity. This number must be unique to this report.

9*b*. OTHER REPORT NUMBER(S): If the report has been assigned any other report numbers *(either by the originator or by the sponsor)*, also enter this number(s).

10. AVAILABILITY/LIMITATION NOTICES: Enter any limitations on further dissemination of the report, other than those imposed by security classification, using standard statements such as:

(1) "Qualified requesters may obtain copies of this report from DDC."

(2) "Foreign announcement and dissemination of this report by DDC is not authorized."

(3) "U. S. Government agencies may obtain copies of this report directly from DDC. Other qualified DDC users shall request through _____."

(4) "U. S. military agencies may obtain copies of this report directly from DDC. Other qualified users shall request through _____."

(5) "All distribution of this report is controlled. Qualified DDC users shall request through _____."

If the report has been furnished to the Office of Technical Services, Department of Commerce, for sale to the public, indicate this fact and enter the price, if known.

11. SUPPLEMENTARY NOTES: Use for additional explanatory notes.

12. SPONSORING MILITARY ACTIVITY: Enter the name of the departmental project office or laboratory sponsoring *(paying for)* the research and development. Include address.

13. ABSTRACT: Enter an abstract giving a brief and factual summary of the document indicative of the report, even though it may also appear elsewhere in the body of the technical report. If additional space is required, a continuation sheet shall be attached.

It is highly desirable that the abstract of classified reports be unclassified. Each paragraph of the abstract shall end with an indication of the military security classification of the information in the paragraph, represented as *(TS)*, *(S)*, *(C)*, or *(U)*.

There is no limitation on the length of the abstract. However, the suggested length is from 150 to 225 words.

14. KEY WORDS: Key words are technically meaningful terms or short phrases that characterize a report and may be used as index entries for cataloging the report. Key words must be selected so that no security classification is required. Identifiers, such as equipment model designation, trade name, military project code name, geographic location, may be used as key words but will be followed by an indication of technical context. The assignment of links, rules, and weights is optional.

DISTRIBUTION

Addressee	No. of Copies
Space and Missile Systems Organization Air Force Systems Command Norton Air Force Base, California 92409 Attn: RNSR (Maj. M. Mauldin)	1
Space and Missile Systems Organization Air Force Systems Command Norton Air Force Base, California 92409 Attn: SMYDM-1	1
Air University Library (AUL) Maxwell AFB, Ala 36112	1
Capt. F. Munoz RNSE Space and Missile Systems Organization Norton Air Force Base, California 92409	1
Aerospace Corporation P. O. Box 5866 San Bernardino, California 92402 Attn: Don Seiveino	10
Defense Documentation Center Cameron Station Alexandria, Virginia 22314	20
Arnold Engineering Development Center Tullahoma, Tennessee 37388 Attn: AES	1
AVCO Everett Research Laboratories 2385 Revere Beach Parkway Everett, Massachusetts 02149 Attn: P. Rose	1
U. S. Naval Ordnance Laboratory White Oak, Silver Springs, Maryland 20390 Attn: K. Lobb	1
Cornell Aeronautical Laboratory, Inc. P. O. Box 235 Buffalo, New York 14200 Attn: J. Carpenter	2
Institute for Defense Analyses 400 Army-Navy Drive Arlington, Virginia 22202 Attn: Classified Library	1

Addressee	No. of Copies
SPL-32 Naval Plant Representative Office Special Projects Office Lockheed Missiles and Space Company P. O. Box 504, Sunnyvale, California 94088	3
NASA-Ames Research Center Moffett Field, California 94035 Attn: H. K. Larson T. A. Canning	3
Assistant Deputy for Naval Applications Space and Missile Systems Organization Norton Air Force Base, California 92409 Attn: RNN	1
AVCO Corporation Missile Systems Division 201 Lowell Street Wilmington, Massachusetts 01887 Attn: REST Program Office A. Pallone V. DeCristina	3
General Electric Company-RSD Missile and Space Division Space Technology Center King of Prussia, Pennsylvania 19101 Attn: D. Nestler	2
BAMIRAC, University of Michigan Ann Arbor, Michigan 48103 Attn: Roy Nichols	1
Director of Defense Research and Engineering (Strategic Weapons) The Pentagon Washington, D. C. 20330 Attn: Capt. A. Julian	1
Massachusetts Institute of Technology Lincoln Laboratory P. O. Box 73 Lexington, Massachusetts 02173 Attn: BMRS Project	2
Advanced Research Projects Agency The Pentagon Washington, D. C. 20301 Attn: C. McLain	1

Addressee	No. of Copies
Navy Department Special Project Office Washington, D. C. Attn: SP-272	2
TRW Systems, Inc. One Space Park Redondo Beach, California 90278 Attn: L. Hromas	1
Air Force Flight Dynamics Laboratory Wright Patterson Air Force Base, Ohio 45433 Attn: A. Draper	1
Office of Aerospace Research Aerospace Research Laboratories Thermomechanics Branch Wright Patterson Air Force Base, Ohio 45433	1